UNIVERSIDAD DE GRANADA

Doctoral Thesis

Design, Characterization and Simulation of Electronic and Optoelectronic Nanodevices based on Bidimensional Materials

---

Author:
José María González Medina

Supervisors:
Dr. Francisco Javier García Ruiz
Dr. Isabel María Tienda Luna

A thesis submitted in fulfillment of the requirements
to obtain the International Doctor degree as part of the
Programa de Doctorado en Física y Ciencias del Espacio
in the

Pervasive Electronics Advanced Research Laboratory
Departamento de Electrónica y Tecnología de los Computadores

Granada, 25$^{\text{th}}$ November, 2019

UNIVERSIDAD DE GRANADA

Doctoral Thesis

Diseño, Caracterización y Simulación de Nanodispositivos Electrónicos y Optoelectrónicos basados en Materiales Bidimensionales

---

Author:
José María González Medina

Supervisors:
Dr. Francisco Javier García Ruiz
Dr. Isabel María Tienda Luna

A thesis submitted in fulfillment of the requirements
to obtain the International Doctor degree as part of the
Programa de Doctorado en Física y Ciencias del Espacio
in the

Pervasive Electronics Advanced Research Laboratory
Departamento de Electrónica y Tecnología de los Computadores

Granada, 25th November, 2019

Editor: Universidad de Granada. Tesis Doctorales
Autor: José María González Medina
ISBN: 978-84-1306-442-0
URI: http://hdl.handle.net/10481/59761

To Ana

With electronics, they just get smaller and smaller.

Amy Heckerling

Acknowledgements

Antes de empezar con este ladrillo, quisiera dar las gracias a unos cuantos seres que han tomado como propia la absurda y titánica tarea de apoyarme a lo largo de estos últimos cuatro años, algunos incluso desde antes. Lo primero de todo, quisiera dar las gracias a mis directores Fran Ruiz e Isa Tienda y a mi tutor Andrés Godoy por todo su apoyo y paciencia, y por las charlas tan constructivas mantenidas con ellos. Y no conforme con tres supervisores, quiero meter también en el saco a Enrique González como cuarto mosquetero, que me ha ayudado en igual medida. Entre todos, me han enseñado todo lo que sé, desde la evaluación de la probabilidad de túnel en heterointerfaces, hasta saber vestir adecuadamente en un congreso. Gracias por haberme hecho posible hacer realidad este sueño.

También quisiera dar las gracias a Andrés Castellanos y Zlatan Stanojevic, y sus respectivos equipos, quienes me han dado la oportunidad de visitarles en sendas estancias en sus centros de trabajo, y con los que tanto he aprendido. Quiero darle las gracias a Andrés y a Félix por abrirme los ojos en el campo de lo experimental y ayudarme en la medida de resultados que han sido de gran utilidad para esta tesis. Bueno, a Zlatan quizá no se lo agradezco tanto, que no me enseñó qué era aquella palabra, *oida* o como se escriba, y fui objeto de diversión por parte de un grupo de vieneses en un avión de vuelta a Madrid. Aunque con el tema de la linealización de las ecuaciones quizá sí que deba darle las gracias...

Por supuesto, quiero agradecer al Departamento de Electrónica y Tecnología de Computadores, no solo a la institución en sí, también a las personas que lo conforman, muchos de los cuales conocí previamente durante mi periodo como alumno de teleco, y que en uno u otro momento me han ayudado con alguna idea o papeleo. También agradecer a Francisco Gámiz, por su apoyo durante mi tiempo en su grupo de investigación en nanoelectrónica, así como a Noel Rodríguez por la ayuda prestada en el más reciente periodo de tiempo en su grupo de investigación PEARL (cuyo nombre completo aconsejo consultar por internet, merece la pena).

El trabajo en equipo no termina aquí, también quiero hacer mención a mis com-

pañeros y amigos de despacho, en especial a Alex Toral, con el que he compartido mis miserias sobre el simulador y sobre la vida del doctorando en general. El resto, consideraos mencionados y agradecidos en igual medida, que me falta página y ya sabéis que os aprecio mucho y todo eso.

Quisiera dar las gracias al Ministerio de Educación, Cultura y Deporte por haber financiado este proyecto a través del contrato FPU 14/02579. El esfuerzo de la institución pública en ir mejorando las condiciones de trabajo que tenemos los doctorandos becados durante estos últimos años ha sido más que destacable, y me alegra haber sido testigo de ese cambio.

Cómo no, quiero dar las gracias a mi familia, que me ha seguido ayudando y dando su amor después de tantos años. Estoy feliz por poder ver el amanecer después de tan oscura noche, y que nos acompañen casi todos en este mundo. Gracias también a mi abuela Marina, ojalá puedas ver que lo he conseguido allá donde estés. Descansa en paz.

La lista de amistades que en un momento u otro me han apoyado, o me han pegado un guantazo cuando era necesario, es bastante larga. Por agrupar un poco, y yendo por partes como Jack el Destripador, gracias al trío de sujetos que desde el instituto no ha cejado en sus intentos por sacarme de mis casillas. A los colegas de rol, por transportar mi mente por mundos increíbles. A mis compañeros de promoción, con muchos de los cuales sigo en contacto y cuyo consejo de sabios siempre tiene una respuesta para algo. A la parejita de Descenteando, ellos sabrán por qué, creo que tiene que ver algo con que son maravillosas personas. Y a todos aquellos que mi tonta cabeza esté pasando por alto, gracias de corazón.

Dejo para el final a la persona más importante de todas, ahora que voy cargado de emociones a estas alturas del texto. Podría escribir cientos de líneas sólo para ella, pero me he prometido no pasar de las dos páginas de agradecimientos. Quiero agradecer todo el apoyo y cariño que me ha dado Ana, quien a pesar de la distancia durante este último año y medio, nunca ha dejado de animarme y consolarme. Me dirijo a ti directamente, porque mereces todo mi agradecimiento, porque eres la luz que de manera desinteresada me ha guiado, en los días más nublados, y en las más claras mañanas, así como el sonido de la alegría para los buenos momentos. Solo doy gracias al destino y a nuestras locas cabezas el que un día nos llamase la atención una cría que juega con bichos y un niñato que hace ruiditos raros. Sigamos otros diez años juntos, y quiera la vida dejarnos multiplicar ese tiempo al menos por siete...

Contents

Part I

Prologue

Physical constants

Here are summarized the physical constants considered in this woek. The materials parameters are collected in Appendix D.

ε_0	vacuum permittivity	$8.85418782 \times 10^{-12}$ F/m
m_0	electron rest mass	$9.10938291 \times 10^{-31}$ Kg
h	Planck's constant	$6.62606957 \times 10^{-34}$ J×s
$\hbar$	reduced Planck's constant	$1.05457172 \times 10^{-34}$ J×s
k_B	Boltzmann's constant	$1.38064881 \times 10^{-23}$ J/K
q	elementary charge	$1.60217656 \times 10^{-19}$ C

Acronyms

2D Two dimensional.

AFM Atomic force microscopy.

BJT Bipolar Junction Transistor.

BTBT Band-to-band tunnel.

BTE Boltzmann transport equation.

CVD Chemical Vapor Deposition.

DD Drift-Diffusion.

DoS Density of states.

EMA Effective Mass Approximation.

FDM Finite differences method.

FET Field Effect Transistor.

FinFET Fin field effect transistor.

FTO Fluorine-doped Tin Oxide.

GIS Graphene-insulator-Silicon stack.

GS Graphene-Silicon stack.

Ho Homopolar phonon mode.

ITO Indium Tin oxide.

LA Longitudinal acoustic phonon mode.

LO Longitudinal optical phonon mode.

MRT Momentum relaxation time.

MuJ Multi Junction solar cells.

POP Polar optical phonon mode.

SAMANTA Simulator of Multipurpose Advanced Nanodevices for Transport Applications.

SBH Schottky barrier height.

SMU Source-measurement unit.

SOS Semiconductor-Oxide-Semiconductor.

SP1D Schrödinger-Poisson one dimensional.

SPC Scanning photocurrent.

SRH Shockley-Read Hall recombination.

TA Transversal acoustic phonon mode.

TCF Transparent Conductive Films.

TE Thermionic Emission.

TFE Thermionic-Field Emission.

TMD Transition Metal Dichacolgenide.

WKB Wentzel-Kramers-Brillouin approximation.

List of Symbols

$\mathbf{A}$ Area.

$\alpha_{\mathbf{np}}$ Non-parabolicity factor.

$A^*_{\mathbf{n}}$ Electron Richardson constant.

$A^*_{\mathbf{p}}$ Hole Richardson constant.

$\boldsymbol{B}$**'** Bernoulli function.

$B_{\mathbf{Rad}}$ Radiative capture probability.

ρ Charge distribution.

n Electron density.

$n_{\mathbf{i}}$ Intrinsic density.

p Hole density.

n_0 Electron density in equilibrium.

p_0 Hole density in equilibrium.

$N^+_{\mathbf{D}}$ Ionized donor impurities.

$N^-_{\mathbf{A}}$ Ionized acceptor impurities.

$N_{\mathbf{T}}$ Trap density.

$C_{\mathbf{n}}$ Electron Auger capture probability.

$C_{\mathbf{p}}$ Hole Auger capture probability.

$\boldsymbol{J_n}$ Electron current density.

$\boldsymbol{J_p}$ Hole current density.

$\delta_{\mathbf{n}}$ Electron contribution of the tunnelling mechanism.

$\delta_{\mathbf{p}}$ Hole contribution of the tunnelling mechanism.

$D_{\mathbf{it}}^{\mathbf{a}}$ DoS for acceptor traps.

$D_{\mathbf{it}}^{\mathbf{d}}$ DoS for donor traps.

$D_{\mathbf{n}}$ Electron diffusivity.

$D_{\mathbf{p}}$ Hole diffusivity.

$D_{\mathbf{ph}}$ Deformation potential of the specified phonons.

$D_{\mathbf{ref}}$ Reference graphene-Silicon photodiode.

D_x Graphene-Silicon photodiode with x microns width of GIS stack.

$E_{\mathbf{c}}$ Conduction band.

$E_{\mathbf{D}}$ Dirac point for graphene.

$E_{\mathbf{v}}$ Valence band.

$E_{\mathbf{i}}$ Intrinsic level.

$E_{\mathbf{fn}}$ Electron pseudo-Fermi level.

$E_{\mathbf{fp}}$ Hole pseudo-Fermi level.

$\chi_{\mathbf{sc}}$ Semiconductor electron affinity.

$E_{\mathbf{T}}$ Trap energy.

$E_{\mathbf{g}}$ Energetic bandgap.

$E_{\mathbf{p}}$ Kinetic energy.

$E_{\mathbf{a}}$ Centred energy of Gaussian trap DoS.

$\boldsymbol{E}$ Energy subbands.

$E_{\mathbf{ext}}$ Uniform external electric field.

$E_{\mathbf{field}}$ Electric field.

E_x Energy at position x.

$E_{\mathbf{v,W}}$ Valence band minimum far from the junction.

$x_{\mathbf{E}}$ Spatial position with energy E.

$\Delta E_{\mathbf{c}}^{\pm}$ Conduction band jump at each side of a junction.

$E_{\mathbf{c}}^{\mathbf{max}}$ Conduction band maximum at a junction.

$E_{\mathbf{c,I}}^{\mathbf{min}}$ Conduction band minimum at a junction.

$E_{\mathbf{c,W}}$ Conduction band maximum far from the junction.

$\Delta E_{\mathbf{v}}^{\pm}$ Valence band jump at each side of a junction.

$E_{\mathbf{v}}^{\mathbf{min}}$ Valence band minimum at a junction.

$E_{\mathbf{v,I}}^{\mathbf{max}}$ Valence band maximum at a junction.

E_i Energy subbands.

ε Relative permittivity.

$\boldsymbol{\varepsilon}$ Dielectric tensor.

$\varepsilon_{\mathbf{D}}$ Scalar dielectric function.

η_i Orthogonal wavefunctions.

$f_{\mathbf{s}}$ Occupation probability in the semiconductor.

$\mathcal{F}_{1/2}$ Complete Fermi–Dirac integral of index 1/2.

$\mathcal{F}_{1/2}^{-1}$ Inverse operator of the complete Fermi–Dirac integral of index 1/2.

$f_{\mathbf{m}}$ Occupation probability in the metal.

$f^{\mathbf{n}}$ Electron occupation probability.

$f^{\mathbf{p}}$ Hole occupation probability.

$F_{j,i}$ Form factor between the i-th and j-th subbands.

$G_{\mathbf{n}}$ Electron generation rate.

$R_{\mathbf{n}}$ Electron recombination rate.

$G_{\mathbf{p}}$ Hole generation rate.

$R_{\mathbf{p}}$ Hole recombination rate.

$g_{\mathbf{v}}$ Valley degeneracy.

H_{ν} Step function.

$I_{\mathbf{ph}}$ Photocurrent.

$\mathbf{k}$ Position in the reciprocal space.

α Light absorption coefficient.

$E_{\mathbf{ph}}$ Photon energy.

λ Light wavelength.

ω Light frequency.

$P_{\mathbf{opt}}$ Light power density.

$m^{\mathbf{n}}_{\mathbf{eff}}$ Electron effective mass.

$m^{\mathbf{p}}_{\mathbf{eff}}$ Hole effective mass.

$M_{i,j}$ Matrix element.

N_{II} Volumetric density of Coulomb centres.

$\mu_{\mathbf{n}}$ Electron mobility.

$\mu_{\mathbf{p}}$ Hole mobility.

$\nabla\cdot$ Divergence operator.

∇ Gradient operator.

$N_{\mathbf{c}}$ Electron effective density of states.

$N_{\mathbf{v}}$ Hole effective density of states.

$n_{\mathbf{ph}}$ Phonon number.

$\nu_{\mathbf{F}}$ Fermi velocity of graphene.

O Error coefficient.

$\omega_{\mathbf{ph}}$ Phonon frequency.

$\phi_{\mathbf{m}}$ Metal workfunction.

$\delta\phi_{\mathbf{m}}$ Barrier lowering of the metal workfunction.

ψ Electric potential.

Ψ Wavefunctions.

$\psi_{\mathbf{B}}$ Schottky barrier height.

$\psi_{\mathbf{pc}}$ Scattering potential.

$\mathbf{Q}$ Transition between the initial and final state $\|\|$.

$Q_{\mathbf{it}}$ Interface charge.

$Q_{\mathbf{S}}$ Space charge per unit area.

$\mathbf{R}$ Responsivity.

$\boldsymbol{r}$ Vector position.

$R_{\mathbf{SRH}}$ SRH recombination.

$R_{\mathbf{Rad}}$ Radiative recombination.

$R_{\mathbf{Aug}}$ Auger recombination.

$G_{\mathbf{light}}$ Light generation.

$\boldsymbol{r}_{\mathbf{I}}$, $\boldsymbol{r}_{\mathbf{i}}$ Interface vectors position.

$\mathbf{sgn}$ Sign function.

$\sigma_{\mathbf{E}}$ Standard deviation of Gaussian trap DoS.

T Temperature.

t Time.

$\tau_i^{\mathbf{ph}}$ MRT of the specified phonons in the i subband.

τ_i Momentum relaxation time of the i-th subband.

$\tau_{\mathbf{n}}$ Electron mean lifetime.

$\tau_{\mathbf{p}}$ Hole mean lifetime.

$T_{\mathbf{n}}$ Electron transmission probability.

$T_{\mathbf{p}}$ Hole transmission probability.

$U_{\mathbf{Kane}}$ Band-to-band tunnelling net generation-recombination, Kane model.

$U_{\mathbf{bb}}$ Non local BTBT net generation-recombination.

$g_{\mathbf{bb}}$ Kane or Hurkx model for non local BTBT net generation-recombination, Kane model.

$V_{\mathbf{R}}$ Reverse bias.

$v_{\mathbf{s}}$ Sound velocity for a given phonon process.

$v_{\mathbf{th}}^{\mathbf{n}}$ Electron thermionic velocity in the contact.

$v_{\mathbf{th}}^{\mathbf{p}}$ Hole thermionic velocity in the contact.

Abstract

PEARL Research Group
Departamento de Electrónica y Tecnología de los Computadores

Design, Characterization and Simulation of Electronic and Optoelectronic Nanodevices based on Bidimensional Materials

by José María González Medina

This Doctoral Thesis aims to study the electronic and optoelectronic properties of devices based on 2D materials and their heterostructures, with emphasis in photodiodes and phototransistors.

For this purpose, a numerical method to self-consistently solve the 2D Poisson and Drift-Diffusion equations is developed, which also allows the evaluation of the 1D Schrödinger equation to calculate the carrier mobility. The code is able to handle arbitrary combinations of semiconductor and isolator materials, solving the direct or band-to-band tunneling in heterojunctions, and considering Ohmic or Schottky contacts. Generation-recombination effects such as light generation, SRH, Auger and Radiative recombinations are also included. Finally, traps with arbitrary energetic profile are implemented. To accelerate the convergence of the simulator, the Newton-Rhapson linearisation scheme is implemented.

The numerical method developed is applied in this Thesis to evaluate different electronic and optoelectronic devices of interest based on bidimensional materials.

First, a theoretical study of the electron mobility in field effect transistors based on MoS_2 is performed, where it is shown that, at room temperature, polar optical phonons constitute the most important scattering mechanism, while at low temperature acoustic phonons and Coulomb-limited mobility need to be considered.

In collaboration with Prof. Max Lemme (RWTH Aachen) and his group, a pho-

todiode with interdigitated graphene-silicon and graphene-insulator-silicon regions is analyzed in detail. Experimental results show that the presence of the insulator regions increases the device photoresponse. Our simulations demonstrate that this improvement is due to the degradation of the graphene-silicon interface.

Later, a $MoTe_2$ channel phototransistor is studied, with emphasis in the influence of traps on the photocurrent, through the so-called photogating effect, which in the appropriate conditions can provide a high photoconductive gain.

Finally, a low-cost fabrication technique for submicron phototransistors based on MoS_2 with graphene contacts, developed in collaboration with Dr. Andrés Castellanos (IEEE-CSIC), is presented. A full characterization is performed: structural, electronic and optoelectronic. The simulations allow us to estimate the most relevant parameters of the fabricated devices (i.e., mobility, Schottky barrier height, traps profile, etc.) and analyze with detail the active area and responsivity of the devices.

In summary, our work delves into the potential applications of bidimensional materials and which elements should be taken into account in their fabrication, focusing on the influence of contacts and the quality of the interfaces with other materials.

Resumen

PEARL Research Group
Departamento de Electrónica y Tecnología de los Computadores

Diseño, Caracterización y Simulación de Nanodispositivos Electrónicos y Optoelectrónicos basados en Materiales Bidimensionales

por José María González Medina

Esta Tesis Doctoral tiene como objetivo el estudio de las propiedades electrónicas y optoelectrónicas de dispositivos basados en materiales 2D y heteroestructuras que los contengan, con especial énfasis en fotodiodos y fototransistores.

Para ello, se desarrolla un simulador que resuelve autoconsistentemente las ecuaciones de Poisson y Deriva Difusión en dos dimensiones, y que permite también resolver la ecuación de Schrödinger para evaluar la movilidad de portadores. El programa admite combinaciones arbitrarias de materiales aislantes o semiconductores, considerando túnel directo o banda a banda en las heterouniones, así como contactos óhmicos o de tipo Schottky. Es posible también considerar efectos de generación-recombinación que modelan distintos fenómenos físicos, tales como generación por luz o recombinaciones SRH, Auger y Radiativa. Por último, se ha implementado el modelado de trampas con perfiles energéticos arbitrarios. Para acelerar la convergencia del código, se hace uso del método de linealización de Newton-Rhapson.

El método numérico desarrollado se aplica en la Tesis a la evaluación de distintos dispositivos electrónicos y optoelectrónicos de interés basados en materiales bidimensionales.

En primer lugar, se realiza un estudio teórico de la movilidad electrónica en transistores de efecto campo basados en MoS_2, donde se observa la importante influencia de la dispersión debida a los fonones ópticos polares a temperatura ambiente, y de los fonones acústicos y la dispersión de Coulomb a baja temperatura.

En colaboración con investigadores del grupo del Prof. Max Lemme (RWTH Aachen), se analiza un fotodiodo formado por heterouniones interdigitadas de grafeno-silicio y grafeno-aislante-silicio. En este fotodiodo se ha comprobado experimentalmente la mejora de la fotorespuesta debido a la presencia de la región oxidada. Nuestras simulaciones demuestran que esta mejora es debida a la degradación de la interfaz entre el grafeno y el silicio.

Se estudia también un fototransistor con canal de $MoTe_2$, haciendo énfasis en la influencia de las trampas en la fotocorriente, a través del denominado efecto de 'photogating', que en las condiciones apropiadas puede dar lugar a una elevada ganancia fotoconductiva.

Por último, se presenta una técnica de bajo coste desarrollada en colaboración con el Dr. Andrés Castellanos (IEEE-CSIC) para la fabricación de fototransistores submicra de MoS_2 y contactos de grafeno, y se caracterizan estructural, electrónica y ópticamente los dispositivos resultantes. Las simulaciones realizadas nos permiten estimar los parámetros más relevantes de los dispositivos fabricados (movilidad, barrera Schottky, perfil de trampas, etc.) y analizar con detalle el área activa y responsividad de los dispositivos.

En conjunto, el trabajo desarrollado profundiza en las aplicaciones potenciales de los materiales bidimensionales y en qué elementos deben tenerse en cuenta en su fabricación, enfocándose en la influencia de los contactos y de la calidad de las interfaces con otros materiales.

Chapter 1

Introduction

1.1 The prelude of a dream come true

For most of us, any ordinary day would start setting off the alarm of our mobile phone. Then, we connect with the news application, read what has happened on the other side of the world while we were sleeping, and continue with our morning routine. One of these regular mornings, people from this side of the globe read a piece of news from NASA announcing: "American Astronauts will land on the Moon in 2024: NASA Accepts Challenge" [1]. Two immediate reactions may be born in our brains: *That is wonderful!*, and *What business do we have in the Moon?*. In no case we ask ourselves about the viability of the project, as we trust that there is a corporation supporting it with the determination, the facilities, the talent and the economical resources necessary to success in such endeavor. The NASA might as well have announced the next invention of the gravitic spaceship, like the one mentioned in the Foundation saga of Isaac Asimov, and we would have relied on the astonishing possibility that some inventive (or crazy) enough team would be capable of dealing with it.

That wonderful naivety, derived from the confidence in ourselves, is product of a continuous and successful race, in which the opponent has been usually the human being itself. More than 2000 years has our calendar, but just the last 70 years are enough to dizzy any inattentive person. The society has changed its way to wake up, to eat, to dress, even to think. The unerring basis where this deep change is founded is the continuous technology evolution. Every step forward, whether big or small, had its own role modifying the society. And, in turn, the basis of this technology is grounded on a

concept as simple as effective: the information, whose foundations were established by Claude Shannon, the father of the information theory [2].

In the past, the possibility of storing, carrying, sharing and displaying information was complex, expensive and time consuming. Even after the invention of the vacuum tubes, already developed at the beginning of the 20th century, managing information was challenging. Fortunately, during the same years in which the basis of the information theory were being established, the key solution to achieve this task, the solid state transistor [3], was developed. Initially, the Bipolar Junction Transistor, or BJT, invented in 1948 by Bardeen, Brattain and Shockley, would lead to develop the first solid state commercial radio, known as Regency TR-1 [4]. Just one decade afterwards, in 1959, two breakthroughs sparked the revolution of the information and communication technologies: The invention of the Metal-Oxide-Semiconductor (MOS) transistor by Mohamed Atalla and Dawon Kahng at Bell Labs [[5]] and the integrated circuit. There is some controversy about the fathers of this last invention, though we can mention here Jack Kilby from Texas Instrument and Bob Noyce from Fairchild Semiconductor.

These elements were rapidly commercialized after overcoming the numerous problems that their development had to face. Some of these challenges were related to the lack of knowledge of the physical mechanisms controlling the carrier transport inside the semiconductors, the inherent problems to grow different materials and their interfaces, or the lack of reliability of the final products. So much so, that Donald G. Fink, Philco's director of research, talked about the potential of the transistor in this way: "Is it a pimpled adolescent, now awkward, but promising future vigor? Or has it arrived at maturity, full of languor, surrounded by disappointments?" [6]. Nowadays, it is clear that his first assertion was the right one.

Each progress in the solid state devices development has approached us to our present society. The basic element of this technology revolution, the so-called Metal-Oxide-Semiconductor Field-Effect Transistor (MOSFET), has seen how its first concept was muted and adapted, in an endless effort to meet a prediction, or better a promise, known as Moore's law in honour to Gordon Moore, who quite rightly estimated in 1965 the market tendency: that every 12 months, the number of components per chip would duplicate [7]. One decade later, this formula was revised to every 18 months. Almost like a dogma of faith, the companies and research centres have striven since then to accomplish this law. Today, complex designs endeavour to solve the different issues that the next technological nodes face [8, 9]. Some of these improvements are the use of strained materials [10, 11] to improve the carrier mobility; of high-κ insulators

between the gate and the channel to reduce the leakage current [12, 13, 14]; or the application of several gates controlling the channel, instead of the standard planar top-gate of traditional bulk devices [15, 16, 17], giving rise to different non-planar Multiple Gate designs. In this way, the Silicon technology has been stretched to fulfill the market and society demands (and in other cases creating new ones).

As a third leg of the stool, the electronic devices used to manage the important information need to be supplied with energy. In this context, the interest for efficient photovoltaic generation systems is rocketing due to two main reasons. First is the growing concern created by the global warming, that requires the shift to a new paradigm of energy generation based on renewable sources. In this sense, wind and solar energies are expected to cover almost one third of the global energy needs by 2023 [18]. Second, is the massive deployment of autonomous sensors and systems that support the so-called Internet-of-Things. Most of them will be located far from wired power supplies and some kind of energy harvesting system must be incorporated to increase the operative life of those systems.

In the case of sun light harvesting, solid state materials play a main role in the photovoltaic generation. The first efforts to develop solar panels based on Silicon were leaded in 1954 by Daryl Chapin, Calvin Fuller and Gerald Pearson, fabricating 6% efficiency harvester [19]. Since then, the efficiency of photovoltaic devices have not stopped improving. As an example, Multi Junctions solar cells (MuJ) created stacking multiple materials with gradual bandgaps (the third generation of solar cells [20]), have demonstrated efficiencies above 25% [21] and even 40% in some specific conditions [22]. The development of the photovoltaic industry is so remarkable, that recently the W·h price of their electricity has dropped below the cost of the energy generated from non renewable sources like coal [23].

The progress of all the aforementioned fields is mainly based on the profound knowledge of the Silicon technology acquired after decades of work. However, this material shows some physical limitations that preclude its effective usage in some applications, and brakes its potential in others [24]. To overcome these challenges, numerous alternative routes are being considered, such as the investigation of new materials that complement or substitute Silicon for specific purposes. One of these alternatives is the precursor of works like this Thesis, the isolation of a material known today from Boehm et al.'s work as graphene, or sp^2-hybridized Carbon [25]. Its astonishing properties inspired a debate about the usage of this and other new materials in the world of electronics, which still remains.

1.2 Graphene, the firstborn

The word graphene refers to a portion of a well known material, graphite. Typically used to produce pencils, it is composed of multiple Carbon layers arranged in hexagonal honeycomb panels, with an in-plane distance among atoms of 1.42 Angstrom and 3.45 Angstrom between layers [26]. The covalent bonds that keep the atoms united inside each layer are very strong, but the forces between layers, known as van der Waals forces, are not so intense. This weak interaction among layers facilitates their exfoliation, an useful property for its application as industrial dry lubricant. Graphite has also been commonly used as electrode, because its in-plane conductivity is very high, up to 10^5 S/cm depending on the fabrication process [27, 28]. In addition, graphite has an excellent thermal conductivity. In short, graphite shares many characteristics of metals. However, the most interesting properties of this material bloom when it is exfoliated up to isolate one single Carbon layer. Geim and Novoselov [29] successfully carried out this exfoliation process in 2004, what allowed them to analyse graphene properties experimentally, and awarded them the Nobel prize in physics in 2010 [30]. After the development of different mass production techniques [31], these properties were extensively analyzed.

Graphene shows excellent thermal and mechanical properties, both individually and in combination with other materials. The hybridized sp^2 bonds that compose its hexagonal structure [32] confers upon graphene a big resistance to be deformed, with a Young's module of around 1 TPa, and an intrinsic strength of 130 GPa [33]. Its high fracture toughness is only endangered by the presence of cracks and voids in the sheets [34]. These properties are important for its use in complex nanodevice designs, as enhanced mechanical properties reduce the possibilities of a physical break in fragile tiny devices. "The interface is the device", citing Kroemer's words from his Nobel lecture [35], and indeed, that is a law in this kind of two-dimensional (2D) materials, which presents a high surface to thickness ratio. This feature opens a wide range of possibilities, as graphene can be functionalized and then employed as a container of numerous active principles and compounds, and used to select, carry and deliver biomolecules and pharmaceutical products [36]. Also, it is possible to employ it as a detector of adsorbents, as the presence of ions rapidly modifies its conductivity [37, 38, 39]. Sensors formed by single layers of graphene deposited between two electrodes can work as biotransistors activated or deactivated by the presence of tiny amounts of ions or molecules [40, 41, 42].

The key of graphene, the property that makes this material so interesting, is related to its band structure [43, 44]. Free-standing monochrystalline graphene presents a conical band diagram, as depicted in Fig. 1.1, where the conduction and valence bands are in touch with each other at the so-called Dirac-point, which makes that electrons in graphene behave as massless two-dimensional particles [43]. This feature lends graphene the behaviour of a semi-metal and some additional properties such as:

- Extremely high carrier mobility. Outstanding values, over hundreds of thousands cm^2/Vs, have been measured in ideal conditions [45]. This is substantially higher than the typical 1400 cm^2/Vs electron mobility in Silicon [46] and well above other high mobility materials, such as InAs [47, 48], InSb [49] or InP [50]. Moreover, the 2D nature of this material would shield transistors made of this material from the undesired short channel effects (SCEs).

- Ambipolarity. The Fermi level can be tuned continuously in the conduction or valence band as a function of the applied bias [51, 52]. This property is useful to electrostatically modify the doping of different regions, creating p-n junctions without any chemical doping. Moreover, as its Fermi level can be electrostatically tuned, it could be possible to fit the workfunction of different contacted materials, generating ohmic contacts as their corresponding resistance is minimized [53]. The ambipolar, gap free feature of graphene can be appraised as an advantage, but it would also become a challenge if used as the channel of FETs [54], due to the impossibility of switching it off. To overcome this problem and increase the ON/OFF current ratio, several alternative structures have been proposed, such as tunnel the field-effect transistors [55, 56, 57]. An interesting option is the use of bilayer structures, as they present a finite bandgap when the sheets are under the influence of a transversal electric field, or when a doping is implanted (Figure 1.1).

The fascinating properties of graphene are fuelling applications in a wide variety of emerging fields, not so far just theoretical entelechies, as e.g. topological insulators or valleytronic-based devices [58, 59]. In the case of optoelectronic devices, a high material absorbance is required to maximize the conversion of photons into carriers. For free-doped graphene flakes, their gapless nature allow them to absorb light in a broad spectrum range, from ultraviolet up to terahertz frequencies [60]. For photon energies below 3 eV, the light absorption of one single Carbon sheet is 2.3 % [61], which linearly

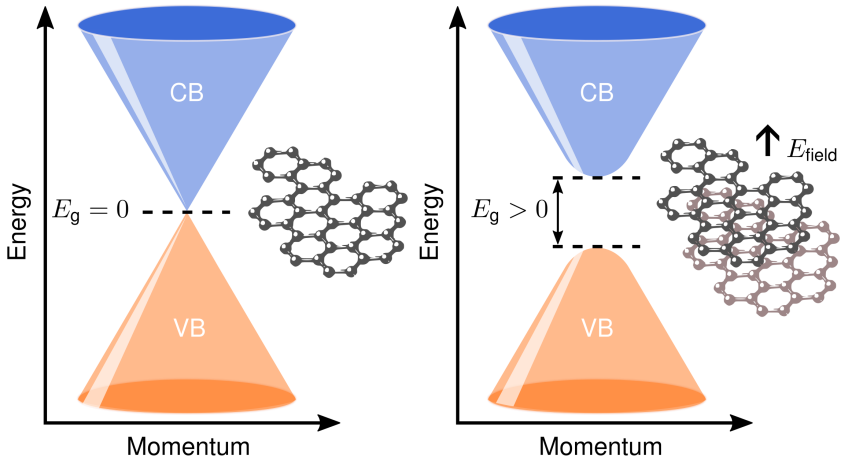

Figure 1.1: Band diagrams of (left) monolayer graphene and (right) bilayer graphene, the latter under a transversal electric field. Conduction and valence bands touch at the Dirac point for pristine monolayer sheets. In the multilayer scenario, the non-null gap between the bands can also be appreciated when the layers are functionalized [65].

increases with the number of layers [62]. This is a spectacular absorbance for just one single atom thick layer, but at the same time this value makes monolayer graphene practically transparent. This fact, together with its high ambipolar conductance, makes graphene a suitable candidate as a transparent electrode to be employed in photovoltaic devices [63, 64].

1.3 The family grows up

The two-dimensional (2D) nature of graphene encompasses as many advantages as technological challenges, and has paved the way to other 2D materials, with complementary properties in such a way that their combination creating heterojunctions can produce new structures and functionalities. A whole new family of 2D materials has recently appeared to complement graphene, each one with their own peculiarities.

Fig. 1.2 depicts some representative members, including native insulators, like hexagonal Boron Nitride h-BN, semiconductors, as most of the Transition Metal Dichalcogenides (TMDs), metals like TiS_2, superconductors, and topological insulators such as $NbSe_2$ and Sb_2Te_3, respectively [32, 66]. The weak interaction between layers due to the van der Waals forces, allows to stack different materials, making new van

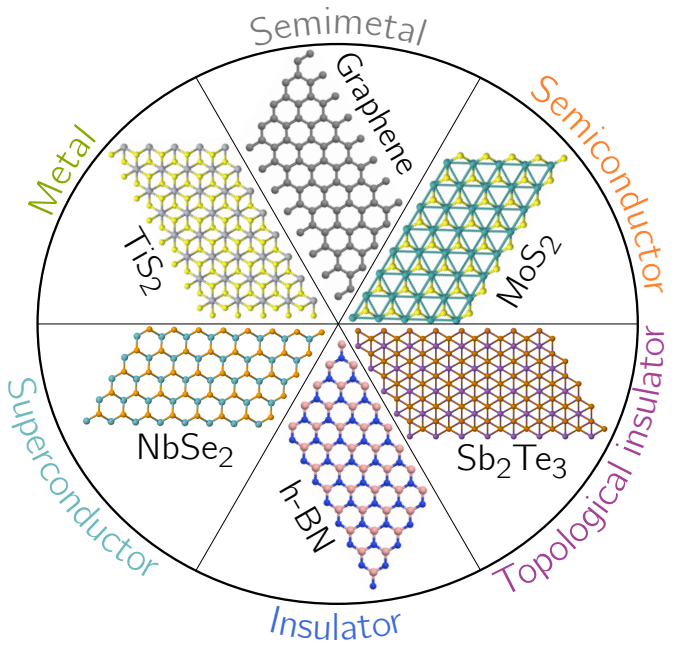

Figure 1.2: The denomination of 2D materials encompasses a wide variety of materials with different properties, which can be combined to design and create a full new set of devices based on them. Figure inspired in [32]. Structures obtained with [69].

der Waals heterostructures [67], in a sort of Lego game as shown in the already iconic picture of Fig. 1.3 [68].

In the case of the TMDs, their cell structure (MX_2) is formed by one transition metal atom (Mo,W) and two chalcogens (S, Se, or Te). The palette is very rich and offers a wide variety of materials that behaves as semiconductors or metals. Even one specific material can show different behaviour depending on its phase, as it is the case of the semiconductor 2H-MoS_2 and the metallic 1T-MoS_2 [70]. In these materials (and others like black Phosphorous [71, 72, 73, 74, 71]), the monolayer material differs from its bulk counterpart, as the quantum confinement makes them transit from an indirect bandgap in the multi layer (ML) situation [75] to a direct one for the single layer (SL) case [76, 77, 78]. In contrast to graphene, some TMDs are semiconductors with sizeable bandgaps, so they may be used in logic circuits [79, 80, 81, 82, 83]. Their atomic body thickness makes them appropriate to control the SCEs, as the channel can be efficiently controlled by the gate [84]. Some of these materials, such as MoS_2 or WS_2, also show high absorption coefficients, around 5-10% [85], values comparable to those obtained

with Silicon. Besides, their different absorption spectra can complement the ones of Silicon and III-V compounds. This property may be useful to design photodetectors for specific wavelength ranges [86, 87, 63, 88, 89], multijunction solar cells with higher efficiencies when combined appropriately [90, 91, 92, 93, 94], as well as ultrathin solar cells [85]. Light emitting diodes have also been fabricated making use of them [95, 96, 97, 98, 99, 100].

In spite of their many advantageous properties, 2D materials still face many challenges. Some of them are related to achieving an optimal, efficient and scalable fabrication process [101, 102, 103]. The synthesis of pristine samples is by itself a difficult task [104, 105]. In addition, the introduction of new materials and fabrication techniques is not a straightforward procedure as it requires time and expensive investments. To relax the complexity of this process, a first approach would be the coexistence of both bulk and 2D materials, in a way that the inherent characteristics of each one can be combined in specific applications [106, 107, 108]. This combination may face new difficulties such as the presence of interface traps and point defects at the interface between bulk and 2D semiconductors, which increases their contact resistance [109, 110, 111]. The combination of 2D and 3D materials also rises the phonon scattering rate, dropping the carrier mobility and increasing the recombination rates, and consequently clouding their potential as logical or optoelectronic devices [112, 113]. Hence, numerous challenges have still to be overcome before these materials result in practical devices outperforming current ones [110, 114].

At this point, we could wonder how we can distinguish between a little or a big step in the technology evolution. Who knows whether the day the first field effect transistor was manufactured, this was considered a little or a great step. In any case, nowadays there is no doubt about its transcendence. In a parallel reasoning, it seems already demonstrated that the petty action of sticking graphite to a piece of adhesive tape has produced a great step forward in the science of materials and other related fields. However, for the time being it is still not so clear whether they will produce such a huge impact on the society. In order to get that far, it is required to acquire a deeper knowledge of their properties and working principles.

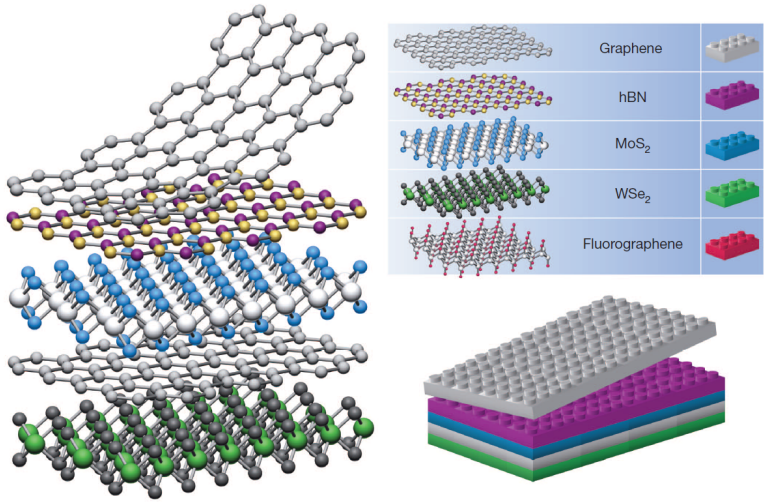

Figure 1.3: Vertical stacking of 2D materials forming heterostructures. Reprinted by permission from Springer Nature, Van der Waals heterostructures, A. K. Geim and I. V. Grigorieva, copyright © 2013 [68].

1.4 Objectives

Understanding the physical mechanisms that rule the behaviour of 2D materials, their heterojunctions and devices, is essential to assess how far it is possible to progress making use of them. Both, theoretical and experimental results will help to complete the remaining pieces of the puzzle, providing us with new and smart solutions to complement or even surpass the Silicon technology.

With this aim in mind, this Thesis is focused on the study of the electronic and optoelectronic properties of different devices based on 2D materials, with emphasis on photodiodes and phototransistors. The main objectives of this work are:

- The development of a numerical simulator designed to study the electrostatics and charge transport performance of arbitrary electronic and optoelectronic devices, paying special attention to the involved heterostructures.

- The numerical analysis of 2D-based devices, aiming to analyze different properties, including:

  - The electron mobility limited by different scattering mechanisms in back-gated transistors with few-layer MoS_2 as channel.

  - The influence of the interfaces in the light-to-current (mA/W) conversion capability of hybrid bulk-2D interdigitated Schottky and MIS heterojunctions.
  - The impact of interface traps on the photogating effect in phototransistors based on few-layer 2D materials.
  - The contact resistance and Schottky barrier height in junctions encompassing few-layer 2D materials. Here we include the development of new techniques to manufacture symmetrical, low cost, n-type contacts for 2D materials.

1.5 Outline

After this brief introductory Chapter, the main document is divided into two parts: the first one deals with the description of the developed numerical tool, and the second one focuses on the calculated results, together with the discussion of the main conclusions. A more detailed summary is found next:

- The first part consists of a comprehensive shelling of the numerical tool developed to study the 2D materials based nanodevices. Chapter 2 presents all the equations applied in the simulator, named SAMANTA. This Chapter is complemented by Appendices A to D. The appendix sections detail some mathematical issues: the discretization of the equations included in the simulator is presented in Appendix A, and their linearisation using the Newton method in Appendix B. Appendix C includes some relevant considerations about the boundary conditions of the structure under study. Finally, the physical magnitudes of the studied semiconductors are compiled in Appendix D.

- The second part comprises the results simulated and measured in different devices, inspired by real experiments. Such results are presented and discussed along four Chapters:

  - Chapter 3 calculates the phonon and Coulomb scattering limited electron mobility in a back-gated transistor, where the channel consists of few-layer MoS_2. The relative contribution of each mechanism is assessed at different temperatures, electron densities and semiconductor thicknesses.
  - Chapter 4 explores the hybridization of bulk Silicon devices by adding graphene as a top contact, producing photodiodes for potential light detectors.

This analysis is extended to ponder the effect of degraded 2D-bulk interfaces.

  - Chapter 5 presents a twofold study. It firstly analyzes the importance of the tunnel current through the contacts formed by metals deposited over few-layer $MoTe_2$ channels, and secondly, the influence of the photogating effect enhanced by interface traps at the oxide-semiconductor junction of the $MoTe_2$ phototransistors.
  - Chapter 6 explains a new experimental technique developed to create symmetrical graphite contacts for arbitrary 2D materials. Then, the Schottky junction and the optoelectronic properties of some graphite-MoS_2 phototransistors are studied both, experimental and numerically.

- Finally, the main conclusions of this Thesis, as well as the future work are enumerated in Chapter 7.

Part II

Simulator

Chapter 2

Electron devices models: background

2.1 Introduction

Numerical tools have become essential to evaluate the behaviour of complex electronic systems, where the material physical properties and devices features mix in an intricate way. In this Thesis, we have designed and implemented from scratch a simulation tool to study the electrostatics and transport properties of arbitrary structures made of metals, oxides and semiconductors in a two dimensions system. We have called it SAMANTA: Simulator for All Modern Assembled Nanodevices Transport Applications. This Chapter aims to introduce the equations used for its implementation, as well as a brief explanation about the simulator workflow.

The simulator comprises the Poisson and continuity equations, with the transport evaluated in a drift-diffusion scheme. This level of approximation is the more appropriate to model current experimental devices based on 2D-materials, whose dimensions are above the carrier mean free path and can be accurately explained under a semi-classical drift-diffusion framework [108, 115].

The rest of this Chapter is organized as follows. The expressions for Poisson and continuity equations are presented in Section 2.2. In the case of metal-semiconductor, semiconductor-semiconductor and semiconductor-oxide-semiconductor junctions, a thermionic emission (TE) plus direct tunnel model (TFE, Thermionic-Field Emission) is used to simulate the charge transport. This solver is presented in Section 2.3 for the

thermionic scenario and in Section 2.4 for the TFE model in metal-semiconductor junctions. For the rest of heterointerfaces, the implementation of the TFE model is described in Section 2.5. The tunnel is complemented with the local and non-local band-to-band tunnelling (BTBT) model in Section 2.6. In addition, several generation and recombination models are added to the continuity equations, and presented in Section 2.7: Shockley-Read-Hall SRH recombination; Auger recombination; radiative recombination; and light generation. Additionally, SAMANTA is able to evaluate trap profiles at the interfaces of the device, including oxides, metals or other semiconductors. The theoretical background for this feature can be found in Section 2.8. There is one extra module, called SAMANTA-SP1D, explained in Section 2.9, which can solve the one dimensional Schrödinger-Poisson equations, useful to obtain the wavefunctions and energy levels of a confined system, and which can be thus used as a preliminary step to evaluate the carrier mobility for a certain material system. The flowchart of the program is presented in Section 2.10. Finite differences are employed, together with a Newton linearisation method, to self-consistently solve the equations. All the numerical details are given in Appendixes A to C.

2.2 The Drift-Diffusion and Poisson equation system

This Section describes the core equations considered in the simulator, i.e. the continuity and Poisson equations, applied to evaluate the potential and the carrier density at each position of a 2D system. The complete simulation framework is based on three sets of equations: the Poisson equation, the continuity equation for electron and holes and the drift-difussion equation for electron and holes.

The electric potential $\psi(\mathbf{r})$ and the charge distribution $\rho(\mathbf{r})$ are related through the Poisson equation:

$$\nabla \cdot [\boldsymbol{\varepsilon}(\mathbf{r}) \nabla \psi(\mathbf{r})] = -q\rho(\mathbf{r}) \tag{2.1}$$

where q is the electron charge and $\boldsymbol{\varepsilon}(\mathbf{r})$ is the dielectric tensor at the 2D location $\mathbf{r} = (x, y)$. Since 2D materials can be anisotropic due to their layered structure, the dielectric constant is directionally dependent, what implies not only a different dielectric constant for each (x, y) but also different values for different directions. In this work,

we have considered $\boldsymbol{\varepsilon}(\mathbf{r})$ as a diagonal 2-rank tensor:

$$\boldsymbol{\varepsilon}(\mathbf{r}) = \begin{pmatrix} \varepsilon_{xx}(\mathbf{r}) & 0 \\ 0 & \varepsilon_{yy}(\mathbf{r}) \end{pmatrix} \tag{2.2}$$

so to evaluate the anisotropy of the dielectric constant in the in-plane and out-of-plane directions of the 2DM.

The charge density $\rho(\mathbf{r})$ is given by:

$$\rho(\mathbf{r}) = p(\mathbf{r}) - n(\mathbf{r}) + N_{\mathrm{D}}^{+}(\mathbf{r}) - N_{\mathrm{A}}^{-}(\mathbf{r}) + N_{\mathrm{T}}(\mathbf{r}) \tag{2.3}$$

where $n(\mathbf{r})$ and $p(\mathbf{r})$ are the electron and hole densities, respectively, whose equations are presented in Section 2.5, $N_{\mathrm{D}}^{+}(\mathbf{r})$ and $N_{\mathrm{A}}^{-}(\mathbf{r})$ are the ionized donor and acceptor impurities, discussed in Appendix B.1, and $N_{\mathrm{T}}(\mathbf{r})$ is the trap density, evaluated using the pseudo Fermi levels positions as explained in Section 2.8.

The charge conservation is taken into account through the continuity equation for electron and holes [116], that can be derived from Ampere and Gauss laws:

$$\frac{\partial n(\mathbf{r})}{\partial t} = \frac{1}{q}\nabla \cdot \boldsymbol{J}_{\mathrm{n}}(\mathbf{r}) + G_{\mathrm{n}} - R_{\mathrm{n}} \tag{2.4a}$$

$$\frac{\partial p(\mathbf{r})}{\partial t} = -\frac{1}{q}\nabla \cdot \boldsymbol{J}_{\mathrm{p}}(\mathbf{r}) + G_{\mathrm{p}} - R_{\mathrm{p}} \tag{2.4b}$$

where $\boldsymbol{J}_{\mathrm{n}}(\mathbf{r})$ ($\boldsymbol{J}_{\mathrm{p}}(\mathbf{r})$) are the electron (hole) current densities, G_{n} (G_{p}) is the electron (hole) generation rate and R_{n} (R_{p}) is the electron (hole) recombination rate. Both generation and recombination rates will be introduced later in Section 2.7. For the continuity equation, we only evaluate the stationary state, so the left hand sides in Eq. (2.4) are set to zero.

Finally, the hole/electron currents comprises two terms: the drift component, which is driven by the electric field, and the diffusion component, which is governed by the electron density gradient. They can be written as:

$$\boldsymbol{J}_{\mathrm{n}}(\mathbf{r}) = q\mu_{\mathrm{n}}(\mathbf{r})\, n(\mathbf{r})\, \nabla\psi(\mathbf{r}) + D_{\mathrm{n}}(\mathbf{r})\, \nabla n(\mathbf{r}) \tag{2.5a}$$

$$\boldsymbol{J}_{\mathrm{p}}(\mathbf{r}) = q\mu_{\mathrm{p}}(\mathbf{r})\, p(\mathbf{r})\, \nabla\psi(\mathbf{r}) - D_{\mathrm{p}}(\mathbf{r})\, \nabla p(\mathbf{r}) \tag{2.5b}$$

where $\mu_{\mathrm{n}}(\mathbf{r})$ ($\mu_{\mathrm{p}}(\mathbf{r})$) is the electron (hole) mobility; $D_{\mathrm{n}}(\mathbf{r})$ ($D_{\mathrm{p}}(\mathbf{r})$) is the electron

(hole) diffusivity; k_B is the Boltzmann constant and T is the temperature. The diffusive constant has been substituted following the Einstein relation for nondegenerate semiconductors by $D_{n,p}(\mathbf{r}) = \mu_{n,p}(\mathbf{r}) k_B T$ [116].

At the limits and boundaries of the system, boundary conditions must be specified, as explained in Appendix C. Nevertheless, additional effects need to be taken into account when potential barriers and non-ideal contacts are present. In heterojunctions or metal-semiconductor interfaces, we use either the thermionic emission (TE) model, or the thermionic plus direct tunnel, i.e. thermionic-field emission (TFE) model, which is specially relevant when the energy barrier is large, but spatially thin. The next two Sections explain the thermionic model for metal-semiconductor junctions with low Schottky barriers and the general TFE model for all the scenarios.

2.3 Thermionic model for Schottky contacts

For most of the electronic devices, the semiconductor material is connected to the outside environment via metallic contacts. These connections are part of the boundary conditions of the system (whose details are explained in Appendix C) and give birth to potential barriers for the current flow that must be taken into account in the continuity equation. In this Section, we focus on the specific case of the Schottky contacts.

A Schottky barrier is an energy barrier formed at metal-semiconductor junctions. Isolated metals are characterized by their metal workfunction, as shown in Fig. 2.1, which is typically different from the Fermi level position of the semiconductor. When both materials are contacted, their Fermi levels must line up, after a charge transference between the materials, shifting the bands and generating a Schottky barrier at the junction. In SAMANTA, we have focused on making a general model valid to a wide set of structures and materials, although simpler models could be considered for 2D materials [117].

At the interface, the current that flows from/to the metal contact must be modified as cannot be described by a drift-diffusive paradigm. Let us consider the subset $\mathbf{r}_I \subseteq \mathbf{r}$, which refers to all the Schottky interface points of the device. In the continuity equations, the current density that flows to the contact at the $\mathbf{r}_I$ location is computed using a thermionic model [118],

$$J_n(\mathbf{r}_I) = -q v_{th}^n(\mathbf{r}_I)\left(n(\mathbf{r}_I) - n_0(\mathbf{r}_I)\right) \tag{2.6a}$$

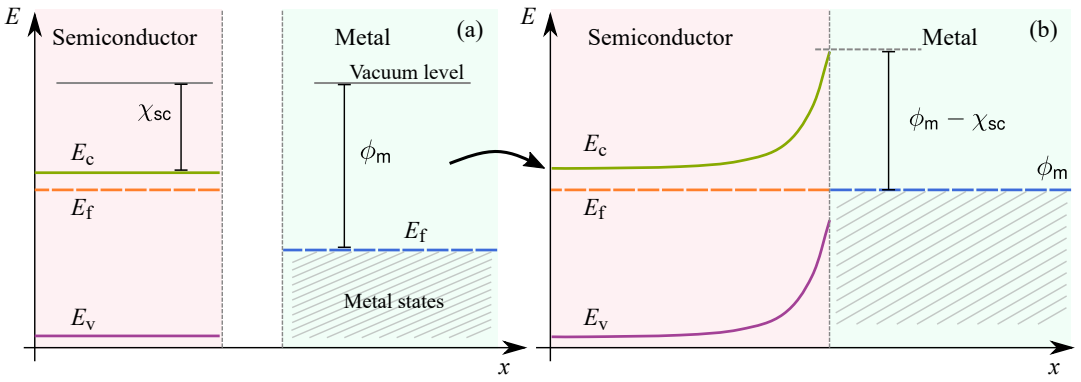

Figure 2.1: (a) Band diagram of a metal-semiconductor junction with a p-type contact and an n-type semiconductor before joining them. (b) Band diagram of the forming junction after contacting the materials. The lining up of the Fermi levels normally induces a Schottky contact with a built-in potential $\psi_{\mathrm{bi}} = \phi_{\mathrm{m}} - \chi_{\mathrm{sc}}$.

$$J_{\mathrm{p}}\left(\mathbf{r}_{\mathrm{I}}\right) = q v_{\mathrm{th}}^{\mathrm{p}}\left(\mathbf{r}_{\mathrm{I}}\right)\left(p\left(\mathbf{r}_{\mathrm{I}}\right) - p_0\left(\mathbf{r}_{\mathrm{I}}\right)\right) \tag{2.6b}$$

where $p_0\left(\mathbf{r}_{\mathrm{I}}\right)$ and $n_0\left(\mathbf{r}_{\mathrm{I}}\right)$ are the hole and electron densities in equilibrium, respectively (see Section 2.5), and $v_{\mathrm{th}}^{\mathrm{n,p}}\left(\mathbf{r}_{\mathrm{I}}\right)$ is the thermionic velocity of the contact for each kind of carrier, evaluated as:

$$v_{\mathrm{th}}^{\mathrm{n}}\left(\mathbf{r}\right) = \frac{A_{\mathrm{n}}^{*}\left(\mathbf{r}\right) T^2}{q N_{\mathrm{c}}\left(\mathbf{r}\right)} \tag{2.7a}$$

$$v_{\mathrm{th}}^{\mathrm{p}}\left(\mathbf{r}\right) = \frac{A_{\mathrm{p}}^{*}\left(\mathbf{r}\right) T^2}{q N_{\mathrm{v}}\left(\mathbf{r}\right)} \tag{2.7b}$$

Here, T is the temperature, $N_{\mathrm{c}}\left(\mathbf{r}\right)$ and $N_{\mathrm{v}}\left(\mathbf{r}\right)$ are the semiconductor electron/hole effective densities of states and $A_{\mathrm{n}}^{*}\left(\mathbf{r}\right)$ and $A_{\mathrm{p}}^{*}\left(\mathbf{r}\right)$ are the Richardson constants of the contacted semiconductor for electrons and holes, respectively, which are defined as

$$A_{\mathrm{n,p}}^{*}\left(\mathbf{r}\right) = 4\pi m_{\mathrm{eff}}^{\mathrm{n,p}}\left(\mathbf{r}\right) q k_{\mathrm{B}}^2 / \hbar^3 \tag{2.8}$$

where $m_{\mathrm{eff}}^{\mathrm{n}}\left(\mathbf{r}\right)$ $\left(m_{\mathrm{eff}}^{\mathrm{p}}\left(\mathbf{r}\right)\right)$ is the effective mass of electrons (holes), and $\hbar$ is the reduced Planck constant.

The thermionic velocity models the quality of the contact, that is, its ability to absorb/emit the carriers. A high thermionic velocity implies low carrier accumulation close to the the contact. $n_0\left(\mathbf{r}\right)$ and $p_0\left(\mathbf{r}\right)$ are evaluated in equilibrium by setting the potential, defined as the difference between the Fermi level and the conduction

band $\psi(\mathbf{r}) = q[E_f(\mathbf{r}) - E_c(\mathbf{r})]$, to $\psi(\mathbf{r}_I) = q[\phi_m(\mathbf{r}_I) - \chi_{sc}(\mathbf{r}_I)]$, with ϕ_m the metal workfunction and χ_{sc} the electron affinity of the semiconductor.

The thermionic emission is included in SAMANTA by computing the current components pointing to the contact at the interface between the metal and the semiconductor in the continuity equation (2.4) using the expressions from equation (2.6).

2.4 Direct tunnel in metal-semiconductor junctions

In a metal-semiconductor junction in equilibrium, the Fermi level of the semiconductor must be aligned with the metal workfunction ϕ_m, as depicted in Fig. 2.2a, generating an energy barrier at the interface. This barrier can be seen as a resistance (R_{th} in Fig. 2.2b) in series with the channel resistance, therefore limiting the current. In general, an ohmic contact (where the conctact resistance goes to zero) is desired to avoid this problem. However, in many cases, specially when the semiconductor is a 2D material, the metal workfunction is pinned to a value far from the desired ohmic contact [109, 110, 119], and Schottky junction is formed. The simulated contact resistance can greatly modify the behaviour of the device. Additionally, quantum mechanically, the energetic barrier can also be tunnelled, resulting in thermionic-field emission (TFE) tunnel current. Another resistance (R_{tunn}) in parallel with R_{th}, that can be several times lower than the latter, appear.

The TFE model, as illustrated in Fig. 2.2a, is due to the fact that many times the energy barrier is spatially thin, specially in 2D materials. In those cases, the carriers can flow via direct tunnel from one side of the junction to the other, increasing the total current that can operate in the device for the same bias conditions.

To include this tunnel effect, we have followed the formulation presented in the works of Yang et al. [120] and Chang and Sze [121]. A Wentzel-Kramers-Brillouin (WKB) approximation is used to evaluate the direct barrier between junctions of different materials. If the total tunnel current is injected only at the interface the tunnel current must first drift to that point along the barrier. In many situations, this leads to a bad evaluation of the actual tunnelling. This is specially relevant when the doping density of the semiconductor is high. In this scenario, the barrier can be high and the carriers cannot first drift along the strong potential barrier to later tunnel at the interface. To overcome this problem, TFE must be considered in a region of points not restricted to those exactly on the interface between both materials but including a

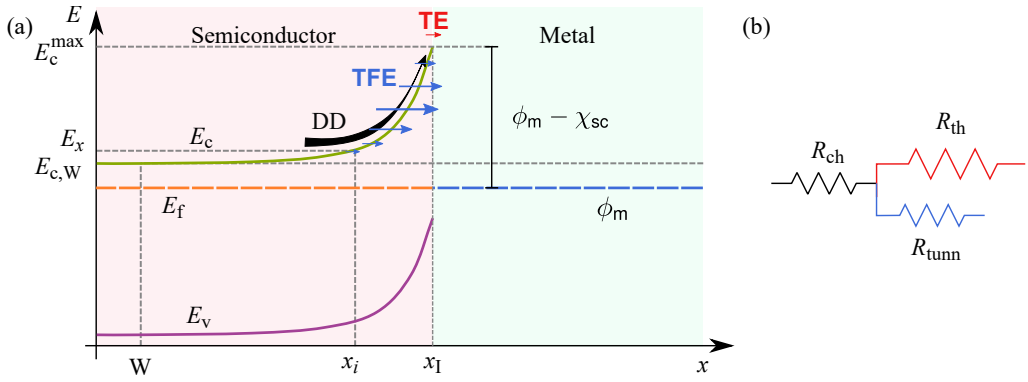

Figure 2.2: (a) Band diagram of a metal-semiconductor junction with a p-type contact and a n-type semiconductor in equilibrium conditions. (b) Semiconductor and contact resistances, the last one formed by the resistance related with the thermionic emission, which can be high due to the band bending, and the resistance due to the thermionic-field emission.

region of a few-nanometers close to it. So, in a similar way as in [122, 123], instead of adding all the tunnel current to the metal-semiconductor interface, we have distributed their contributions along the positions inside the semiconductor close to the barrier.

To this purpose, in 1D, the electron tunnel current from $\mathbf{r}_i$ to $\mathbf{r}_\mathrm{I}$, $J_\mathrm{Tn}(\mathbf{r}_i)$ – where $\mathbf{r}_\mathrm{I}$ is one arbitrary point exactly at the junction, and $\mathbf{r}_i$ a point in the semiconductor close to $\mathbf{r}_\mathrm{I}$ – is evaluated as:

$$J_\mathrm{Tn}(\mathbf{r}_i) = q v_\mathrm{th}^\mathrm{n}(\mathbf{r}_i) N_\mathrm{c}(\mathbf{r}_i) \gamma_\mathrm{n}(\mathbf{r}_\mathrm{i}) \{-f_\mathrm{s}^\mathrm{n}(\mathbf{r}_i)[1 - f_\mathrm{m}^\mathrm{n}(\mathbf{r}_I)] + f_\mathrm{m}^\mathrm{n}(\mathbf{r}_I)[1 - f_\mathrm{s}^\mathrm{n}(\mathbf{r}_i)]\} \quad (2.9)$$

and the corresponding hole current as:

$$J_\mathrm{Tp}(\mathbf{r}_i) = q v_\mathrm{th}^\mathrm{p}(\mathbf{r}_i) N_\mathrm{v}(\mathbf{r}_i) \gamma_\mathrm{p}(\mathbf{r}_\mathrm{i}) \{[1 - f_\mathrm{s}^\mathrm{p}(\mathbf{r}_i)] f_\mathrm{m}^\mathrm{p}(\mathbf{r}_I) - f_\mathrm{s}^\mathrm{p}(\mathbf{r}_i)[1 - f_\mathrm{m}^\mathrm{p}(\mathbf{r}_I)]\} \quad (2.10)$$

where $f_\mathrm{s}(\mathbf{r}_i)$ and $f_\mathrm{m}(\mathbf{r}_I)$ are the Fermi-Dirac occupation functions at different positions of the semiconductor and at the metal interface, respectively, evaluated as:

$$f(\mathbf{r}) = \frac{1}{1 + \mathrm{e}^{\frac{E_\mathrm{f}(\mathbf{r}) - E(\mathbf{r})}{k_\mathrm{B} T}}} \quad (2.11)$$

where E_f refers to the pseudo-Fermi level of electrons in Eq. (2.9) and holes in Eq.

(2.10). The tunnel contribution $\gamma_{\mathrm{n}}(\mathbf{r}_i)$, $\gamma_{\mathrm{p}}(\mathbf{r}_i)$ can be calculated as

$$\gamma_{\mathrm{n}}(\mathbf{r}_i) = \frac{1}{k_{\mathrm{B}}T} T_{\mathrm{n}}(E_{\mathrm{c}}(\mathbf{r}_i))\,\Delta E_{\mathrm{c}}(\mathbf{r}_i) \tag{2.12a}$$

$$\gamma_{\mathrm{p}}(\mathbf{r}_i) = \frac{1}{k_{\mathrm{B}}T} T_{\mathrm{p}}(E_{\mathrm{v}}(\mathbf{r}_i))\,\Delta E_{\mathrm{v}}(\mathbf{r}_i) \tag{2.12b}$$

where the transmission probability $T(E)$ is obtained using the WKB approximation. Here we assume a 1D system, so $\mathbf{r}_i \to x_i$ and $\mathbf{r}_{\mathrm{I}} \to x_{\mathrm{I}}$ and define the variable E_{x} as the conduction band value at the spatial position x_i, that is, $E_{\mathrm{x}} = E_{\mathrm{c}}(x_i)$. The general form of the transmission probability for electrons is [120]:

$$T_{\mathrm{n}}(E_{\mathrm{x}}) = \begin{cases} \exp\left(-\frac{4\pi}{h}\int_0^{x_{\mathrm{i}}}\left[2m^{\mathrm{n}}_{\mathrm{eff}}(x)\left\{E_{\mathrm{c}}(x) - E_{\mathrm{x}}\right\}\right]^{1/2}\mathrm{d}x\right) & , E_{\mathrm{c}}^{\min} \le E_{\mathrm{x}} < E_{\mathrm{c}}^{\max} \\ 1 & , E_{\mathrm{c}}^{\max} \le E_{\mathrm{x}} \end{cases} \tag{2.13}$$

where h is the Planck constant, $E_{\mathrm{c}}(x)$ is the conduction band value at position x, $E_{\mathrm{c}}^{\max} = E_{\mathrm{c}}(x_{\mathrm{I}})$ is the maximum of the conduction band at the interface, and $E_{\mathrm{c}}^{\min} = \max\left[E_{\mathrm{c,I}}^{\min}, E_{\mathrm{c,W}}\right]$, where $E_{\mathrm{c,W}}$ refers to the semiconductor conduction band far from the interface and $E_{\mathrm{c,I}}^{\min}$ refers to the minimum value of the conduction band at the interface, which in this case it is simply $E_{\mathrm{c}}^{\max}$. In the next Section we will see how this term can be different in heterojunctions. In a similar way, the transmission probability for holes in one dimension is:

$$T_p(E_{\mathrm{x}}) = \begin{cases} \exp\left(-\frac{4\pi}{h}\int_0^{x_{\mathrm{i}}}\left[2m^{\mathrm{p}}_{\mathrm{eff}}(x)\left\{E_{\mathrm{x}} - E_{\mathrm{v}}(x)\right\}\right]^{1/2}\mathrm{d}x\right) & , E_{\mathrm{v}}^{\min} < E_{\mathrm{x}} \le E_{\mathrm{v}}^{\max} \\ 1 & , E_{\mathrm{x}} \le E_{\mathrm{v}}^{\min} \end{cases} \tag{2.14}$$

with $E_{\mathrm{v}}^{\max} = \min\left[E_{\mathrm{v,I}}^{\max}, E_{\mathrm{v,W}}\right]$, and similar definitions for the rest of variables apply, considering the valence band.

2.4.1 Image charges barrier lowering

Image charges induced at the surface of the metal due to the presence of opposite charge particles in the semiconductor reduce the barrier height that carriers have to face [118, 124]. The barrier lowering $\phi_\delta(\mathbf{r})$ is conventionally modelled as proportional to the module of the electric field $|E_{\mathrm{field}}(\mathbf{r})|$ close to the metal-semiconductor interface

and is evaluated as

$$\phi_\delta(\mathbf{r}) = \sqrt{\frac{q|E_{\text{field}}(\mathbf{r})|}{4\pi\varepsilon(\mathbf{r})}} \tag{2.15}$$

where $\varepsilon(\mathbf{r})$ is the value of the dielectric constant normal to the interface. This model normally adds a small correction of the barrier, which however has a profound effect on current transport processes in metal-semiconductor systems.

The barrier lowering is added to the interface equation, which now is not a fixed Dirichlet condition (for more details about the boundary conditions, see Appendix C). If we initially set the interface voltage to $\psi_0 = \phi_{\text{m}} - \chi_{\text{sc}}$, the final potential in equilibrium conditions is

$$\psi(\mathbf{r}_{\text{I}}) = \psi_0(\mathbf{r}_{\text{I}}) + \phi_\delta(\mathbf{r}_{\text{I}}) \tag{2.16}$$

where $\mathbf{r}_{\text{I}}$ refers to the interface location.

2.5 Heterojunctions and direct tunnel

An heterojunction consists of the union of two different materials with, therefore, different properties, such as electron affinity, energy gap or electron and hole effective densities of states. When the two materials are connected, under equilibrium conditions, their Fermi levels are lined up and thus a band bending results [125]. This block of the simulator is intended to get a more refined way to evaluate van der Waals heterostructures, following a procedure similar to the one described in [126] and inspired by the formulation presented in Yang et al. [120], Lundstrom et al. [127] and Verschraegen et al. [128] works.

Figure 2.3a depicts the band diagram of an abrupt heterojunction, formed by two materials with different electron affinities and bandgaps. These differences make the conduction and valence bands to be discontinuous resulting in barriers for both carriers. This is a special case of a more general situation, in which an oxide is present between the two semiconductors, as in Fig. 2.3b. The potential inside the oxide varies linearly, so the shape of the conduction and valence bands is linear. In the simplest case, where only two semiconductors are involved, the left heterojunction interface is placed at the $\mathbf{r}_{\text{I}}$ location and divides the structure into two parts, each of them corresponding to one material. The properties of each semiconductor are labelled with a minus (left semiconductor) or plus (right semiconductor) superscript. Similarly, in the scenario with an intermediate oxide, the left interface is labelled by $\mathbf{r}_{\text{I}}$. For electrons, the

maximum of the conduction band $E_{\mathrm{c}}^{\max}$ is used to define the barrier height. $E_{\mathrm{c,I}}^{\min}$ is the minimum of the conduction band at the junction, which can be also placed either at the left or the right side. Here we consider a one dimensional scenario. The $\Delta E_{\mathrm{c}}^{\pm}$ values are the differences between the maximum value of the conduction band at the interface, and the conduction band value for each semiconductor, that is, $\Delta E_{\mathrm{c}}^{+} = E_{\mathrm{c}}^{\max} - E_{\mathrm{c}}^{+}$ and $\Delta E_{\mathrm{c}}^{-} = E_{\mathrm{c}}^{\max} - E_{\mathrm{c}}^{-}$. In the case without intermediate oxide, this value matches with the difference between the affinities of each material at the junction. For the sake of simplicity in the notation, we define E_{x} as the energy at the x_i position, so $E_{\mathrm{x}} = E_{\mathrm{c}}(x_i)$, and $E_{\mathrm{c,W}}$ as the maximum of the conduction band at a point far from the heterojunction. Similar definitions can be made for holes: $\Delta E_{\mathrm{v}}^{\pm}$ is the valence band gap for each side and $E_{\mathrm{v}}^{\min}$ is the minimum of the valence band at the interface. E_{x} and $E_{\mathrm{v,W}}$ have also the same definitions but referring to the valence band, with $E_{\mathrm{x}} = E_{\mathrm{v}}(x_i)$ when the equations are referred to the hole current.

The drift-diffusion current expressions at the regions close to the junction are substituted by the thermionic emission equations, in which we have included a $1 + \gamma_{\mathrm{n}}(\mathbf{r}_{\mathrm{I}})$ term, which considers the thermionic-field emission contribution, TFE. So here we directly sum both the thermionic and tunnel contributions at the interface, which is similar to the procedure presented in [120]. In $\gamma_{\mathrm{n}}(\mathbf{r}_{\mathrm{I}})$, the product of the occupation and transmission probabilities is integrated, obtaining the tunnel contribution. The net electron current at the interface x_{I} is the sum of the left and right current components [120, 128]:

$$\begin{aligned} J_{\mathrm{n}}(\mathbf{r}_{\mathrm{I}}) =& J_{\mathrm{n}}^{-}(\mathbf{r}_{\mathrm{I}}) - J_{\mathrm{n}}^{+}(\mathbf{r}_{\mathrm{I}}) = \\ & - q v_{\mathrm{th}}^{-}\left(1 + \gamma_{\mathrm{n}}(\mathbf{r}_{\mathrm{I}})\right) n^{-} \exp\left(-\frac{\Delta E_{\mathrm{c}}^{-}}{k_{\mathrm{B}}T}\right) + q v_{\mathrm{th}}^{+}\left(1 + \gamma_{\mathrm{n}}(\mathbf{r}_{\mathrm{I}})\right) n^{+} \exp\left(-\frac{\Delta E_{\mathrm{c}}^{+}}{k_{\mathrm{B}}T}\right) \end{aligned} \tag{2.17}$$

where $v_{\mathrm{th}}^{\pm}$ and $n^{\pm}$ are the mean electron thermal velocity and the electron density for each semiconductor. This probability is evaluated in the same way as in 2.13. $\gamma_{\mathrm{n}}(\mathbf{r}_{\mathrm{I}})$ is obtained by integrating the transmission probability for all the energies:

$$\gamma_{\mathrm{n}}(\mathbf{r}_{\mathrm{I}}) = \frac{\exp\left(\frac{E_{\mathrm{c}}^{\max}}{k_{\mathrm{B}}T}\right)}{k_{\mathrm{B}}T} \int_{E_{\mathrm{c}}^{\min}}^{E_{\mathrm{c}}^{\max}} \exp\left(-\frac{E_{\mathrm{x}}}{k_{\mathrm{B}}T}\right) T_{\mathrm{n}}(E_{\mathrm{x}})\, \mathrm{d}E_{\mathrm{x}} \tag{2.18}$$

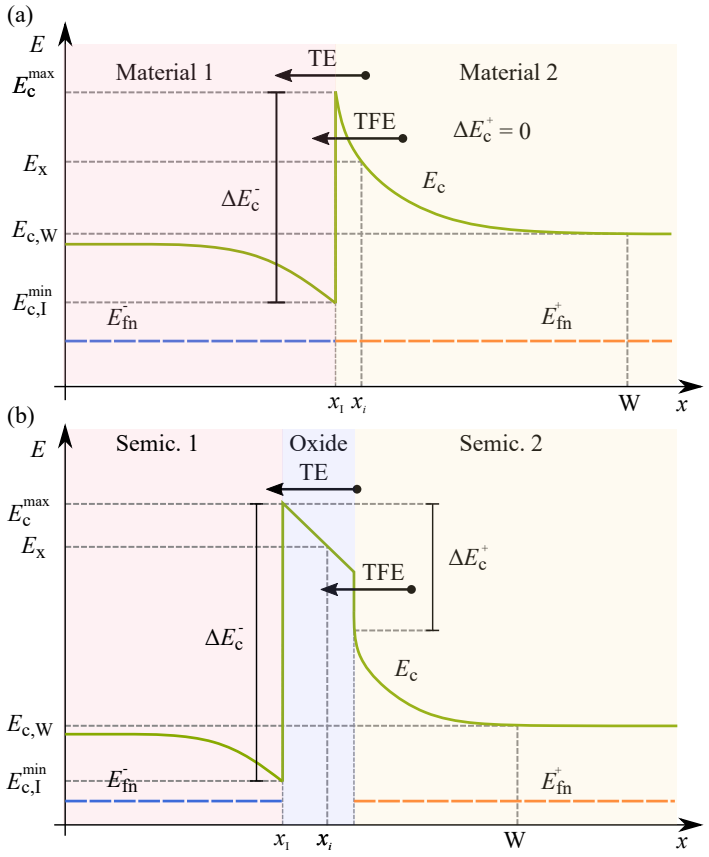

Figure 2.3: Conduction band diagram of an abrupt heterojunction between (a) only two semiconductors and (b) two different semiconductors and an oxide.

The hole current is evaluated in a similar way:

$$J_{\mathrm{p}}\left(\mathbf{r}_{\mathrm{I}}\right)=qv_{\mathrm{th}}^{-}\left(1+\gamma_{\mathrm{p}}\left(\mathbf{r}_{\mathrm{I}}\right)\right)p^{-}\exp\left(\frac{\Delta E_{\mathrm{v}}^{-}}{k_{\mathrm{B}}T}\right)-qv_{\mathrm{th}}^{+}\left(1+\gamma_{\mathrm{p}}\left(\mathbf{r}_{\mathrm{I}}\right)\right)p^{+}\exp\left(\frac{\Delta E_{\mathrm{v}}^{+}}{k_{\mathrm{B}}T}\right) \quad (2.19)$$

where $\gamma_{\mathrm{p}}\left(\mathbf{r}_{\mathrm{I}}\right)$ at an arbitrary interface location $\mathbf{r}_{\mathrm{I}}$ is evaluated as

$$\gamma_{\mathrm{p}}\left(\mathbf{r}_{\mathrm{I}}\right)=\frac{\exp\left(\frac{-E_{\mathrm{v}}^{\min}}{k_{\mathrm{B}}T}\right)}{k_{\mathrm{B}}T}\int_{E_{\mathrm{v}}^{\min}}^{E_{\mathrm{v}}^{\max}}\exp\left(\frac{E_{\mathrm{x}}}{k_{\mathrm{B}}T}\right)T_{\mathrm{p}}\left(E_{\mathrm{x}}\right)\mathrm{d}E_{\mathrm{x}} \quad (2.20)$$

using the transmission probability calculated as in 2.14.

The model adds some special considerations in equilibrium conditions. Here, the

discontinuity in the conduction and valence bands caused by the difference of the parameters of each semiconductor has to be explicitly included in the Fermi function. Taking one of the semiconductors as a reference (noted as $^{\text{ref}}$), we evaluate [127]

$$\begin{aligned} n_0(\mathbf{r}) =& N_{\text{c}}(\mathbf{r})\,\mathcal{F}_{1/2}(\eta_{\text{c}}), \\ &\text{with } \eta_{\text{c}} = \frac{\psi(\mathbf{r})}{k_{\text{B}}T} + \frac{\chi_{\text{sc}}(\mathbf{r}) - \chi_{\text{sc}}^{\text{ref}}}{k_{\text{B}}T} + \frac{1}{2}\ln\left[\frac{N_{\text{v}}^{\text{ref}}\exp\left(-E_{\text{g}}^{\text{ref}}/k_{\text{B}}T\right)}{N_{\text{c}}^{\text{ref}}}\right] \end{aligned} \tag{2.21a}$$

$$\begin{aligned} p_0(\mathbf{r}) =& N_{\text{v}}(\mathbf{r})\,\mathcal{F}_{1/2}(\eta_{\text{v}}), \\ &\text{with } \eta_{\text{v}} = -\frac{\psi(\mathbf{r})}{k_{\text{B}}T} - \frac{\chi_{\text{sc}}(\mathbf{r}) - \chi_{\text{sc}}^{\text{ref}}}{k_{\text{B}}T} - E_{\text{G}}(\mathbf{r}) - \frac{1}{2}\ln\left[\frac{N_{\text{v}}^{\text{ref}}\exp\left(-E_{\text{g}}^{\text{ref}}/k_{\text{B}}T\right)}{N_{\text{c}}^{\text{ref}}}\right] \end{aligned} \tag{2.21b}$$

where $\chi_{\text{sc}}(\mathbf{r})$ is the electron affinity, $E_{\text{g}}(\mathbf{r})$ is the band gap, and $N_{\text{c}}(\mathbf{r})$ and $N_{\text{v}}(\mathbf{r})$ are the effective densities of states for electrons and holes, respectively.

2.6 Band to band tunnelling current

Previously, we discussed the tunnel phenomena in junctions of different materials within the same band (conduction or valence). In this Section, we study a different scenario, in which the conduction band, in some spatial locations, is energetically aligned to the valence band in other positions. This is the typical scenario of a PN diode under reverse bias. Under equilibrium or low bias, see Fig. 2.4a, below the thermal voltage of the diode, the electrons (holes) from the conduction (valence) band can be energetically aligned with unoccupied states of the valence (conduction) band. They have a probability to tunnel from one band to the other, filling the unoccupied state, in a recombination-like process. Similarly, under reverse bias, as depicted in Fig. 2.4b, very few electrons are able to flow from the N doped region to the P doped. However, close to the PN interface, there can be some occupied states in the valence band which are energetically aligned with the conduction band. If the distance is narrow enough, an electron can jump from the valence band to the conduction band, leaving a hole behind, in which we can denote as a generation process. Here we use Kane's model, which derives from the WKB approximation in triangular bands, and that locally evaluates the band to band contribution as a net generation-recombination U, which depends on

the electric field [129, 130]:

$$U_{\text{Kane}}(\mathbf{r}) = AE^{\alpha}(\mathbf{r}) \exp\left(-\frac{B}{|E(\mathbf{r})|}\right) \tag{2.22}$$

where A, B and α are fitting parameters, and $E(\mathbf{r})$ is the electric field. This BTBT method is local, which means that electrons and holes are generated or recombined in the same spatial location, what can be inaccurate. Another drawback about using this procedure is that it can give a non physical solution in equilibrium conditions, as this model mathematically allows a non-zero generation-recombination rate, promoting an unexpected current. To fix this problem, Hurkx's model adds a prefactor that reduces to zero the current in equilibrium conditions [131]:

$$H(\mathbf{r}) = \frac{n(\mathbf{r})\, p(\mathbf{r}) - n_{\text{i}}^2(\mathbf{r})}{(n(\mathbf{r}) + n_0(\mathbf{r}))\,(p(\mathbf{r}) + p_0(\mathbf{r}))} \tag{2.23}$$

So the final generation-recombination using the Hurkx's models is:

$$U_{\text{Hurkx}}(\mathbf{r}) = U_{\text{Kane}}(\mathbf{r})\, H(\mathbf{r}) \tag{2.24}$$

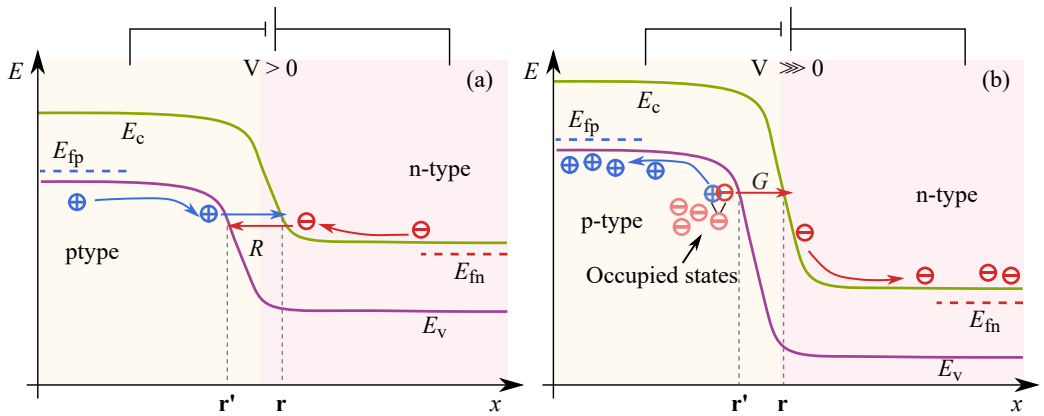

Figure 2.4: Band diagram of a PN junction with (a) a low bias, and (b) a reverse bias. In (a), electrons flow from the n-conduction band to the p-valence band, filling unoccupied states, which can be modelled as a recombination process. In (b), electron-hole pairs are generated from p-valence band the occupied states, as electron jump to the n-conduction band, leaving a hole.

2.6.1 Non local band to band tunnelling current

Usually, non local methods are more accurate when evaluating the band-to-band tunnelling. In addition, they are physically more correct. It is possible to adapt the previously presented models in a non local way. To do that, all the positions where band-to-band tunnelling is possible (when valence band is aligned with conduction band) are evaluated, and the different generation-recombination contributions are added up. The expression that evaluates all the contributions from different $\mathbf{r}'$ into one single point $\mathbf{r}$ is [130]:

$$U_{\mathrm{bb}}(\mathbf{r})\,\Delta\mathbf{r} = \sum_{(\mathbf{r}')} g_{\mathrm{bb}}\left(E_{\mathrm{eff}}\left(\mathbf{r},\mathbf{r}'\right)\right)\Delta\left(\mathbf{r}'\right) \tag{2.25}$$

where $\Delta(\mathbf{r})$ is the area associated to the location $(\mathbf{r})$ and $g_{\mathrm{bb}}(E)$ is a generation-recombination rate calculated using the Hurkx or Kane's model, that is, $g_{\mathrm{bb}}(E) = U_{\mathrm{Kane}}(\mathbf{r})$ or $g_{\mathrm{bb}}(E) = U_{\mathrm{Hurkx}}(\mathbf{r})$, and changing its electric field by the effective electric field, defined as

$$E_{\mathrm{eff}}\left(\mathbf{r},\mathbf{r}'\right) = \Delta\psi/|\mathbf{r}\text{-}\mathbf{r}'| \tag{2.26a}$$

$$\Delta\psi = \psi(\mathbf{r}) - \psi\left(\mathbf{r}'\right) \tag{2.26b}$$

where $|\mathbf{r}\text{-}\mathbf{r}'|$ is the distance between points. For all the tunnel current situations, it must be fulfilled that $E_{\mathrm{c}}(\mathbf{r}) < E_{\mathrm{v}}(\mathbf{r}')$, for elastic transitions, or $E_{\mathrm{c}}(\mathbf{r}) < E_{\mathrm{v}}(\mathbf{r}')$ for inelastic ones.

2.7 Generation and Recombination processes

Many physical phenomena that affect the transport can be modelled introducing a generation-recombination rate that, in turn, is added to the drift-diffusion scheme through the continuity equations. In this way, we have already seen the band-to-band tunnelling models. The following subsections present the details of other processes taken into account in this Thesis. Such phenomena included in the simulator are: Schockley-Red-Hall effect, Auger and radiative recombinations, and light generation.

2.7.1 Schockley-Read-Hall recombination and generation

The SRH model [132] describes the statistic of the recombination and generation of carriers occurring through the mechanism of trapping. The bandgap of the semicon-

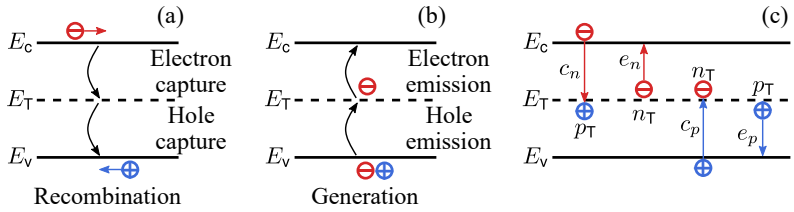

Figure 2.5: Graphical description of the various events that happen during SRH generation or recombination process: (a) Recombination processes. (b) Generation processes. (c) Relations with the trapped charges.

ductors tend to be larger than the kinetic energy of the carriers, making difficult the promotion of a direct band-to-band generation event. But when the crystalline structure of the material is not perfect, for instance due to the presence of doping impurities, a mid gap level, in between the conduction and the valence band, can be placed, so a generation-recombination event can occur with a lower kinetic energy. The energy of the carrier is exchanged in the form of a phonon. Four mechanisms, depicted in Fig. 2.5, are described by the SRH model [116]:

- Hole emission, e_p, in which an electron jumps from the valence band to the trapped level.
- Hole capture, c_p, an electron moves from an occupied trap to the valence band and annihilating a hole.
- Electron emission, e_n, an electron jumps from the trapped level to the conduction band.
- Electron capture, c_n, an electron moves from the conduction band to an unoccupied trap.

The evaluation of this process is given by [133]

$$U_{\mathrm{SRH}}(\mathbf{r}) = \frac{n(\mathbf{r})\,p(\mathbf{r}) - n_{\mathrm{i}}^2(\mathbf{r})}{\tau_{\mathrm{p}}(\mathbf{r})\left(n(\mathbf{r}) + n_{\mathrm{i}}(\mathbf{r})\exp\left(\frac{E_{\mathrm{T}}(\mathbf{r})}{k_{\mathrm{B}}T}\right)\right) + \tau_{\mathrm{n}}(\mathbf{r})\left(p(\mathbf{r}) + n_{\mathrm{i}}(\mathbf{r})\exp\left(\frac{-E_{\mathrm{T}}(\mathbf{r})}{k_{\mathrm{B}}T}\right)\right)} \tag{2.27}$$

where $\tau_{\mathrm{n}}(\mathbf{r})$ and $\tau_{\mathrm{p}}(\mathbf{r})$ are the mean lifetime of electrons and holes, respectively, $E_{\mathrm{T}}(\mathbf{r})$ is the defect energy level relative to the intrinsic level $E_{\mathrm{i}}(\mathbf{r})$, which depends on the selected simulated defect, and $n_{\mathrm{i}}(\mathbf{r})$ is the intrinsic carrier density.

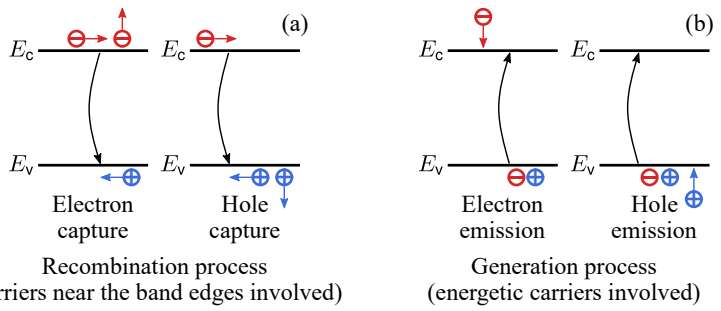

Figure 2.6: Graphical description of the various events that happen during Auger generation or recombination process: (a) Recombination processes. (b) Generation processes.

2.7.2 Auger generation/recombination

This process is a the three particle transition that implies the recombination or generation of a carrier without absorbing or emitting the necessary energy from a photon. Instead, another carrier gives or takes the necessary energy to promote a carrier capture or emission, in four-step process schemed in Fig. 2.6 [134, 116]:

- Electron capture: an electron from the conduction band moves to the valence band, transmitting the excess energy to another electron in the conduction band. In the valence band the electron recombines with a hole.
- Hole capture: an electron from the conduction band moves to the valence band transmitting the excess energy to a hole in the valence band, which moves away from the valence band edge. The electron recombines with a hole.
- Electron emission: an electron from the valence band moves to the conduction band by consuming the energy of a high energetic electron in the conduction band and leaving a hole in the valence band.
- Hole emission: an electron from the valence band moves to the conduction band by consuming the energy of a high energetic hole in the valence band. A hole is left at the valence band edge.

This process is stronger in materials with low energy gap and high carrier densities. The energy exchange can be trap assisted. This mechanism has been proved of relevance in 2D materials [135, 113]. The model used in SAMANTA relates the carrier

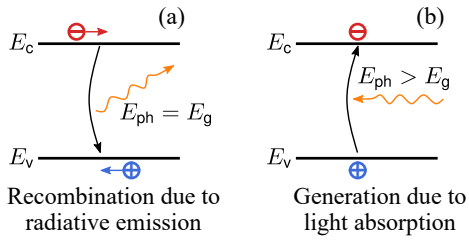

Figure 2.7: Graphical description of the (a) the radiative recombination and (b) the light generation processes: (a) Recombination processes. (b) Generation processes.

concentrations with $C_n(\mathbf{r})$ ($C_p(\mathbf{r})$), which are the Auger capture probabilities when the increased carrier is an electron (hole) [134]:

$$U_{Aug}(\mathbf{r}) = \left(C_n(\mathbf{r})\, n(\mathbf{r}) + C_p(\mathbf{r})\, p(\mathbf{r})\right)\left(n(\mathbf{r})\, p(\mathbf{r}) - n_i^2(\mathbf{r})\right) \tag{2.28}$$

2.7.3 Radiative recombination

A radiative recombination provokes that an electron loses energy of the order of the bandgap, which is emitted as a photon, and moves from the conduction to the valence band. Figure 2.7a depicts the carrier transition. This process is stronger for narrow direct gap semiconductors and it can be modelled by the following equation [134]:

$$R_{Rad}(\mathbf{r}) = B_{Rad}(\mathbf{r})\left(n(\mathbf{r})\, p(\mathbf{r}) - n_i^2(\mathbf{r})\right) \tag{2.29}$$

where $B_{Rad}(\mathbf{r})$ is the radiative emission rate, i.e. the number of electrons N recombined per unit time, which depends on the light frequency ω (which means, it also depends on the photon energy E_{ph}) and follows the rule

$$\frac{\partial N}{\partial t} = -B\rho(\omega)\, N \tag{2.30}$$

where B is the Einstein B proportionality constant for photon induced emission, and $\rho(\omega)$ is the radiation of the incident field at frequency ω.

2.7.4 Light generation

Photon-assisted generation promotes electron-hole pairs when the photon energy is higher than the gap of the semiconductor, in the case of direct-gap materials. Figure 2.7b

depicts the carrier generation process. The effect depends only on the light intensity and the absorption coefficient, which can be assumed constant with the potential. Photon power decreases exponentially as the light crosses the system. For a punctual monochrome source light located at ($\mathbf{r}_0$), the generation rate at a semiconductor position ($\mathbf{r}$) can be computed as [136, 137]

$$G_{\text{light}}(\mathbf{r}) = \frac{P_{\text{opt}}(\mathbf{r}_0)}{E_{\text{ph}}} \alpha(\mathbf{r}) \exp\left(-\alpha(\mathbf{r}) |\mathbf{r}\text{-}\mathbf{r}_0|\right) \tag{2.31}$$

where $\mathrm{P}_{\text{opt}}(\mathbf{r}_0)$ is the light power density, E_{ph} is the photon energy, $\alpha(\mathbf{r})$ is the absorption coefficient and $|\mathbf{r}\text{-}\mathbf{r}_0|$ is the distance between each point and the beam.

The absorption coefficient can be extracted from the absorbance using the Beer-Lambert law. Absorbance (A) is the logarithmic of the transmission coefficient, that is, $\mathrm{A} = \log_{10}(\mathrm{T})$. Beer-Lambert law relates the transmission coefficient with the absorption coefficient as:

$$\alpha(\mathbf{r}) = -\frac{\log(\mathrm{T}(\mathbf{r}))}{|\mathbf{r}\text{-}\mathbf{r}_0|} \tag{2.32}$$

2.8 Traps

At the junctions between different materials, defects, due to the disrupted periodicity of the lattice, can appear, inducing unsatisfied bonds. The interface traps are energetically located in the forbidden band and affect the device performance, as they can screen carriers or trap them. In ideal pristine 2D materials, no traps are present. However, the absence of dangling bonds in these materials promotes the appearance of unsatisfied bonds in the oxide beneath them and could give place to a high density traps profiles [109, 119]. This section explains the models that have been used in SAMANTA to add the influence of interface traps in few-layer 2D materials.

The charge at the interface can be evaluated for acceptor and donor traps. In this case, a Density of States (DoS) profile is defined for each of them: $D_{\text{it}}^{\text{a}}(E)$ and $D_{\text{it}}^{\text{d}}(E)$. The net charge of the interface is evaluated as [138]

$$Q_{\text{it}} = Q_{\text{it}}^{\text{d}} + Q_{\text{it}}^{\text{a}} = q \int_{-\infty}^{\infty} D_{\text{it}}^{\text{d}}(E) \left[1 - f\left(E - E_{\text{f}}^{\text{p}}\right)\right] \mathrm{d}E + q \int_{-\infty}^{\infty} D_{\text{it}}^{\text{a}}(E) f(E - E_{\text{f}}^{\text{n}}) \, \mathrm{d}E \tag{2.33}$$

where $f(E - E_{\text{f}})$ is the Fermi distribution. The Fermi level can be obtained from the

carrier concentration as:

$$\frac{E_{\mathrm{f}}^{\mathrm{n}} - E_{\mathrm{c}}}{k_{\mathrm{B}}T} = \mathcal{F}_{1/2}^{-1}\left(\frac{n}{N_{\mathrm{c}}}\right) \tag{2.34a}$$

$$\frac{E_{\mathrm{v}} - E_{\mathrm{f}}^{\mathrm{p}}}{k_{\mathrm{B}}T} = \mathcal{F}_{1/2}^{-1}\left(\frac{p}{N_{\mathrm{v}}}\right) \tag{2.34b}$$

where $\mathcal{F}_{1/2}^{-1}(u)$ is the inverse of the Fermi-Dirac integral function, for which we employ the following approximation [139]:

$$\mathcal{F}_{1/2}^{-1}(u) \simeq \frac{\ln(u)}{1-u^2} + \frac{\left(3\sqrt{\pi}u/4\right)^{2/3}}{1+\left[0.24+1.08\left(3\sqrt{\pi}u/4\right)^{2/3}\right]^{-2}} \tag{2.35}$$

As for $D_{\mathrm{it}}(E)$, it is possible to select an arbitrary energetic profile. Some fixed profiles have been defined, but SAMANTA is capable to use experimental results or even a DoS obtained from first-principles simulations. It is possible to evaluate isolated states or amphoteric compounds, in which the ions can act as donor or acceptor traps, depending on the Fermi level position. Figure 2.8 depicts some models of amphoteric densities of states using various profiles. In all the cases one of the curves can be neglected in order to obtain only the term corresponding to the donor or acceptor traps.

For a Gaussian profile, see Fig. 2.8a, the density of states is defined as

$$D_{\mathrm{it}}(E) = D_{\mathrm{it}}^{\mathrm{max}} \exp\frac{(E-E_{\mathrm{a}})^2}{2\sigma_{\mathrm{E}}^2} \tag{2.36}$$

where $\mathrm{D}_{\mathrm{it}}^{\mathrm{max}}$ refers to the maximum surface trap density per energy unit, which is set to a gaussian distribution centred in the trap energy E_{a} with standard deviation σ_{E}. In the case of a constant distribution, depicted in Fig. 2.8b, the expression is simply:

$$D_{\mathrm{it}}^{\mathrm{d}}(E) = D_{\mathrm{it}}^{\mathrm{max}}, \quad (E < E_{\mathrm{a}}) \tag{2.37a}$$

$$D_{\mathrm{it}}^{\mathrm{a}}(E) = -D_{\mathrm{it}}^{\mathrm{max}}, \quad (E > E_{\mathrm{a}}) \tag{2.37b}$$

For the band tail distribution, shown in Fig. 2.8c, the density of states is evaluated as:

$$D_{\mathrm{it}}(E) = D_{\mathrm{it}}^{\mathrm{max}} \exp\left(\frac{-E+E_{\mathrm{g}}/2}{\omega}\right), \quad \text{with} \quad \omega = \frac{E_{\alpha}}{\ln(\alpha_{\mathrm{D}})} \tag{2.38}$$

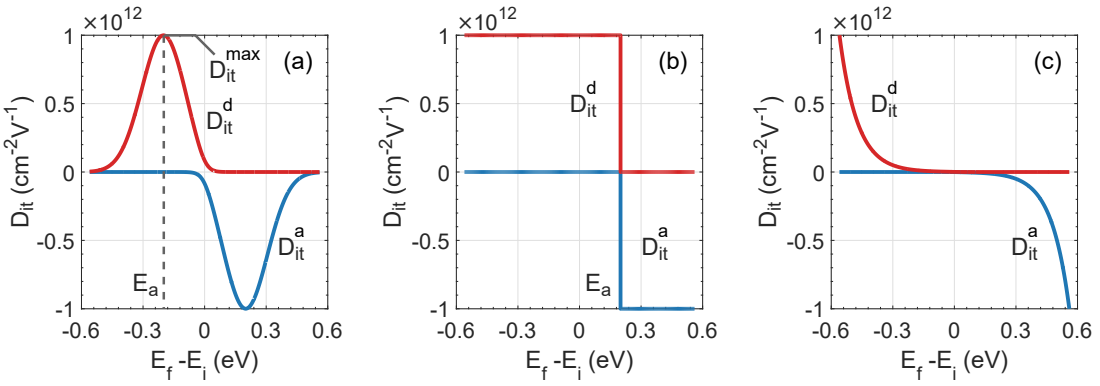

Figure 2.8: Models of amphoteric densities of states using (a) Gaussian profile, (b) constant profile and (c) band tail profile. Red line refers to donors traps, while blue line corresponds to the acceptor traps.

where the exponential decays in a way that the DoS in E_α is the 10% from the value in the conduction/valence band. All the distributions can be applied for both donor and acceptor traps at the same time, behaving as amphoteric traps.

The charge in Eq. (2.33) is a surface charge. In real devices we do not have a perfectly flat surface, and therefore the traps are distributed in a certain region close to the interface. The evaluated traps are thus distributed along a volume, with a spatial distribution function. In the simulator, we employ a Gaussian distribution. Let $\mathbf{r}_\mathrm{I}$ an interface point, and $\mathbf{r}$ the positions in which the traps are distributed, the expression is given by

$$Q_\mathrm{it}\left(\mathbf{r}\right) = Q_\mathrm{it}\left(\mathbf{r}_\mathrm{I}\right) A_\mathrm{gau} e^{\left(-|\mathbf{r}-\mathbf{r}_\mathrm{I}|^2/2\sigma_\mathrm{g}^2\right)} \tag{2.39}$$

where x follows the direction perpendicular to the interface, starting from the interface, σ_g^2 is the variance and $\mathrm{A_{gau}}$ is the amplitude of the Gaussian distribution, defined by

$$A_\mathrm{gau} = \frac{t_\mathrm{i}}{\sigma_\mathrm{g} t_\mathrm{o}\sqrt{\pi/2}}\mathrm{erf}\left(\frac{t_\mathrm{o}}{\sigma_\mathrm{g}\sqrt{2}}\right) + t_\mathrm{i}\left(e^{-t_o^2/2\sigma_\mathrm{g}^2} - 1\right) \tag{2.40}$$

here t_i and t_o are the thickness of the material and the non-null region respectively, and $\mathrm{erf}(x)$ is the error function [140].

2.9 The SAMANTA-SP1D block

The 2D Drift-Diffusion model gives a good electrostatic and transport description of the simulated structures, provided that the band structure of the channel materials and the carrier mobilities are accurate. In some cases, though, for example in back-gated few-layer 2D-based materials devices, the quantum well formed by the created heterostructure (insulator and semiconductor) can modify the electrostatics (band structure) and transport (mobility) properties of the materials. In such cases, a more detailed analysis has to be carried out. In our simulator, the block SAMANTA SP1D has been developed to do it. By solving self-consistently the one dimensional Schrödinger-Poisson equations, we evaluate the electrostatic potential, the wavefunctions and their corresponding energy levels, which can be later employed to calculate the carrier mobility (see Chapter 3). These elements let us evaluate the electron density more precisely inside the semiconductor.

Similar to Eq. (2.1), the one dimensional Poisson equation in the y confinement direction is used to calculate the potential:

$$\frac{\partial}{\partial y}\varepsilon\left(y\right)\frac{\partial}{\partial y}\psi\left(y\right)=-\rho\left[\psi\left(y\right)\right], \tag{2.41}$$

where $\psi\left(y\right)$ is the electric potential, $\varepsilon\left(y\right)$ is the position dependent permittivity, and $\rho\left[\psi\left(y\right)\right]$ is the charge density. It is possible to use Dirichlet boundary conditions at the metal interfaces, and Neumann conditions at the borders of the system. The charge density is calculated from the 2D electron gas density of states expression [141] using the orthogonal wavefunction envelopes $\xi_i\left(y\right)$ and their corresponding energy subbands E_i obtained from the Schrödinger equation. Here, we use the parabolic Effective Mass Aproximation (EMA) to solve the stationary, single-electron Schrödinger equation as [142]

$$\left(-\frac{\hbar^2}{2}\frac{\partial}{\partial y}\frac{1}{m_{\mathrm{eff}}^{\mathrm{n}}\left(y\right)}\frac{\partial}{\partial y}+\chi_{\mathrm{ref}}-\chi\left(y\right)-q\psi\left(y\right)\right)\xi_i\left(y\right)=E_i\xi_i\left(y\right) \tag{2.42}$$

where $m_{\mathrm{eff}}^{\mathrm{n}}\left(y\right)$ corresponds with the effective mass along the y direction, χ_{ref} is a reference electron affinity and $\chi\left(y\right)$ the corresponding to the y position. The Schrödinger equation is solved for each considered conduction band valley. After normalizing the magnitude of the wavefunctions, the electron density is evaluated by adding up the

contribution of all the conduction band valleys as [143]

$$n\left(y\right)=g_{\mathrm{s}}g_{\mathrm{v}}\sum_{i}g\left(E_{i}\right)\left\|\xi_{i}\left(y\right)\right\|^{2} \tag{2.43}$$

where the g_{s} and g_{v} refer to the spin and valley degeneracies, respectively, and $g_{\mathrm{I}}\left(E_{i}\right)$ is the integrated density of states of a 2D electron gas confined in 1D:

$$g_{\mathrm{I}}\left(E_{i}\right)=\frac{m_{\mathrm{eff}}^{\mathrm{n}}k_{\mathrm{B}}T}{2\pi\hbar^{2}}\log\left(1+\exp^{-(E_{i}-E_{\mathrm{f}})/k_{\mathrm{B}}T}\right) \tag{2.44}$$

2.10 Program workflow

SAMANTA evaluates several modules along the simulation procedure. To facilitate the understanding of this process, Figure 2.9 shows the flowchart of a common iteration.

The simulation starts with the geometry mesh, obtained from the material blocks and contact parameters, and determines the boundary conditions, which are necessary for heterostructures and external boundaries.

After that, the finite difference solvers are executed. First, the device is evaluated under equilibrium conditions. This gives some initial values for the potential and carrier densities, which are useful to boost the simulations in non equilibrium conditions. This module also contributes to the calculation of the boundary conditions for metal-semiconductor interfaces and generation-recombination rates. Every iteration, different modules that works in conjunction with the Poisson equation (that is, impurity ionization, barrier lowering and traps) update the corresponding terms of each equation. Fermi statistics are used to calculate the electron and hole densities. Finally, after evaluating the equation, it is modified adding the terms corresponding to the Newton linearisation method. The module ends when convergence has been reached.

After that, if everything worked properly, the non-equilibrium resolutor starts. This model evaluates the selected equations which satisfies the needs of the specific device. Each submodule also includes its linearisation using the Newton method. The necessary submodules for the continuity equations are run, including:

- Generation and recombination modules, including band-to-band tunneling.
- Drift-Diffusion equations following the continuity equations.
- The TE or TFE model for contacts is selected, including the barrier lowering when

it is desired. This model modifies the corresponding terms to the Drift-Diffusion equations.

- Finally, the Drift-Diffusion terms are also modified in case of presence of heterojunctions.

Finally, the matrix for the Poisson equation is evaluated, including the impurity ionization, the presence of traps at the selected interfaces, and eventually the full Poisson equation. All the three matrices obtained for the potential and carrier densities are combined and solved. This process is repeated until a convergence criteria is satisfied, similar to the one presented in [144, 145]. After that, the non-equilibrium solver can be directly recalled with a new bias, without running the equilibrium-conditions block.

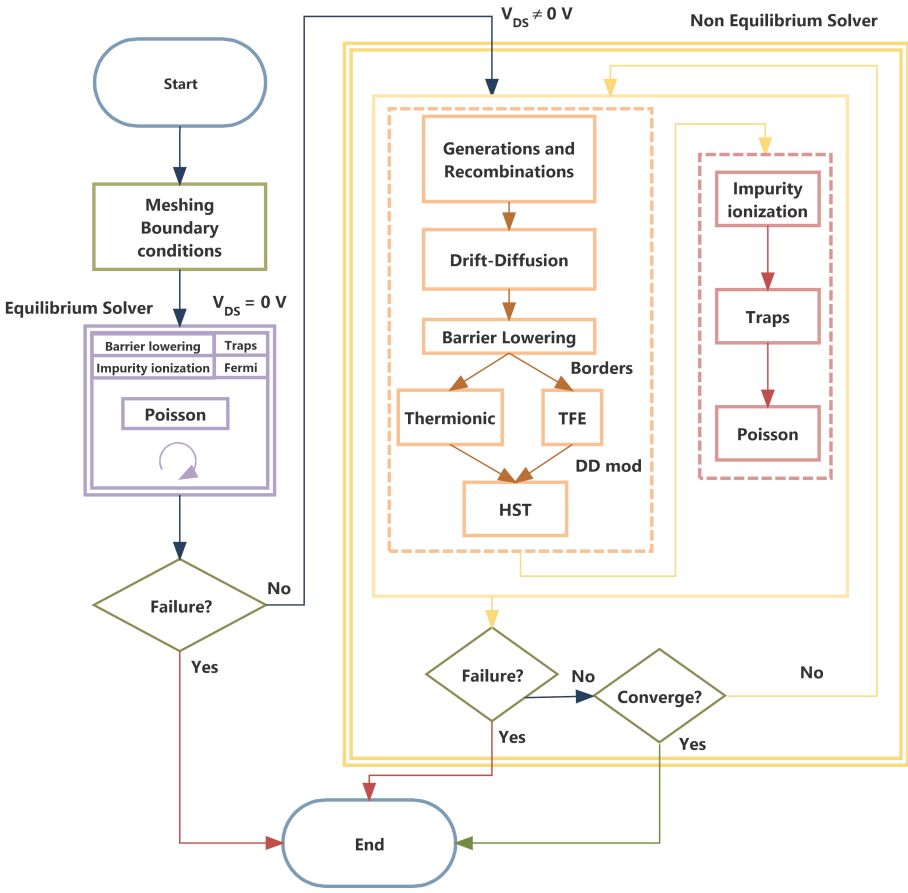

Figure 2.9: Flowchart of SAMANTA. The equilibrium model is evaluated in the beginning, but after this first iteration it is not necessary to repeat this operation for every bias.

Part III

Results

Chapter 3

Electron mobility in few-layers MoS_2 MOSFET

3.1 Introduction

As schematized during the Introduction of this Thesis, the scientific community's interest on bidimensional materials has grown during the last few years, as they are considered as one of the best alternatives to the traditional Si-based technology. Among 2D materials, the so-called transition metal dichalcogenides (TMDs) present interesting properties to design and fabricate ultra-thin body devices. One special feature of some materials belonging to this family, such as MoS_2, is their variable bandgap as a function of the thickness [78, 146, 147] or the applied stress [148]. In the case of MoS_2, there is also a transition from direct-band (monolayer) to indirect gap (multilayer) [147], that may be harnessed in electronic and optoelectronic devices design, as for example, to manufacture more efficient multijunction solar cells [149].

TMD semiconductors, are interesting candidates for their use in field-effect transistors (FET). Their 2D nature could allow the fabrication of ultra-thin FETs, improving the channel control by the gate, which would result in lower power consumption and the reduction of the short channel effects [56, 57, 150]. Moreover, the 2D nature of the material may be useful to reduce interfacial states and surface roughness, mitigating the induced degradation of the carrier mobility appearing in ultra-thin Silicon FETs [151].

In order to analyse the potential of MoS_2-based devices, their electrostatic and

transport properties need to be studied. The carrier mobility (μ) of these materials is limited by phonon-scattering processes, which are unavoidable, but also by other surface related scattering processes, and in particular by trapped charge (the so-called Coulomb-limited mobility). Some works have dealt with monolayer mobility [152, 153, 154, 155, 156] as well as for thick MoS_2 FET structures, in this case employing bulk expressions [157]. However, a comprehensive analysis of the behaviour of TMD-based devices with few nanometers thickness (roughly, from 2 nm to 10 nm), which we will denominate *few-layer* thicknesses, is still lacking.

Here, we focus on phonon-and Coulomb limited electron mobility of few-layer MoS_2 back-gated transistors, as at the current state of the technology, back-gated transistors are specially suitable for fabrication: the 2D samples can be placed directly on the gate oxide without the necessity of additional fabrication steps.

To perform this study, we employ the SAMANTA-SP1D suite presented in Chapter 2, which self-consistently solves the Schrödinger and Poisson equations in the confinement direction of the heterostructure. The effective mass extracted from *ab initio* simulations is employed [148, 158] to take into account the quantum confinement through the Schrödinger equation, as well as other parameters of special relevance for the mobility evaluation [159, 160, 161, 162]. The energy levels and wavefunctions achieved from the Schrödinger-Poisson equations are then used to evaluate the electron mobility using the Kubo-Greenwood technique [163, 164]. Our results [165], also presented in this Chapter, prove that the electronic mobility in pristine samples of MoS_2 is strongly limited by phonon and Coulomb scattering, obtaining a good agreement with the experimental results presented in the literature.

The outline of this Chapter is as follows. First, in Section 3.2, we present the mobility evaluation model, including the different scattering mechanisms here considered. In Section 3.3, the device under study is presented, as well as the simulation parameters employed. After that, Section 3.4 analyses the Coulomb-limited mobility as a function of gate bias, thickness and temperature. Section 3.5 adds the effect of Coulomb scattering in the study. Finally, Section 3.6 summarizes the main conclusions of this work.

3.2 Mobility evaluation

Carrier mobility is a decisive physical parameter in semiconductor technology, specially suitable to seize the limits of each material or heterostructure. Here we explain how this parameter can be evaluated under the Momentum Relaxation Time (MRT) approximation in conjunction with the Kubo-Greenwood formula, and we provide an overall explanation of the procedure followed to obtain the final evaluation expressions for the mobility as a function of the different scattering mechanisms considered. As we will see, the evaluation of the mobility requires the previous analysis of the electrostatics of the confined system, which we perform using the SAMANTA-SP1D module explained in Section 2.9.

In the case of few-layer MoS_2, the electrostatic analysis is performed considering the configuration of its conduction band. This is important, as some parameters, such as the band gap or the valley degeneracy, depends on the selected band structure. Figure 3.1 shows that six identical minima of the conduction band are placed at the corners of the Brillouin region, called K points, for a monolayer MoS_2, but shifted to an intermediate position along the Λ direction (joining the Γ and K points) in multilayer MoS_2. Therefore, the valley degeneracy (g_v) for monolayer MoS_2 would be 2 (as each minima is shared between the three adjacent Brillouin zones) but is increased to 6 for any other number of layers.

3.2.1 Momentum Relaxation Time

In a one dimensional confined system, the electrostatics in equilibrium can be evaluated employing the Schrödinger-Poisson equations system. In addition, perturbations due to particle interaction with the environment may be added in what we call scattering mechanisms, which can set the system out of equilibrium. In the Boltzmann Transport Equation (BTE), the term corresponding to the variation of the distribution function over time due to the collisions between particles can be written as [141]

$$\frac{\partial f\left(\boldsymbol{k}\right)}{\partial t} = S_{\text{in}}\left(\boldsymbol{k}\right) - S_{\text{out}}\left(\boldsymbol{k}\right) \tag{3.1}$$

where $S_{\text{in}}\left(\boldsymbol{k}\right)$ ($S_{\text{out}}\left(\boldsymbol{k}\right)$) stands for the rate of particles changing their wavevectors to (from) $\boldsymbol{k}$. In this context, the Momentum Relaxation Time (MRT) approximation considers the perturbations in the system to cause small deviations from the equilibrium, and assumes a uniform transport condition (i.e., that all the macroscopic quantities are

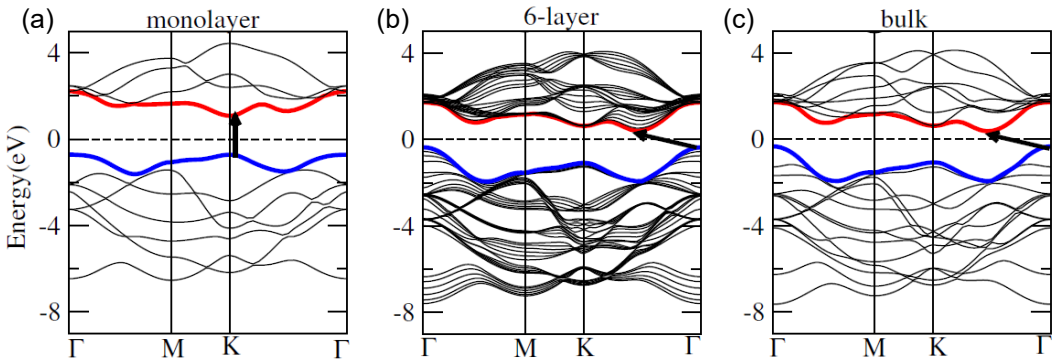

Figure 3.1: Band structure of (a) monolayer, (b) six layer and (c) bulk MoS_2 semiconductor. In the bulk and few-layer cases, the conduction band minima are placed in the Λ direction, and the valence band maxima at the Γ point, giving an indirect bandgap. The material shifts to a direct although larger gap when it is exfoliated up to its monolayer thickness, moving both the conduction band minima and valence band maxima to the K point. Reprinted by permission from Springer P.K. Eur. Phys. J. B, Electronic structure of transition metal dichalcogenides monolayers 1H-MX2 (M = Mo, W; X = S, Se, Te) from ab-initio theory: new direct band gap semiconductors, A. Kumar and P. K. Ahluwalia, copyright © 2012 [76].

independent of the $\mathbf{r}$ position in the transport plane). Under these conditions, if an electric field $\boldsymbol{F} = F_\alpha \hat{\mathbf{e}}_\alpha$ is applied, and then disappears at a given time, Eq. (3.1) for the i-th subband becomes

$$\frac{\partial f_i(\boldsymbol{k})}{\partial t} \simeq -\frac{\delta f_i(\boldsymbol{k})}{\tau_{i,\alpha}(\boldsymbol{k})} = -\frac{f_i(\boldsymbol{k}) - f_0(E_i(\boldsymbol{k}))}{\tau_{i,\alpha}(\boldsymbol{k})} = S_{\text{in}}(\boldsymbol{k}) - S_{\text{out}}(\boldsymbol{k}) \tag{3.2}$$

which means that the deviation $\delta f_i(\boldsymbol{k})$ of the occupation function $f_i(\boldsymbol{k})$ with respect to its equilibrium $f_0(E_i(\boldsymbol{k}))$ decays governed by the time constant $\tau_{i,\alpha}(\boldsymbol{k})$.

Using Eq. (3.2), it is possible to calculate the electron mobility. To do so, the corresponding time constant of each scattering mechanism for each state $(i,\boldsymbol{k})$ have to be evaluated first. Here, three assumptions are considered in the physical modelling of these scattering events [166]:

- The collisions is considered instantaneous, as they occur in a very short time scale.
- The collisions originate a change in the particles trajectory, which modify their wavenumber, but there is no change of their spatial positions.

- The scattering interaction is weak.

Under these assumptions, the scattering balance can be calculated using the Fermi Golden Rule, which provides an expression for the scattering rates $S_{i,j}\left(\boldsymbol{k},\boldsymbol{k'}\right)$ given a perturbation potential $\tilde{\psi}\left(\mathbf{r}\right)$ associated to the corresponding scattering mechanism. A more detailed explanation of this procedure for a 1D gas can be found in [140]. The general expression of the scattering rate is:

$$S_{i,j}\left(\boldsymbol{k},\boldsymbol{k'}\right)=\frac{2\pi}{\hbar}\left|M_{i.j}\left(\boldsymbol{k},\boldsymbol{k'}\right)\right|^{2}\delta\left[E'-E\pm\hbar\omega\right] \tag{3.3}$$

where $\delta\left(x\right)$ is the Dirac function, $\hbar\omega$ is the energy exchanged in the interaction and $M_{i,j}$ is the matrix element for the interaction between an initial state (i,$\boldsymbol{k}$) with energy E and a final state (j,$\boldsymbol{k}$') with energy E', which under the effective mass approximation (EMA) for 1D confined-systems in the y direction has the general expression:

$$M_{i,j}\left(\boldsymbol{k},\boldsymbol{k'}\right)=\langle\xi_{i}\left(\boldsymbol{k},y\right)|\tilde{\psi}\left(\boldsymbol{k},y\right)|\xi_{j}\left(\boldsymbol{k'},y\right)\rangle. \tag{3.4}$$

It strongly depends on the scattering mechanism considered, demanding a separated analysis for each one of them. With this scattering rate definition, the final expression of the flux balance reads:

$$S_{\mathrm{in},i}-S_{\mathrm{out},i}=-\delta f_{i}\left(\boldsymbol{k}\right)\sum_{j,\boldsymbol{k'}}S_{i,j}\left(\boldsymbol{k},\boldsymbol{k'}\right)\left[\frac{1-f_{0}\left(E'\right)}{1-f_{0}\left(E\right)}\right]\left[1-\frac{\tau_{j,\alpha}\left(\boldsymbol{k'}\right)}{\tau_{i,\alpha}\left(\boldsymbol{k}\right)}\frac{v_{j,\alpha}\left(\boldsymbol{k'}\right)}{v_{i,\alpha}\left(\boldsymbol{k}\right)}\right] \tag{3.5}$$

where we have defined the electron velocity as $v_{i,\alpha}\left(\boldsymbol{k}\right)=\hbar^{-1}\nabla E_{i}\left(\boldsymbol{k}\right)$. This equality can be used in Equation (3.2) to obtain an implicit expression of the MRT, as it is present in both sides of the equation, giving:

$$\frac{1}{\tau_{i,\alpha}\left(\boldsymbol{k}\right)}=\sum_{j,\boldsymbol{k'}}S_{i,j}\left(\boldsymbol{k},\boldsymbol{k'}\right)\left[\frac{1-f_{0}\left(E'\right)}{1-f_{0}\left(E\right)}\right]\left[1-\frac{\tau_{j,\alpha}\left(\boldsymbol{k'}\right)}{\tau_{i,\alpha}\left(\boldsymbol{k}\right)}\frac{v_{j,\alpha}\left(\boldsymbol{k'}\right)}{v_{i,\alpha}\left(\boldsymbol{k}\right)}\right] \tag{3.6}$$

An explicit expression of the MRT can be obtained under the approximation of small differences between $\tau_{i,\alpha}\left(\boldsymbol{k}\right)$ and $\tau_{j,\alpha}\left(\boldsymbol{k'}\right)$ for all subbands and wavevectors, which reduces this equation to:

$$\frac{1}{\tau_{i,\alpha}\left(\boldsymbol{k}\right)} = \sum_{j,\boldsymbol{k}'} S_{i,j}\left(\boldsymbol{k},\boldsymbol{k}'\right)\left[\frac{1-f_0\left(E'\right)}{1-f_0\left(E\right)}\right]\left[1-\frac{v_{j,\alpha}\left(\boldsymbol{k}'\right)}{v_{i,\alpha}\left(\boldsymbol{k}\right)}\right] \tag{3.7}$$

The contributions of each one of the scattering mechanisms per subband are summed up to evaluate the total momentum relaxation time as:

$$\frac{1}{\tau_{i,\text{total}}\left(\boldsymbol{k}\right)} = \sum_{s}\frac{1}{\tau_i^s\left(\boldsymbol{k}\right)} \tag{3.8}$$

where the superscript s is used to denote the corresponding scattering mechanism.

The next step is to evaluate the mobility of each subband μ_i, once $\tau_{i,\text{total}}\left(\boldsymbol{k}\right)$ is calculated. Considering the assumptions of the MRT, we use the so-called Kubo-Greenwood formula [163, 164]. Let us start defining the current density per unit length due to the i-th subband of a 2D electron gas in one of its directions α:

$$J_{i,\alpha} = \frac{q^2}{A}F_\alpha\sum_{\boldsymbol{k}} v_{i,\beta}\left(\boldsymbol{k}\right)v_{i,\alpha}\left(\boldsymbol{k}\right)\tau_{i,\alpha}\left(\boldsymbol{k}\right)\left|\frac{\partial f_0\left(E_i\left(\boldsymbol{k}\right)\right)}{\partial E}\right| \tag{3.9}$$

where $\tau_{i,\alpha}\left(\boldsymbol{k}\right)$ includes all the scattering mechanisms considered. At the same time, if we assume a linear relation between current and electric field we also have:

$$J_{i,\alpha} = \left(qn_i\right)\left(\mu_{i,\alpha\alpha}F_\alpha + \mu_{i,\alpha\beta}F_\beta\right) \tag{3.10a}$$

$$J_{i,\beta} = \left(qn_i\right)\left(\mu_{i,\beta\alpha}F_\alpha + \mu_{i,\beta\beta}F_\beta\right) \tag{3.10b}$$

where n_i is the inversion electron density of the i-th subband without accounting for the valley degeneracy. Combining both equations, we can obtain the four components of the electron mobility. For example, the mobility component in the α direction when an electric field in the same direction (F_α) is applied can be evaluated as:

$$\mu_{i,\alpha} = \frac{J_{i,\alpha}}{qn_iF_\alpha} = \frac{q}{n_iA}\sum_{\boldsymbol{k}} v_{i,\beta}\left(\boldsymbol{k}\right)v_{i,\alpha}\left(\boldsymbol{k}\right)\tau_{i,\alpha}\left(\boldsymbol{k}\right)\left|\frac{\partial f_0\left(E_i\left(\boldsymbol{k}\right)\right)}{\partial E}\right| \tag{3.11}$$

The sum over $\boldsymbol{k}$ of a generic function can be changed by an integral over the corresponding kinetic energy $E_\text{p} = E - E_i$ and angle θ [141]. For circular, parabolic bands, the mobility gets independent of the angle as well as of the direction of the electric field. In that case, the mobility is a scalar, which we can simply denominate $\mu_i = \mu_{i,\alpha\alpha} = \mu_{i,\beta\beta}$, and $\mu_{i,\alpha\beta} = \mu_{i,\beta\alpha} = 0$. Equation (3.11) reduces to:

$$\mu_i = \frac{q}{n_i \pi \hbar^2} \int_0^\infty \mathrm{d}E_\mathrm{p}\, E_\mathrm{p} \tau_i \left(E_\mathrm{p}\right) \left| \frac{\partial f_0 \left(E\right)}{\partial E} \right|, \tag{3.12}$$

Finally, we can note that, when temperature is not too low, there can be many subbands carrying a significant charge in the inversion layer, so the total current density is given by the sum of the contribution of the different subbands, and the average or effective mobility μ, including the contribution of the different energy levels of each of the valleys ν, can be evaluated as:

$$\mu = \sum_\nu \sum_i \frac{n_{i,\nu}}{\sum n_{i,\nu}} \mu_{i,\nu} \tag{3.13}$$

3.2.2 Scattering mechanisms analysis

There are various classifications in which we can divide the scattering processes, and it is worth to emphasize them before describing each of the scattering mechanisms that should be considered in MoS_2-based devices.

- **Intravalley vs. Intervalley**. An intravalley transition provokes a small variation of $\boldsymbol{k}$, thus maintaining the carrier in the same valley it was before the transition (see Figure Fig. 3.2). On the other hand, in an intervalley transition, the value of $\boldsymbol{k}$ can be greatly modified as the electron jumps from one valley to another, as depicted in Figure 3.3, which represents this kind of transitions for a Brillouin cell of a monolayer MoS_2 flake.

- **Intraband vs. Interband**. It only makes sense to consider this kind of splitting in intravalley transitions. An intraband transition maintains the potential energy and only modifies either the energy or the wave vector (or both) inside the same subband. An interband transition allows the conservation of energy through a variation of both, potential and kinetic energies.

- **Elastic vs. Inelastic**. An elastic transition does not change the total energy of the carrier before and after the transition, but only its wave vector. On the contrary, an inelastic transition provokes a change of its energy, and as a consequence requires the emission or absorption of a phonon with energy $\hbar\omega$ in the process.

- **Isotropic vs. Anisotropic**. Some scattering mechanisms depends on the initial $\boldsymbol{k}$ and final $\boldsymbol{k}$' wave vector, more specifically, on the angle between both wave

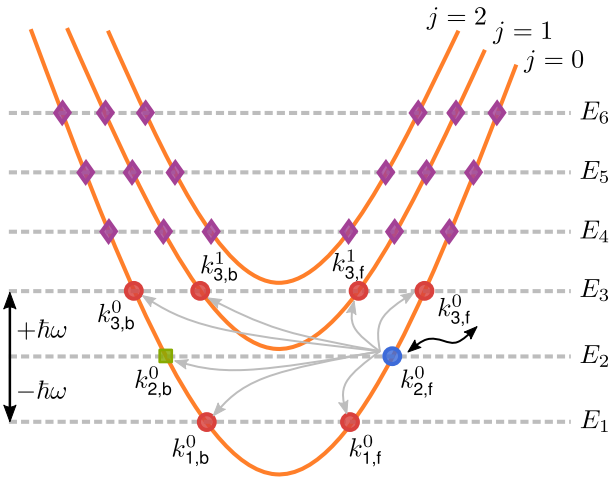

Figure 3.2: Intravalley transitions of an electron in a cut of a parabolic band. The f and b subscripts refer to the two possible states in the plotted cut. During the process, the **k** moment is slightly changed. If the scattering mechanism is elastic, the energy of the electron does not change, and the transition corresponds to the one depicted as a green square, which is also an intraband transition. For inelastic processes, the energy level of the electron may change between discretized states due to the absorption or emission of a phonon with energy $\pm\hbar\omega_{\text{ph}}$, allowing the change of its potential energy, marked as red circles.

vectors. This is the situation of anisotropic mechanisms. In contrast, for isotropic processes, the MRT evaluation is independent of the angle between the initial and final wave vectors, simplifying considerably the scattering rate evaluation.

In this Section we explain how to calculate the MRT associated to different scattering mechanisms, in particular those related to crystal vibrations (phonons) and fixed charges in the semiconductor (Coulomb), that are of most interest to evaluate the mobility in MoS_2 devices [157]. More details on the derivation of the employed expressions can be found in [141].

At any finite temperature, the atoms in the crystal lattice oscillate with respect to their nominal positions. Such vibrations of the lattice produce perturbations of the potential corresponding to the ideal lattice, which become a noticeable source of carrier scattering, in particular at room temperature. The quantization of the lattice vibrations, identifying the different vibration modes by their corresponding wave vector and energy gives rise to the concept of phonons. The phonon modes are closely related to mechanical strain in the crystal. In fact, the propagation of an acoustic wave corre-

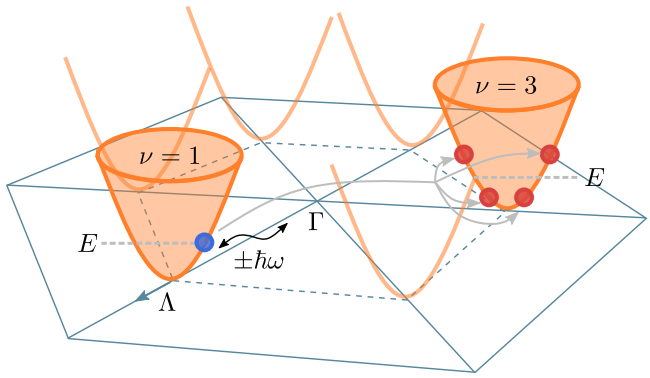

Figure 3.3: Intervalley transition of an electron due to the absorption or emission of a phonon with energy $\pm\hbar\omega_{\mathrm{ph}}$. The solid hexagon encircles the Brillouin region, whereas the dashed one the positions of the bands in the multilayer scenario. During the intervalley process, the **k** moment is greatly modified. At the same time, as the depicted process is inelastic, the energy level of the electron is altered, allowing the change of its potential energy, as well as its global position in the cell.

sponds to an spatial and time dependent strain of the crystal, which alters its band structure. The local strain is associated with an energy shift of the crystal electronic bands. Such an energy shift is what we interpret as the phonon scattering potential, which is the magnitude required to evaluate the matrix element of the associated scattering rate. There are several types of phonons that have to be considered in the assessment of the carrier mobility. In the case of MoS_2, the following should be taken into account: longitudinal and transversal acoustic phonons (LA and TA), longitudinal optical phonons (LO), homopolar phonons (Ho), and polar optical phonons (POP) due to Frölich interaction.

In a similar way, a Coulomb centre produces a perturbation potential which can effectively scatter the carriers in a semiconductor device. For instance, in an MOS transistor, such electrically charged centres are the ionized dopants in the channel, as well as the fixed charges, either in localized states at the semiconductor-oxide interface or in the gate-oxide stack. As the presence of fixed or trapped charges at the interfaces between MoS_2 and the insulators is expected, the Coulomb scattering mechanism should also be considered for a realistic evaluation of the devices mobility.

Acoustic phonons

LA and TA phonons can be classified as intravalley, isotropic and elastic phonon scattering processes. Thus, the MRT calculation is reduced to a sum over the different subbands belonging to the same valley and each value of $\boldsymbol{k}$ of the scattering rate. To do it, the corresponding matrix element has to be evaluated, by means of the calculation of the deformation potential for acoustic and optical phonons, as explained in [141]. For one valley, the final expression of the MRT in this case is:

$$\frac{1}{\tau_i^{\mathrm{ac}}(E)} = \frac{2\pi k_{\mathrm{B}} T D_{\mathrm{ac}}^2}{\rho \hbar v_{\mathrm{s}}^2} \sum_j F_{j,i}\; g_j(E) \tag{3.14}$$

As this is an intravalley transition, the summation runs over the subbands j corresponding to the same valley as the i-th subband. We define D_{ac} as the deformation potential, ρ is the semiconductor volumetric density, $g_j(E)$ corresponds to the density of states of the j-th subband for a 2D gas, v_{s} is the sound velocity in the material for each given phonon process, and $F_{j,i}$ is the form factor between the i-th and j-th subbands, which is calculated as:

$$F_{j,i} = \int_y \left| \xi_j^*(y)\, \xi_i(y) \right|^2 dy. \tag{3.15}$$

Only final states with positive kinetic energy are allowed in this evaluation.

Homopolar and Longitudinal Optical phonons

In the case of Ho and LO phonons, they are modelled as inelastic isotropic processes. Ho phonons are intravalley, and they are evaluated using the following expression:

$$\frac{1}{\tau_i^{\mathrm{Ho}}(E)} = \frac{\pi D_{\mathrm{Ho}}^2}{\omega_{\mathrm{Ho}} \rho} \sum_j F_{j,i} \left[n_{\mathrm{Ho}} + \frac{1}{2} \mp \frac{1}{2} \right] \left[\frac{1 - f_0(E \pm \hbar\omega_{\mathrm{Ho}})}{1 - f_0(E)} \right] g_j(E \pm \hbar\omega_{\mathrm{Ho}}), \tag{3.16}$$

where, $\hbar\omega_{\mathrm{Ho}}$, D_{Ho} and n_{Ho} are the homopolar phonon energy, optical deformation potential and phonon number, respectively. The phonon number can be calculated as:

$$n_{\mathrm{Ho}} = \frac{1}{e^{\frac{\hbar\omega_{\mathrm{Ho}}}{k_{\mathrm{B}} T}} - 1}. \tag{3.17}$$

As for LO phonons, they are intervalley transitions, where the electron changes its state from valley ν to valley ω, and therefore the valley degeneracy of the transition, $\mu_{\omega\,\nu}$ should be considered in the calculation (5 for thicker devices, 1 for monolayer flakes). In addition, it must be employed the corresponding values $\hbar\omega_{\mathrm{LO}}$, n_{LO} and D_{LO}. Recalling the form factor to include the intervalley transition as $F_{\nu\,i}^{\omega\,j}$, the final expression is

$$\frac{1}{\tau_i^{\mathrm{LO}}(E)} = \frac{\pi D_{\mathrm{LO}}^2}{\omega_{\mathrm{LO}}\rho}\sum_j \mu_{\omega\,\nu} F_{\nu\,i}^{\omega\,j}\left[n_{\mathrm{LO}} + \frac{1}{2} \mp \frac{1}{2}\right]\left[\frac{1 - f_0\left(E \pm \hbar\omega_{\mathrm{LO}}\right)}{1 - f_0(E)}\right] g_{\omega\,j}\left(E \pm \hbar\omega_{\mathrm{LO}}\right), \tag{3.18}$$

where the form factor is

$$F_{\nu\,i}^{\omega\,j} = \int_y \left|\left(\xi_j^{\omega}(y)\right)^* \xi_i^{\nu}(y)\right|^2 dy. \tag{3.19}$$

Polar Optical phonons

Polar Optical phonons are intravalley anisotropic inelastic processes, for which the following expression should be used:

$$\left|M_{i,j}(Q)\right|^2 = \frac{Q^2\hbar\omega_{\mathrm{POP}}}{4AQ}\left(\frac{1}{\varepsilon(\infty)} - \frac{1}{\varepsilon(0)}\right)\left(n_{\mathrm{POP}} + \frac{1}{2} \pm \frac{1}{2}\right) I_{i,j}(Q) \tag{3.20}$$

which depends on the transition between the initial and the final state $Q = \left|\boldsymbol{k} - \boldsymbol{k}'\right|$. Here, $\varepsilon(0)$ and $\varepsilon(\infty)$ refer to the static and high frequency dielectric constant, respectively; $\hbar\omega_{\mathrm{POP}}$ is the POP energy and n_{POP} the corresponding phonon number, which is evaluated as in Eq. (3.17). The upper and lower signs correspond to the emission and absorption processes, respectively. The term $I_{i,j}(Q)$ is the form factor associated to this scattering mechanism, which must include the dependence between the initial and final wave vectors and is therefore calculated as

$$I_{i,j}(Q) = \int_y dy \xi_j^*(y)\,\xi_i(y) \cdot \left(\int_{y'} dy' \xi_j^*\left(y'\right) e^{-Q|y-y'|} \xi_i\left(y'\right)\right). \tag{3.21}$$

When substituting in Equation (3.3), and this in turn in Equation (3.6), a complex expression dependent of $\boldsymbol{k}$ and $\boldsymbol{k}$' is obtained. We have simplified this equation consi-

dering circular and parabolic subbands, and modifying the sum over $\boldsymbol{k}$' by an integral over the angle of $\boldsymbol{Q}$, θ. For an arbitrary function multiplied by the Dirac function, we have [141]:

$$\begin{aligned}\sum_{\boldsymbol{k}'} f\left(k'\right)\delta\left(E'-E-\Delta E\right) &= \frac{1}{\left(2\pi\right)^2}\iint_{\boldsymbol{k}'} f\left(\boldsymbol{k}'\right)\delta\left(E'-E-\Delta E\right)\mathrm{d}k'_{\mathrm{x}}\mathrm{d}k'_{\mathrm{z}} = \\ &= \frac{1}{\left(2\pi\right)^2}\iint_{\boldsymbol{k}'} f\left(k',\theta\right)\delta\left(E'-E-\Delta E\right)k'\left(\theta\right)\mathrm{d}k'\mathrm{d}\theta\end{aligned} \tag{3.22}$$

where k' is the $\boldsymbol{k}$' module. We know the integral of a function multiplied by the Dirac function at an arbitrary position x_0 is the value of the function in that position x_0. Here we combine this fact with the relation between energy and wave vector for parabolic bands:

$$v_j = \frac{1}{\hbar}\frac{\mathrm{d}E}{\mathrm{d}k'} = \frac{\hbar}{m^{\mathrm{tr}}\left(\theta\right)}k'\left(\theta\right) \tag{3.23}$$

where m^{tr} is the effective mass in the transport direction, which is a constant value along all the integral. Using the first equality and the Dirac property, we can solve one of the integrals:

$$\frac{1}{\left(2\pi\right)^2}\iint_{\boldsymbol{k}'} f\left(\boldsymbol{k}'\right)\delta\left(E'-E-\Delta E\right)\mathrm{k}'\mathrm{d}k'\mathrm{d}\theta = \frac{1}{\left(2\pi\right)^2}\int_{\theta} f\left(\theta\right)\frac{1}{\left|\hbar v_j\left(\theta\right)\right|}k'\left(\theta\right)\mathrm{d}\theta \tag{3.24}$$

and using the second equality, we can delete the k' dependency:

$$\begin{aligned}\frac{1}{\left(2\pi\right)^2}\int_{\theta} f\left(\theta\right)\frac{1}{\left|\hbar v_j\left(\theta\right)\right|}k'\left(\theta\right)\mathrm{d}\theta &= \frac{1}{\left(2\pi\right)^2}\int_{\theta} f\left(\theta\right)\frac{m^{\mathrm{tr}}\left(\theta\right)}{\hbar^2 k'\left(\theta\right)}k'\left(\theta\right)\mathrm{d}\theta = \\ &= \frac{1}{\left(2\pi\hbar\right)^2}\int_0^{2\pi} m^{\mathrm{tr}}\left(\theta\right)f\left(\theta\right)d\theta\end{aligned} \tag{3.25}$$

Specifying to the scattering rate in Equation (3.25) to the POP matrix element and substituting in Equation (3.6), an expression of the MRT dependent of this Q difference is given by

$$\frac{1}{\tau_i^{\mathrm{POP}}(E)} = U \sum_j m^{\mathrm{tr}} \left[\frac{1 - f_0(E \pm \hbar\omega_0)}{1 - f_0(E)}\right] \int_0^{2\pi} d\theta I_{i,j}(Q) \frac{1}{Q} \left(1 - \frac{|\boldsymbol{k}'|}{|\boldsymbol{k}|}\cos(\theta)\right) \quad (3.26)$$

where the electron velocities quotient has been substituted according to the equality in (3.23) by a term dependent of $\boldsymbol{k}$', $\boldsymbol{k}$ module and the angle between them, and U is given by

$$U = \frac{q^2 \hbar \omega_{\mathrm{POP}}}{8\pi\hbar^3} \left(\frac{1}{\varepsilon(\infty)} - \frac{1}{\varepsilon(0)}\right) \left(n_{\mathrm{POP}} + \frac{1}{2} \pm \frac{1}{2}\right) \quad (3.27)$$

Coulomb centres

Finally, we have included the Coulomb scattering associated with the presence of fixed charges in the semiconductor. Coulomb scattering is an intravalley elastic scattering mechanism, in which we have included the non parabolicity of the bands to generate a more general formula. The MRT of the Coulomb scattering follows the formula [141, 167]

$$\frac{1}{\tau_i(E,\theta)} = \frac{H_\nu(E_{\mathrm{p}})}{2\pi\hbar^3} [1 + 2\alpha_{\mathrm{np}} E_{\mathrm{p}}] \int_0^{2\pi} \mathrm{d}\theta' m_{xy}(\theta') |M_{i,j}(\boldsymbol{Q})|^2 \left[1 - \frac{\cos(\theta')}{\cos(\theta)}\right]. \quad (3.28)$$

Here, H_ν is the step function, α_{np} is the non-parabolicity factor and $m_{xy}(\theta')$ is a ratio between the confinement and the transport effective masses, following

$$m_{xy}(\theta') = \left[\frac{\cos^2(\theta')}{m_x} + \frac{\sin^2(\theta')}{m_y}\right]^{-1} \quad (3.29)$$

where the θ' is the angle between the final state j of the electron with wave vector $\boldsymbol{k}'$ and the electric field. The angle θ has a similar meaning, in this case considering the initial state i with wave vector $\boldsymbol{k}$. The vector $\boldsymbol{Q}$ has the same meaning as in the POP scattering rate evaluation, that is $\boldsymbol{Q} = \boldsymbol{k}' - \boldsymbol{k}$. Its module is the distance between them, and can be evaluated as $Q^2 = k^2 + k'^2 - 2kk'\cos(\theta' - \theta)$. Finally, the matrix element $|M_{i,j}(\boldsymbol{Q})|^2$ has been evaluated considering the screening effect. The screening produced by the free carriers in the inversion layers has a large impact in the Coulomb scattering rate, so neglecting the screening in calculation of the scattering rates may result in a

vast over-estimation of their values. Considering this effect, the matrix element can be calculated as

$$|M_{i,j}(\boldsymbol{Q})|^2 = \int_y \left|M^0_{i,j}(\boldsymbol{Q}, y_0)\right|^2 N_{\mathrm{II}}(y_0)\,\mathrm{d}y_0 \tag{3.30}$$

where N_{II} is the volumetric density of Coulomb centres and the screening matrix element $\left|M^0_{i,j}(\boldsymbol{Q}, y_0)\right|^2$ is evaluated using the scalar dielectric function $\epsilon_{\mathrm{D}}(\mathbf{Q})$, which adds the screening effect:

$$\left|M^0_{i,j}(\boldsymbol{Q}, y_0)\right|^2 = \int_y \xi^*_j(y)\,\frac{\psi_{\mathrm{pc}}(\boldsymbol{Q}, y, y_0)}{\epsilon_{\mathrm{D}}(\boldsymbol{Q})}\xi_i(y) \tag{3.31}$$

Here, the $\psi_{\mathrm{pc}}(\boldsymbol{Q}, y, y_0)$ is the scattering potential, calculated using the method explained in [168, 169, 170] for oxide-semiconductor-oxide stacks. This Equation is applied only in intra-subband transitions. For inter-subband transitions, the dielectric function is approximately equal to one. The scalar dielectric function can be calculated as:

$$\epsilon_{\mathrm{D}}(\boldsymbol{Q}) = 1 - \sum_{\nu,i}\frac{q^2}{Q(\varepsilon_{\mathrm{sc}} + \varepsilon_{\mathrm{ox}})}\Pi_{\nu,i,i}(\boldsymbol{Q}) \tag{3.32}$$

where $\Pi_{\nu,i,i}(\boldsymbol{Q})$ is the polarization factor, evaluated in a more general way as

$$\Pi_{\nu,i,j}(\boldsymbol{Q}) = \sum_{\boldsymbol{k}}\frac{f_{\nu,j}(\boldsymbol{k}+\boldsymbol{Q}) - f_{\nu,i}(\boldsymbol{k})}{E_{\nu,j}(\boldsymbol{k}+\boldsymbol{Q}) - E_{\nu,i}(\boldsymbol{k})} \tag{3.33}$$

and $f_{\nu,i}(\boldsymbol{k})$ is the occupation function of the subband (ν, i), which for low fields can be reduced to the one corresponding to the Fermi-Dirac occupation function:

$$f_{\nu,i}(\boldsymbol{k}) = f_0(E_{\nu,i}(\boldsymbol{k})) \tag{3.34}$$

where the sum over $\boldsymbol{k}$ has been converted to an integral according to Eq. (3.22), so we finally evaluate:

$$\Pi_{\nu,i,j} = \frac{2g_\nu m^{\mathrm{tr}}}{2\pi\hbar^2}\int_0^\infty (1 + 2\alpha_{\mathrm{np}}E_{\mathrm{p}}\mathrm{d}E_{\mathrm{p}})\int_0^{2\pi}\frac{f_0(k,q,\theta) - f_0(k)}{E_{\nu,j}(k,q,\theta) - E_{\nu,i}(k)} \tag{3.35}$$

3.3 Device under study

Due to their interest in logical applications, we have focused this chapter on the analysis of the electron mobility of back-gated Metal-Insulator-Semiconductor transistors, with MoS_2 as the channel material, for various thickness T_{sc} ranging from 2nm to 10nm. The device under study is inspired in the experimental device presented by Kim et al. in [157]. The structure is depicted in Figure 3.4, where Al_2O_3 is employed as a gate insulator, with thickness $T_{ox} = 50$ nm, and Ti is the metal gate used. The device channel is oriented along the x direction, being y the confinement direction (as assumed in the rest of this Chapter). Both x and z directions are assumed large enough, so that the thick long channel device can be accurately modelled employing the SAMANTA-SP1D module. This allows us to evaluate the potential, wave vector, energy levels and electron densities, values that will be used later to calculate the phonon and Coulomb electron limited mobility in the transport direction.

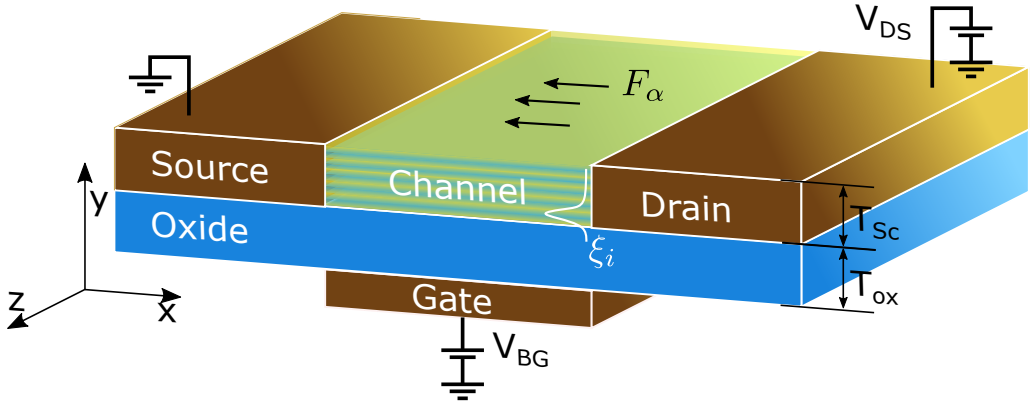

Figure 3.4: Back-gated transistor studied in the confinement direction. The plot also includes the direction of the electric field F_α in the transport direction, as well as a representation of one wavefunction ξ_i.

3.3.1 Material Parameters

The aforementioned model needs several material parameters for both, electrostatic and transport descriptions, which have been extracted from [157, 148, 171, 172, 152] and are summarized in Table 3.1 and Table 3.2, respectively.

The few-layer MoS_2 conduction band has been modelled as six equivalent parabolic Λ valleys ($g_v = 6$), with the effective mass values extracted from [148]. The in-plane

effective mass has been considered as isotropic, and thus it coincides with the transport effective mass m_{sc}^{*tr}. It is calculated as $\sqrt{m_{\parallel}^{*} m_{\perp}^{*}}$, with $m_{\perp}^{*}$ and $m_{\parallel}^{*}$ the values perpendicular and parallel to the Λ direction, respectively.

For the mobility calculations, several specific parameters related to the scattering mechanisms are needed. Some of them can be found in the literature for bulk [157] and monolayer [152] structures. However, which parameters provide the best fit for few-layer flakes is not clear. In this study we chose to employ those parameters available from the bulk published data sets, and complete the gaps employing the corresponding monolayer MoS_2 constants. The obtained values are presented in Table 3.2. This approach can be justified from the fact that several parameters found in the literature for both monolayer and bulk MoS_2, such as $\hbar\omega_{POP}$ and $\hbar\omega_{Ho}$, have been modelled with almost identical values [152, 173, 157].

Parameter	Unit	Value
ϕ_m	(eV)	5.2 †
χ_{sc}	(eV)	4.3 †
ε_{sc}	(ε_0)	7.6 †
ε_{ox}	(ε_0)	9 ◇
m_{sc}^{conf}	(m_0)	0.49 *
m_{ox}	(m_0)	0.2 □
m_{sc}^{tr}	(m_0)	0.62 *
g_v	$(-)$	6 †
ΔE_C	(eV)	2.6 †

Table 3.1: Parameters employed to perform the electrostatic simulations: † [157]; * [148]; ◇ [171]; □ [172]. The "sc" subscript refers to the semiconductor, whereas the "ox" one to the oxides. The "tr" superscript refers to the transport direction, and the "conf" to the one corresponding to the confinement direction. The ΔE_C parameter is the semiconductor-insulator potential barrier.

Parameter	Unit	Value
$D_{\text{ac}}^{\text{LA}}$	(eV)	2.6
$D_{\text{ac}}^{\text{TA}}$	(eV)	1.0
ρ	$\left(\text{kg}\cdot\text{cm}^{-3}\right)$	7.03×10^{-3}
$\text{v}_{\text{s}}^{\text{LA}}$	$\left(\text{cm}\cdot\text{s}^{-1}\right)$	6.7×10^{5}
v_{s}^{TA}	$\left(\text{cm}\cdot\text{s}^{-1}\right)$	4.2×10^{5}
$D_{\text{op}}^{\text{Ho}}$	$\left(\text{eV}\cdot\text{cm}^{-1}\right)$	4.1×10^{8} (*)
$D_{\text{op}}^{\text{LO}}$	$\left(\text{eV}\cdot\text{cm}^{-1}\right)$	2.6×10^{8} (*)
$\hbar\omega_{\text{Ho}}$	(meV)	52
$\hbar\omega_{\text{LO}}$	(meV)	48 (*)
$\hbar\omega_{\text{POP}}$	(meV)	49

Table 3.2: Parameters employed to calculate the electron mobility in few-layer structures, extracted from [157]. The (*) values are taken from monolayer calculations [152].

3.4 Phonon scattering results

In this Section, the phonon-limited electron mobility in few-layer MoS_2-devices is analysed. We evaluate the effect of the temperature, the back gate bias and the channel thickness. The back-gated transistor under study was presented in the previous Section (Fig. 3.4).

First, we have validated the results of our simulator by comparing them with the experimental data provided by Kim *et al.* [157], whose dimensions are $\text{T}_{\text{sc}} = 30$ nm and $\text{T}_{\text{ox}} = 50nm$. In the experimental conditions, the total inversion electron density is set to $N_{\text{i}} = 1.6\times10^{12}\,cm^{-2}$, so we have tuned the back gate bias in the simulations to achieve the same inversion charge. Under these conditions, the electron mobility as a function of temperature is shown in Fig. 3.5. The results show an excellent agreement between the experimental data and our simulation results for temperatures higher than 200 K. Next Section will demonstrate that to provide more accurate results for lower temperatures, Coulomb scattering needs to be included.

Once the numerical approach is validated, we focus on the analysis of the contribution of the different phonon scattering mechanisms on the total mobility. To do it, we deal first with a relatively thick device, with $\text{T}_{\text{sc}} = 10$ nm, and change both the temperature and bias conditions. The electron mobility has been evaluated isolating each of the different phonon mechanisms, and compared with the total phonon-limited mobility as a function of the temperature. The achieved results are depicted in Fig.

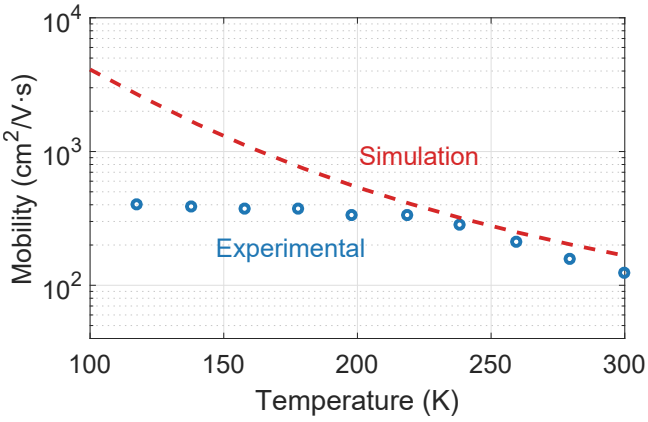

Figure 3.5: Comparison between experimental results (circles), extracted from [157], and simulation results (dashed line).

3.6. Here, two values of the inversion charge N_i have been plotted, in weak inversion regime, $N_i = 10^{11}$ cm^{-2} (solid), and in strong inversion regime, $N_i = 7 \times 10^{12}$ cm^{-2} (dashed). In all the cases, the phonon-limited mobility increases as the temperature is reduced. LO and Ho phonons have a negligible role in all the temperature interval considered (although it should be noted that the influence of the scattering mechanism when isolated from the rest may be underestimated, as the Matthiessen's rule is not applicable). For temperatures above 200 K, the most degrading scattering mechanism is the polar optical phonons, and the total mobility clearly follows the POP-limited mobility trend. In contrast, at lower temperatures, the POP mobility increases very abruptly and acoustic phonons become the dominant rate. As for the influence of the inversion charge, the trend in all the scattering mechanisms is shared, showing a reduction of the mobility when N_i is increased, except for the case of the polar optical phonons, where the behaviour is the opposite. As a consequence of this trade-off, the total mobility for the two N_i values considered is almost the same in the range of temperatures between 200 K and 500 K.

The influence of the channel thickness is analysed in detail in Fig. 3.7, where two temperatures have been considered: T=300 K (Fig. 3.7a) and T=100 K (Fig. 3.7b). MoS_2 thicknesses from 2 nm to 10 nm are studied, and the same values of N_i as in Fig. 3.6 are employed. Here, the POP-limited mobility depicts a non-monotonic behaviour with the device size. In contrast, acoustic phonon-limited mobility simply decreases with the device size. As for the total phonon-limited mobility, it follows the trend of the most limiting scattering mechanisms at each temperature: i) at room temperature,

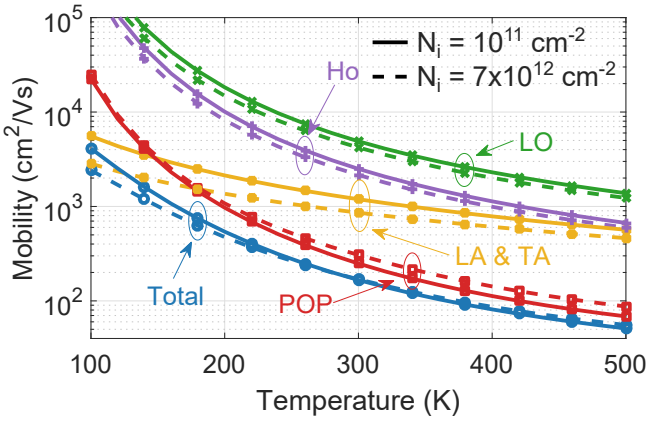

Figure 3.6: Total phonon-limited mobility (blue circles) as a function of the temperature, and contribution of each scattering process: LO (green cross), Ho (purple plus signs), LA and TA already combined (yellow asterisks) and POP (red squares). The semiconductor thickness for this evaluation is $T_{sc} = 10$ nm. We have considered two values of N_i: weak, $N_i = 10^{11}$ cm^{-2} (solid lines) and strong, $N_i = 7 \times 10^{12}$ cm^{-2} (dashed lines) inversion.

as POP is the main scattering mechanism, its non-monotonic behaviour is reflected into the total phonon-limited mobility. ii) As the temperature is decreased, as shown in Fig. 3.7b for T = 100 K, the POP and acoustic phonon contributions are flipped, so the total mobility increases monotonically as a function of the semiconductor thickness, following the acoustic phonon-limited mobility trend.

Finally, Fig. 3.8 shows the total phonon-limited mobility at room temperature as a function of the inversion charge N_i, for three different semiconductor thickness: $T_{sc} = 2$ nm, 5 nm and 10 nm. As shown, the calculated mobility presents the non-monotonic trend with the device thickness already depicted in Fig. 3.7a. The highest value of mobility for the studied thickness interval, in the whole N_i range considered, is obtained for $T_{sc} = 5$ nm channel. In very thin devices, such as $T_{sc} = 2$ nm (corresponding to only three layers of the 2D material), the strong quantization and its influence on the scattering form factors provokes a strong reduction of the mobility.

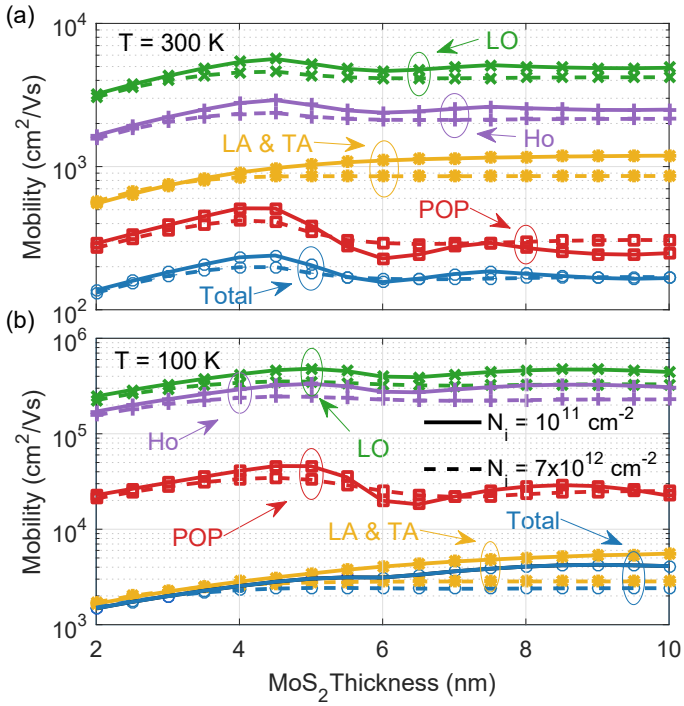

Figure 3.7: Phonon-limited mobility dependence on the semiconductor thickness for (a) T = 300 K and (b) T = 100 K. The contribution of each scattering mechanism is also depicted, using the same symbol code as in Fig. 3.6. Two values of N_i are considered: $N_i = 10^{11}\,cm^{-2}$ (solid lines) and $N_i = 7 \times 10^{12}\,cm^{-2}$ (dashed lines). Device thickness from 2 nm to 10 nm are simulated.

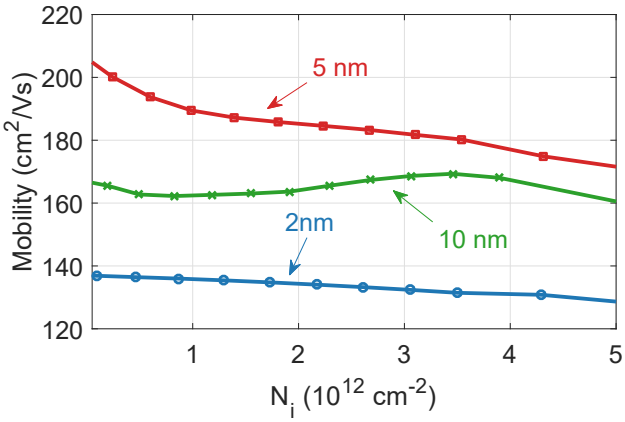

Figure 3.8: Phonon-limited mobility versus inversion electron density at room temperature for three thicknesses: $T_{sc} = 2$ nm (blue circles), $T_{sc} = 5$ nm (red squares) and $T_{sc} = 10$ nm (green crosses).

3.5 Coulomb scattering results

As shown in the previous Section, the calculation of the mobility taking into account only phonon models provides a very good fit to experimental results detailed in [157] at $N_i = 1.6 \times 10^{12}$ cm^{-2} for temperatures above 200 K (see Fig. 3.5). For lower temperatures, the phonon models deviate from the experimental results and additional mechanisms are needed to explain the measured data. In particular, Coulomb scattering should be considered for an accurate modelling at this range of temperatures. So that, we have included Coulomb scattering in our simulations employing the model presented in Section 3.2.2 and we have sought to improve the fit with the experimental mobility [157] in an extended range of temperatures.

The best overall fit was achieved when employing a volumetric density of Coulomb centres of 6.9×10^{16} cm^{-3} in the whole semiconductor. For that value, we have recalculated the mobility as depicted in Fig. 3.9, together with the decomposition for each one of the scattering mechanisms as well as the experimental results. As can be seen, the Coulomb-limited mobility has a strong influence for the whole range of temperatures. The reason may be found in the fact that the value for N_i is not large enough to effectively screen the Coulomb potential. At higher N_i values, the influence of Coulomb limited mobility should be reduced.

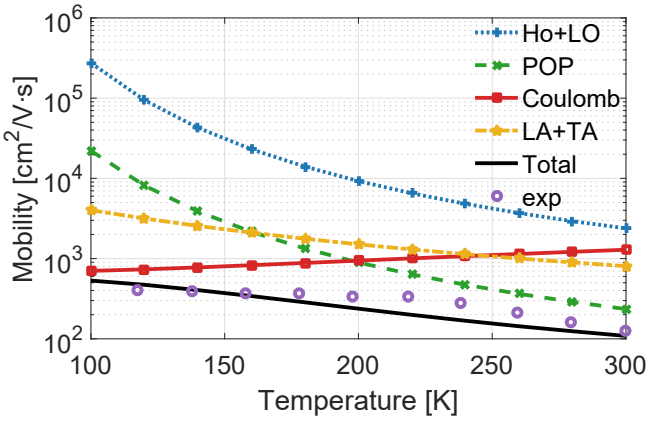

Figure 3.9: Calculated mobility as a function of temperature. Comparison with experimental results, considering both phonon and Coulomb scattering. This second effect includes the screening produced by the carriers in the inversion layer.

3.6 Conclusions

Phonon limited electron mobility

Back-gated FETs with a channel formed by few-layers of MoS_2 have been analysed in its one-dimensional confinement direction using the SAMANTA-SP1D solver. The band structure of the semiconductor has been modelled using the effective mass approach. By applying the Kubo-Greenwood formula, the phonon-limited mobility was calculated, obtaining a solution in good agreement with experimental data for medium and high temperatures. Our results demonstrate that the polar optical phonons govern the phonon-limited mobility for high temperatures, and acoustic phonons play an important role for low temperatures. The phonon-limited mobility has also shown a non monotonic dependence with thickness, with a maximum around $T_{sc} \simeq 5$nm. This effect is related to the form factor behaviour in the POP scattering mechanism. Thinner flakes drop their mobility due to the strong quantum confinement.

Coulomb scattering for low temperatures

Coulomb scattering, including the screening effect, is modelled considering anisotropic bands and a scalar dielectric function. Our results let us conclude that this scattering mechanism is the most important degradation element of the electron mobility for low temperatures.

Chapter 4

Graphene-Silicon Photodiodes

4.1 Motivation

Optoelectronic devices based on graphene are getting the attention of a large number of research groups and the industry during the last years [174]. Two key factors encourage this interest. The first one is the broadband spectral range of graphene [60, 175], caused by the uniqueness of its conical and gap-less energy dispersion relation which provides a noticeable responsivity from Terahertz to the visible range. The second factor is the ultrafast response [176, 177] owing to the exceptionally high carrier mobility, the high saturation velocity and an important internal quantum efficiency of around 30% [178]. All these ingredients turn this material into a very good option to be used as part of numerous optoelectronic devices.

Despite these promising properties, photodetectors and solar cells exclusively based on graphene experience an extremely low absorption, eventually leading to a small photoresponsivity [62]. The cointegration of graphene with traditional semiconductors is proposed as the solution to fabricate practical hybrid devices, benefiting from the unique properties of each material.

The extremely low photon absorption and reduced sheet resistance of graphene makes it a suitable transparent electrode which could be placed on top of the absorbing material without shadowing it. This idea is a common approach in the design of optoelectronic devices, currently implemented by means of the so-called Transparent Conductive Films (TCFs), with Indium Tin Oxide (ITO) and Fluorine-doped Tin Oxide (FTO) as their more popular representatives. But although these materials present a

high level of transparency and conductivity, they suffer a variety of notable drawbacks, such as their chemical instability, brittleness, and high cost due to the scarcity of Indium [179, 180].

So that, the transparency and high conductivity of graphene, as well as its reduced cost, abundance and flexibility makes it prone to replace TCFs and traditional opaque metals currently employed to collect photogenerated carriers. Hence, we begin focusing on a simple photodetector structure, which combines graphene above n-type Silicon, an heterostructure extensively employed due to its ease of fabrication as well as its widespread application, specially among photovoltaic devices [181, 182].

To date, most of the studies dedicated to these hybrid graphene-Silicon photodiodes are focused on improving their performance, using the responsivity as the main figure of merit (FOM). This parameter depends on numerous aspects of the fabricated heterostructure, among which we can highlight:

- The number of graphene layers. The use of more than one layer reduces the sheet resistance, but also drops the transmission coefficient. The optimum number of layers can be estimated as a trade-off between both factors, although the fabrication process can also play a noticeable role [183, 184].
- The use of Antirreflective coatings (ARC), useful to reduce the reflection of the incident light [185].
- The graphene workfunction, which can be tuned via electrostatic [186] or chemical doping [177, 183, 187, 188], allows to shift the Fermi level in a controlled way. The difference with the workfunction of the doped substrate sets a built-in potential that lets the photogenerated carriers to be separated and extracted from the absorber layer to the graphene flake, originating a photocurrent.
- The inclusion of an interfacial insulator between graphene and Silicon [189, 190]. So that, an increment of the photoresponsivity due to the presence of SiO_2 has been experimentally demonstrated [191, 192, 193].

However, there is still a lack of clear understanding about the physical mechanisms that determine the behaviour of these devices. To shed light on them we have carried out this work in close collaboration with the research group leaded by Professor Max Lemme, at the RWTH Aachen (Germany), where different photodetectors based on a graphene-Silicon heterostructure have been fabricated and thoroughly characterized.

Our numerical simulator has been adapted to reproduce the experimental results thanks to the inclusion of several modules.

4.2 Introduction: overview of the experimental results

The research work developed in this Chapter is founded in the hybrid graphene/Si-based device presented by Riazimehr et al. in [194]. There, a continuous graphene layer was placed across SiO_2 and over a Si trench to form a device consisting of a graphene-Si heterojunction (GS, from now on) and a graphene/SiO_2/Si (GIS) field effect structure.

For the sake of completeness, let us provide some details of the fabrication process employed. The fabrication of the device began with a lightly phosphorous doped n-type Si <100> wafer (2×10^{15} cm^{-3}), over which a silicon dioxide (SiO_2) layer of 85 nm was thermally grown. To get the n-Si substrate exposed, the SiO_2 was partially etched after a standard UV–photolithography step with the desired pattern. Next, the metal electrodes were defined in a second photolithography step by sputtering of 20 nm chromium (Cr) and 80 nm gold (Au) and lift-off process. To achieve good ohmic contacts, the metals were deposited immediately after the native oxide removal. Then, a graphene layer grown by a CVD process was transferred on top of the pre-patterned substrate, ensuring the covering of the electrodes, part of the SiO_2 and the n-Si substrate. Prior to graphene transfer, the native SiO_2 grown on the Si substrate was removed, ensuring good electrical contact between graphene and Si substrate. The last photolithography step was the oxygen plasma etching of graphene to define the junction areas. The total surface covered by the GS junctions were ranging between 0.64 mm^2 and 1.6 mm^2. Here we have just sketched the fabrication process, a thorough explanation can be found [194].

The experimental work of Riazimehr et al. [194] started with a detailed analysis of the so-called reference device D_{Ref}, shown in Fig. 4.1a, in which Scanning Photocurrent (SPC) measurements were carried out. In this process, a laser of $\lambda = 532$ nm, spot size of 2.4 μm and light intensity of 5 μW, was swept along all the active area of the photosensor for a fixed V_R. At each position, the laser is stopped enough time to acquire a stationary value of the current. Finally, a complete map of the current measured in the whole device is achieved and the results are depicted in Fig. 4.2 for $V_R = -1$ V and $V_R = -2$ V. There, we can observe that, for the larger reverse bias, the GIS stack provides a much higher contribution (around one order of magnitude) than the GS

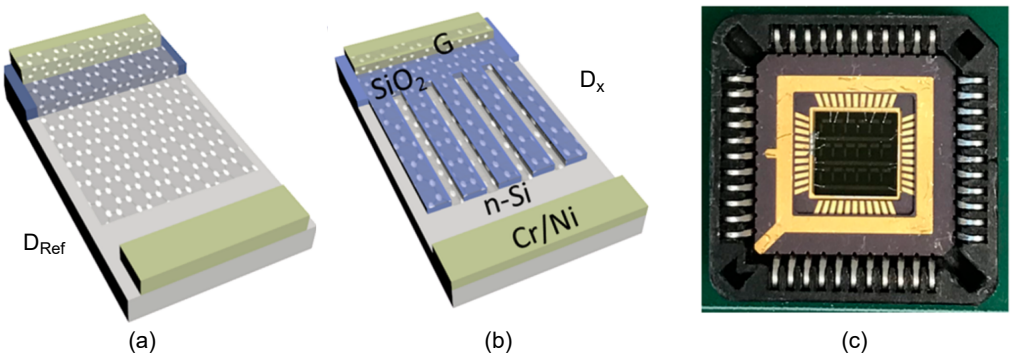

Figure 4.1: Schematics of the full D_{ref} (a) and D_x (b) fabricated devices. (c) Photograph of a wire-bonded diode chip in its chip package. Figure extracted from [195].

Schottky junction.

Those results led them to modify the design of the photodetectors in an attempt to improve the device performance. As a result of this research, the interdigitated Schottky and GIS structures shown in Fig. 4.1b were fabricated. Two different oxide widths, 30 and 100 microns, were considered to analyse its influence on the device performance. The interdigitated devices were named as D_x, with x referring to the finger width. The three photosensors were compared when uniformly illuminated with a monochromatic light source of 30 $\mu W/cm^2$, showing noticeable differences in the responsivity, as depicted in Fig. 4.3. These findings highlight the advantages achieved using interdigitated GIS structures in these kind of photosensors.

Hence, in this Chapter, we will try to gain insight in the main mechanisms explaining the differences between those devices, providing useful conclusions for the enhancement of their efficiency. The Chapter is comprised of three main sections, each one targeting different aspects:

- Analysis in dark conditions of the reference device, used to calibrate most of the physical magnitudes.

- Results in illumination conditions using a lamp that covers the entire device. We start studying the different photosensors in ideal conditions, and then we evaluate the impact induced by the degradation of different magnitudes, specially those related with the quality of the graphene-Silicon interface.

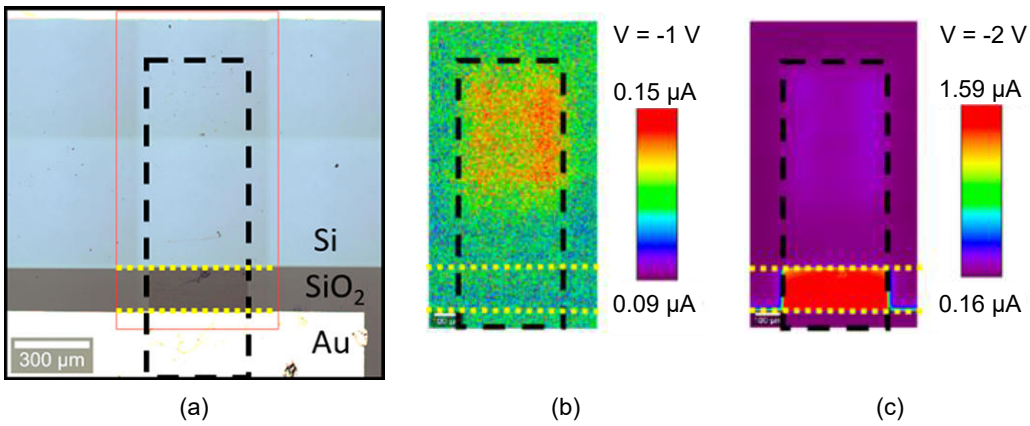

Figure 4.2: (a) Optical micrograph of the D_{Ref} device. The black dashed rectangle demarcates the graphene flake. (b) and (c) Measured current using a Scanning PhotoCurrent (SPC) with $\lambda = 532$ nm and spot size of 2.4 μm. Light power intensity is 5 μW. Results for (b) $V_R = -1$ V and (c) $V_R = -2$ V. Figure extracted from [194].

- Results under laser illumination. We emulate the Scanning PhotoCurrent (SPC) measurements in our simulations, paying special attention to the most degraded scenarios, to see the differences between the GIS and the GS stacks.

Each section provides a description of the scheme employed during the simulation, as well as of the physical variables used to carry them out. The Chapter finishes putting forth the main conclusions of this study.

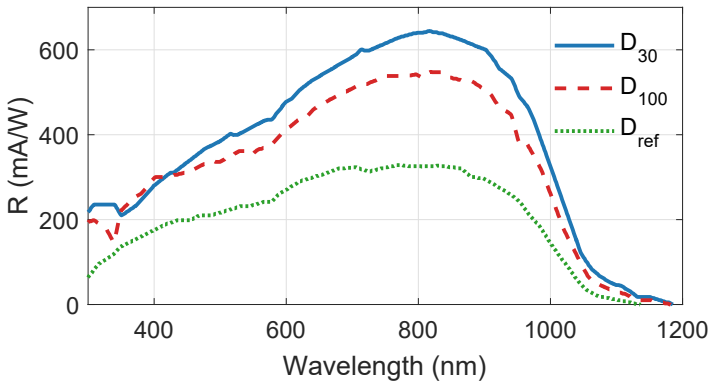

Figure 4.3: Measured responsivity for different light wavelengths at a reverse bias $V_R = -2$ V. Results for (solid line) D_{30}, (dashed line) D_{100} and (dotted line) D_{Ref} devices. Figure extracted from [195]

4.3 Reference device in dark conditions

The reference device is inspired by the photodiodes fabricated and characterized in [194] and already shown in Fig. 4.1a. In order to carry out the numerical simulations of these devices, we have considered a cross-section as depicted in Fig. 4.4.

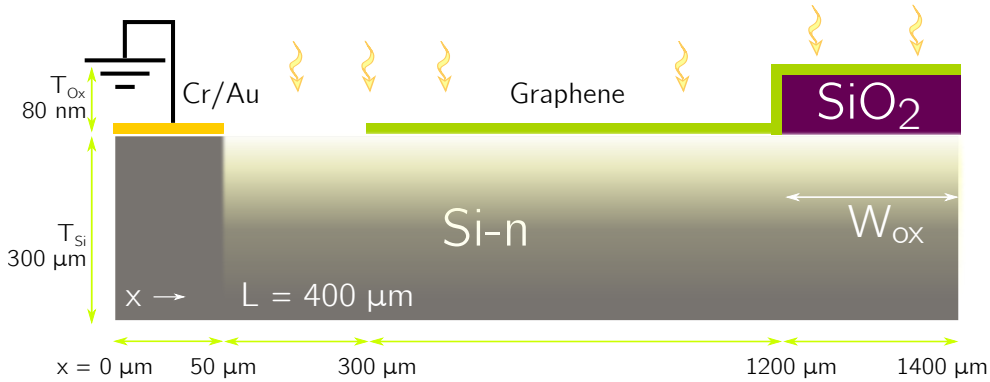

Figure 4.4: Schematic of reference device D_{Ref} similar to the one presented in [194].

The thickness of the oxide is $T_{ox} = 20$ nm, a value high enough to prevent the electron tunnelling through it. In the simulations, both graphene and SiO_2 are considered transparent, so the photons are not absorbed when they pass through both materials for the whole range of wavelengths employed in this study. In addition, we assume that the potential is constant along the graphene layer, neglecting any potential drop. For the simulation we have considered the same substrate thickness as for the real device, $T_{Si} = 300$ μm. This thickness ensures that all the photogenerated carriers are taken into account in the evaluation, because it has been checked that, under uniform lamp illumination, the carriers can diffuse far away from the top interface.

To carry out the simulations, we have employed the material parameters presented in Table 4.1, where the meaning of each symbol is explained in Chapter 2. Most of the simulations performed in this Chapter have also employed these parameters, although there are Sections where some of them are modified to assess their impact.

In this section we compare the experimental measurements achieved in [194] with the numerical results obtained after simulating the device depicted in Fig. 4.4 in dark conditions. In particular, we have focused on calibrating the dark current (I_{dark}). This procedure aims to adjust one of the main parameters in this structure, the graphene Fermi level ($E_{f,gr}$). As demonstrated in [196], due to the reduced DoS of graphene,

Parameter	Value
ϕ_{ref} (eV)	4.52
ϕ_{gr} (eV)	4.82
$\mathrm{E_g}$ (eV)	1.12
χ (eV)	4.05
$\tau_{\mathrm{bulk}}(\mu\mathrm{s})$	1
μ_{n} $\left(\mathrm{cm}^2/\mathrm{V\,s}\right)$	1500
μ_{p} $\left(\mathrm{cm}^2/\mathrm{V\,s}\right)$	400
$\mathrm{v_{th}}$ (cm/s)	1000
$\mathrm{N_D}$ $\left(\mathrm{cm}^{-3}\right)$	2×10^{15}

Table 4.1: Material parameters used in the simulations of the graphene-Silicon photodetectors.

$E_{\mathrm{f,gr}}$ changes with the reverse bias as the substrate depletion charge is modified. As graphene tends to present an intrinsic p-type doping, in addition to the charge needed to compensate the fixed charge due to ionized donors in the surface of the Si substrate close to the graphene film, these contributions shift $E_{\mathrm{f,gr}}$ from the theoretical Dirac point E_{D} that could be expected in an isolated material. This behaviour is described with the equation [196]:

$$E_{\mathrm{D}} - E_{\mathrm{f}} = -p_0 \hbar \nu_{\mathrm{F}} \sqrt{\pi p_0 + Q_{\mathrm{S}}} \tag{4.1}$$

where $\hbar$ is the reduced Planck constant, $\nu_{\mathrm{F}} = 1.1 \times 10^8$ cm/s is the Fermi velocity, p_0 is the p-doping concentration of graphene and Q_{S} is the space charge per unit area formed in the depletion region below the graphene contact. The Dirac point is located 4.5 eV below the vacuum energy. To achieve a good fit with the experimental results, the initial hole concentration of graphene is set to $p_0 = 6.3 \times 10^{12}$ cm^{-2}, resulting in a graphene workfunction $\phi_{\mathrm{gr}} = 4.82$ eV. As the electron affinity of Silicon is $\chi = 4.05$ eV, the resulting Schottky barrier height (SBH) between graphene and Silicon is estimated as 0.77 eV, a value quite similar to the one calculated in [194]. As for the metal workfunction, it has been set to $\phi_{\mathrm{ref}} = 4.52$ eV.

These parameters, together with those displayed in Table 4.1, were used in the calculation of the dark current. A comparison between the data measured (symbols) [194] and the simulated current density (solid-line) is shown in Fig. 4.5. A very good agreement is achieved between both approaches, especially in the reverse bias region, which is the one employed in the photodetector operation.

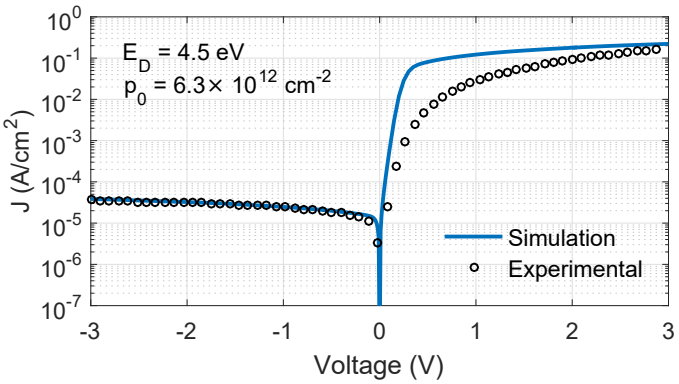

Figure 4.5: Current density in the reference device in dark conditions. Experimental data (circles), extracted from [194], and simulated results (solid line) show a good agreement, especially for reverse bias.

4.4 Analysis under Lamp Illumination

The next analysis tries to explain the physical processes that determine the device behavior under a uniform surface illumination.

Before proceeding with the simulations, let us present the model employed for the interdigitated photodetector D_x. This device exhibits a complex structure where the three spatial dimensions are relevant, complicating its analysis by means of our 2D simulator. To deal with this challenge we have considered the structure depicted in Fig. 4.6, which corresponds to a transversal cut of one finger and assuming that the rest of fingers behave in a similar way as the one under study, reducing the computational burden required to simulated the whole structure. The reference contacts (Cr/Ni) are placed on both sides of the finger. The active area is formed by a stack of graphene-SiO_2-Silicon (GIS) surrounded by graphene-Silicon (GS) heterojunctions. Graphene width (W_g) at each side of the GIS stack is fixed to 20 μm, and the insulator/finger width (W_{ox}) is varied as part of our study. We assume a fixed value of the graphene layer of 0.5 mm^2, similar to the one employed in the experiments. So that, a different number of identical fingers are covered by the graphene layer depending on the chosen value of W_{ox}. In our simulation of the D_{30} device a total width of W_g+W_{ox}+W_g = 70 μm is considered and its length is fixed to 7.14 mm to achieve a final surface of 0.5 mm^2. For D_{100} a total width of 140 μm must be employed and its length is reduced to 3.57 mm to achieve the same surface.

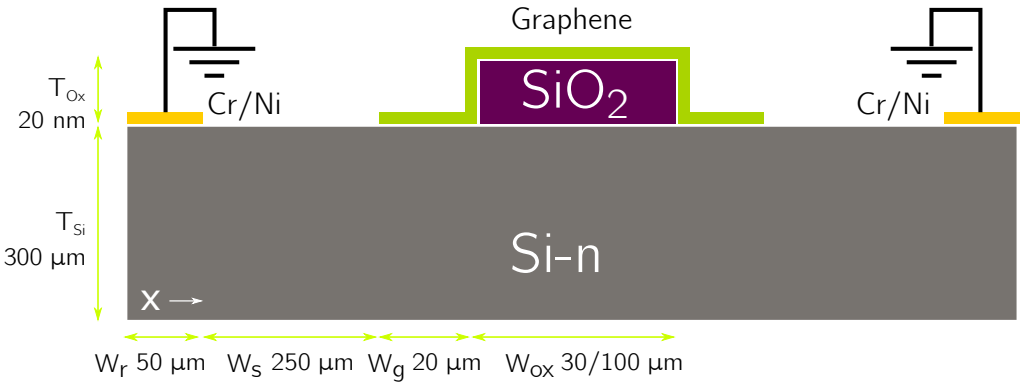

Figure 4.6: Schematic of device D_x where one finger of width $W_{ox} = x$ is coated by a graphene sheet with two lateral sides of $W_g = 20$ μm. The length of the finger corresponds to the out-of-plane dimension and it is scaled to keep a constant area of 0.5 mm^2.

For the light wavelengths considered, both oxide and graphene have been safely assumed as transparent. The applied light intensity is a parameter that can be varied, and from it the total current is estimated. Hence, the device responsivity is evaluated as the ratio of the photocurrent I_{ph} to the light power density P_{opt} multiplied by the active area A:

$$R = I_{\text{ph}} / \left(A \cdot P_{\text{opt}} \right) . \tag{4.2}$$

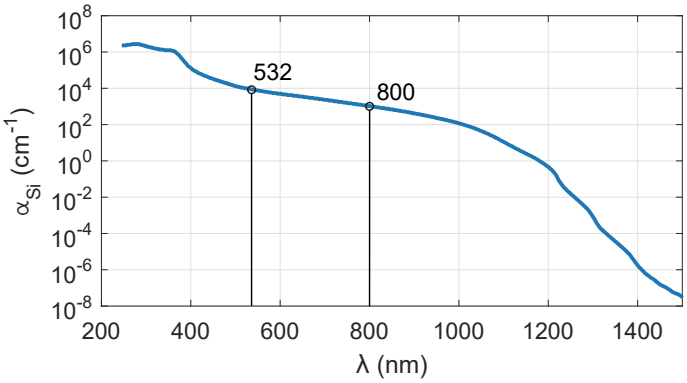

Figure 4.7: Absorption coefficient of Silicon *vs.* light wavelength in nm. Highlighted wavelengths, 532nm and 800nm are the ones employed in the simulations. Data for this Figure have been extracted from [197].

Hence, the responsivity reports on the achieved photocurrent per Watt of applied

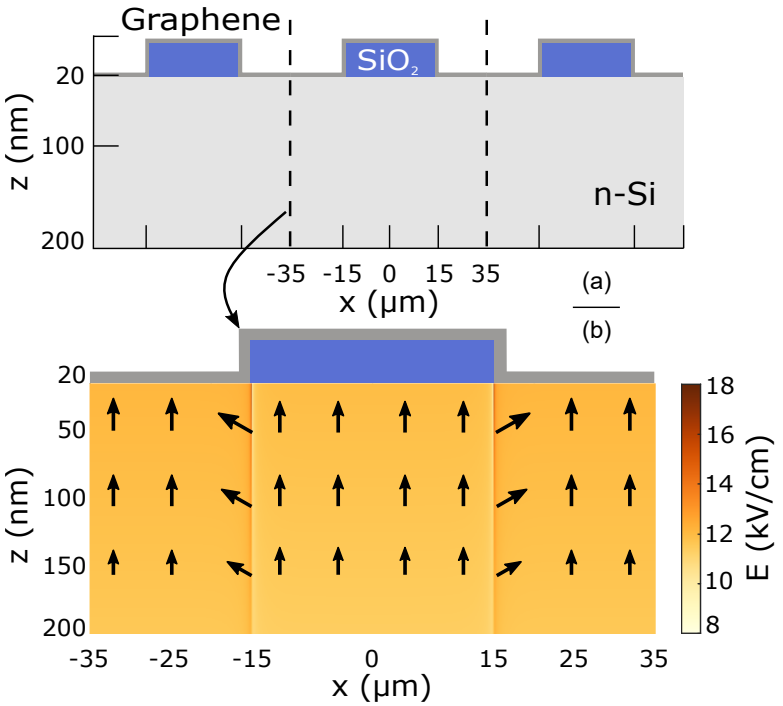

Figure 4.8: (a) Scheme of the fingers of D_{30}, showing the x-axis for (b). (b) Module of the electric field in the GIS region of D_{30}. Arrows indicate the direction of the field.

optical power. To reproduce the experimental values of R achieved in [195], we have illuminated the D_{30} photodiode with a monochromatic 800 nm light, placed above it. The device operates with a reverse bias of $V_R = -2$ V and the parameters contained in Table 4.1 have been used to simulate the structure. The absorption coefficient (α) for Silicon is a function of the light wavelength employed to illuminate the device. In this sense, Figure 4.7 depicts this parameter for a wide range of wavelengths and the two highlighted λ values correspond to those used in our study, $\alpha(532\text{ nm}) = 7850$ cm^{-1}, and $\alpha(800\text{ nm}) = 850$ cm^{-1}, respectively. As photons are absorbed following the Lambert's law, we can safely estimate the distance that photons have to traverse along the Si-substrate to be absorbed in a 95% as $3/\alpha$.

First, the electric field below the GS and GIS heterojunctions is analyzed. To do so, Figure 4.8a indicates the z-x axes employed in the representation of the D_{30} device. Please, be aware of the different scale employed for the vertical and horizontal axes, nm and μm, respectively.

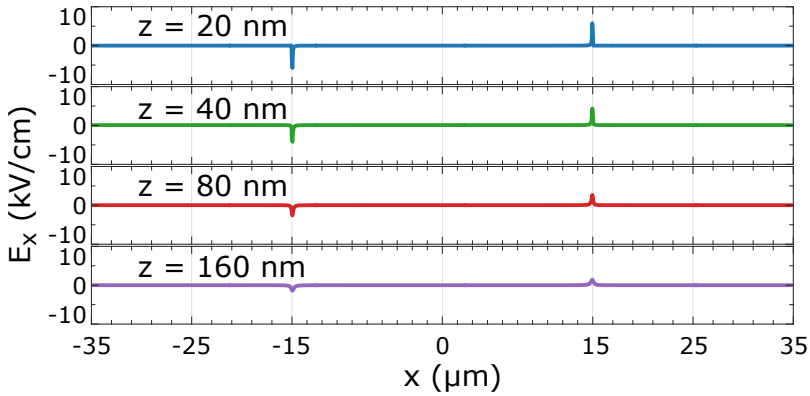

Figure 4.9: Lateral electric field component in the Silicon substrate for the D_{30} device and different depths (z), for $V_R = -2$ V. Positive and negative values indicate electric fields aiming to the right or left, respectively.

Figure 4.8b shows the calculated electric field for the D_{30} device in both x and z directions. A twofold representation has been employed. The colour scale indicates the magnitude of the electric field as stated by the vertical colour column on the right side and the arrows serve as eye-guide to approximately show the direction and intensity of the field. As can be observed, the electric field is uniform below the GS and the GIS regions, pointing to the graphene contact due to the negative applied voltage. However, at the edge between both junctions the electric field is more intense and pointing from the GIS to the GS junction. This lateral electric field component reveals itself as determinant to understand the device behaviour, as its presence is responsible of the high carrier injection in the corner via drift current.

In Fig. 4.9 a zoom of the lateral electric filed (E_x) is depicted for different depths below the graphene-Si interface, located at $z = 20$ nm. It should be highlighted how the E_x component is negligible in the whole substrate except for the transition region between both heterojunctions. The E_x value is maximum at z=20 nm and decreases as going inside the substrate. This lateral electric field extracts the holes photogenerated in the Silicon substrate below the GIS junction and previously pushed by the vertical field (E_z) up to the proximity of the oxide interface. As these holes accumulate below the insulator they are extracted by the lateral field and injected into the graphene contact.

Fig. 4.10 shows the band diagram along the x-axis for $z = 20$ nm in the D_{30} device. Electrons are removed from the regions close to the interface while holes are attracted

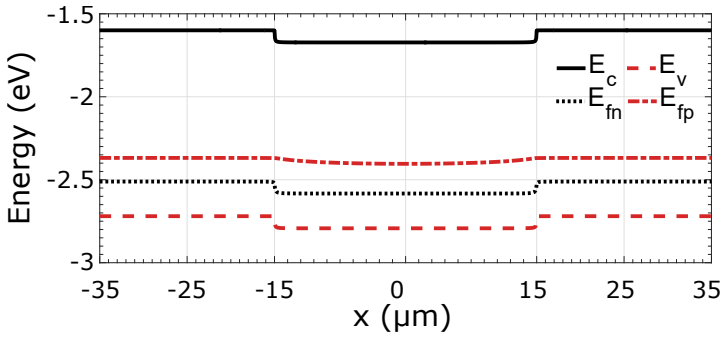

Figure 4.10: Band diagram of the GS and GIS regions of D_{30} for $V_R = -2$ V. The high graphene workfunction, combined with the strong electric field reduces (increases) significantly the surface electron (hole) concentration, causing the pseudo-Fermi levels approach to the valence band.

there due to the strong electric field aforementioned. Both, the conduction and the valence bands in the GIS junction are displaced with respect to the GS one, creating a band-step in the transition region around $x = \pm 15$ μm. This difference is originated by the small voltage drop in the oxide region, absent in the GS junction as the graphene contacts directly on the silicon. This fact can be clearly observed in Fig. 4.11.

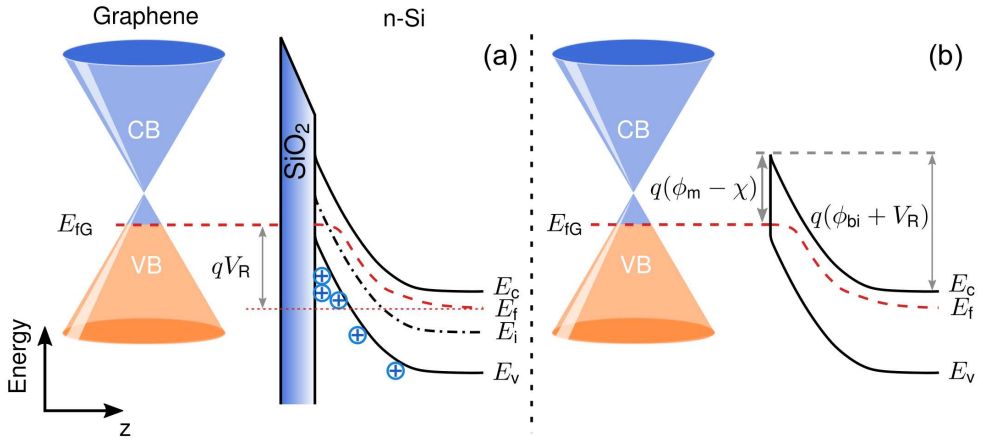

Figure 4.11: Illustration of the band diagrams for (a) the graphene-insulator-silicon junction and (b) the graphene-silicon junction. In the first case the reverse bias is shared between the SiO_2 and the Si while in the second one it is totally applied on the substrate.

Let us now focus on the current balance in the device, mainly in the hole contribution, as the presence of the electron counterpart close to the interface is quite limited. The presence of both drift and diffusion currents is represented in Fig. 4.12. As the device is symmetric, vertical and horizontal contributions are plotted separately in the left and right side of the device, respectively. Below the GS block, the presence of drift current is predominant in both directions. For the GIS junction, the large concentration of holes gathered below the SiO_2 is displaced to the lateral contacts by the concentration gradient, so that diffusion current pushes the holes below the oxide up to the graphene, because tunnel current through the oxide is forbidden.

Next, we can graphically check the current flow in the substrate as depicted in Fig. 4.13a. Deep inside the semiconductor, the arrows present the same length in both the GS and the GIS stacks, indicating that the magnitude of the current is similar. Moreover, at those locations the horizontal current is negligible. However, the current decreases in the center of the device as it approaches to the insulator, and from there it splits to the lateral contacts. In the transition region between both junctions, the lateral electric field (E_x) drifts the holes to the graphene contact, achieving the maximum injected current at that point. Fig. 4.13b shows the vertical current density (J_{pz}) at the interface. The current can not be injected in the graphene contact in one single point due to the finite thermionic velocity in the GS junction, distributing them in a wider area to be absorbed. This diffusion process takes place very close to the interface.

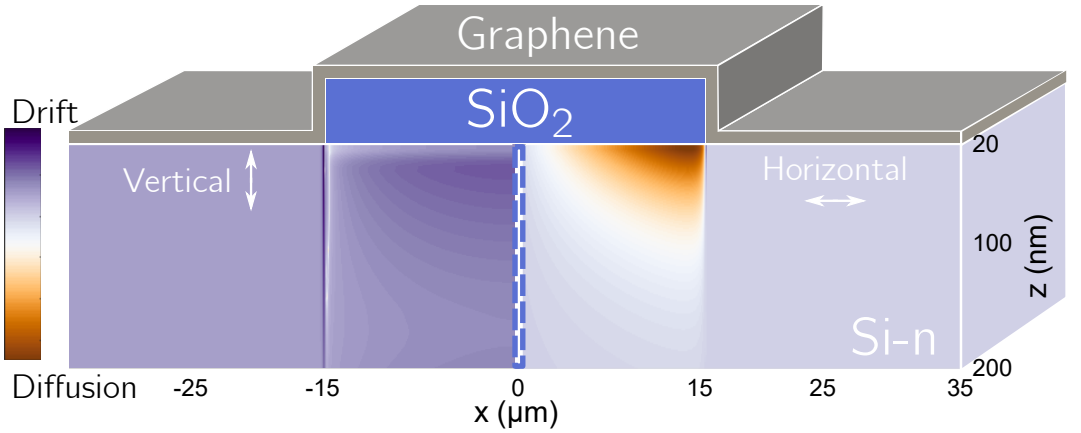

Figure 4.12: Drift and diffusion current influence in vertical (left) and horizontal (right) directions. Below the oxide, diffusion current displaces the holes to the contacts. In the corner drift current in both horizontal and vertical directions pushes these holes to graphene.

Now, let us study the linearity of the photocurrent as a function of the applied light power density. Henceforth, we study the two interdigitated experimental devices, D_{30} and D_{100}. Figure 4.14 shows I_{ph} for two different values of the light power density, $P_{opt} = 25\,\mu W/cm^2$ and $P_{opt} = 100\,\mu W/cm^2$, as a function of the reverse bias. For these illumination intensities, the increment in the light intensity results into the same increase in the photocurrent, indicating that both devices are in the linear regime. This result agrees with the previous analysis of Fig. 4.13, which showed how the magnitude of the current density deep inside the Silicon is the same in both the GIS and GS regions. For $V_R = -2$ V, we see the photocurrent is 26% higher for D_{30} than for D_{100}.

The calculated responsivities for these photocurrent values are 848 mA/W and 672 mA/W for D_{30} and D_{100} respectively. The difference between D_{30} and D_{100} agrees with the experimental results in [195], where it is even wider (around 630 and 370 mA/W, respectively). This is probably caused by the presence of other defects not considered in this first iteration. The measured results, more similar to the simulated ones for high reverse voltage, suggest that the performance of the device is close to the ideal one. This means the difference between both experimental devices is not specially caused by the interface quality, but by the structure dissimilarities.

These analysis let us conclude that, for non degraded interfaces, the D_{30} photosensor shows a similar contribution to the photocurrent from the different regions. The carriers photogenerated below the insulator diffuse to the contacts. This extra path

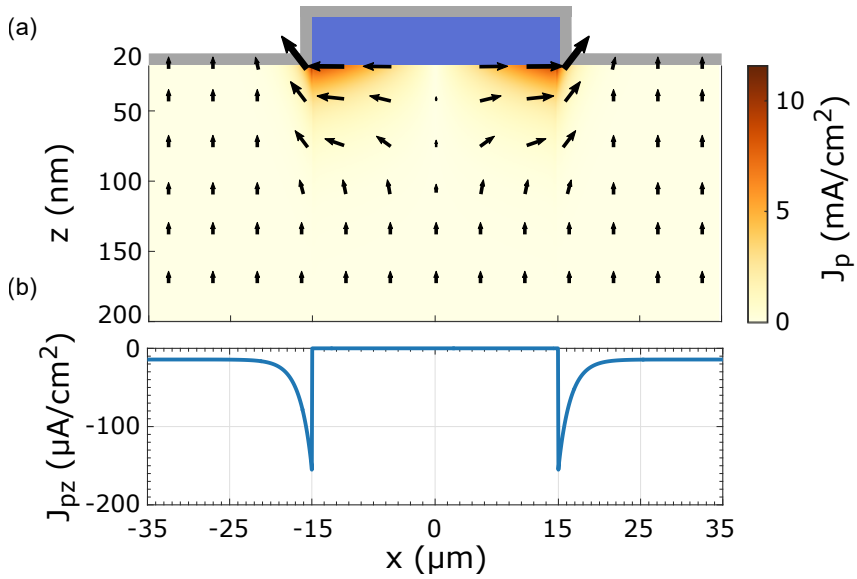

Figure 4.13: (a) Hole current in the Silicon substrate of D_{30}, for $V_R = -2$ V. Arrows indicate the direction of the current. Current below the insulator splits and flows to the contacts via diffusion. (b) Vertical component of the hole current (J_{pz}) at the interface ($z = 20$ nm). Maximum injection is reached at the edges between the GS and the GIS junctions, indicating a strong carrier injection. Hole current is reduced for $|x| > 15$ μm until a constant value is reached whose origin corresponds to the holes photogenerated right below that point and drift by E_z.

may be useful to explain the degraded behaviour of D_{100}. As the current model in these simulations include a SRH recombination, the bulk carrier lifetime might be low enough to recombine part of the holes that flow from the GIS region to the GS ones. Figure 4.15 lets us check this fact. As can be seen, this Figure depicts the hole density below the interface between the Silicon and the insulator/graphene for both D_{30} and D_{100}. The GS regions of D_{30} have been extended to allow the comparison. The hole density in the GIS region for the wider device is around one order of magnitude higher than for the narrower one, as holes are not as efficiently extracted as in the D_{30} photosensor. In the next analysis the degradation applied to the graphene-Silicon interface will show how the difference between D_{30} and D_{100} can narrow.

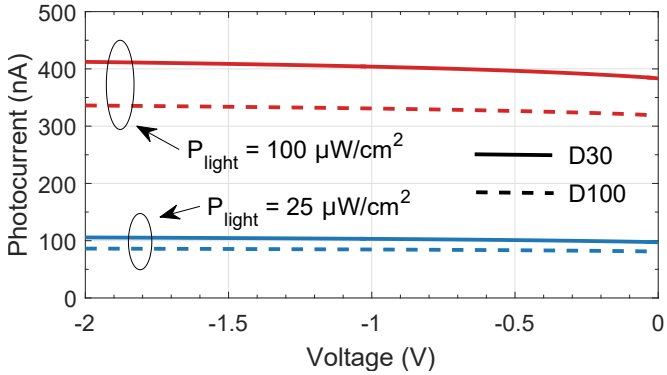

Figure 4.14: I_{ph} *vs.* voltage in D_{30} and D_{100} devices two uniform light intensities, 25 μW/cm^2 and 100 μW/cm^2. Final responsivity of the whole device and the lower power intensity is 848 mA/W for D_{30} and 672 mA/W for D_{100}.

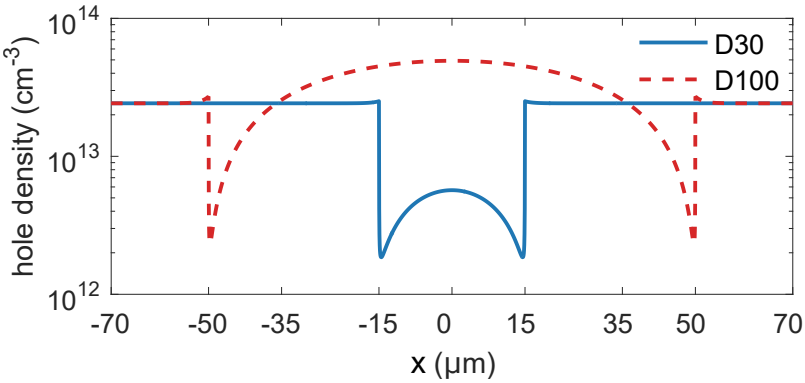

Figure 4.15: Hole density in the GIS and GS interfaces for D_{30} and D_{100}, for $V_R = -2$ V. GS regions of D_{30} have been extended to conduct the comparison.

4.4.1 Light wavelength dependence

A noticeable aspect to analyse is the variation of the photocurrent with the wavelength of the applied light. This behaviour can be attributed to the dependence of the absorption coefficient (α) with λ. As it was shown in Fig. 4.7, lower values of α are related to higher λ, as they correspond to less energetic photons. Assuming an exponential absorption of those photons inside the substrate, we can consider that a distance of $3/\alpha$ is a reasonable estimation of the substrate depth where carriers are photogenerated. The thickness of the depletion region below the contact is of a few microns and, therefore, most of the contributing carriers are photogenerated below it.

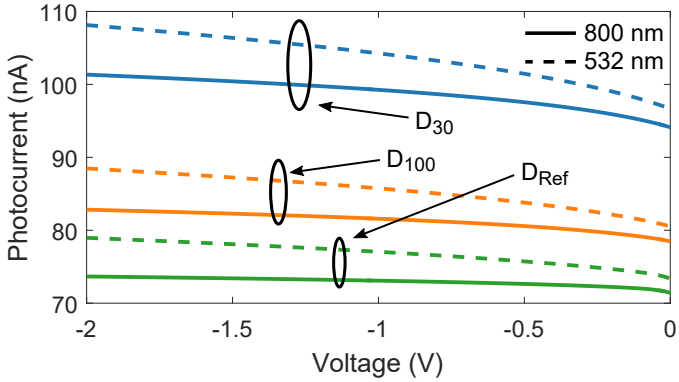

Figure 4.16: Photocurrent *vs.* voltage in the D_{30}, D_{100} and D_{Ref} photodiodes illuminated with two different light wavelengths, 532 nm (dashed) and 800 nm (solid), respectively. The lower λ value produces a higher photocurrent, due to the higher absorption coefficient.

Fig. 4.16 depicts the I-V plots simulated for the three photodiodes under study, D_{30}, D_{100} and D_{ref}, illuminated with two different wavelengths, 800 nm and 532 nm, at the same power density of 25 $\mu W/cm^2$. The lower the wavelength the higher the absorption coefficient and, therefore, the path length that carriers have to traverse to be extracted through the contacts is reduced: as aforementioned, 95 % of the photons are absorbed in the absorption length $L_{abs} = 3/\alpha$, which for the wavelengths of our study results in $L_{abs}(532nm)$ =3.8 μm and $L_{abs}(800nm)$ = 35.3 μm. The probability of recombination increases for those carriers that are photogenerated deep inside the substrate. This fact explains the differences achieved among different wavelengths, with a consistent larger contribution for lower λ values.

Moreover, when carriers are photogenerated within the depletion region they are quickly attracted to the proximity of the contact. Therefore, the dependence with the

reverse bias is also more prominent for the lower wavelength as the increasing depletion width allows the collection of a higher amount of photogenerated carriers.

4.4.2 Evaluation of parameters

Once the basic characteristics of the photodetector have been analyzed, this Section is devoted to the assessment of the impact of different material and device parameters on its performance. In particular, relevant parameters related to the graphene-silicon interface properties will be considered, while the bulk properties, associated with the silicon substrate, will be kept constant to their ideal values. Two important factors considered for their evaluation are the thermionic injection velocity and the graphene workfunction. Moreover, a low quality interface can be characterized by a high density of interface traps, which would results in a carrier mobility degradation, a higher surface recombination or the presence of a high surface doping.

Each of the considered parameters will be degraded in a thin region of thickness T_{int} = 20 nm below the graphene layer, and the impact of such degradation on the device behaviour will be evaluated. We assess the impact of each parameter individually, namely, a specific magnitude is modified while the rest are kept constant to its initial, non-degraded, value.

Thermionic velocity (v_{th})

The quality of the graphene-Silicon interface determines the easiness for carriers to be injected into the contact. The thermionic velocity is a key parameter in the thermionic-emission (TE) model that explains the behaviour of Schottky contacts. Hence, in this section we have considered four different thermionic velocities, covering a wide range of values (from 10^0 cm/s to 10^3 cm/s) [198], in two different photodiodes, D_{30} and D_{100}, for both, dark and illumination conditions ($\lambda = 800$ nm and $P_{opt} = 25\ \mu W/cm^2$). The results depicted in Fig. 4.17 demonstrate the limited impact of this parameter on the total current achieved for both, illuminated (a) and dark (b) conditions. Only under illumination and for very low biases we can appreciate a photocurrent reduction for the lower recombination velocities. However, these differences disappear for larger reverse bias conditions.

Figure 4.17 (b) demonstrates that dark current is independent of v_{th} and the same magnitude is achieved for both devices, D_{30} and D_{100}. The reason is I_{dark} mainly

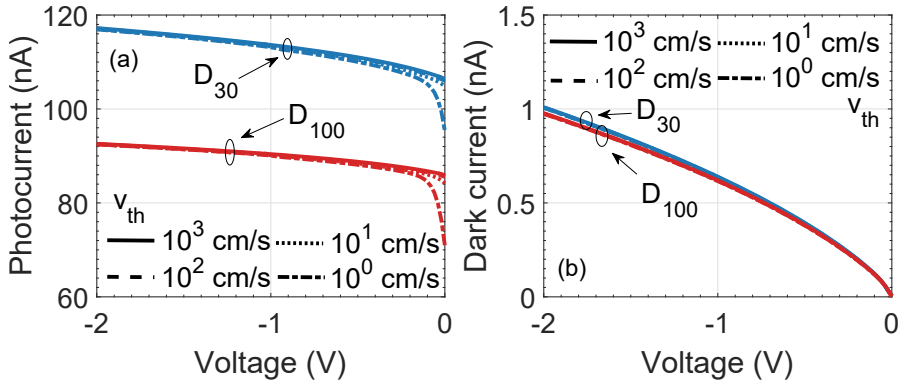

Figure 4.17: Photocurrent (a) and dark current (b) *vs.* voltage in the D_{30} and D_{100} photodiodes evaluated with four different recombination velocities. Only for (a) a small degradation of the photocurrent is appreciated at low biases. (a) is illuminated with λ=800 nm and P_{opt}=25 μW/cm^2.

depends on the substrate quality and the distance between contacts, being both parameters identical in this case.

In spite of the limited influence of v_{th} on the measured current, we have noticed appreciable changes in the carrier density below the SiO_2. To analyse this phenomena Fig. 4.18 plots the electron and hole densities in the middle of the finger, at $(x, z) = (0, 20\text{ nm})$. In dark conditions (bottom row), the influence of the thermionic velocity results negligible for both types of carriers. Under illumination (top row), the electron density becomes independent of v_{th} for reverse biases lower than -0.4V. This result could be expected as the electric field generated by V_{R} pushes the electrons far from the top interface as seen in the previous analysis related to Fig. 4.8. However, under illumination, the hole density is modified when v_{th} increases from its lowest value. It is very interesting, from the viewpoint of the finger efficiency, to compare the hole density behaviour for both devices as D_{30} shows a consistent lower hole density as D_{100} for all the v_{th} values simulated. Moreover, hole density tends to decrement with the reverse bias in D_{30} while for D_{100} the opposite behaviour can be observed, as holes tend to accumulate below the central point of the Si/SiO_2 region. This different trend agrees with the result depicted in Fig. 4.15, allowing us to conclude that narrower fingers are more efficient extracting the photogenerated carriers.

As the reverse voltage is incremented, holes can be extracted more efficiently through the lateral edges of the GIS junction reducing the hole density in its central region. However, for the D_{100} device, the insulator is wide enough to hide the effect of those lateral

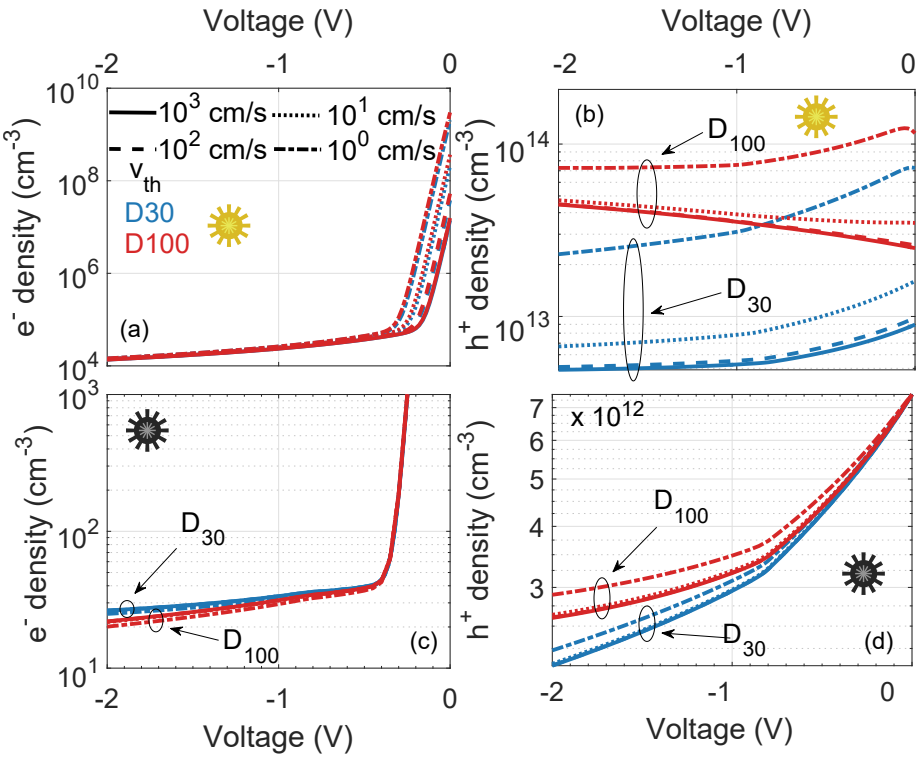

Figure 4.18: Electron (left) and hole (right) densities under the oxide, in the middle of the finger *vs.* voltage in the D_{30} and D_{100} photodiodes for different v_{th} values in dark (bottom row) and under illumination (top row).

drains. In that sense, we can find a close analogy to the channel in a MOSFET and the reduction of channel charge close to the drain edge when drain bias increases.

Graphene workfunction (ϕ_{gr})

In this section we analyse the impact of the graphene workfunction on the performance of the photosensor. In contrast to metals, graphene presents a variable workfunction as a result of the limited DoS, thus, the position of E_f can be modified due to the presence of puddles, imperfections and even the applied bias that modifies the space charge region below the contact. Hence, depending on those factors the Fermi position can be shifted in a limited range around the selected value of 4.82 eV. As a higher value of ϕ_{gr} would only enhance the hole extraction, no degradation would be seen in this case. Therefore, we analyse a lower value of $\phi_{gr} = 4.70$ eV.

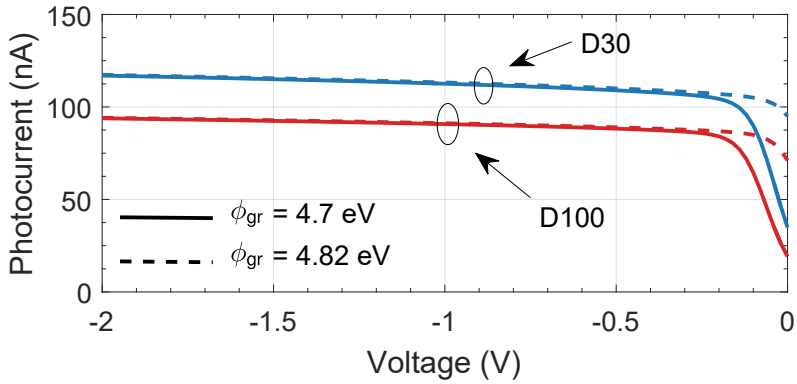

Figure 4.19: Photocurrent *vs.* voltage in the D_{30} and D_{100} photodiodes for different graphene workfunctions.

The results shown in Fig. 4.19 demonstrate that only at very low reverse voltages slight differences are appreciated. Moreover we have checked that these differences are significant only for low v_{th} values. For this reason, in Fig. 4.19 a value of $v_{th} = 1$ cm/s was considered, as for higher v_{th} values negligible differences between both ϕ_{gr} were achieved. The reason behind this behaviour lies in the fact that a reduced graphene workfunction results in a lower built-in potential in the Schottky contact, reducing the amount of holes attracted by the contact. However, for a high enough reverse voltage those differences are masked and the current saturates to similar values, independently of ϕ_{gr}.

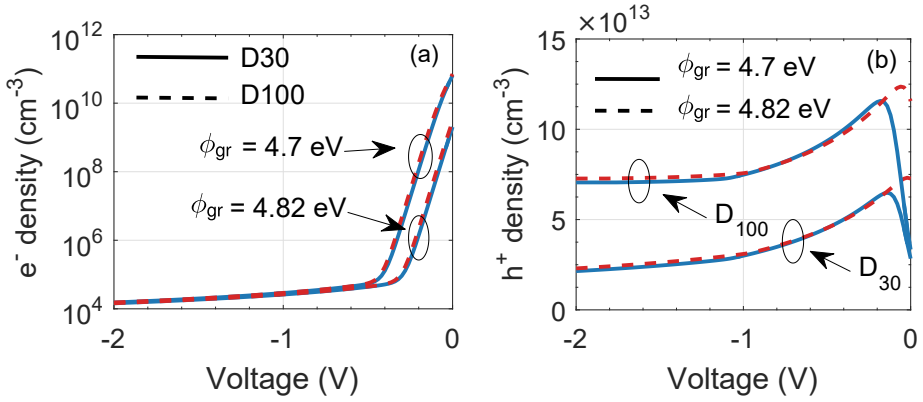

Figure 4.20: Electron (a) and hole (b) densities under the oxide *vs.* voltage in D_{30} and D_{100} photodiodes for different graphene workfunctions and uniform illumination of 25 μW/cm^2. Thermionic velocity is set to v_{th} = 1 cm/s. Lower workfunction reduces the amount of holes attracted to the oxide interface for low biases.

Fig. 4.20 analyses the carrier concentration below the insulator for two different ϕ_{gr} values under a uniform illumination of 25 μW/cm^2. For low bias, the smaller workfunction produces a higher electron concentration which decreases, as it could be expected, up to a saturated value when the reverse voltage increases. Simultaneously, the hole density drops continuously as the reverse bias increases and the D_{100} device shows a higher hole concentration then its D_{30} counterpart, for the same reasons explained in the previous section. The workfunction value depicts a noticeable impact on the voltage value necessary to achieve a null current, namely the open circuit voltage, as a higher positive voltage is needed to reduce the potential barrier created by the graphene-silicon junction.

Carrier lifetime under the graphene and the oxide

In this section we provide a critical analysis of the impact of carrier lifetimes τ on the measured photocurrent. The variation of the time constant is related with the quality of the materials and the interfaces, those being related with the fabrication process of the device as the SiO_2 is eliminated after an etching process is applied (see Ref. [195]).

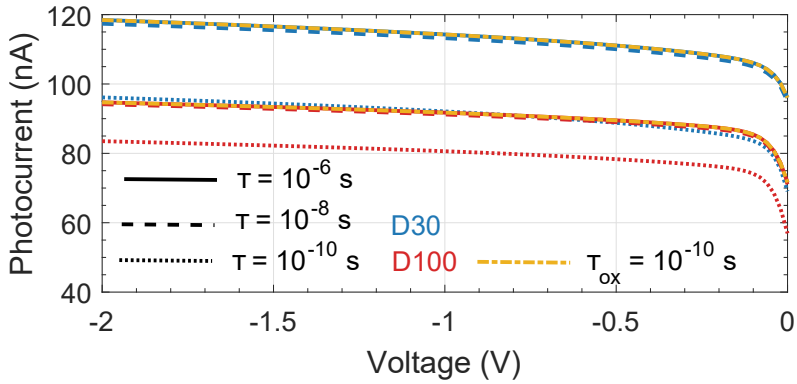

Figure 4.21: Photocurrent *vs.* voltage in the D_{30} and D_{100} photodiodes for different recombination times in a 20 nm thickness below the oxide (dashed-dotted line) and under the graphene.

As the quality of the interfaces at the GS and GIS junctions is quite different, this parameter τ will be changed independently at each one in a region of thickness T_{int} = 20 nm below the graphene layer and the oxide, respectively. Figure 4.21 depicts the photocurrent evolution for three different recombination times under graphene, τ=1 μs (solid), 10 ns (dashed), and 0.1 ns (dotted), and a constant value under the

oxide, $\tau_{ox} = 1\ \mu s$. A low recombination time indicates a degraded interface region, which implies an increased recombination probability and a degradation of the device performance. Figure 4.21 indicates that the achieved current is quite similar for τ =1 μs and τ =10 ns, and only for the lowest $\tau = 0.1$ ns (dotted) a noticeable difference is observed.

Finally, to assess the influence of the carrier lifetime below the oxide, τ_{ox} has also been reduced to 0.1 ns while τ below the graphene is kept constant to its highest value, 1 μs. The calculated photocurrent (yellow dashed-dotted line in Fig. 4.21) is similar to that achieved with the much higher value of τ_{ox} =1 μs, indicating the reduced impact of that parameter on the device performance. The reason for its limited influence is the reduced thickness where this degradation is considered, as the carriers circulate in a much wider path below the SiO_2. Moreover, as the insulator has been grown in a thermal process, a high quality of the Si-SiO_2 interface should be expected, leading to a large value of τ_{ox}, enhancing the important role played by the GIS junction in the photodiode performance.

Variable doping under the graphene

Charged species in the surface of the active layer can originate from oxygen, organic impurities, or metal atoms due to metallic contamination introduced from the graphene's transfer process [199]. In some cases, water and molecular oxygen have been found to diffuse into the active layer through grains and pinholes in the graphene layer. The presence of fixed charges at the interface between graphene and Silicon can seriously hinder the extraction of photogenerated carriers as they screen the electric field below the contacts. In this analysis, the presence of these fixed charges located in the surface of the substrate are represented as an extra doping density in a thin region of 20 nm, right below the graphene layer. The presence of these charges modifies the electrostatics of the device, reducing the depletion region where the photogenerated electron-hole pairs are separated by the electric field. To model this phenomena, two different densities of donor impurities have been located below the graphene for the D_{30} device.

The calculated results are plotted in Fig. 4.22, including a curve with the standard background doping ($N_D = 2 \times 10^{15}$ cm^{-3}) for comparison purposes. The first doping density, $N_D = 10^{18}$ cm^{-3}, produces a considerable reduction of the photocurrent at low reverse bias, but for $V_R < -0.3$ V the current achieved is similar to the one in the

standard situation. Hence, we increase the value of the surface doping up to $N_D = 10^{19}$ cm^{-3}, to assess its impact. In contrast with the rest of curves depicted until now, this one presents a S-shape, and the photocurrent achieved is considerably lower than the previous ones for the whole range of applied bias. It has been checked that most of the current contribution for $\|V_R\| < 1$ V comes from the oxide region. For $\|V_R\| > 1$ V, carriers originated below the GS junction can flow and are extracted by the contact. This additional contribution is manifested by the increasing slope obtained around -1 V.

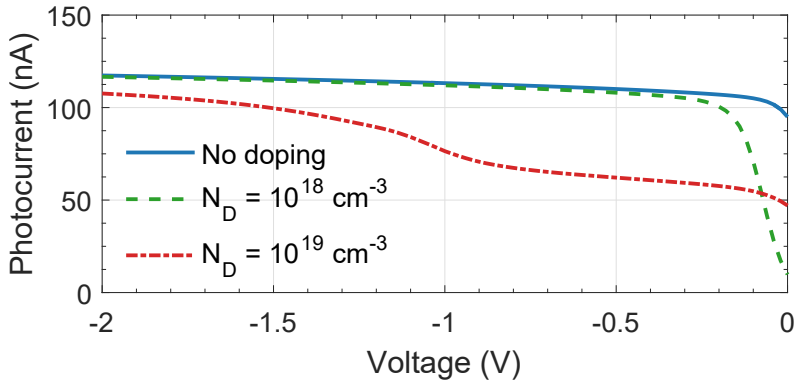

Figure 4.22: Photocurrent *vs.* voltage in the D_{30} photodiode for different doping densities under the graphene contacts ($T_{int} = 20$ nm).

The electric field below the oxide does not suffer modifications compared with the previous situations, as the considered doping is located just right below the GS junction. The effect of this extra doping is similar, to some extent, to the concept of back-surface field commonly employed in solar cells to avoid the recombination at the surface through the reduction of the minority carrier concentration [200]. Only for high enough reverse bias, the field is able to traverse this highly doped region, increasing significantly the thickness of the depletion region and boosting the amount of collected photocarriers. However, the asymptotic photocurrent is always lower than the one without this extra doping.

To gain further insight on this phenomenon, E_z is depicted inside the device substrate for $V_R = -0.5$ V in Fig. 4.23, with the inset zooming the interface area. For the applied reverse voltage, the high doping at the silicon surface screens the contact charge. Hence, the depletion region below the graphene does not extend far inside the substrate. On the other hand, the electric field can penetrate deeper below the oxide, as no extra donor doping is present in the GIS stack. Graphene-Silicon interfaces pre-

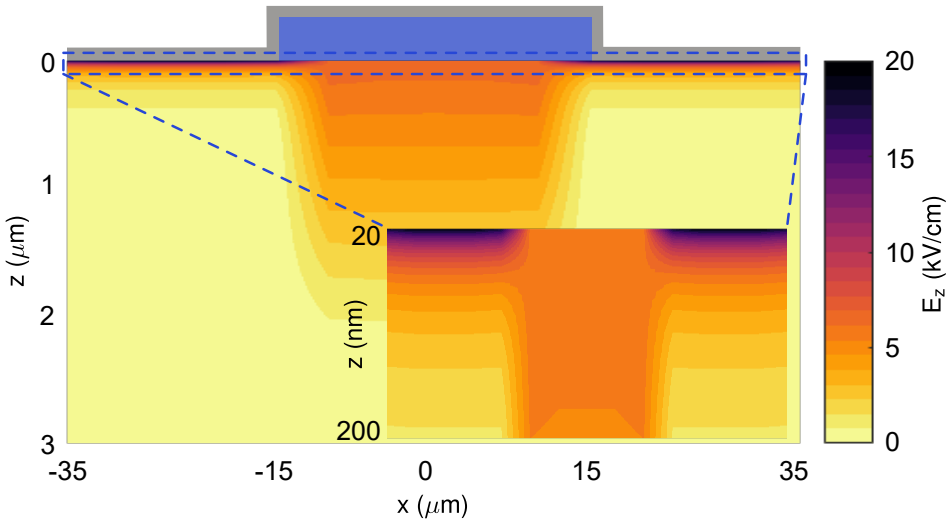

Figure 4.23: Vertical component of the electric field (E_z) for the D_{30} photodiode with an applied bias of $V_R = -0.5$ V, and a donor doping density of $N_D = 10^{19}$ cm^{-3} below graphene in a thickness of 20nm. Inset shows a zoom of the interface, where a strong electric field is originated by the presence of a high donor doping.

sent a strong electric field in a narrow region due to the high doping located in that region, giving rise to a much shorter depleted region as shown in Fig. 4.23. For $|V_R| >$ 1 V, more charge is necessary to screen the graphene contact, depleting deeper regions below the contacts, and increasing the amount of photocarriers collected. This is the physical reasons behind the S-shape in the photocurrent. Moreover, this S-shape in the photocurrent is very similar to the experimental results shown in [195], where it is even more pronounced.

Variable carrier mobility

Close to the Si-substrate interface with air and graphene, carrier mobility can be severely reduced due to the presence of charged traps and defects. In this section, we assess the impact of these non-idealities on the mobility of both, electrons and holes, located in a region of thickness T_{int}. Fig. 4.24 depicts the calculated I-V characteristics for both D_{30} and D_{100} with $T_{int} = 100$ nm (dashed) and $T_{int} = 20$ nm (solid) when μ_n and μ_p are halved respect to their bulk value right below the GS regions. As it is observed in the Figure, the photocurrent is systematically reduced as the degraded region gets thicker, and the reduced mobility impacts I_{ph} uniformly in the whole bias range.

Hence, we conclude that this parameter plays a noticeable role in the performance of the device as it affects its responsivity. In this study, we have modelled the mobility degradation as a step function in a limited depth just to demonstrate its relevance. However, a more elaborated model could be proposed to fit the numerical simulations with the experimental results.

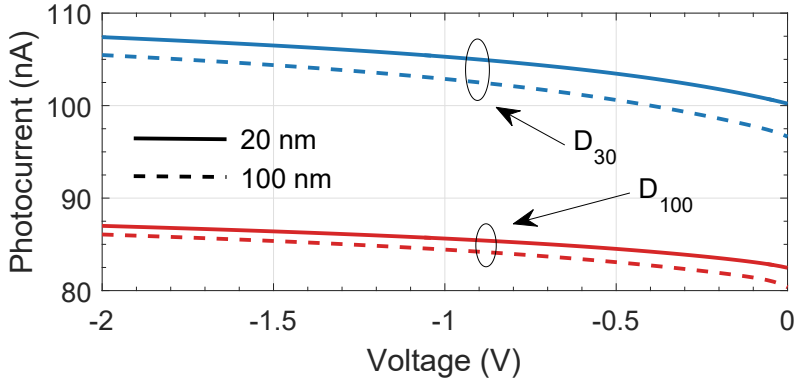

Figure 4.24: Photocurrent *vs.* voltage in the D_{30} (blue) and D_{100} (red) devices when the carrier mobility is lowered to half of its bulk value in a region of thickness $T_{\text{int}} = 20$ nm (solid) and $T_{\text{int}} = 100$ nm (dashed) right below the GS junction.

As in previous discussions, electron and hole concentrations under the centre of the oxide are depicted in Fig. 4.25 for the usual bias range, with the mobility degradation limited to $T_{\text{int}} = 20$ nm. For electrons there are no discernible differences between both, D_{30} and D_{100} devices when mobility is halved. However, for holes, the reduced mobility produces a higher accumulation, more noticeable for wider fingers. Holes photogenerated below the SiO_2 are firstly pushed vertically by E_z and then they move laterally due to a concentration gradient until they reach the lateral contacts. As mobility and diffusion coefficients are related by the Einstein relation, the increased difficulty of holes to diffuse laterally results in a higher hole density below the insulator.

The D_{30} device depicts an interesting situation as the hole concentration increases or decreases depending on μ_p. The resulting trend depends on the balance of two factors. First, as the reverse bias increases a higher amount of photogenerated holes are collected and guided to the Si-SiO_2 interface by the vertical field. Second, an increasing reverse bias also produces higher lateral fields at the edges of the GS-GIS junctions. If the mobility, and therefore the diffusion coefficient is high enough, this demand of carriers in the lateral contacts can be supplied and therefore the hole density at the centre will

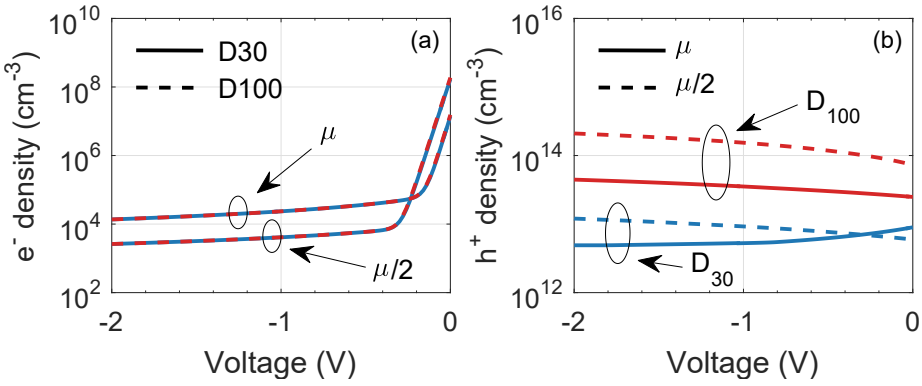

Figure 4.25: Electron (a) and hole (b) densities under the oxide *vs.* voltage in the D_{30} and D_{100} photodiodes when mobility under the interfaces corresponds to the bulk value and half of its value.

be reduced. But, if the mobility is low, the amount of received photoholes is higher than those that are extracted through the lateral contacts, resulting in the increased hole density observed for $\mu/2$. For the D_{100} device, due to the higher width of the finger, an increased amount of holes are collected and therefore, even for the high μ scenario the hole concentration in the centre of the SiO_2 grows.

Therefore, after this analysis we can conclude that the optimal finger width is closely dependent on the carrier mobility efficiency. In the case examined here, the D_{100} device is less efficient than the D_{30}, and this efficiency depends on the diffusion coefficient and the carrier lifetime. In an extreme situation (specially in the D_{100} finger), if very low mobilities were considered, the GIS region would behave similarly to an isolated Metal-Insulator-Semiconductor structure, which would produce a quick hole accumulation with the increase of the reverse voltage.

4.5 Laser analysis

In the previous section we have analysed the behaviour of the photodiodes when a uniform illumination is applied on its surface. Now, we focus on the relative contribution of each one of the regions that constitute the device under study. To do so, we consider a similar situation to the experimental scanning spectroscopy shown in Fig. 4.2, where a laser with a fixed power density and wavelength scans the whole device surface while the photocurrent is permanently monitored. This process will allow us to weigh the

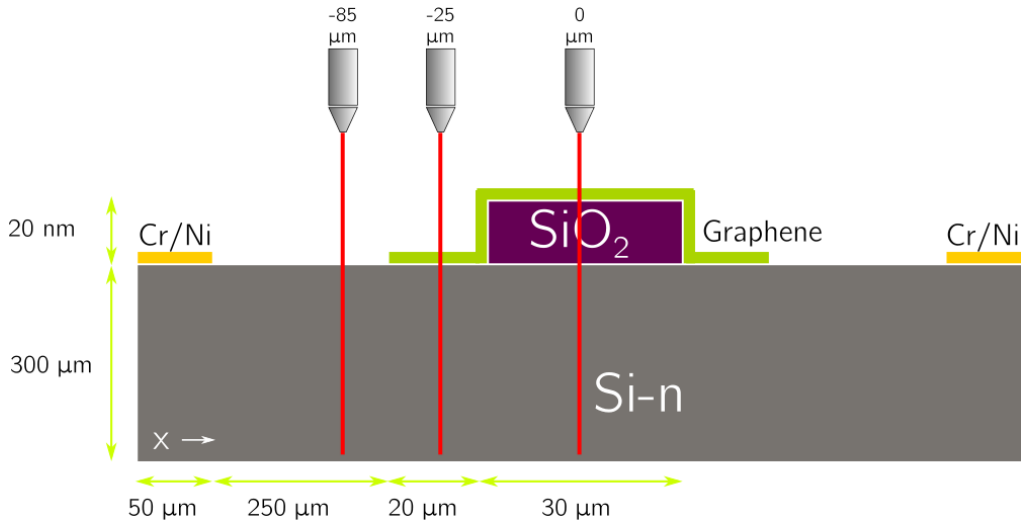

Figure 4.26: Schematic of the D_{30}/D_{100} devices under test, depicting the laser positions: on the air-Si surface, 50 μm away from the graphene edge, on the centre of the left graphene-Si contact and on the middle of the GIS junction. The values on top of the laser beam correspond to the positions employed in the D_{30} device.

relative contribution of each region on the total photocurrent.

We begin this section studying the effect of a laser beam applied on three different locations along the x-direction of both, the D_{30} and D_{100} devices. Fig. 4.26 represents the situation corresponding to the finger of 30 nm width. For the D_{100} device, an extra 35nm should be added to the laser locations with respect to the numbers shown in that Figure:

1. At the centre of the GIS region, position $x = 0$ μm.
2. At the centre of the graphene-Silicon junction; x = -25 μm for D_{30} and x = -60 μm for D_{100}.
3. At the air-graphene region, 50 μm away from the graphene edge; $x = -85$ μm for D_{30} and $x = -120$ μm for D_{100}.

In some of the simulation sets, the selected laser positions will be shifted, and it will indicated accordingly. The experiments carried out in [194] made use of a laser spot with a diameter of 2 μm. To simulate a similar situation we consider the laser beam as a rectangle of 1 μm $\times$ 3.14 μm area, achieving an equivalent illuminated surface.

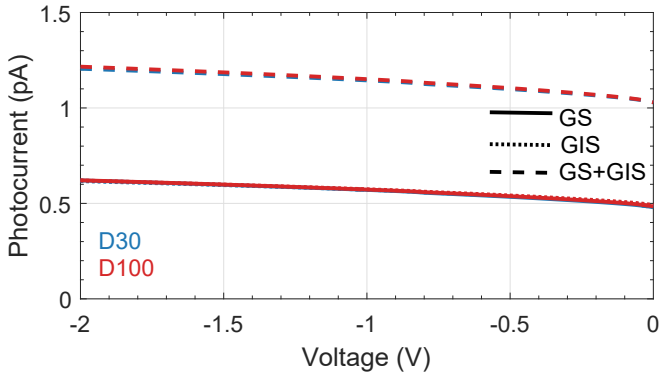

Figure 4.27: Photocurrent *vs.* voltage of devices D_{30} (blue) and D_{100} (red) when a laser beam is applied on the GS interface (solid), on the center of the GIS junction (dotted), and onto both points simultaneously (dashed). Light power density is set to $P_{\text{opt}} = 25\,\mu\text{W/cm}^2$, with an area of 1 μm $\times$3.14 μm.

In our first evaluation, the laser power density is the same of the previous section, where a uniform illumination of 25 μW/cm^2 was employed. The structure implemented in this case is assumed as ideal, namely, without specific degradation. The results, depicted in Fig. 4.27, do not show visible differences between the laser focused on the GS (solid) or on the GIS (dotted) section. The reason for this lies in the very low applied power, as the laser spot is illuminating a surface $\sim 10^5$ times lower than the lamp. The case where the laser is applied on the air-Si region is not plotted, as the current is negligible compared with the previous two situations. The simultaneous application of two lasers on the GS and GIS junctions produces a total I_{photo} (dashed) identical to the addition of the individual contributions.

Fig. 4.28 depicts the hole density generated by the laser spot of $\lambda = 800$ nm and $P_{\text{opt}} = 25\,\mu\text{W/cm}^2$ for the D_{100} device with a laser beam located on the GIS junction (a) and the GS contact (b). Note that the maximum carrier density is much lower than those achieved in the previous Section with the lamp illumination. Here, carriers are photogenerated in the region where the laser is focused and from there, they rapidly diffuse far away due to the pronounced concentration gradient. In the case of holes, as depicted in Fig. 4.28, they need more than 50 μm from the laser location to return to their bulk value. This distance is large enough to cover the whole D_{100} insulator if the beam is placed at its centre. On the contrary, when a uniform illumination is considered, the substrate increases its carrier concentration uniformly, without the

lateral gradients presently observed.

Here, the carrier concentration and the photocurrent cannot be fairly compared with the uniform illumination due to the large differences in the total applied power in both situations. So that, using the same light intensity for the laser beam as for the lamp provides very different carrier concentrations and therefore different photocurrents. That is why higher laser intensities has also been analyzed, so as the achieved photocurrent is comparable to those of uniform lamp analysis. To do so, we consider two higher laser intensities of 15 W/cm^2 and 150 W/cm^2. Those intensities correspond to a power of 0.68 μW and 6.8 μW, respectively, on the same spot area of 3.14 μm^2.

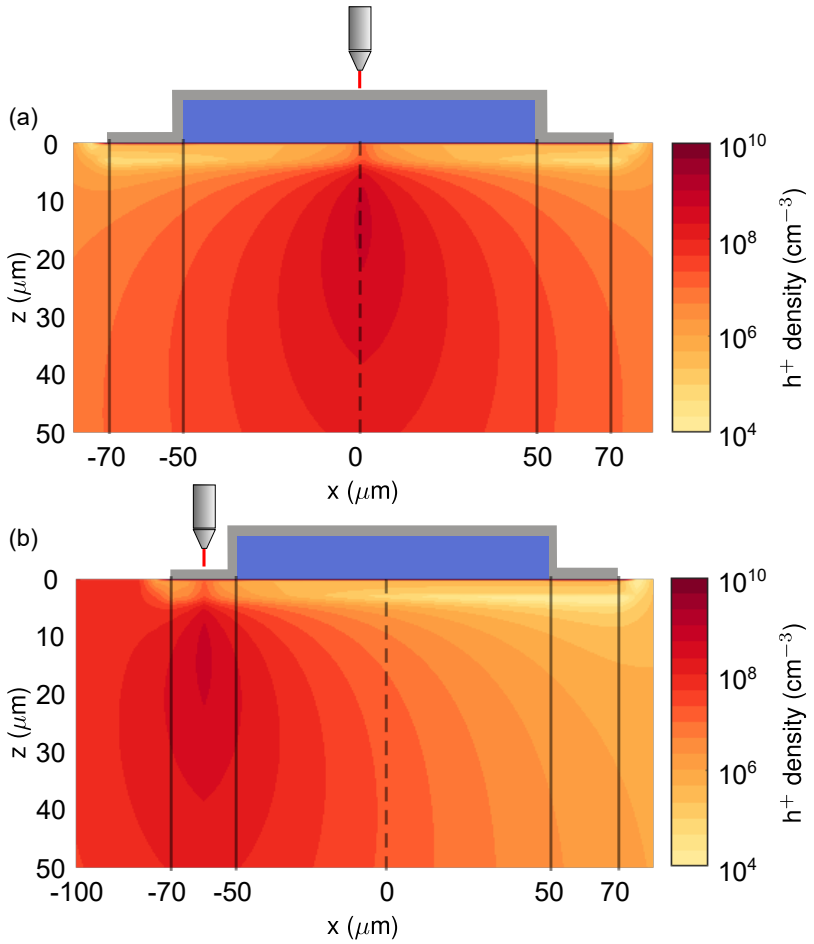

Figure 4.28: Hole concentration in the D_{100} photodiode originated by an applied 25 μW/cm^2 laser beam with $V_R = -2$ V on the centre of the GIS junction (a) and on the centre of the GS one (b).

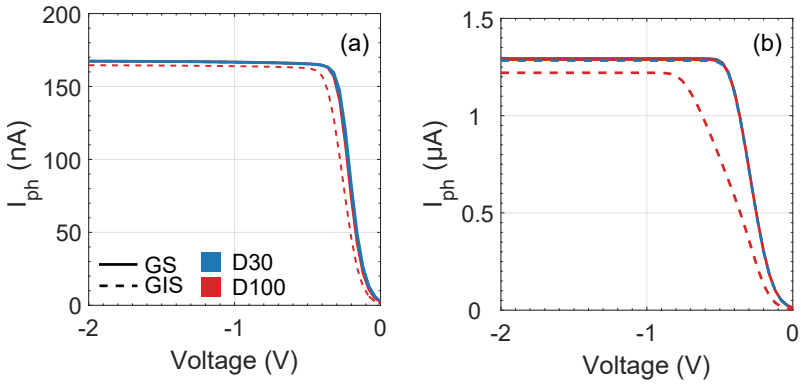

Figure 4.29: Photocurrent *vs.* voltage in D_{30} (blue) and D_{100} (red) for a laser power density of (a) 15 W/cm^2 and (b) 150 W/cm^2 when the spot is focused on the GS (solid) and GIS (dashed) junctions interfaces.

The obtained photocurrents for the ideal D_{30} and D_{100} devices are depicted in Fig. 4.29. The 15 W/cm^2 laser intensity provides a total value of the photocurrent quite similar to the one achieved with the uniform lamp illumination, above 100 nA, as in Fig. 4.14. Applying the laser spot on the GS or the GIS junctions generates in this situation a similar behavior for both devices. Only the photocurrent generated when the laser is focused on the GIS junction of the D_{100} is slightly lower than for D_{30}. The reason can be found in the longer path that holes must traverse in this device to reach the contacts, increasing the probability to be recombined. The situation is similar when a higher light intensity is applied, 150 W/cm^2, Fig. 4.29 (b). The applied power is augmented in a factor $\times 10$, so the photocurrent increase achieved is in this range ($\simeq \times 8$).

For both applied powers, I_{ph} quickly grows with the reverse voltage to reach its saturation value. Nevertheless, higher $|V_{\mathrm{R}}|$ values are needed for the larger laser power: this effect is particularly well observed in the GIS curve of the D_{100} device. This behaviour is similar to the experimentally measured, where the saturated I_{ph} is reached at different V_{R} values depending on the applied light intensity.

To simulate a more realistic situation, we have assessed the impact of different non-idealities making use of the parameters included in Table 4.2, that correspond to a degraded situation compared with the ideal one.

Additionally, we have considered a trap distribution spatially distributed below the graphene layer in a 2 nm thickness. Its energy profile follows a Gaussian distribution centred 0.2 eV below the mid-gap, with a variance of $\sigma_{\mathrm{E}} = 0.15$ eV and a maximum

Parameter	Value
T_{int} (nm)	20
τ_{int}(ns)	1
$\mu_{\text{n,int}}$ $\left(\text{cm}^2\,\text{V}^{-1}\,\text{s}^{-1}\right)$	15
$\mu_{\text{p,int}}$ $\left(\text{cm}^2\,\text{V}^{-1}\,\text{s}^{-1}\right)$	4
v_{th} (cm/s)	1

Table 4.2: Set of parameters used to simulate degraded conditions in D_{30} and D_{100} photodiodes in Fig. 4.30.

value of $D_{\text{it}}^{\text{max}} = 5 \times 10^{13}$ $\text{eV}^{-1}\text{cm}^{-2}$. This high trap density can be caused during the fabrication process as the SiO_2 coating is removed through a wet etching step. Besides, it has been experimentally demonstrated that heterointerfaces can also have a noticeable trap charge density, due to incomplete bonds or the interaction between atoms of the different interfaces [201, 202]. When a negative bias is applied to the contact, the hole pseudo-Fermi level approaches the valence band and the traps become positively charged as they are unoccupied. This Gaussian distribution is equivalent to apply an uniform donor doping density of 2×10^{20} cm^{-3} in a thickness of 2 nm. The presence of these positive charges originates a similar effect to those observed during the lamp analysis when a donor doping density was regarded.

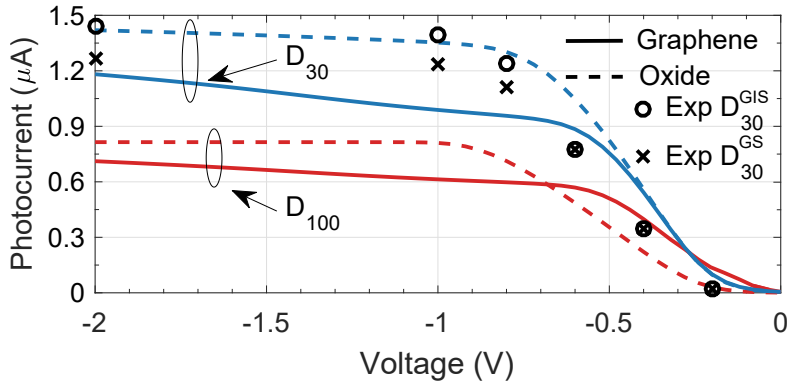

Figure 4.30: Photocurrent *vs* voltage in the D_{30} (blue) and D_{100} (red) photodiodes when a laser beam is applied on the GS (solid) and the GIS (dashed). Simulation results (lines) were calculated making use of the degraded conditions indicated by Table 4.1 and an laser intensity of 110 $\mu\text{W/cm}^2$. Symbols represent experimental results. Circles/crosses correspond to the GIS/GS junction of the D_{30} device.

This final evaluation has been carried out for both D_{30} and D_{100} photosensors and

Fig. 4.30 gathers the main results when a laser of 110 W/cm^2 is applied. That power density corresponds to a 5 μW laser with a spot diameter of 2.4 μm. Those values are similar to those employed in [195]. The experimental measurements for the 30 nm width finger have been included in the figure (symbols) as a comparison with the simulation results. These solid and dashed curves highlights the noticeable impact of the non-idealities located in the GS junction as they reduce considerably the photocurrent compared with the same illumination in the GIS region.

The consequence of these non-idealities is the reduction of I_{ph} when the laser beam is placed on the graphene, as well as the observed S-shape curve in both the GS and the GIS tests. The saturation voltage increases as the charged traps screens the gate voltage, reducing the extension of the depletion width beneath the graphene, as it happened in the lamp analysis with the interface donor density.

Overall, the degradation reduces the maximum photocurrent available for a fixed light intensity. Moreover, the presence of the oxide is important to increase the efficiency of the photosensor, specially if the graphene-Silicon interface is degraded, as it is usually the case for the non-optimized technology. However, the width of the finger must be careful selected as it is demonstrated by the experimental results, where the D_{100} photodiode depicted a lower efficiency than the device with a shorter finger.

This analysis proves the importance of the interface locally to the laser position, as it was demonstrated by the good agreement between simulations and experimental results shown in Fig. 4.30.

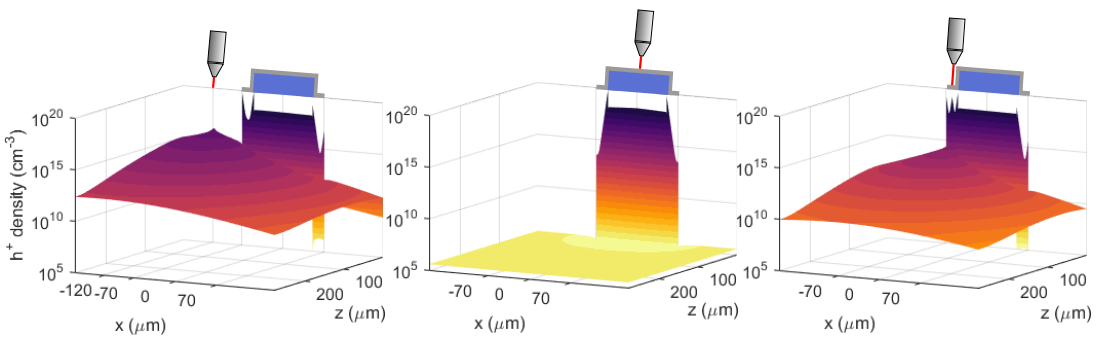

Figure 4.31: Hole density in the D_{100} device for $V_R = -2$ V when a laser beam of 110 μW/cm^2 is focused on the (a) air-substrate junction, (b) GIS region and (c) GS junction. Degraded conditions are imposed in these cases (see Table 4.2). Top row: Tilted view of the hole density from the xz-plane. Bottom row: Vertical view of the hole density on the xz-plane.

To finish this section we focus our attention to Fig. 4.31, that shows the hole distribution generated by the laser beam focused on three different locations of the D_{100} photodiode for $V_R = -2$ V. It has to be stressed how holes are spread in the substrate for the first and third scenarios, while in the second one, photogenerated carriers are picked up by the electric field, reducing considerably their spreading through the substrate. This gives an idea of the photosensor efficiency, depending on the easiness for the holes to be attracted to the Silicon surface.

4.6 Conclusions

Photodiode performance in ideal conditions

For non-degraded interfaces, the graphene-Silicon heterojunction can provide the best performance as the photogenerated carriers are collected directly by the graphene contact. In this situation, the presence of the GIS stack forces the carriers to flow to the contacts, first by drift and as they accumulate below the gate insulator as a lateral diffusion current. This longer path makes carriers prone to suffer recombination.

Interface degradation

During the fabrication procedure, the interface between graphene and Silicon can be seriously degraded, affecting a variety of parameters that have been analysed. Thermionic velocity and graphene workfunction degradation can modify the short-circuit current and the saturation voltage. Carrier lifetime and mobility degradation reduces the maximum photocurrent achievable. Traps and doping density at the interface originate an S-shaped I-V characteristic, due to the screening of the electric field.

Scanning Photocurrent

Laser analysis shows how the degradation of the silicon surface in contact with the graphene layer affects the device performance when that region is locally illuminated. The presence of the SiO_2 with a high quality interface increases the available I_{photo} in good agreement with the experimental results. This fact is especially noticeable for high light densities.

Chapter 5

Photogating in $MoTe_2$ Phototransistors

5.1 Introduction

In the forefront of technological maturity, and intensively studied for a variety of materials and structures, are photodetectors [86]. So far, graphene and transition metal dichalcogenides (TMDs) are promising candidates to this purpose, as discussed in the Introduction of this Thesis. Regardless, the complexity of the device structure and comprising materials, 2D photodetectors are still quite influenced by non-idealities. In particular, traps and charges at the channel-substrate interface can impact strongly or even dominate the device photoresponse. The influence of traps can, indeed, be translated into a beneficial mechanism, by which the trapped minority carriers contribute to increase the photocurrent. The so-called photogating effect [203] has already been observed experimentally in several 2D photodevices [204, 205], but apart from some simplified analytical models [206, 150] there is still a lack of deep understanding on its actual role. Here, by means of detailed numerical simulations, we explore and rationalize the photogating effect in 2D photodetectors considering a $MoTe_2$ phototransistor, and analyse different traps characteristics, illumination and bias conditions.

This Chapter is structured in three parts. First, we validate the simulator against experimental results in dark and illumination conditions in Section 5.2. Next, we investigate and rationalize the photogating effect, considering different traps and contact-metal features in Section 5.3. Finally, we discuss the main conclusions in Section 5.4.

5.2 Device structure and metal considerations

The photosensor here considered is inspired in the experimental realization described in [207]. It consists of the back-gated phototransistor schematically depicted in Fig. 5.1. The semiconductor channel consists of a few-layer $MoTe_2$ sheet, 8.4 nm-thick, and 5 μm $\times$ 8 μm long and wide, respectively. It lays on top of a bulk SiO_2 substrate (280 nm thick), back-gated by a p-type doped Silicon. The few-layer $MoTe_2$ channel is contacted by two Au/Cr electrodes acting as source and drain, respectively. The response of the photosensor is analysed under a 637-nm monochromatic beam above the device. The diameter of the spot light is 50 μm, completely covering the channel.

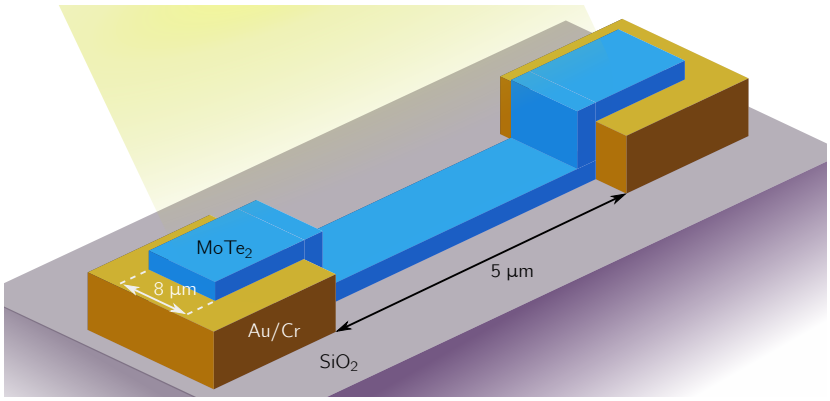

Figure 5.1: 3D schematic depiction of the $MoTe_2$ photosensor (not to scale).

To obtain both electrostatic and optoelectronic parameters, two experimental results have been employed: 1) the transfer curves in dark conditions for various drain voltages, and 2) the output characteristics for different light intensities. First of all, we have calibrated the $MoTe_2$ parameters, as well as the metal workfunction, whose values are shown in Table 5.1. The electron affinity is set to 4 eV, close to the *ab-initio* value [208] while the band gap has been set to 1.07 eV, which is not far to the corresponding value of monolayer $MoTe_2$ [209, 210]. This is a reasonable value, as the change from monolayer to bulk in $MoTe_2$ is just around 0.15 eV [211]. As for carrier mobility, the values considered in the simulations are slightly lower than the ones extracted in [207], which are 5.9 $cm^2V^{-1}s^{-1}$ and 0.3 $cm^2V^{-1}s^{-1}$ for holes and electrons, respectively.

However, in the experimental extraction, the contact resistance is obliterated, what, indeed, is a key factor to obtain the right trend of the transfer curves. The few-layer $MoTe_2$ is contacted by two Au electrodes playing the role of Schottky source and drain

Parameter	Value
N_D (cm^{-3})	10^{17}
χ (eV)	4
E_g (eV)	1.07
ϕ_m (eV)	4.6
μ_n $(cm^2\,V^{-1}\,s^{-1})$	0.06
μ_p $(cm^2\,V^{-1}\,s^{-1})$	1.24

Table 5.1: Material parameters used for the $MoTe_2$ simulation.

contacts with metal workfunction $\phi_m = 4.6$ eV. This low workfunction can be explained by the promotion of overlapped orbital states (also called metal-induced gap states) [212, 213] that pin the Fermi level, resulting in a high contact resistance. The junction between Au and the few-layer $MoTe_2$ is, therefore, non-ohmic, as we can see in the experimental transfer curves, presented in Fig. 5.2, where the slow current response is not governed by the channel resistance, but by the contacts one. For low-doped semiconductors and low V_{GS}, the evaluation of a thermionic model with a Schottky barrier would be sufficient to model the response. However, in this case the doping density is expected, as in most TMDs samples, to be high. The large doping density affects to the bands at the metal junction, depleting the semiconductor at the interface, and allowing a tunnelling current component if the barrier thickness is thin enough [121].

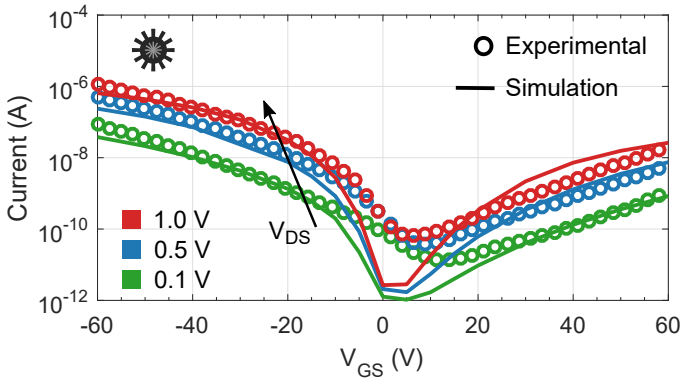

Figure 5.2: Experimental (symbols) and simulated (lines) transfer characteristics of the $MoTe_2$ transistor in dark conditions for different V_{DS} values.

The slow current response with V_{GS} can be explained in terms of the channel and contact resistances. In particular, the large V_{GS} applied should rapidly increases the

channel conductivity, but the result points out that there is another resistance controlled by the gate bias which slowly decreases as V_{GS} is incremented. This is the contact resistance, which apparently becomes the main actor controlling the device response. In order to assess the influence of the contact, a distributed tunnel model in conjunction with the barrier lowering explained in Section 2.4 are used. The contact behaviour can be checked out in the band diagram depicted in Fig. 5.3. This diagram, as well as a zoom of the source contact, have been plotted for $V_{GS} = 10$ V and $V_{DS} = 0.2$ and 1 V. As can be seen, the Fermi level is always close to the conduction band, which would lead to a very low channel resistance. However, the current is lower than the expected under ohmic conditions. This is caused by the high energy barrier presents in both contacts. As the doping density of this sample is not specially high, the tunnel barrier is thick enough to prevent the flow of carriers. When the gate voltage increases, the barrier is thinned, reducing the contact resistance and slowly increasing the device current. The importance of this resistance can be contrasted in the first band structure, where two different biases are shown. As the drain to source voltage is increased, the bands tend to shift down in energy in the left corner, where the source is located. This effect lowers the electric field in the channel, dropping the final drift current. The current is therefore limited by the tunnel probability for these bias conditions. The contact resistance reduction caused by the gate voltage is too weak unless the barrier lowering induced by the charge image in the contacts is considered. This model shifts the metal workfunction closer to the conduction or valence band, reducing the barrier height. Te change is up to 0.2 eV for high gate biases, reducing the barrier in the case of electrons, from 0.6 eV to 0.4 eV, and in the case of holes from 0.47 to 0.27 eV.

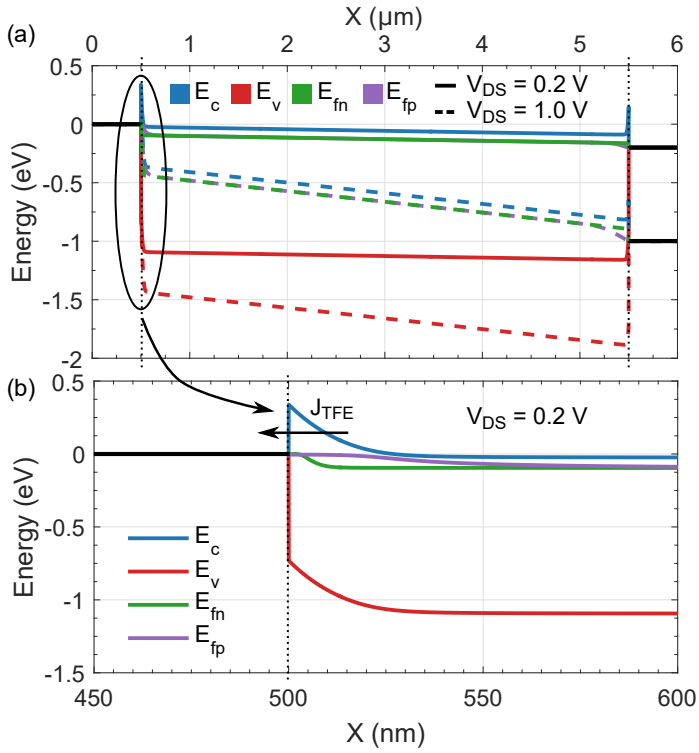

Figure 5.3: (a) Band diagram of the device in dark conditions for V_{GS} = 10 V and V_{DS} = 0.2 V (solid) and 1 V (dashed). (b) Zoom of the source contact for V_{DS} = 0.2 V.

After the calibration of the electrostatic parameters, the light absorption coefficient α, as well as the traps required to suit the photogating effect are also adjusted. The absorption values are extracted from [209] and are close to the measured absorbance of monolayer samples. In the case of traps, their features and a more extensive discussion of their influence on the photocurrent is provided in the next Section. Here, we focus only on the effect of the contact resistance and the light absorption.

Using the previously extracted parameters, the output curves are compared in Fig. 5.5 for three different light power magnitudes and V_{GS} = 10 V. As can be seen, the simulation results (solid lines) fit very well with the experimental ones, keeping the linear regime for the applied biases. If we consider a modified situation with higher channel conductivities balanced with lower absorption coefficients (dashed lines) the resulting curves tend to saturate as the drain voltage is increased, due to the dominant role played by the contact resistance, showing the importance of this effect also when the device is illuminated. The energetic barrier that carriers have to traverse is mitigated

as the light intensity increases, due to its narrowing with the increment of photogenerated carrier density close to the metal-semiconductor interface. Figure 5.5 also shows other curves with reduced absorption coefficient and carrier mobilities (dashed). The improvement of the channel conditions reveals the limitation of the photocurrent due to the contact resistance.

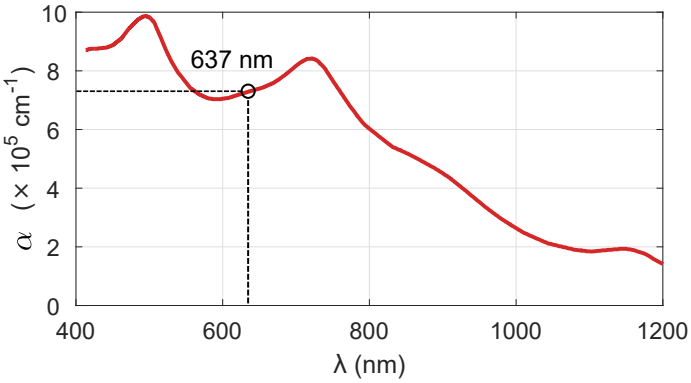

Figure 5.4: Absorption coefficient, α, of few-layer $MoTe_2$ for different light wavelengths after [209].

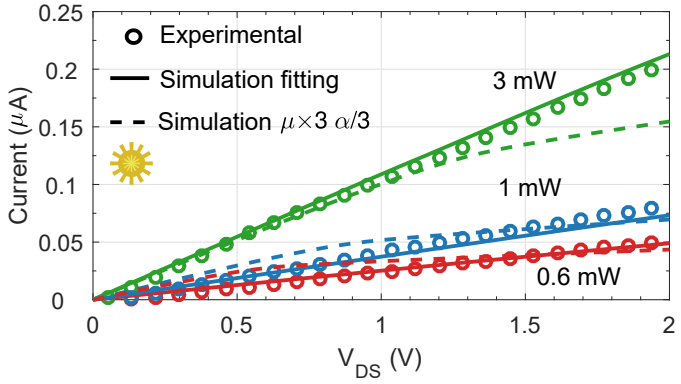

Figure 5.5: Experimental (symbols) and simulated (lines) output characteristics for $V_{GS} = 10$ V under three different optical powers.

5.3 Photogating analysis

In order to understand the role of defects and imperfections and exemplify how they can impact or even control 2D photodetectors, we have investigated how the energetic features (amplitude, position, dispersion) of the traps influence the photocurrent under

different bias and illumination conditions. We have considered the presence of hole deep traps following a Gaussian energetic distribution, which would correspond to deep localized states. The magnitude, standard deviation and energetic position of the traps are evaluated in this Section. Here we focus on positive gate bias, but negative biases would also produce a photogating effect if acceptor-like traps were evaluated. An schematic depiction of the photogating effect induced by the traps is shown in Fig. 5.6: the noticeable influence of charged traps in localized states close to the interface, playing the role of local gates, leads to a large photoconductive gain [203].

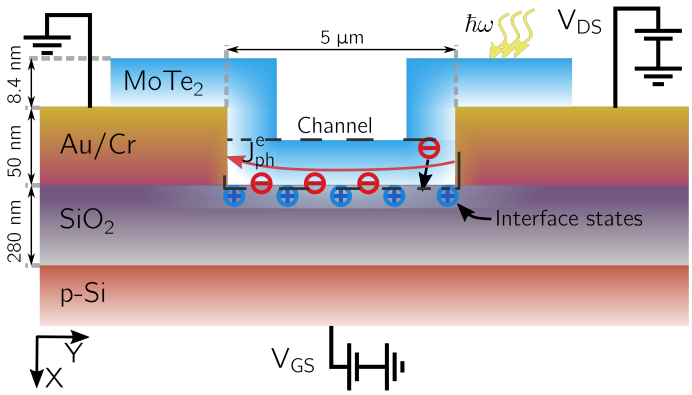

Figure 5.6: Schematic depiction of the $MoTe_2$ photosensor. The interface traps promote the photogating effect, due to the reduction of the channel resistance for electrons.

The first analysis checks out the effect of a regular trap profile with different light intensities. An energetic Gaussian profile with an amplitude of 3.5×10^{12} cm^{-2} eV^{-1}, an standard deviation of 35 meV, and centred 0.1 eV below the intrinsic level is used. The integration of that trap distribution for all the available energies would produce a total surface density of 3×10^{11} cm^{-2}. The traps are uniformly extended in a 0.7 nm thick spatial profile inside the oxide. Then, the calculated photocurrent with and without the presence of traps as a function of V_{GS} is depicted in Fig. 5.7, for $V_{DS} = 1$ V, and two different metal workfunctions, $\phi_m = 4.6$ eV (a) and 4.4 eV (b). As can be seen, there is a remarkable difference between low and high light power intensities. For the case with the higher calibrated metal workfunction:

- Without traps, the photocurrent increases linearly with the light intensity. On the other hand, the curve as a function of the gate voltage presents an starting increasing trend, up to certain point, where the hole depletion in the channel

causes the photocurrent reduction.

- In presence of traps, the photoresponse is quite different. First, for gate biases larger than 10 to 20 V, it shows a photoconductive gain due to the photogating effect. This behaviour is specially remarkable for the lower light intensities and higher gate voltages, where the evaluated photocurrent can be orders of magnitude larger than the traps-free scenario. In this case, the hole population is not a relevant factor for the photocurrent, as the photogating effect is caused by an improvement of the electron channel conductivity. The traps are occupied with the photogenerated holes, so the enhancement is not degraded unless a very high gate bias completely depletes the holes of the channel.

- The available trap density is determined by the Gaussian energetic profile: once all the traps have been activated, there is not any further improvement of the channel conductivity. As a consequence, the difference between the photocurrent in presence/absence of traps gets narrower as the light intensity is increased.

In order to study the impact of the contact resistance, this analysis is repeated with a lower metal workfunction, $\phi_m = 4.4$ eV (Fig. 5.7b). In presence of traps, I_{ph} is clearly boosted, w.r.t. $\phi_m = 4.6$ eV; additionally, the photoconductive gain quickly becomes saturated with V_{GS} because the contact resistance is lower than the channel resistance and affects to a lesser extent to the collection of the photogated electrons. On the other side, in the absence of traps, photocurrent shows less differences, what confirms that holes have a lower contribution to the total photocurrent when $\phi_m = 4.6$ eV.

Next, we study how the increment of the conductivity due to the photogating effect impacts on the current distribution along the channel. Figure 5.8 illustrates the electron drifted-diffused photocurrent density in absence/presence of traps for $V_{GS} = 60$ V, $V_{DS} = 1$ V, $\phi_m = 4.6$ eV and $P_{opt} = 40$ μW. As it can be deduced, positively charged traps augment the electron population close to the oxide interface boosting the current density in that region. It is interesting to remark the effect of the tunnel current in the source contact (located in the left side of the channel, x=0 μm). As the current approaches to the contact, it is injected through the energy barrier (what is appreciated as a reduction of the drift-diffusion current). In the case with traps, the increment of carriers at the proximity of the interface lets a higher amount of current to be injected.

We have extended the analysis to other workfunctions emulating different metals contacting the $MoTe_2$ channel. In particular, we have varied the metal workfunction of

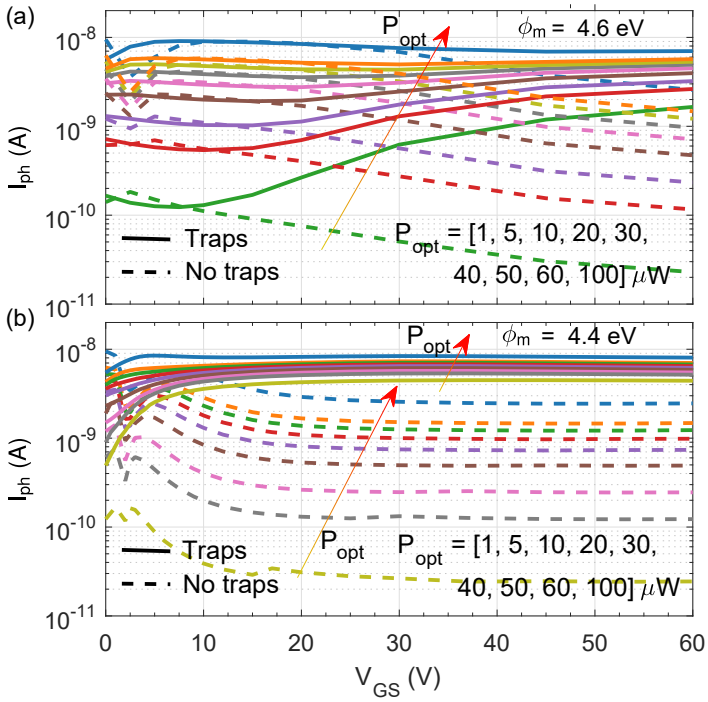

Figure 5.7: Photocurrent as a function of the gate voltage for different light intensities in presence (solid) and absence (dashed) of traps for $V_{\mathrm{DS}} = 1$ V and $\phi_{\mathrm{m}} = 4.6$ eV. b) Same as a) with $\phi_{\mathrm{m}} = 4.4$ eV.

both contacts from $\phi_{\mathrm{m}} = 4.3$ eV up to $\phi_{\mathrm{m}} = 4.7$ eV focusing only on one light intensity, $P_{\mathrm{opt}} = 40\mu$W, which results in an intermediate photoconductive gain. Figure 5.9 shows I_{ph} *vs.* V_{GS} for different metal workfunctions. As can be seen, low metal workfunctions produces the lowest photocurrent without traps, and the highest including them, while high workfunctions yield very low photoconductive gains, and I_{ph} is less dependent on the gate voltage sweep. In more detail, we can split the effect of the metal workfunction on the photocurrent into three broad scenarios:

- Low workfunctions ($\phi_{\mathrm{m}} = 4.3$eV) result in high energy barriers for holes, originating low photocurrents regardless the gate bias for the traps-free scenario. On the contrary, when traps are activated, the low workfunction reduces the contact resistance for electrons, giving rise to a photoconductive gain of a factor 4.

- As the metal workfunction is increased, more holes can be injected into the contacts, balancing both carrier contributions. The contact resistance for electrons is increased, degrading the impact of the photogating. So that, the final photo-

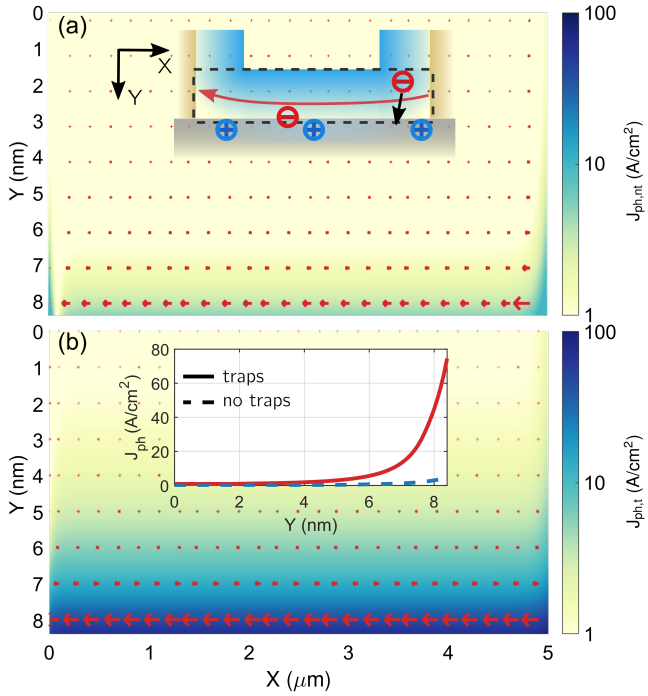

Figure 5.8: Photocurrent density in the channel when traps are disabled (a) and enabled (b). Dashed black line in the inset of (a) shows the section of the device which is being plotted. Inset in (b) depicts J_{ph} in the middle of the channel. $V_{GS} = 60$ V and $V_{DS} = 1$ V.

current is mainly due to photoconduction.

- For the higher metal workfunctions, I_{ph} increases continuously with V_{GS} in presence of traps. This fact is due to the progressive reduction of the contact resistance with V_{GS}, which lets the photogating effect to be predominant.

In order to quantify the photogating gain, we have calculated the ratio of I_{ph} in presence and absence of traps, and the responsivity for V_{GS} sweeping from 0 V up to 60 V and for optical powers from 0 μW up to 100 μW. Metal workfunction is set to $\phi = 4.4$ eV, and the results are plotted in Fig. 5.10. The maximum gain induced by traps happens for low P_{opt} and high V_{GS} and can achieve more than two orders of magnitude (due to the low value of I_{ph} in the traps-free scenario). Trap-induced gain is reduced for the lowest V_{GS} values while it keeps high (around one order of magnitude) for moderate V_{GS} regardless the optical power. A similar analysis is reproduced for $\phi = 4.6$ eV in Fig. 5.11, showing the same trend, although this workfunction presents

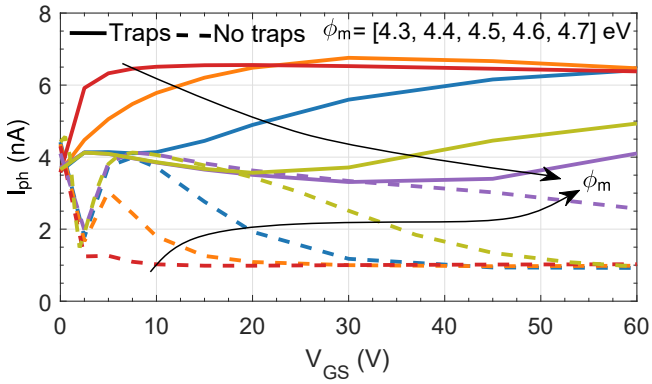

Figure 5.9: Photocurrent as a function of the gate voltage for different metal workfunctions, in presence (solid) and absence (dashed) of traps for $V_{\mathrm{DS}} = 1$ V and $P_{\mathrm{opt}} = 40\mu$W.

lower gains.

Finally, we have investigated how the device is affected by the specific features of the trap profile. In particular, we have varied both the position of the Gaussian profile and its standard deviation. To avoid the influence of the contact resistance, we kept the metal workfunction to a value of 4.4 eV. An intermediate light intensity, $P_{\mathrm{opt}} = 40\mu$W, is used. The maximum integrated trap profile is kept constant to 3×10^{11} cm^{-2} so to compare the different profiles in fair conditions. The amplitudes and σ of the considered Gaussian profiles are summarized in Table 5.2.

σ_{E} (meV)	$\mathrm{D_{it}}$ $\left(\mathrm{cm^{-2}eV^{-1}}\right)$
35	3.5×10^{12}
50	2.45×10^{12}
65	1.88×10^{12}

Table 5.2: σ_{E} (Standard desviation) and D_{it} (Amplitude) of the Gaussian profile for a constant integrated trap density of 3×10^{11} cm^{-2}. The parameters of the first row, with the Gaussian centered 0.1 eV below the intrinsic level, defines the default trap profile used in most of the analysis carried out in this Chapter.

Fig. 5.12 shows I_{ph} as a function of V_{GS} for $V_{\mathrm{DS}} = 1$ V. The actual position of the traps profile highly alters the photogating response. As the centre of the profile (E_{trap}) is shifted closer to the valence band, the number of active traps (for low-to-medium optical powers) is severely diminished, and I_{ph} behaves in a more similar fashion to the traps-free scenario. In particular, for $E_{\mathrm{trap}} = E_{\mathrm{i}} - 0.4$ eV, there is almost not

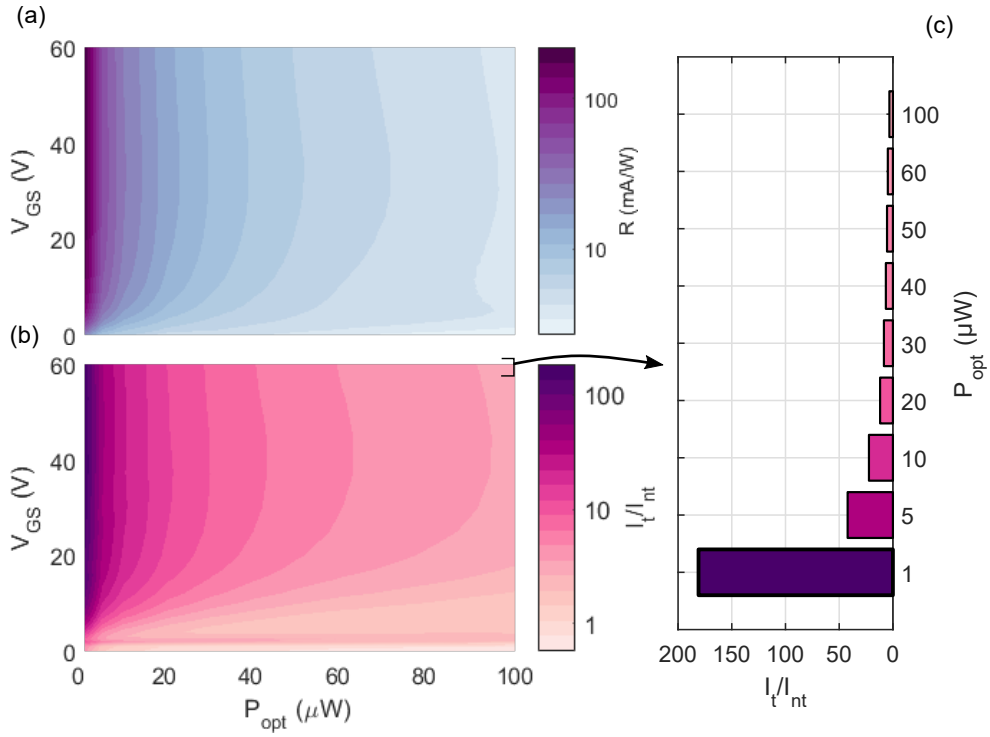

Figure 5.10: (a) Responsivity and (b) Photocurrent ratio with traps and without traps as a function of the gate voltage and the light intensity, for $V_{DS} = 1$ V, and $\phi_m = 4.4$ eV (c) Zoom of the photocurrent ratio for $V_{GS} = 60$ V.

photogating effect, while for $E_{trap} = E_i - 0.3$ eV some impact in I_{ph} is still observed. Less impacting is the standard deviation change that results in variations in I_{ph} below 7%. Interestingly, a smaller σ results in a higher I_{ph} when the traps profile is nearer to E_i, while for E_{trap} centred closer to E_v, a lower I_{ph} is observed. This fact can be understood from Fig. 5.13, which shows the energetic trap profile for the different standard deviations studied, as well as for two positions of the Gaussians. The hole Fermi level in the channel, at the vicinity of the oxide interface is indicated as a vertical dashed line, for $V_{GS} = 60$ V and $V_{DS} = 1$ V. From the results we conclude:

- As the position of the Gaussian is located above the Fermi level ($E_{trap} = E_i - 0.2$ eV), spreading its DoS produces that a higher amount of states falls below E_{fp}, so those traps are not activated.

- In contrast, if the Gaussian profile is placed ($E_{trap} = E_i - 0.4$ eV) well below

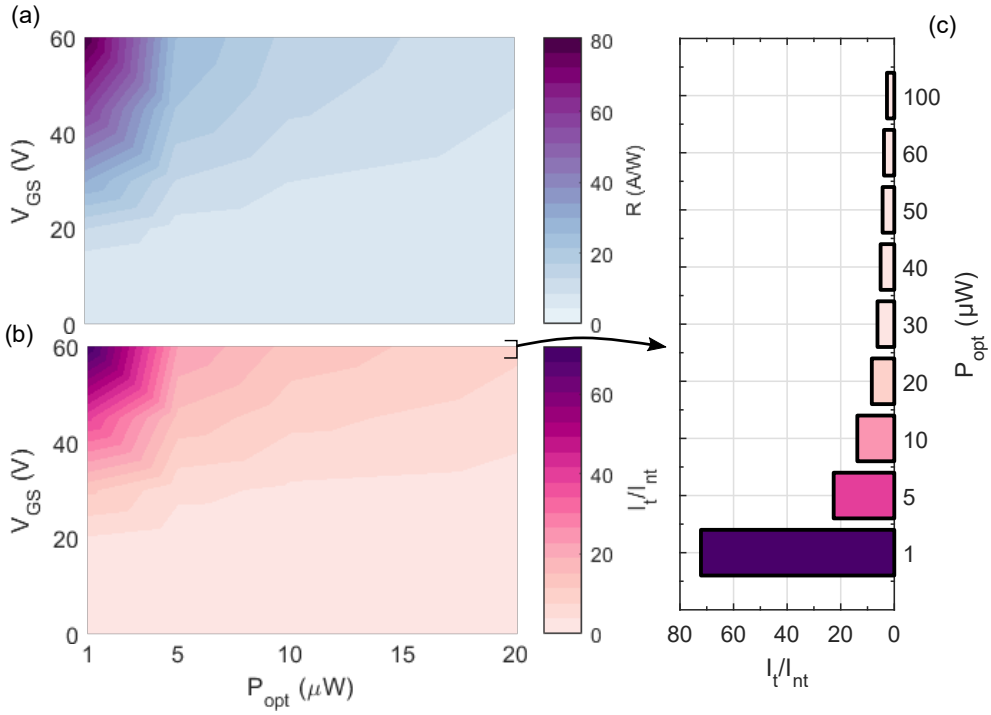

Figure 5.11: (a) Responsivity and (b) Photocurrent ratio with traps and without traps as a function of the gate voltage and the light intensity, for $V_{\mathrm{DS}} = 1$ V, and $\phi_{\mathrm{m}} = 4.6$ eV (c) Zoom of the photocurrent ratio for $V_{\mathrm{GS}} = 60$ V.

E_{fp}, an increment in the standard deviation leads to a higher number of activated traps and therefore an increase in the photoconductive gain.

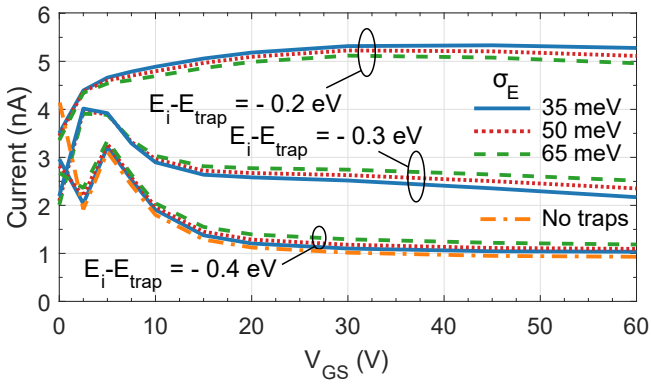

Figure 5.12: Photocurrent for various trap profiles, varying its standard deviation, amplitude and energetic position for $P_{\text{opt}} = 40\mu$W, $\phi_{\text{m}} = 4.4$ eV and $V_{\text{DS}} = 1$ V.

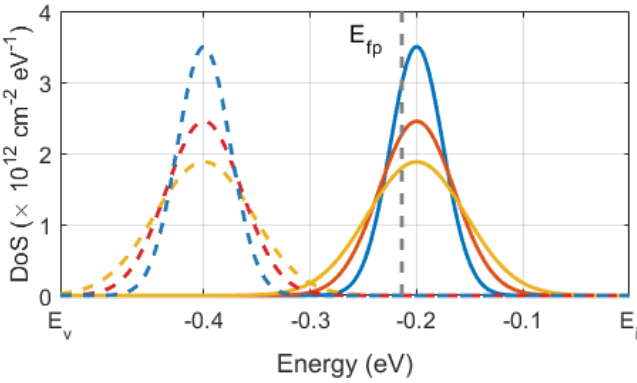

Figure 5.13: Density of states of different trap profiles, varying the standard deviation of the Gaussian profile and its energetic position. The hole Fermi level in the channel, close to the oxide interface is plotted (vertical dashed line) for $V_{\text{G}} = 60$ V, $V_{\text{DS}} = 1$ V, $P_{\text{opt}} = 40\mu$W, and $\phi_{\text{m}} = 4.4$ eV

5.4 Conclusions

Metal considerations in highly doped TMD semiconductors

In this chapter, we have checked the impact of interface traps in the behaviour of a $MoTe_2$ photosensor. In particular, the device parameters have been calibrated against experimental results using a distributed direct metal-semiconductor tunnelling current model including the image charge barrier lowering effect. Using this model, we have reproduced to a very good degree of accuracy the experimental transfer and output characteristics in dark and illumination conditions, respectively.

Photogating effect

We have then investigated the photogating effect as an important feature of photodevices based on 2D materials, which must be considered to properly model them. The traps have been placed at the interface between the oxide and the channel sheet. For low light intensities, we have observed that the total photocurrent is dominated by the photogating effect, especially for low metal workfunctions. Photogating has been analysed for different trap profiles, showing that the photoconductive gain is enhanced with very deep level traps and narrower energetic profiles.

Chapter 6

Graphene-MoS_2 Phototransistors

6.1 Motivation

At the current stage of technology, 2D material-based devices are strongly affected by the interfacial regions between the metal leads and the 2D crystals, which in most cases define the device response as much as the intrinsic material properties do it. We already discussed this fact in a $MoTe_2$ phototransistor (see Chapter 5), where the metal contacts presented a strong Fermi level pinning, setting a heavy contact resistance that controlled the device response. There is a consequent interest to develop efficient, affordable techniques able to create contacts with a reduced impact on the overall performance of the device.

Here we introduce a novel technique based on van der Waals bonded contacts using few-layer graphene that can be employed to define sub-micrometer channels, in a simple and cost-effective way. The technique is based on the mechanical cut of graphene flakes by means of an atomic force microscopy (AFM) suspended micro-tip. The resulting cut defines the channel length where the 2D crystal is later deposited. The technique is exemplified by fabricating a MoS_2 photosensor, achieving large ON currents and high photo-responsivity.

6.2 Introduction

There is a recurrent Achilles' heel spoiling the expected response of most 2D material-based devices: the contact resistance, that in most cases is playing a comparable role to the intrinsic 2D crystal properties in determining the device performance [214]. The conventional 3D solution to the contacts question (i.e. the chemical doping of an intermediate region between the semiconductor and the metal) is, so far, not a feasible and controllable alternative in 2D materials. Nevertheless, a similar behaviour may be accomplished taking advantage of the stacking versatility of 2D crystals [68]. In particular, the conciliation of metal leads and 2D materials could be reached by using intermediate layers, specifically graphene. Graphene presents ohmic contacts with most of the transition metal dichalcogenides (TMDs) [67], and improved charge injection with metals making it an optimal substitute to the doping interfacial region in 2D crystals. Indeed, graphene-TMDs contacts are less affected by the Fermi level pinning than photolitographed metal-TMDs contacts [215, 216, 217], due to their cleaner van der Waals interface. On the other hand, the graphene-metal contact is favoured by the semi-metallic nature of graphene, and the possibility to improve the injection by edge-patterning [114].

However, building these metal-graphene-TMD heterostructures is often jeopardized by the complicated spatial alignment of several flakes of 2D materials. This constitutes a major limitation for the fabrication of sub-micrometer channels, as it implies the precise placement of two electrically isolated graphene flakes or the use of complex lithography techniques. In order to face these limitations, in this Chapter we analyse an original and cost-reduced fabrication technique that should enable high quality contacts to 2D materials, in which sub-micron channel lengths can be achieved by mechanically cutting few-layer graphene flakes using an Atomic Force Microscope (AFM) tip. The proposed technique, that plays the role of a mechanic lithography, enables the fabrication of sub-micrometer MoS_2-based photodevices with graphene-gold contacts, and it is easily extendible to any other 2D-crystal device, provided that a good electrical contact with graphene is granted.

In the following we report the fabrication technique employed electrically and optically characterizing the graphene-metal contacts before and after the AFM cut in Section 6.3. Later, the electronic and photonic response of a fabricated multilayer MoS_2 photodevice are characterized and analysed in Section 6.4, observing photoresponsivities as high as 113 A/W. This Section includes the experimental results of a

similar device, in this case using a monolayer MoS_2 sheet as channel. We complete the study with thorough numerical simulations of the physical mechanisms controlling the device current photoresponse and electrical conduction in Section 6.5. The Chapter finishes with the corresponding conclusions in Section 6.6.

6.3 Device fabrication

In first place, both graphene and MoS_2 flakes are exfoliated from bulk materials using a viscoelastic stamp (GelFilm by GelPak) made of Polydimethylsiloxane (PDMS). In general, exfoliated MoS_2 tends to behave as an n-type semiconductor, due to the natural presence of transition elements, specially Rhenium [104]. Both MoS_2 few-layer and monolayer scenarios have been studied, due to the improved mobility and light absorption of the multilayer case [143] and the direct gap of the monolayer material. The thicknesses of the exfoliated graphene and MoS_2 are characterized by AFM measurements (ezAFM, NanoMagnetic Instruments), resulting in 9.7 nm for the few-layer MoS_2 flake (corresponding to around 15 layers) and 2.3 nm for the graphene flake (roughly 6 layers).

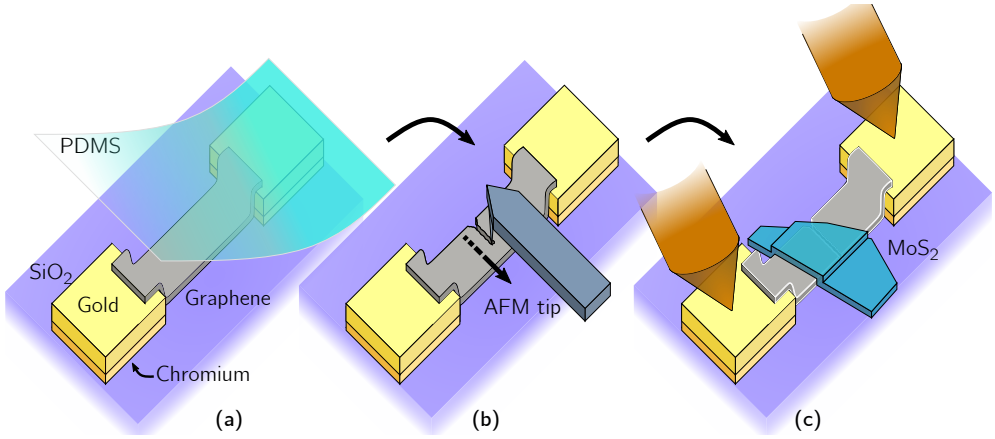

Figure 6.1: Fabrication process of the device. (a) The few-layer graphene (grey) is deposited onto the pre-patterned Cr/Au contacts (yellow) using a viscolastic stamp. (b) Next, the tip of the AFM cantilever is placed gently touching the oxide close to the flake. The board is moved toward the tip, breaking the graphene flake and forming two split sides. (c) A MoS_2 flake (blue) is deposited in the same way as in (a), contacting both sides of the graphene flake. The measurement tips are placed touching the Gold contacts.

Figure 6.1 schematically depicts the process followed to fabricate the phototransistors from these materials. First, the few-layer thick graphene is transferred onto a SiO_2 (280 nm) / p-Si substrate, where Cr/Au leads (2/70 nm thickness) have been previously patterned (Figure 6.1a). An optical image of the deposited graphene flake can be seen in Fig. 6.2a. The structure is annealed for one hour at 200 °C, in order to improve the adhesion of the flake to the substrate. Electrical measurements are performed at this point to check that the current in the graphene flake is not modulated by the back gate, confirming the semimetallic nature of the graphene layer, as seen in Fig. 6.3. From it, one can observe the good electrical contact between the Au and graphene [216]-

Next, the deposited graphene flake is cut in order to create the channel region. Laser-mediated techniques have been successfully used to ablate MoS_2, obtaining very good and uniform cuts even for thick flakes in a controllable way with times exposures $\simeq$ 0.1s. We used a Raman laser with $P = 28$ mW, $\lambda = 532$ nm and diameter $d = 1$ μm attempting to vaporize the graphene flakes. However, no change was found when it was applied to the graphene flakes, neither for monolayer nor thicker graphene flakes, even when the time exposure to the light was increased beyond 100 s.

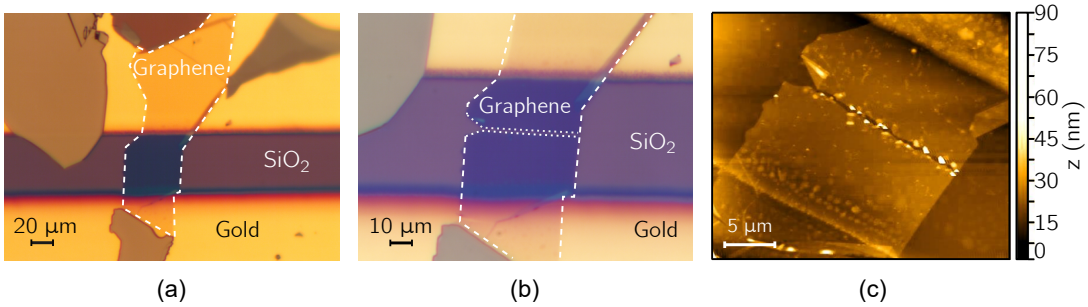

Figure 6.2: Few-layer graphene flake before (a) and after (b) the cut. The graphene (dark blue above the SiO_2) is higlighted by the white dashed line. The cut is indicated by the dotted line. Graphene is placed on top of the SiO_2 board (purple) overlapping both contacts (yellow). (c) AFM picture of the graphene flake after the cut.

Alternatively, we designed a way to mechanically cut the flakes. To do it, we use a brand new AFM tip (spring-constant $K = 42$ N/m, Bruker, model NCHV-A) to define the channel length by mechanically slitting the graphene flake, Fig. 6.1b. The tip is directed at a 75°angle over the graphene plane, at a slow pace, $\simeq 10$ μm/s, to improve the quality of the cut edges- Dotted lines in Fig. 6.2b frame the formed channel. Figure 6.2c shows an AFM image of the resulting structure. Once the graphene is divided into

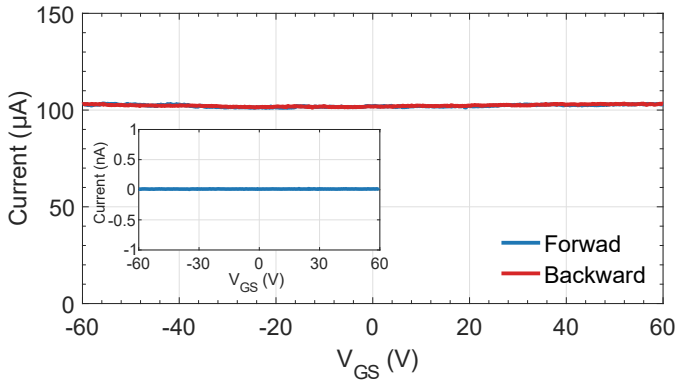

Figure 6.3: Experimental $I_{DS} - V_{GS}$ curve before cutting the few-layer graphene. The curve shows a very low gate modulation of the few-layer graphene. Inset shows the absent of current flow after the cut.

two sections, electrical characterization is used to check that they are isolated (see Fig. Fig. 6.3 inset). For the tested device, the distance between the two graphene flakes is optically measured. The photographed channel is digitally processed to obtain the distance from one side of the channel to the other pixel by pixel, with a sampling resolution of 12 nm. The analysis carried out provides the histogram of the channel length depicted in Fig. 6.4. As can be seen, the channel length is in the range between 200 and 600 nm, and can be modelled with a Gaussian distribution, with a mean value of $\mu = 396$ nm and a variance of $\sigma = 120$ nm.

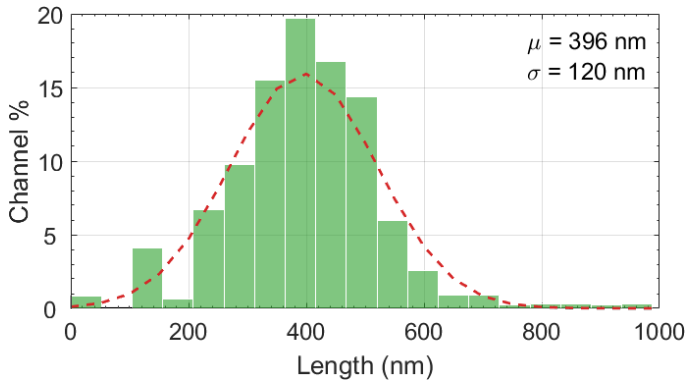

Figure 6.4: Histogram of the flake channel length along its width. The sampling resolution is 12 nm.

After this process, the exfoliated MoS_2 flakes are deposited on top of the two graphene sections (Fig. 6.1c). The final achieved phototransistor is shown in Fig. 6.5a. An

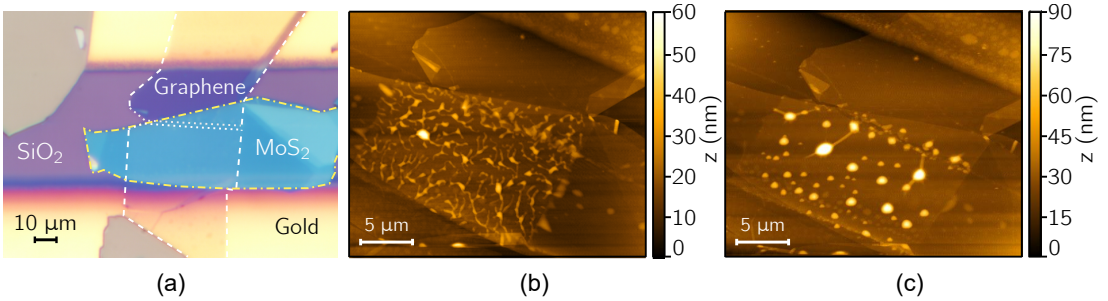

Figure 6.5: (a) Optical image of the final device where the 10 nm thick MoS_2 flake (light blue, framed by the yellow dashed lines) is deposited. (b) AFM picture of the final device before annealing, demonstrating how the graphene groove is overlapped by the MoS_2 flake. Bright spots may correspond to blisters in the MoS_2 flake, where OH groups accumulate between the MoS_2 and the graphene surfaces. (c) The same sample after annealing.

AFM image is depicted in Fig. 6.5b, showing the appearance of some blisters in the MoS_2 flake over the graphene, which may be caused by an electrocatalytic activity when the flakes are contacted, that would provoke the accumulation of OH groups between both surfaces [218, 219]. To eliminate these deposits, the resulting device is annealed at 350 °C for 18 hours in vacuum (0.1 mbar). This process reduced the number of blisters at the surface, as depicted in Fig. 6.5c, at the cost of spoiling a few of them. The irregularities of the cut generates many blisters close to the channel region, a fact that may severely affect the device performance.

Figures 6.2, 6.3, 6.4 and 6.5, that have been used to illustrate the fabrication process, correspond to the few-layer MoS_2 device. Figure 6.6 presents the information regarding the fabricated monolayer MoS_2 device. Figures 6.6a to c show the different steps for the fabrication process. We successfully fabricated a monolayer MoS_2 phototransistor with an average channel length of 852 nm: the channel is longer than the one achieved for the multilayer device, although the cut is more uniform (Fig. 6.6d). The AFM images (Fig. 6.6e and f) were captured after the annealing process, and they confirm the monolayer thickness of the MoS_2 flake.

During the experimental process, we have detected that the graphene surface is less suitable to mechanically deposit MoS_2 than the insulator and metal surfaces, as it did not stick properly to the graphene surface. This drawback is particularly noticeable when employing monolayer MoS_2 flakes, which are more fragile and prone to cracks and folds. Thus the experiment had to be repeated several times until we successfully

got a monolayer MoS_2 transistor without cracks. The best approach to get it is to start depositing part of the flake on top of the oxide substrate, so that it is well grabbed, reducing the damage in the flake when it is separated from the PDMS in the graphene region.

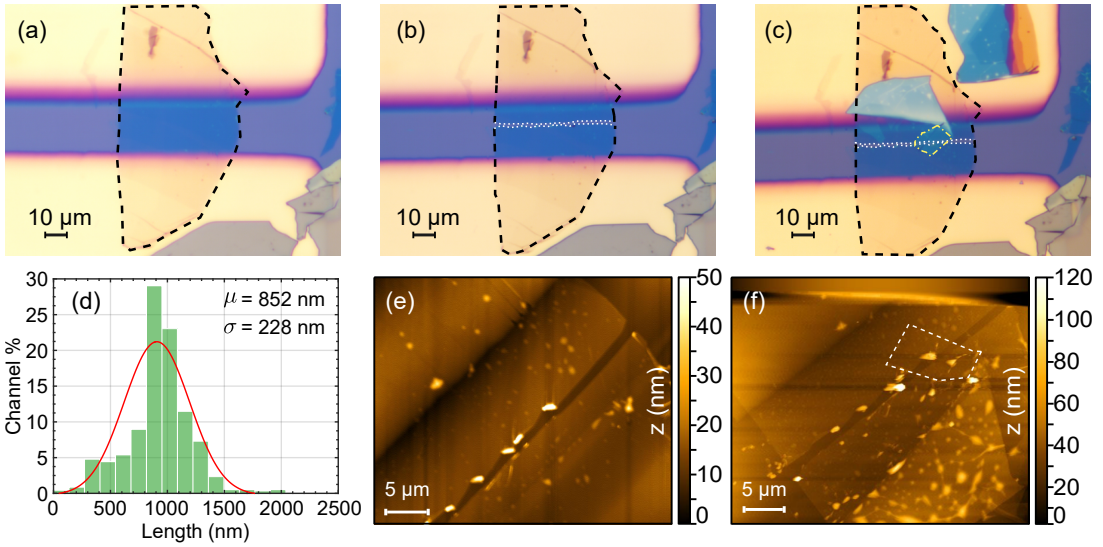

Figure 6.6: (a) Optical image of the final device where the few-layer graphene is deposited, (b) cut and (c) completed with the monolayer MoS_2 flake. (d) Histogram of the channel length, with an average value of 852 nm. (e) AFM image after the cut and (f) after depositing the MoS_2 layer and annealing. The monolayer surface presents less blister than in the multilayer region.

6.4 Experimental results

In this Section, we present the electrical and optical characterization results achieved for the fabricated graphene-MoS_2 phototransistors. Let us first focus on the few-layer MoS_2 device.

First, the device current (I_{DS}) was measured in dark conditions by connecting the Source-measurement unit (SMU Keithley 2450) probes to the Au contacts attached to the graphene flakes, to avoid their scratching, as shown in Fig. 6.1c. The output curves are depicted in Fig. 6.7, where several values of the back gate voltage, from -10 V to 60 V, were applied. The results reveal the symmetry of the contacts, which is well preserved after applying the mechanical cut technique.

Figure 6.8 shows the transfer characteristic of the device before (Fig. 6.8a) and after annealing (Fig. 6.8b). The curves were taken with a double (forward and backward) sweep, at a pace of 8 V / min. As can be seen, there is a strong difference between the results for the forward and backward direction, specially in the results before annealing (presenting a shift in the threshold voltage of around 40 V). The reason may be the presence of traps in the MoS_2 semiconductor and in the interface with the substrate. We hypothesize this behaviour is closely related to the blisters seen before in Fig. 6.5b. As a consequence, the device annealing softens this effect and reduces the differences between the forward and backward sweeps, as shown in Fig. 6.8b.

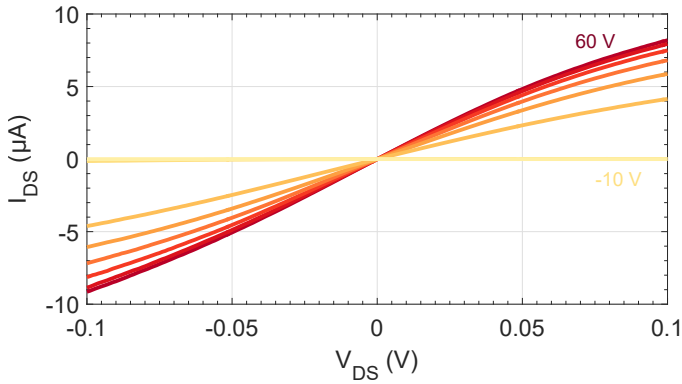

Figure 6.7: Experimental $I_{DS} - V_{DS}$ curve for V_{GS} values from -10 V to +60 V in steps of +10 V.

As depicted in Fig. 6.8b, a negative value of the threshold voltage is obtained, revealing the n-doped nature of the MoS_2 flake. For high positive gate voltages, the current begins to saturate, indicating the presence of a Schottky barrier between the graphene and the MoS_2 flake.

From the experimental curve it is possible to extract the field-effect effective electron mobility in low field transport, assuming the contact resistance is low enough, as [141]

$$\mu = \frac{L_{ch}}{W_{ch}} \left(\frac{dI_{DS}}{dV_{GS}} \right) \frac{t_{ox}}{V_{DS} \varepsilon_{ox}} \tag{6.1}$$

where L_{ch} and W_{ch} are the channel length and width, respectively, t_{ox} and ε_{ox} are the insulator thickness and permittivity, and V_{GS} and V_{DS} are the back-gate and drain to source voltages respectively. From this expression, the estimated electron mobility in the fabricated device is 6 $cm^2/V{\cdot}s$ (for the forward curve) and 10 $cm^2/V{\cdot}s$ (for the backward curve).

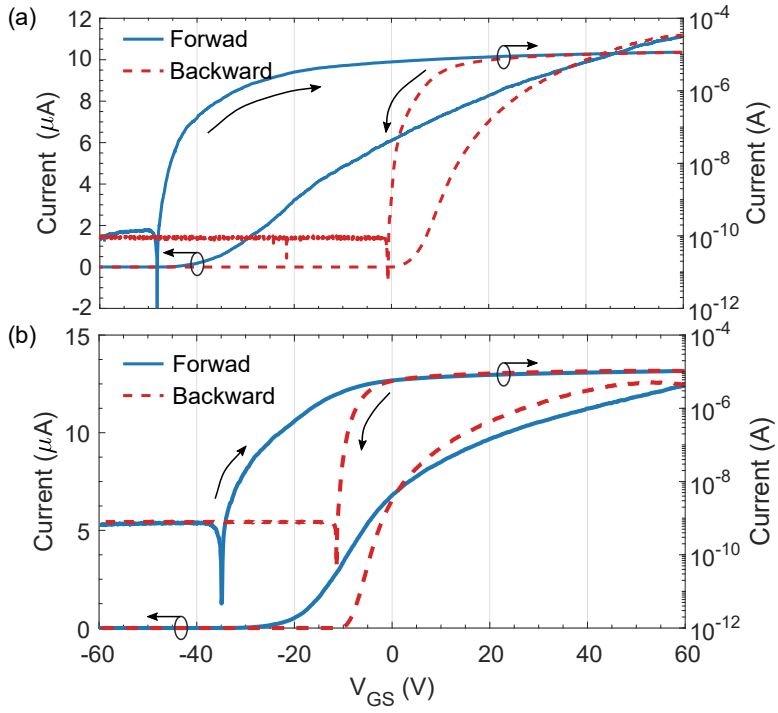

Figure 6.8: Transfer characteristic for $V_{DS} = 0.1$ V. (a) Before annealing, (b) after annealing. Solid lines refer to the forward sweep, whereas dashed lines refer to the backward one.

In order to evaluate the photodetection responsivity, the device is biased at V_{GS} = 0 V and V_{DS} = 0.1 V and exposed to a monochromatic light source, with P_{opt} = 27.7 μW, spot diameter 757 μm, and varying wavelength (λ) values from 420 nm to 850 nm. The light is applied through an ON-OFF keying shift with 0.1 Hz frequency. The applied laser power was measured by shinning the LED's light on a power meter console (Thorlabs PM100D).

The measured current has been recorded and is depicted as a function of time in Figure 6.9, for each of the applied wavelengths. Regardless the AC changes provoked by the light turning on and off, there is a very slow drift in the captured current, which may be caused by the presence of very slow traps, although this effect needs to be confirmed. If enough time is allowed for the experiment, a stationary state is reached. The photocurrent is then extracted using the current measured during the last minute (corresponding to the last six cycles of the applied laser signal). First, the current is filtered to delete any remaining slow drift caused by the traps. After that, a median

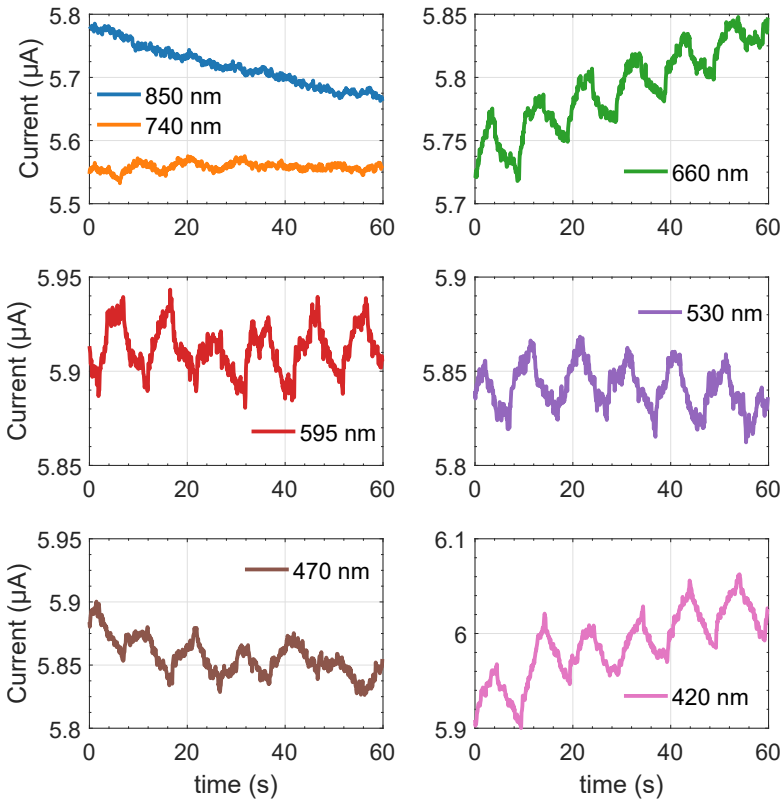

Figure 6.9: Current *vs.* time for different light wavelengths after annealing the few-layer MoS_2 device. $V_{DS} = 0.1$ V and $V_{GS} = 0$ V. A time varying square wave photo signal of frequency 0.1 Hz is applied.

filter is applied to suppress high frequency noise. Finally, the photocurrent is evaluated as $\langle I_{DS,ON} - I_{DS,OFF} \rangle$, i.e., the average value of the difference between the ON and OFF current states.

The results for the extracted photocurrent are depicted in Fig. 6.10 as a function of the wavelength, and show a peak at $\lambda = 660$nm, coinciding with one of the excitons of MoS_2, and consistently with the energy gap of bulk MoS_2 [220]. For wavelength values higher than 660 nm, the photoresponse shows a rapid decay, as can be expected in a MoS_2 device, and this fact demonstrates that graphene has little or none influence in the photocurrent, as its photoresponse is higher for these longer wavelengths [62, 221]. In order to evaluate the device responsivity, the following expression is employed:

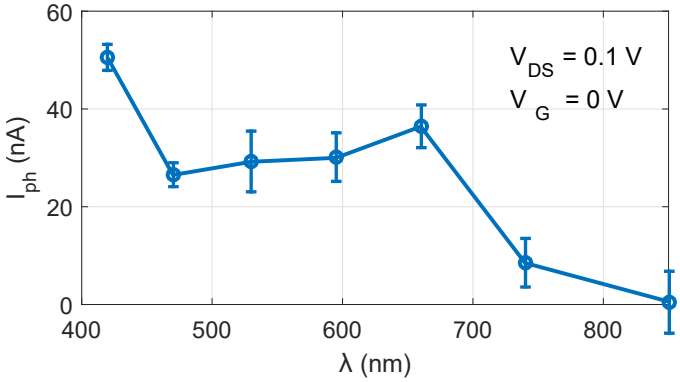

Figure 6.10: Photocurrent extracted for the few-layer MoS_2 device as a function of the wavelength for bias conditions $V_{GS} = 0$ V and $V_{DS} = 0.1$ V.

$$R = \frac{I_{ph}}{P_{opt}\frac{A_{aa}}{A_{spot}}} \tag{6.2}$$

where P_{opt} is the applied light power, $A_{spot} = 4.5 \cdot 10^5$ μm^2 is the light spot area, and $A_{aa} = 7.23$ μm^2 is the *active area* of the channel contributing to the photocurrent. This expression normalizes the light intensity by the ratio between the area of the beam and the active area of the sample: here, we assume only the channel region acts as an active area. An excellent value of the responsivity, 113 A/W, is obtained at $\lambda = 660$ nm. This responsivity value is in the range of previously published results, that vary from 10^{-3} to 10^5 A/W [222, 223, 224, 225].

The experiment was repeated for the device fabricated with the monolayer MoS_2 flake. The output and transfer curves, measured after the device annealing, are plotted in Fig. 6.11 and Fig. 6.12, respectively. The I_{DS}-V_{DS} curves are not as symmetric as the ones achieved for the few-layer device and presented in Fig. 6.7. The total resistance though is quite similar, with values around 720 mΩ·cm at $V_{GS} = 60$V. As for the transfer curve in Fig. 6.12, it presents a very important hysteresis, even after annealing.

Final photoresponse was analysed, using the same method described for the few-layer device. The measured light power density is 8.12 mW/cm^2. The photocurrent results, shown in Fig. 6.13, are unfortunately too noisy, and the photocurrent extraction was too complicated, even after the filtering process. Only for λ=595 nm and λ=660 nm, reliable values could be extracted, resulting in 6.3 nA and 9.5 nA, respectively.

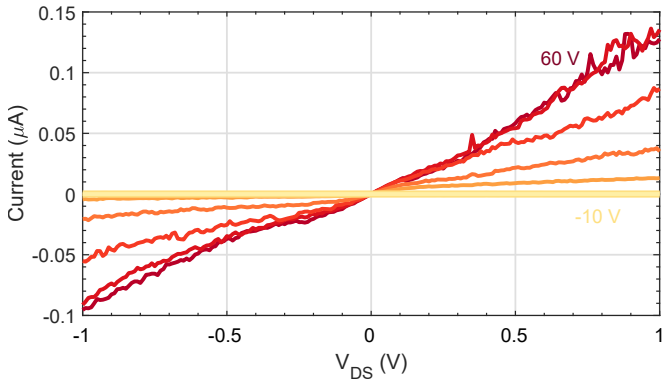

Figure 6.11: I_{DS}-V_{DS} sweep for different gate voltages.

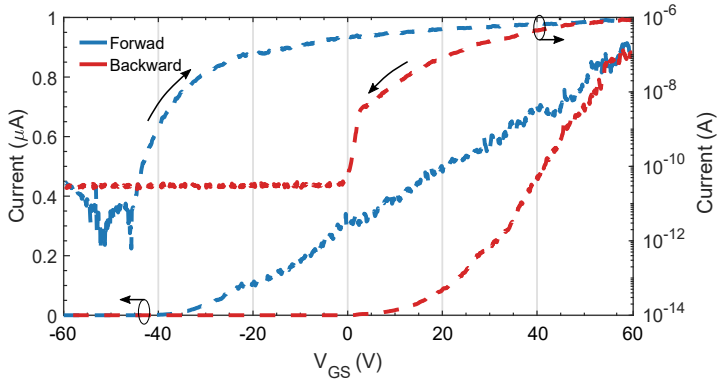

Figure 6.12: Transfer curve after annealing in logarithmic and linear scale for $V_{DS} = 1$ V.

For these values, a maximum responsivity of $R = 9.06$ A/W can be calculated, much lower than the value achieved for the few-layer device. Although this may be caused by the lower thickness of the monolayer nature (which would not be compensated by its direct gap and higher IQE [226, 85]), the results of the experiment are not conclusive and further work would be needed.

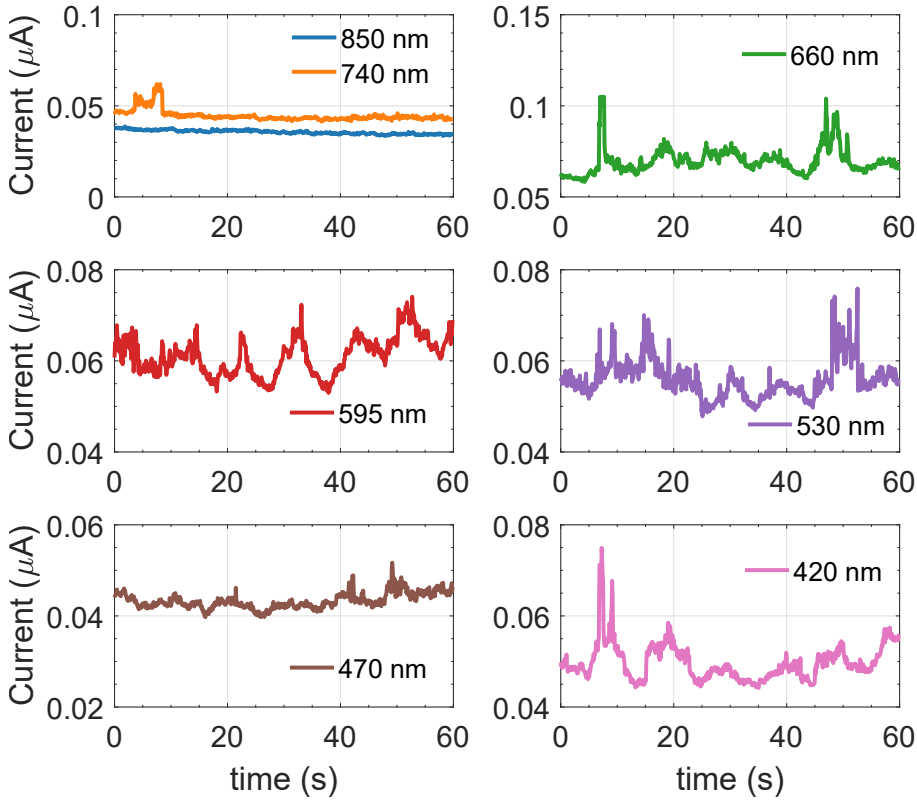

Figure 6.13: Current *vs.* time for different light wavelengths after annealing of the monolayer channel thickness device. $V_{DS} = 1$ V and $V_{GS} = 0$ V. A time varying square wave photo signal of frequency 0.1 Hz is applied.

6.5 Simulation results

To get further insights into the behaviour of the device, detailed numerical simulations of the phototransistor are also carried out. We focus on the few-layer device, that has showed the most promising response in the previous Section.

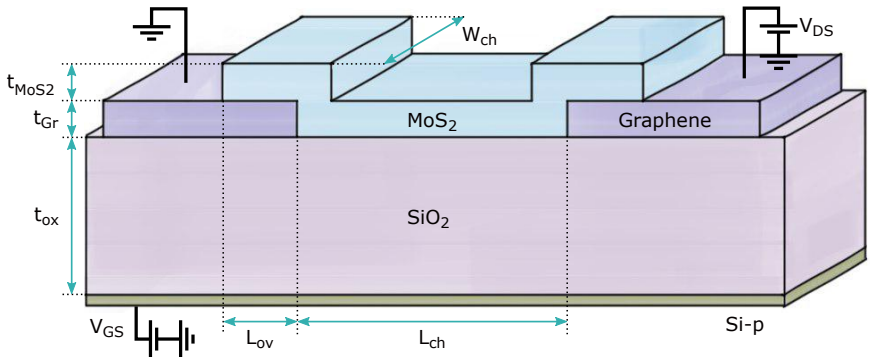

Figure 6.14: Schematic of the simulated few-layer MoS_2 phototransistor, where t_{MoS2} is the MoS_2 thickness, t_{Gr} the few-layer graphene thickness, t_{ox} the oxide thickness, L_{ch} and W_{ch} are the channel length and width, respectively, and L_{ov} stands for the overlapping length of Graphene and MoS_2.

The schematic of the simulated device is presented in Fig. 6.14. The channel length L_{ch} has been adjusted to the mean measured value (395 nm) and the width has been set from the optical images to 17.5 μm. As we noted in Fig. 6.3, graphene has a very low sheet resistance, much lower than the channel resistance in all the measurements that have been performed, so we have neglected any resistance associated to the graphene flakes. The technique applied to slit the graphene and form the channel provides the device with symmetrical electrodes. Thus, source and drain contacts are modelled as metals, whose work-function will be treated as a fitting parameter. All the simulations are performed at room temperature (T = 300 K), i.e., the same conditions of the measurements. The power applied in illumination conditions is $P_{opt} = 6.15$ mW/cm^2, coinciding with the one measured in the multilayer experiment (see Section 6.4). Table 6.1 presents the geometrical parameters employed in the simulations.

Before analysing in detail the behaviour of the devices, we have proceeded to validate the simulator. In this regard, two sets of simulations have been carried out:

- First, under dark conditions, and at room temperature T, the forward sweep of the transfer curve in Fig. 6.12b (after annealing) has been fitted. Figure

Parameter	Value	Parameter	Value
L_{ch} (nm)	395	L_{ov} (nm)	200
t_{MoS2} (nm)	9.7	t_{Gr} (nm)	3.2
t_{ox} (nm)	280	W_{ch} (μm)	17.5

Table 6.1: Geometrical parameters used in the simulations of the few-layer MoS_2 phototransistor.

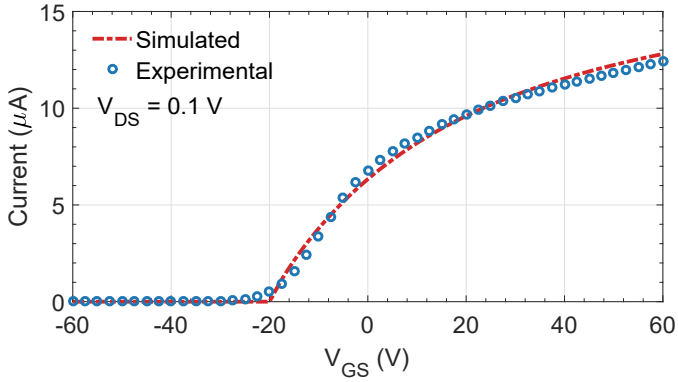

Figure 6.15: Comparison between the experimental forward-direction I_{DS} vs. V_{GS} curve of the few-layer MoS_2 phototransistor after annealing (see Fig. 6.12b), in blue circles, and the simulation results, in dashed red line.

6.15 shows an excellent agreement between the experimental and the simulation curves. To achieve it, a low Schottky barrier height(SBH) between the MoS_2 and the graphene ($\psi_B = 67$ meV) has been considered, resulting in a graphene work-function of $\phi_{gr} = 4.17$ eV. Although the workfunction for graphene is typically a little higher, it has been shown that it can present a wide range of values from 3.5 eV up to 5.1 eV [183]. In addition, it has been demonstrated that a weak Fermi level pinning between few-layer graphene and n-type MoS_2 can appear, reducing the electron barrier height [119]. The small SBH is also consistent with the assumption we made when extracting the electron mobility from the experimental data, i.e., a small contact resistance so Eq. (6.1) to be valid. The electron mobility extracted from the fitting process is $\mu_n = 7.5$ cm$^2/V{\cdot}$s, quite close to the one extracted from the experimental data.

- Next, a set of simulations including light are performed. A monochromatic light with $\lambda = 660$ nm and uniform power density $P_{opt} = 6.15$ mW/cm^2 is applied on the surface of the device (including the channel and the contact regions, to better

emulate the experimental setup). For the wavelength considered, the absorption coefficient is $\alpha = 10^6$ cm^{-1}, according to absorbance results in [220]. Shockley-Read-Hall ($\tau_{SRH} = 5$ ns) and Auger ($C_{Aug} = 5{\times}10^{-25}$ cm^6/Vs) recombination mechanisms are considered. Auger recombination has been demonstrated to have a relevant impact in MoS_2 few-layers flakes under illumination conditions [113, 135, 226], which is the reason why this mechanism has been included in our simulations. The hole mobility has been set to the same value as electron mobility, 7.5 cm^2/Vs. As discussed in Chapter 5, the presence of traps in bulk oxide-semiconductor interface may have a strong impact in the photoresponse of the device. In this case, interfacial traps at the insulator-MoS_2 interface were also included to fit the experimental results: a Gaussian energetic distribution has been assumed (see Fig. 6.16, with its maximum set at $E_a = E_i - 0.32$ eV, a standard deviation of $\sigma_E = 0.16$ eV and $D_{it}^{max} = 5 \times 10^{11}$ cm^{-2}eV^{-1} as a maximum amplitude. They are uniformly distributed in $t_{trap} = 0.65$ nm inside the semiconductor. Through the simulations, we have verified the strong influence of these traps on the high photocurrent measured, as they contribute to the photogating effect, which has been shown by other authors in MoS_2 over opaque substrates [227]. Under these conditions, the achieved photocurrent is 36.14 nA at $\lambda = 660$ nm, a value very close to the experimental measurements.

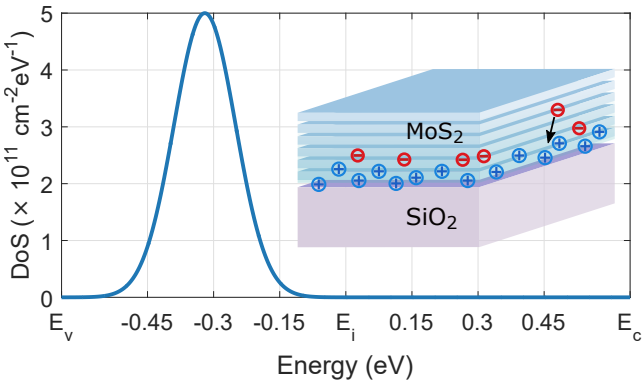

Figure 6.16: Trap density of states used for the validation of the photocurrent in few-layer MoS_2 phototransistors: a Gaussian profile is employed (see Table 6.2 for details). Traps are uniformly distributed along the MoS_2 layer in contact with the insulator substrate (6.5 Å thickness), as depicted in the inset.

To summarize, the parameters that have been extracted during the fitting process of the few-layer MoS_2 device are presented in Table 6.2.

Parameter	Value	Parameter	Value
μ_n ($cm^2/V{\cdot}s$)	7.5	μ_p ($cm^2/V{\cdot}s$)	7.5
N_D (cm^{-3})	$1.5{\times}10^{18}$	ψ_B (meV)	67
τ_{SRH} (ns)	5	C_{Auger} (cm^6/s)	$5{\times}10^{-25}$
α_{660} (cm^{-1})	$9.7{\times}10^5$	P_{opt} (mW/cm^2)	6.15
D_{it}^{max} ($cm^{-2}eV^{-1}$)	$5{\times}11^{11}$	N_{it}^{max} (cm^{-2})	$0.9{\times}10^{10}$
t_{trap} (nm)	0.65	E_a (eV)	E_i-0.32
σ_E (meV)	70	T (K)	300

Table 6.2: Parameters used in the simulations.

Let us now analyse the current flow through the device, which is shown in Fig. 6.19. The schematic of the simulated device is shown in Fig. 6.19a, and 6.19b presents a 'zoom' to the active area where the currents are evaluated. Figures Fig. 6.19c and Fig. 6.19d depict the electron and hole current densities, respectively, in dark conditions, for $V_{GS} = 0$ V and $V_{DS} = 0.1$ V. Due to the n-type character of the MoS_2 channel, electrons are the main contributors to the total current, that is quite homogeneously distributed along the channel thickness.

The photocurrent density is next evaluated, by subtracting the current density in dark conditions to the total current density under illumination. The results are depicted in Figures 6.19e (for electrons) and 6.19f (for holes). When the light is turned on, holes, which are the minority carriers in this device, increase their conductivity. Nevertheless, the n-type contacts block them, and they get trapped in the oxide-semiconductor interface, in a similar way as it happened in the $MoTe_2$ phototransistor studied in Chapter 5. The charged traps generate an electrostatic field in the region close to the oxide channel interface, attracting more electrons and, as a consequence, incrementing the conductivity of the channel in this region (See Fig. 6.19e). The obtained photocurrent is mainly promoted by this photogating effect. As for holes, they slowly diffuse to both contacts, and their contribution to the total photocurrent is negligible. In addition, it can be seen that the electron current coming from the overlapping area (L_{ov}) is quite small. To analyse this effect in more detail, a new simulation has been run where only the channel area is illuminated, as seen in Fig. 6.17. The rest of the parameters are kept as in the experimental validation. Under this condition, the calculated photocurrent is $I_{ph} = 34.92$ nA, only 3.5% lower than when the whole device is illuminated. Thus, it

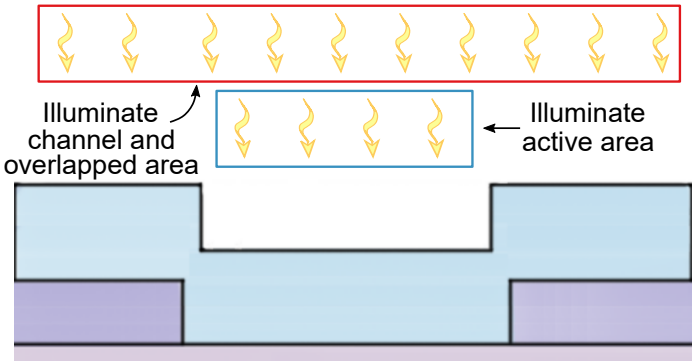

Figure 6.17: Schematic of the active area region: Red square points the total light spot used in the simulations. Blue square shows the incident light where the majority of the photocurrent is obtained.

can be concluded that the active area of the device corresponds to the channel section, supporting the high responsivity of the device calculated in the experimental results via Eq. (6.2).

The influence of the channel length on the device performance is now evaluated, in dark and illumination conditions. Figure 6.18 shows I_{DS} under dark conditions and the photocurrent, for channel lengths ranging from 400 nm to 1200 nm, at $V_{DS} = 0.1$ V and $V_{GS} = 0$ V. It is shown how a larger channel reduces both the dark and the photocurrent, in the last case despite the larger active area. This could be caused by the recombination of the carriers generated in the middle of the channel, or by a degradation of the photogating effect due to the increment of the channel resistance, and highlights the convenience of fabricating short channel phototransistors to increase their responsivity.

Next, we have simulated the effect of the trap density in the photocurrent, maintaining all of the parameters as in the validation (see Table 6.2), except for D_{it}^{max}. The results are depicted in Fig. 6.20 as a function of D_{it}^{max}, and in Fig. 6.21 as a function of the applied gate voltage. Here, V_{DS} is set to 0.1 V. Both figures show an increasing trend of the photocurrent with traps, in line with the results of Chapter 5 and therefore pointing out a photogating effect. Figure 6.20 shows an almost linear relation between I_{ph} and D_{it}^{max} for positive V_{GS} values, while a saturation behavior appears for gate voltages closer to the device threshold voltage ($V_{th} \simeq -20$ V).

In the case of Fig. 6.21 the effect of V_{GS} is more clearly appreciated. Regardless the trap density, the trend as a function of V_{GS} is similar, with a peak value around

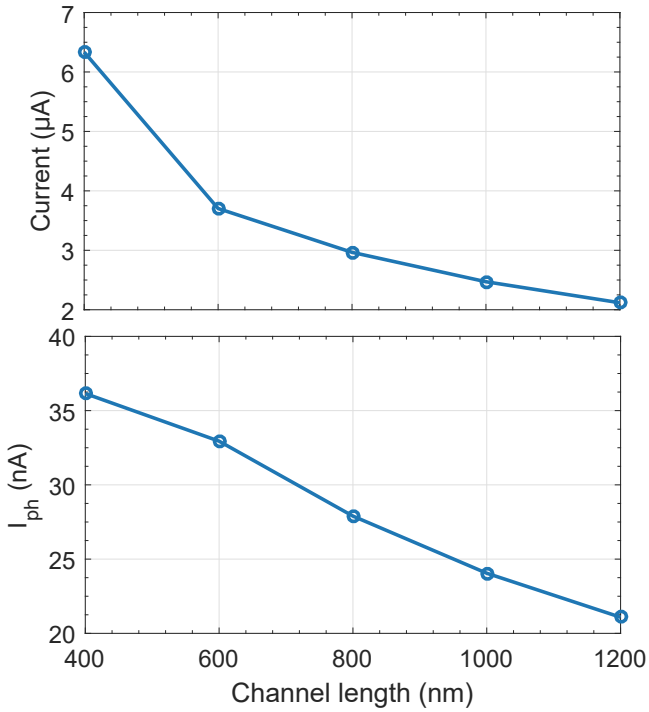

Figure 6.18: Dark current (a) and photocurrent of the device changing the channel length. $V_{DS} = 0.1$ V and $V_{GS} = 0$ V.

the device threshold voltage, and a reduction for higher values of the gate voltage. The reason of this reduction is that charged traps are promoted from the presence of holes at the oxide-semiconductor interface, which strongly depends on the applied bias. So that, an increment of the gate voltage repels the holes from the interface, reducing the number of charged traps and therefore diminishing the photogating effect, and as a consequence decreasing I_{ph}. In addition, it is important to point out that the maximum photocurrent is achieved for a gate bias of around -20 V; this maximum value can be more than one order of magnitude higher than the value calculated for higher gate voltages. For V_{GS} values lower than the threshold voltage, electrons are repelled from the channel and the photocurrent rapidly decreases.

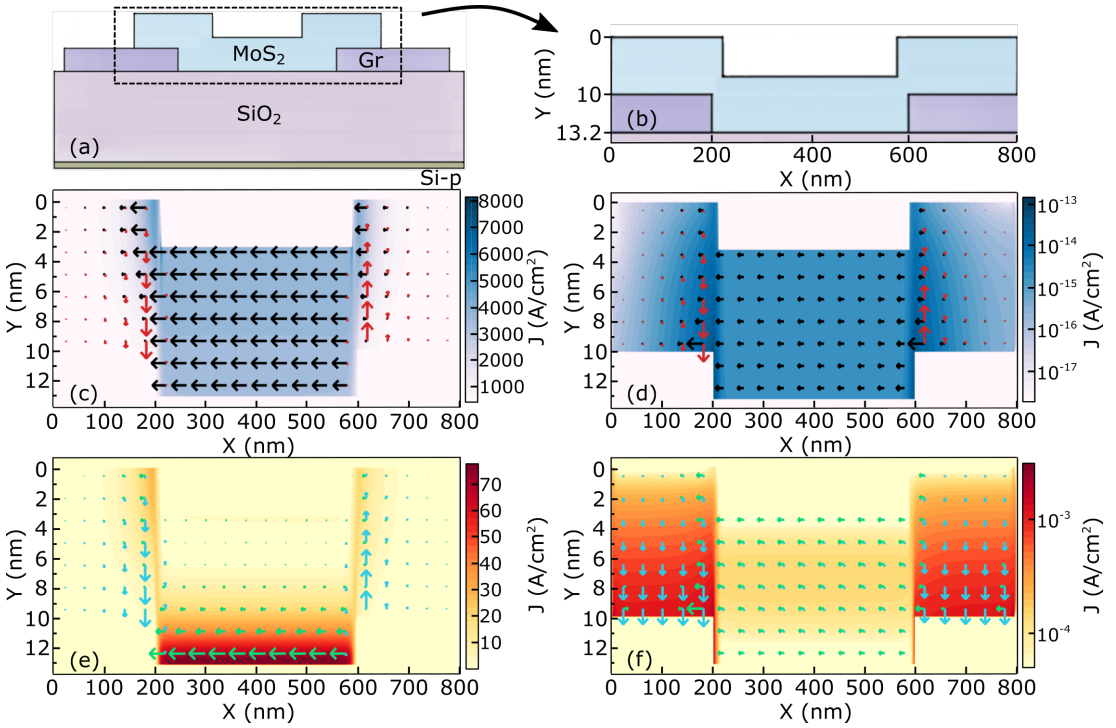

Figure 6.19: Schematic of the simulated device (a) and zoom of the represented region (b) in the rest of figures. Dark current (mid) and photocurrent (bottom) due to electron (left) and hole (right) flow in the device, for $V_{GS} = 0$ V and $V_{DS} = 0.1$ V. Photocurrents are obtained from subtracting the dark current (Figs. c and d) to the total current under illumination.

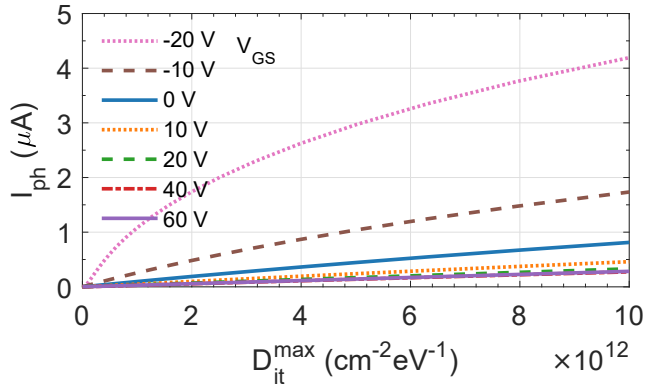

Figure 6.20: I_{ph} as a function of $D_{\text{it}}^{\text{max}}$ for different values of V_{GS}, in a few-layer MoS_2 device with the rest of parameters given in Tables 6.1 and 6.2.

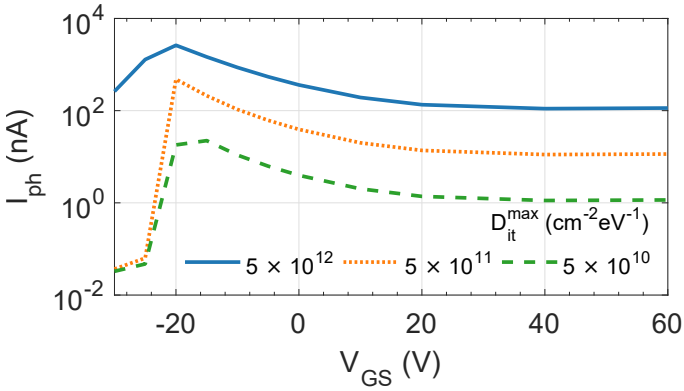

Figure 6.21: Simulated I_{ph} as a function of V_{GS} for different values of $D_{\text{it}}^{\text{max}}$, in a few-layer MoS_2 device with the rest of parameters given in Tables 6.1 and 6.2.

6.6 Conclusions

Sub-micron graphene-contacted channel fabricated with AFM tips

A novel, low-cost technique to fabricate sub-micron channel length 2D-materials-based devices has been presented. After depositing a few-layer graphene flake between two bulk metal contacts, it is slitted to form the device contacts employing an AFM tip. The 2D material forming the channel is deposited then in touch with the resulting graphene layers to form the sub-micron FET structure.

Graphene-MoS_2 photosensors

Using this technique, a few-layer MoS_2 flake is deposited to fabricate a phototransistor, which can be used as a photosensor. The electrical and optoelectronic properties of the resultant device have been studied both experimentally and theoretically. It has been showed that the intermediate graphene layer enables a low Schottky barrier height with the selected semiconductor, providing a low contact resistance. In addition, the fabrication of both contacts from the same graphene flake results in symmetrical contacts, which would be more complicated to get from different mechanically exfoliated graphene. When illuminated, the device shows a high photoresponse, owing to the sub-micron narrow channel length that makes it possible for the photogenerated carriers to flow to the graphene contacts before they are recombined.

Part IV

Conclusions and future work

Chapter 7

Conclusions and future work

7.1 Conclusions

As explained in the Objectives Section, the purpose of this PhD Thesis was the study of electronic and optoelectronic devices based on 2D materials. In this context, the main contributions of this work to the state of the art are the following:

- Development of the SAMANTA simulation tool. It can be described as a self-consistent 2D Poisson-Drift-Diffusion solver, including a 1D Schrödinger-Poisson solver, which is able to deal with different arbitrary materials and geometries. It evaluates the potential and electric charge, either using the continuity equations in the 2D transport scenario, or the evaluated wavefunctions and energy levels in the 1D confinement one. The 2D transport model also allows to evaluate the tunnel current in metal-semiconductor junctions and heterostructures, as well as band to band tunnelling. It also includes different generation and recombination processes, such as the SRH process, light generation, and Auger and radiative recombinations. In addition, it can evaluate arbitrary profiles of interfacial states. All the equations involved are solved by using the finite differences method, linearised with the Newton method.

- Analysis of the carrier mobility in multilayer MoS_2-based back-gated transistors. The Schrödinger-Poisson solver was employed to evaluate the potential, wavefunctions and energy levels of the system, in order to obtain the phonon and Coulomb limited electron mobility. These are calculated evaluating the associated momentum relaxation times and applying them in the Kubo-Greenwood formula.

We checked that the polar optical phonons are the main limiting scattering process for temperatures over 200 K, whereas Coulomb and acoustic phonons govern the device electronic mobility for temperatures below 200 K. The phonon-limited mobility also showed a non-monotonic dependence with thickness, with a maximum around 5 nm. This effect is related with the form factor associated to the polar optical phonon scattering mechanism.

- Study of hybrid graphene-Silicon photodiodes. Experimental results of hybrid graphene-Silicon photodiodes with interdigitated graphene-insulator-semiconductor (GIS) stacks were analysed using the 2D simulator. The presence of these GIS structures was checked to improve the responsivity and photoresponse of devices when the graphene-Silicon interface is degraded, although the wider the oxide regions, the larger the recombination effect. Interface states are the main degradation parameter, as they screen the electric field, reducing the depleted region thickness and eventually diminishing the number of extracted holes.

- Evaluation of $MoTe_2$ based Phototransistors. When bulk metals are used as contacts for few-layer $MoTe_2$, their Fermi level is pinned, forming high Schottky barriers for both carriers. We have demonstrated that this barrier can be overcome via tunnelling provided that there is a high doping density in the semiconductor, keeping the ambipolar behaviour thanks to the narrow bandgap of the few-layer $MoTe_2$. Traps at the oxide-semiconductor greatly enhance the responsivity of the device due to the photogating effect, although this improvement depends on the nature of the traps and the workfunction of the metal contacts.

- Fabrication and simulation of sub-micron few-layer MoS_2 phototransistors. Back-gated transistors were fabricated using a low-cost technique, based on a mechanically cut of a few-layer graphene flake by means of an AFM tip. The sliced graphene was then used as the drain and source contacts for a few-layer MoS_2 back-gated transistor. As contrasted with the simulation results, the Fermi level of the 2D semimetal is pinned when it is contacted with the MoS_2, providing a very low Schottky barrier for electrons. The device was also studied in illumination conditions, achieving a good photoresponse for wavelengths in the range of 420-660 nm. By means of simulations, we determined that this photoresponse was promoted by the trap-assisted photogating effect.

7.2 Future work

The SAMANTA simulator implemented in this Thesis exhibits a great potential for future works in the optoelectronic field of 2D materials, and our aim is to exploit it in further studies on the matter. In addition, expanding the capabilities of this custom tool to other fields, such as biosensing, is interesting. Then, following these concerns, we define the next advances:

- An improved light generation process which considers more physical parameters and the transfer matrix method to include the diffractions and refractions between materials will be implemented. This model could also be expanded to include light emission. This would allow the simulator to provide more accurate results for the optoelectronic behaviour of complex devices.

- Integration of time dependence. The current simulations are performed for stationary conditions: the next steps include the addition of the time dependence in the continuity equations. Also, we will complete this model with time dependent interface traps, as experimental measurements in non-stationary conditions can be highly affected by very low interface states, which can be explained with this model.

- Completing the heterojunctions to include the distributed TFE model. This will allow us to study more complex devices, such as multi-junction solar cells and PN diodes made of different materials. These harvesting components already offer excellent capabilities using classical materials, but their fabrication and study when using 2D materials is still a challenge both theoretically and experimentally. The inclusion of other new 2D materials, such as noble TMDs, can offer a wide variety of optoelectronic devices that should be analysed in detail.

- Integration of densities of states extracted from ab-initio calculations. This will increase the desciption of the properties of the semiconductors, providing more accurate results, specially in thin confined semiconductors. We will implement a 2D continuity model which uses 1D Drift-Diffusion equations to calculate the in-plane current, and the current TFE model for the out-of-plane direction, evaluating the pseudo-Fermi levels with pre-calculated densities of states. This model can be flexible and powerful, and would allow to study complex 2D-based devices.

- Exploiting the 2D Drift-Diffusion transport to simulate electrolyte-gated devices. These type of structures are used for biological and chemical sensors. Using our 2D carrier transport model for the device including the electrolyte and the semiconductor will provide a state of the art simulation environment for this kind of devices. In addition, the evolution towards a time dependent implementation would allow the simulation of very complex scenarios such as neuron-transistors interfaces to study the capabilities of MOSFET devices to detect synapses.

- Modelling of the absorption of ions in the device surface to study chemical sensors. The Site-Binding model is mostly used for the absorption of H^+ and OH^- ions on top of the insulator surface. However, it can be extended to model the absorption of other ions to study chemical sensors. Thus, the combination of the Site-Binding and the 2D ions transport models will provide a quite detailed description of these sensors.

Part V

Appendixes

Appendix A

Finite Differences Method

A.1 Finite difference method basics and notation

This appendix is devoted to present the numerical scheme applied to solve the equations proposed in Chapter 2. To do that, the Finite Differences Method (FDM) [228] is applied. In the FDM, each derivative is splitted into a two-point numerical derivative. Applying Taylor series, the partial derivative of a function $u(x)$ evaluated in x_0 can be approximated by:

$$\left.\frac{\partial u}{\partial x}\right|_{x=x_0} = \frac{u\left(x_0+\Delta x_1\right)-u\left(x_0-\Delta x_2\right)}{\Delta x_1+\Delta x_2} + O\left(\Delta x^2\right) + O'\left(\left|\Delta x_1-\Delta x_2\right|\right) \tag{A.1}$$

where $O\left(\Delta x^2\right)$ is a second order error depending on $\Delta x = \max\left(\Delta x_1, \Delta x_2\right)$, and $O'\left(\left|\Delta x_1-\Delta x_2\right|\right)$ is a first order error due to the difference between Δx_1 and Δx_2.

To apply the previous scheme to a physical system with an arbitrary geometry, this one has to be sliced into small regions, which in a 2D system are rectangular, as shown in Figure A.1. The dashed box represents one of such regions, where each of the physical parameters is defined (e.g., the dielectric constant, the carrier mobilities, etc.). As for the variables of the equations, such as potential, charge and current, they will be evaluated either on the nodes (corners of each region) or on the so-called seminodes (intermediate positions along the edges of the rectangles). The nodes are defined by their position (x_i, y_j). For the sake of simplicity, the notation for an arbitrary magnitude $\mathcal{Y}_{i,j}$ stands for $\mathcal{Y}(x_i, y_j)$. In a similar way, the variables and constants at

the seminodes are represented as $\mathcal{Y}_{i\pm1/2,j}$ and $\mathcal{Y}_{i,j\pm1/2}$.

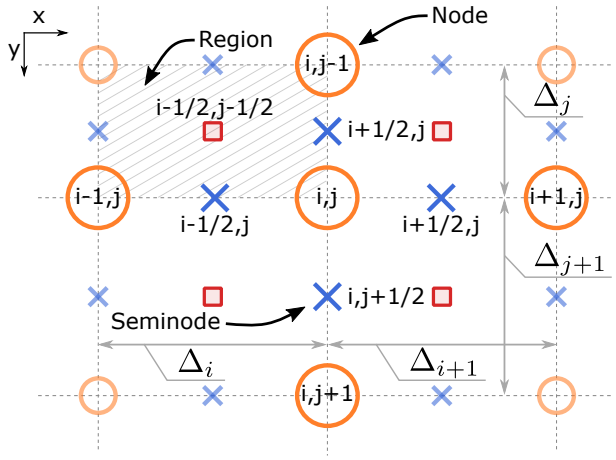

Figure A.1: Schematic of node splitting for finite differences. Materials are divided in regions, represented by the dashed box, each one with its own physical magnitudes, such as mobility, permittivity, light absorption, etcetera. The corners of the regions are the nodes (orange circles), where the potential and carrier density are evaluated. Between the nodes, the seminodes are assigned (blue crosses), in which the current densities are evaluated. The separation between nodes can be non-uniform.

As can be seen, the distance between points can be non-uniform, and it is represented by a Δx_i or Δy_j, depending on the direction. When the equations need for a physical magnitude in a node or seminode, this is evaluated as an average from the corresponding regions. To take into account the non-uniformity of the grid, the average value of a magnitude $\mathcal{Y}$ at the node (i,j) is calculated as:

$$\mathcal{Y}_{i,j} = \sum_{m=-1/2}^{1/2} \sum_{n=-1/2}^{1/2} \frac{A_{i+m,j+n}\mathcal{Y}_{i+m,j+n}}{\sum_{m=-1/2}^{1/2}\sum_{n=-1/2}^{1/2} A_{i+m,j+n}} \tag{A.2}$$

where $A_{i+m,j+n}$ refers to the area of each of the four regions in contact with node (i,j). A similar calculation is performed to obtain the parameters needed at the seminodes.

A.2 2D Poisson and continuity equations

In this Thesis, the bidimensional Poisson equation is solved taking into account the anisotropy of the bidimensional materials (see Section 2.2) as:

$$\nabla\cdot(\boldsymbol{\varepsilon}\left(\mathbf{r}\right)\nabla\psi\left(\mathbf{r}\right))=\left(\frac{\partial}{\partial x}\hat{\imath}+\frac{\partial}{\partial y}\hat{\jmath}\right)\cdot\left(\varepsilon_{xx}\left(\mathbf{r}\right)\frac{\partial\psi\left(\mathbf{r}\right)}{\partial x}\hat{\imath}+\varepsilon_{yy}\left(\mathbf{r}\right)\frac{\partial\psi\left(\mathbf{r}\right)}{\partial y}\hat{\jmath}\right)=-q\rho\left(\mathrm{r}\right) \quad (A.3)$$

which can be rewritten as:

$$\mathcal{P}\left(\mathbf{r},\psi\right)=\frac{\partial}{\partial x}\left[\varepsilon_{xx}\left(\mathbf{r}\right)\frac{\partial\psi\left(\mathbf{r}\right)}{\partial x}\right]+\frac{\partial}{\partial y}\left[\varepsilon_{yy}\left(\mathbf{r}\right)\frac{\partial\psi\left(\mathbf{r}\right)}{\partial y}\right]+q\rho\left(\mathrm{r}\right)=0 \quad (A.4)$$

This notation will be useful later when applying the Newton technique to accelerate the convergence. Let us focus on the discretization of the x dependent derivatives. First, we apply the Finite Difference (FD) scheme to the outer derivative as:

$$\frac{\partial}{\partial x}\left[\varepsilon_{xx}\left(\mathbf{r}\right)\frac{\partial\psi\left(\mathbf{r}\right)}{\partial x}\right]\simeq\frac{\varepsilon_{xx,i+1/2,j}\left[\frac{\partial\psi(\mathbf{r})}{\partial x}\right]_{i+1/2,j}-\varepsilon_{xx,i-1/2,j}\left[\frac{\partial\psi(\mathbf{r})}{\partial x}\right]_{i-1/2,j}}{\left(\Delta x_{i+1}+\Delta x_i\right)/2} \quad (A.5)$$

Next, the FD expression is applied again to the remaining derivatives of $\psi\left(\mathbf{r}\right)$, resulting in:

$$\begin{aligned}\frac{\partial}{\partial x}\left[\varepsilon_{xx}\left(\mathbf{r}\right)\frac{\partial\psi\left(\mathbf{r}\right)}{\partial x}\right]\simeq\frac{2}{\Delta x_{i+1}+\Delta x_i}\Bigg[&\psi_{i+1,j}\frac{\varepsilon_{\mathrm{xx,i+1/2,j}}}{\Delta x_{i+1}}-\\&-\psi_{i,j}\left(\frac{\varepsilon_{\mathrm{xx,i+1/2,j}}}{\Delta x_{i+1}}+\frac{\varepsilon_{\mathrm{xx,i\text{-}1/2,j}}}{\Delta x_i}\right)+\psi_{i-1,j}\frac{\varepsilon_{\mathrm{xx,i\text{-}1/2,j}}}{\Delta x_i}\Bigg]\end{aligned} \quad (A.6)$$

The same procedure can be applied to the y derivatives term to obtain the discretized Poisson equation, which reads:

$$\begin{aligned}\mathcal{P}_{i,j}\left(\psi_{i,j}\right)=&\frac{2}{\Delta x_{i+1}+\Delta x_i}\Bigg[\psi_{i+1,j}\frac{\varepsilon_{\mathrm{xx,i+1/2,j}}}{\Delta x_{i+1}}-\\&-\psi_{i,j}\left(\frac{\varepsilon_{\mathrm{xx,i+1/2,j}}}{\Delta x_{i+1}}+\frac{\varepsilon_{\mathrm{xx,i\text{-}1/2,j}}}{\Delta x_i}\right)+\psi_{i-1,j}\frac{\varepsilon_{\mathrm{xx,i\text{-}1/2,j}}}{\Delta x_i}\Bigg]+\\&+\frac{2}{\Delta y_{j+1}+\Delta y_j}\Bigg[\psi_{i,j+1}\frac{\varepsilon_{\mathrm{yy,i,j+1/2}}}{\Delta y_{j+1}}-\\&-\psi_{i,j}\left(\frac{\varepsilon_{\mathrm{yy,i,j+1/2}}}{\Delta y_{j+1}}+\frac{\varepsilon_{\mathrm{yy,i,j\text{-}1/2}}}{\Delta y_j}\right)+\psi_{i,j-1}\frac{\varepsilon_{\mathrm{yy,i,j\text{-}1/2}}}{\Delta y_j}\Bigg]+\mathrm{q}\rho_{i,j}\left(\psi_{i,j}\right)=0\end{aligned} \quad (A.7)$$

In this equation, the relation between ρ and ψ has been explicitly consigned. As this relation is non-linear, the resulting discretized equation system has to be self-consistently solved. In the next Appendix, a technique to linearise this equation, allowing a better computation performance, will be presented.

Now we focus on the discretization of the continuity equations, presented in Section 2.2. Considering only the x derivative term, for electrons, the divergence of the current seen in Eq. (2.4) can be calculated as:

$$\left.\frac{\partial \boldsymbol{J}_{\mathrm{n}}}{\partial x}\right|_{x_i,y_j} = \frac{J_{\mathrm{n},i+1/2,j} - J_{\mathrm{n},i-1/2,j}}{\left(\Delta x_i + \Delta x_{i+1}\right)/2} \tag{A.8}$$

where the current density is evaluated at the seminodes according to the Scharfetter-Gummel scheme [229, 116], which ensures the stability of the solution. This approach considers the charge as $n = u\mathrm{e}^{\psi}$, where $u\left(x\right)$ is a positive unknown function. Substituting this charge into the electron drift-diffusion equation at the position $i-1/2, j$, after recasting for integration convenient from, one gets:

$$\mathrm{e}^{-\psi_{i-1/2,j}} J_{\mathrm{n},i-1/2,j} = k_{\mathrm{B}} T \frac{\mu_{\mathrm{n},i,j} + \mu_{\mathrm{n},i-1,j}}{2} \frac{du}{dx} \tag{A.9}$$

Now, we integrate both sides between nodes $i-1, j$ and i, j, assuming a linear variation for ψ between the two nodes. The equation becomes

$$-J_{\mathrm{n},i-1/2,j} \frac{\Delta x_{i-1/2,j}}{\psi_{i,j} - \psi_{i-1,j}} \left(\mathrm{e}^{-\psi_{i,j}} - \mathrm{e}^{-\psi_{i-1,j}}\right) = k_{\mathrm{B}} T \mu_{\mathrm{n},i-1/2,j} \left(n_{i,j}\mathrm{e}^{-\psi_{i,j}} - n_{i-1,j}\mathrm{e}^{-\psi_{i-1,j}}\right) \tag{A.10}$$

The final equations at the nodes $i-1/2, j$ and $i+1/2, j$ are then given by

$$J_{\mathrm{n},i-1/2,j} = \frac{q k_{\mathrm{B}} T \mu_{\mathrm{n},i-1/2,j}}{\Delta x_i} \left[n_{i,j} B\left(\frac{\psi_{i,j} - \psi_{i-1,j}}{k_{\mathrm{B}} T}\right) - n_{i-1,j} B\left(\frac{\psi_{i-1,j} - \psi_{i,j}}{k_{\mathrm{B}} T}\right)\right] \tag{A.11a}$$

$$J^{\mathrm{n}}_{i+1/2,j} = \frac{q k_{\mathrm{B}} T \mu^{\mathrm{n}}_{i+1/2,j}}{\Delta x_{i+1}} \left[n_{i+1,j} B\left(\frac{\psi_{i+1,j} - \psi_{i,j}}{k_{\mathrm{B}} T}\right) - n_{i,j} B\left(\frac{\psi_{i,j} - \psi_{i+1,j}}{k_{\mathrm{B}} T}\right)\right] \tag{A.11b}$$

which uses the charge density and the potential at the grid points, and the mobility between points; $B\left(x\right)$ is the Bernoulli function, defined as:

$$B\left(x\right)=\frac{x}{\mathrm{e}^{x}-1},\ \text{ with }\ B\left(0\right)=1. \tag{A.12}$$

So here we reorganize the continuity equation, in a similar way as in Eq. (A.7). Let $\mathcal{W}_{\mathrm{n}}\left(\mathbf{r},\psi,n\right)=0$ and $\mathcal{W}_{\mathrm{p}}\left(\mathbf{r},\psi,p\right)=0$ the continuity equations for electrons and holes, respectively. Coming back to the discretization, in the two dimension scenario, the final continuity equation for electrons is:

$$\begin{aligned}
\mathcal{W}_{\mathrm{n},i,j}\left(\psi,n\right)=&\frac{2}{\Delta x_i+\Delta x_{i+1}}\left[n_{i-1,j}B\left(\frac{\psi_{i-1,j}-\psi_{i,j}}{k_{\mathrm{B}}T}\right)\frac{k_{\mathrm{B}}T\mu_{\mathrm{n},i-1/2,j}}{\Delta x_i}-\right.\\
&-n_{i,j}\left[B\left(\frac{\psi_{i,j}-\psi_{i+1,j}}{k_{\mathrm{B}}T}\right)\frac{k_{\mathrm{B}}T\mu_{\mathrm{n},i+1/2,j}}{\Delta x_{i+1,j}}+B\left(\frac{\psi_{i,j}-\psi_{i-1,j}}{k_{\mathrm{B}}T}\right)\frac{k_{\mathrm{B}}T\mu_{\mathrm{n},i-1/2,j}}{\Delta x_i}\right]+\\
&\left.+n_{i+1,j}B\left(\frac{\psi_{i+1,j}-\psi_{i,j}}{k_{\mathrm{B}}T}\right)\frac{k_{\mathrm{B}}T\mu_{\mathrm{n},i+1/2,j}}{\Delta x_{i+1}}\right]+\\
&+\frac{2}{\Delta y_j+\Delta y_{j+1}}\left[n_{i,j-1}B\left(\frac{\psi_{i,j-1}-\psi_{i,j}}{k_{\mathrm{B}}T}\right)\frac{k_{\mathrm{B}}T\mu_{\mathrm{n},i,j-1/2}}{\Delta y_j}-\right.\\
&-n_{i,j}\left[B\left(\frac{\psi_{i,j}-\psi_{i,j+1}}{k_{\mathrm{B}}T}\right)\frac{k_{\mathrm{B}}T\mu_{\mathrm{n},i,j+1/2}}{\Delta y_{j+1}}+B\left(\frac{\psi_{i,j}-\psi_{i,j-1}}{k_{\mathrm{B}}T}\right)\frac{k_{\mathrm{B}}T\mu_{\mathrm{n},i,j-1/2}}{\Delta x_j}\right]+\\
&\left.+n_{i,j+1}B\left(\frac{\psi_{i,j+1}-\psi_{i,j}}{k_{\mathrm{B}}T}\right)\frac{k_{\mathrm{B}}T\mu_{\mathrm{n},i,j+1/2}}{\Delta y_{j+1}}\right]-R_{\mathrm{n},i,j}+G_{\mathrm{n},i,j}=0
\end{aligned} \tag{A.13}$$

In the case of holes, the corresponding equations for the nodes $i-1/2,j$ and $i+1/2,j$ are

$$J_{\mathrm{p},i-1/2,j}=\frac{qk_{\mathrm{B}}T\mu_{\mathrm{p},i-1/2,j}}{\Delta x_i}\left[p_{i,j}B\left(\frac{\psi_{i-1,j}-\psi_{i,j}}{k_{\mathrm{B}}T}\right)-p_{i-1,j}B\left(\frac{\psi_{i,j}-\psi_{i-1,j}}{k_{\mathrm{B}}T}\right)\right] \tag{A.14a}$$

$$J_{\mathrm{p},i+1/2,j}=\frac{qk_{\mathrm{B}}T\mu_{\mathrm{p},i+1/2,j}}{\Delta x_{i+1}}\left[p_{i+1,j}B\left(\frac{\psi_{i,j}-\psi_{i+1,j}}{k_{\mathrm{B}}T}\right)-p_{i,j}B\left(\frac{\psi_{i+1,j}-\psi_{i,j}}{k_{\mathrm{B}}T}\right)\right] \tag{A.14b}$$

and the final discretized continuity equation for holes is

$$\begin{aligned}\mathcal{W}_{\mathrm{p},i,j}\left(\psi,p\right) = \frac{2}{\Delta x_i + \Delta x_{i+1}} \Bigg[& p_{i-1,j} B\left(\frac{\psi_{i,j}-\psi_{i-1,j}}{k_\mathrm{B}T}\right) \frac{k_\mathrm{B}T\mu_{\mathrm{p},i-1/2,j}}{\Delta x_i} - \\ & - p_{i,j}\left[B\left(\frac{\psi_{i+1,j}-\psi_{i,j}}{k_\mathrm{B}T}\right) \frac{k_\mathrm{B}T\mu_{\mathrm{p},i+1/2,j}}{\Delta x_{i+1}} + B\left(\frac{\psi_{i-1,j}-\psi_{i,j}}{k_\mathrm{B}T}\right) \frac{k_\mathrm{B}T\mu_{\mathrm{p},i-1/2,j}}{\Delta x_i}\right] + \\ & + p_{i+1,j} B\left(\frac{\psi_{i,j}-\psi_{i+1,j}}{k_\mathrm{B}T}\right) \frac{k_\mathrm{B}T\mu_{\mathrm{p},i+1/2,j}}{\Delta x_{i+1}}\Bigg] + \\ & + \frac{2}{\Delta y_j + \Delta y_{j+1}} \Bigg[p_{i,j-1} B\left(\frac{\psi_{i,j}-\psi_{i,j-1}}{k_\mathrm{B}T}\right) \frac{k_\mathrm{B}T\mu_{\mathrm{p},i,j-1/2}}{\Delta y_j} - \\ & - p_{i,j}\left[B\left(\frac{\psi_{i,j+1}-\psi_{i,j}}{k_\mathrm{B}T}\right) \frac{k_\mathrm{B}T\mu_{\mathrm{p},i,j+1/2}}{\Delta y_{j+1}} + B\left(\frac{\psi_{i,j-1}-\psi_{i,j}}{k_\mathrm{B}T}\right) \frac{k_\mathrm{B}T\mu_{\mathrm{p},i,j-1/2}}{\Delta x_j}\right] + \\ & + p_{i,j+1} B\left(\frac{\psi_{i,j}-\psi_{i,j+1}}{k_\mathrm{B}T}\right) \frac{k_\mathrm{B}T\mu_{\mathrm{p},i,j+1/2}}{\Delta y_{j+1}}\Bigg] - G_{\mathrm{p},i,j} + R_{\mathrm{p},i,j} = 0\end{aligned} \tag{A.15}$$

The expressions in Eq. (A.13) and (A.15) are applied only inside the semiconductors. When the current needs to be evaluated at the interfaces, they have to be modified. The next sections deal with these situations.

A.3 Continuity equations at heterojunctions

As seen in Section 2.5, in simple heterojunctions formed by two different semiconductors, the electron and hole densities have different values at each side of the junction. In the simulator, when the system is sliced into several nodes and regions, the heterojunction nodes are split into two nodes. An scheme of this slicing procedure is shown in Fig. A.2. Two split nodes share the same spatial location but their variables can have different values, eg., $n_{i^+,j}$ and $n_{i^-,j}$. The only variable which keeps the same value for both sides is the potential. So we set:

$$n_{i^-,j} \neq n_{i^+,j} \tag{A.16a}$$

$$p_{i^-,j} \neq p_{i^+,j} \tag{A.16b}$$

$$\psi_{i^-,j} = \psi_{i^+,j} \tag{A.16c}$$

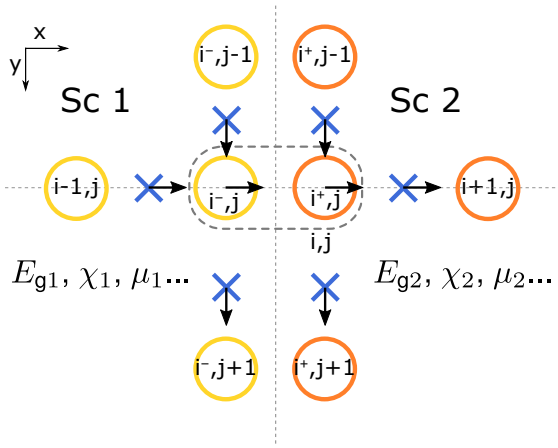

Figure A.2: Schematic of node splitting at an heterojunction. At the interface, nodes are split into two, sharing the same spatial location. In these nodes (labeled with superscript + or -) the electric potential is shared, but the rest of variables can differ. The current at node i, j is divided into one corresponding to node i^-, j and another to node i^+, j.

The material parameters (e.g., affinity, bandgap, mobility, doping, trap density, etc.) assigned to each of the split nodes correspond to the ones of the material of its side.

Following the scheme in Fig. A.2 for heterojunctions between two semiconductors, the current in the negative branch (position i^-, j) can be evaluated as:

$$\frac{\left(J_{i^-,j} - J_{i-1/2,j}\right)}{\Delta x_i/2} + \frac{\left(J_{i^-,j+1/2} - J_{i^-,j-1/2}\right)}{\left(\Delta y_j + \Delta y_{j+1}\right)/2} = \pm q\left(R_{i^-,j} - G_{i^-,j}\right) \tag{A.17}$$

which applies for electrons (right hand side positive sign) and holes (negative sign). A similar expression is employed for the right side (i^+, j):

$$\frac{\left(J_{i+1/2,j} - J_{i^+,j}\right)}{\Delta x_{i+1}/2} + \frac{\left(J_{i^+,j+1/2} - J_{i^+,j-1/2}\right)}{\left(\Delta y_j + \Delta y_{j+1}\right)/2} = \pm q\left(R_{i^+,j} - G_{i^+,j}\right) \tag{A.18}$$

The currents $J_{i^-,j}$ and $J_{i^-,j}$ correspond to the ones presented in Eq. (2.17) for electrons and Eq. (2.19) for holes, whereas the rest of them follow the Drift-Diffusion model presented in Equations (A.11) and (A.14).

For metal-semiconductor interfaces using the TE model, the equation is similar. The

thermionic current is evaluated not at the seminode but at the interface node between the metal and the semiconductor. If we consider the semiconductor is placed on the left side and the metal on the right side of our system, the corresponding discretized continuity equation for electrons and holes is

$$\frac{\left(J_{i,j} - J_{i-1/2,j}\right)}{\Delta x_i/2} + \frac{\left(J_{i,j+1/2} - J_{i,j-1/2}\right)}{\left(\Delta y_j + \Delta y_{j+1}\right)/2} = \pm q\left(R_{i^-,j} - G_{i^-,j}\right) \tag{A.19}$$

where the current $J_{i,j}$ is substituted by Eq. (2.6).

When TFE model is applied at the metal-semiconductor interface, located at the I, j position for this explanation, the tunnel current contributions are distributed along the positions of the potential barrier, as shown in Fig. A.3. To do that, drain points are placed at the i,j positions of the barrier, which collects the Drift-Diffusion current from positions far from the barrier interface. We simply add this current as in the Kirchchoff equation, which we will explain in the next Section. Let us consider the tunnel contributions are evaluated in n nodes from the I, j interface. Selecting a node i, j placed on the left side of the interface I, j, we would have for electrons and holes:

$$\frac{J_{i+1/2,j} - J_{i-1/2,j} + J_{\mathrm{T},i,j}}{\left(\Delta x_i + \Delta x_{i+1}\right)/2} + \frac{J_{i,j+1/2} - J_{i,j-1/2}}{\left(\Delta y_j + \Delta x_{j+1}\right)/2} = \pm R_{i,j} - G_{i,j} \tag{A.20}$$

where $J_{\mathrm{T},i,j}$ corresponds to the tunnelling current presented in Eq. (2.9).

At the interface I, j, we add the thermionic current, following Eq. (2.6). Figure A.4 shows how the current is modelled at the metal-semiconductor interface, using these definitions. Thermionic contribution has been labelled as $J_{\mathrm{th},I,j}$. Final current flowing to/from the metal contact is the sum of the thermionic component at the I, j location and all the tunnel currents coming from the different i, j locations considered, that is

$$J_{I,j} = J_{\mathrm{th},I,j} + \sum_{i=I-n}^{I} J_{\mathrm{T}i,j} \tag{A.21}$$

Note that this expression is not included in the corresponding continuity equation of the interface node I, j, only Eq. (A.19) is used, as the tunnel contribution does not flow from the I, j node. This equation only shows the current assigned to the metal at that position.

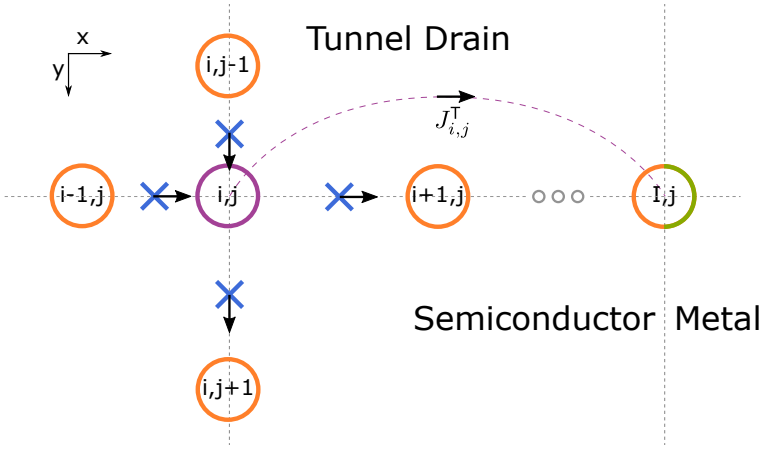

Figure A.3: Schematic of tunnel drains placed along the barrier when using the TFE model at the metal-semiconductor interface. All the currents excepting the tunnel current, labelled as $J^{T}_{i,j}$ in the picture, are evaluated using the Drift-Diffusion model. Tunnel current is drained to the closest metal node.

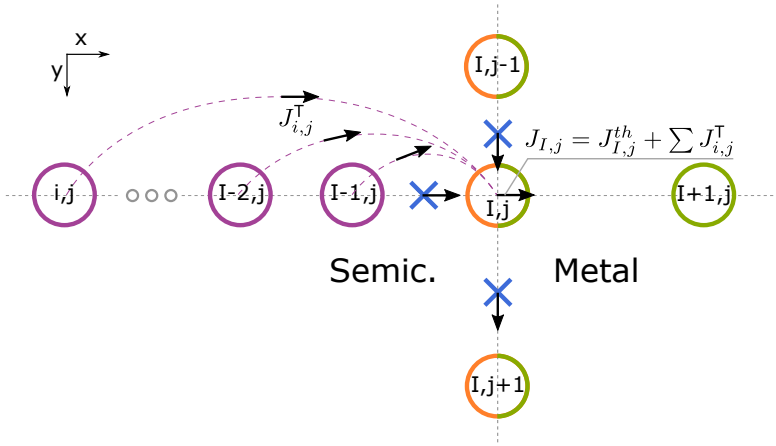

Figure A.4: Schematic of intermediate node in a metal-semiconductor junction using the TFE model. At the interface, the current that flows to the metal is the sum of the thermionic and tunnel currents in that position. The rest of the currents are evaluated using the Drift-Diffusion model.

A.4 Special conditions for corners: Kirchhoff equation

In some cases, there are nodes whose entire area is not freely crossed by the current. That is the case of the nodes at the interfaces and corners between materials. Each node can belong up to four different materials, as it is depicted in Fig. A.5. The current of each direction crosses two of these areas. However, the two regions can not be assigned to its current in all cases. For instance, when a node is an interface between an oxide and the semiconductor, the region that belongs to the oxide is not assigned to the current of the semiconductor parallel to the interface. In the same way, the current of a Schottky contact is not assigned to the region that belongs to the semiconductor. To satisfy these special conditions, the Kirchhoff equation is used [118]:

$$\sum I_{\text{in}} = \sum I_{\text{out}} \tag{A.22}$$

In the 2D discretized system, the current can be calculated by multiplying the current density with the width of the flux, that is, the width of each area, and the thickness of the device, which would correspond to the z dimension and is common for all the regions. Including the deviation caused by the net generation-recombination rate, inside the semiconductor, we obtain:

$$J_{\text{i+1/2,j}}\Delta y_{\text{R}} - J_{\text{i-1/2,j}}\Delta y_{\text{L}} + J_{\text{i,j+1/2}}\Delta x_{\text{D}} - J_{\text{i,j-1/2}}\Delta x_{\text{U}} = \pm q\left(R_{i,j} - Gi,j\right) \tag{A.23}$$

where each Δy, Δx corresponds to the length of the assigned region, and we have used the subscript L, R, U, D for left, right, up and down in the grid, respectively. In a normal node inside the semiconductor, as depicted in Fig. A.5a, $\Delta y_{\text{R}} = \Delta y_{\text{L}} = \left(\Delta y_{\text{j}} + \Delta y_{\text{j+1}}\right)/2$ and $\Delta x_{\text{D}} = \Delta x_{\text{U}} = \left(\Delta x_{\text{i}} + \Delta x_{\text{i+1}}\right)/2$, which gives the continuity equation, Eq. (A.13), Eq. (A.15) in the case of holes. However, in the case of the example in Fig. A.5b, where an oxide and a metal interface have been added, $\Delta x_{\text{D}} = \Delta x_{\text{U}} = \Delta x_{\text{i+1}}/2$ and $\Delta y_{\text{R}} = \Delta y_{\text{j+1}}/2$, as the current can not flow through the oxide, and the region assigned to the metal corresponds with the Δx_{U} width. In the Equation (A.23), the current $J_{i,j-1/2}$ would be substituted by $J_{i,j}$ using the TE model. The current that flows to the right is assigned to the semiconductor.

As we see, the current for each direction is assigned depending on the corresponding material. Each direction shares two quadrants, whose materials can be different. To

select the material priority, it is possible to follow the algorithm presented next:

- If there is a quadrant assigned to a semiconductor, the current is assigned to that semiconductor, and it only flows along the semiconductor quadrant.
- In the case of quadrants with the presence of a metal, if the other quadrant is also a metal or an oxide, the current is assigned to the metal (that is, TE or TFE models) and flows to/from the metal.
- When one quadrant is assigned to an oxide, the width of the quadrant is deleted for the current evaluation.

This algorithm lets us assign the correct quadrants for the currents in those corners where different materials surround a node.

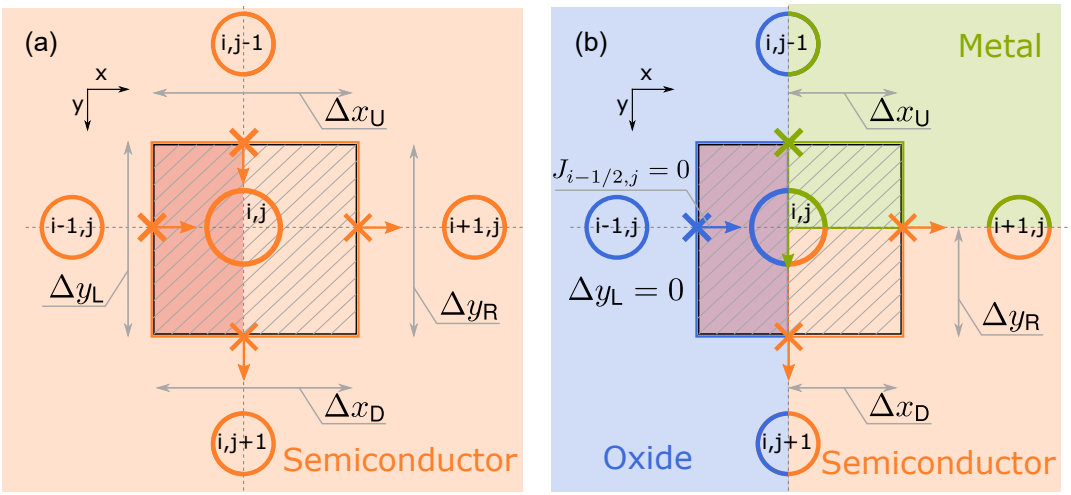

Figure A.5: Schematic of current splitting as a function of the material of each region, showing the criteria to assign the currents for metals and semiconductors. In (a), the typical case inside the semiconductor is depicted. The example in (b) includes an oxide and a metal region. The halves of the region that belong to the oxide are neglected during the currents evaluation, while the current that flows to the metal from the node i, j is assigned to the depicted Δx_U region width.

A.5 1D Schrödinger equation

For the SAMANTA-SP1D code, the Poisson equation is discretized as in the last Section. Here, let us call $\xi_{n\,i}$ the wavefunction value corresponding to the n th energy

level at the i location. In the case of the 1D Schrödinger Equation (2.42), the finite differences method is applied in this way:

$$\frac{\partial}{\partial y}\left(m_{\text{eff}}^{-1}(y)\frac{\partial}{\partial y}\xi_n(y)\right) = \frac{2}{\Delta y_i + \Delta y_{i+1}}\left[\xi_{n\,i+1}\frac{m_{\text{eff}\,i+1/2}^{-1}}{\Delta y_{i+1}} - \right. \\ \left. -\xi_{n\,i}\left(\frac{m_{\text{eff}\,i+1/2}^{-1}}{\Delta y_{i+1}} + \frac{m_{\text{eff}\,i-1/2}^{-1}}{\Delta y_i}\right) + \xi_{n\,i-1}\frac{m_{\text{eff}\,i-1/2}^{-1}}{\Delta y_i}\right] \tag{A.24}$$

The total equation in its matrix form is then

$$\begin{bmatrix} M_0 & N_0 & 0 & 0 & \cdots & 0 & 0 & 0 & 0 \\ L_1 & M_1 & N_1 & 0 & \cdots & 0 & 0 & 0 & 0 \\ 0 & L_2 & M_2 & N_2 & \cdots & 0 & 0 & 0 & 0 \\ \vdots & \vdots & \vdots & \vdots & \ddots & \vdots & \vdots & \vdots & \vdots \\ 0 & 0 & 0 & 0 & \cdots & 0 & L_{n-1} & M_{n-1} & N_{n-1} \\ 0 & 0 & 0 & 0 & \cdots & 0 & 0 & L_n & M_n \end{bmatrix} \Psi = \boldsymbol{E}\Psi \tag{A.25}$$

where Ψ and $\boldsymbol{E}$ refers to the total wavefunctions and energy levels of the system, respectively. The terms L_i, N_i and M_i are

$$L_i = \frac{m_{\text{eff}\,i-1/2}^{-1}}{\Delta y_i}\frac{2}{\Delta y_i + \Delta y_{i+1}}\frac{\hbar^2}{2} \tag{A.26a}$$

$$N_i = \frac{m_{\text{eff}\,i+1/2}^{-1}}{\Delta y_{i+1}}\frac{2}{\Delta y_{i+1} + \Delta y_{i+1}}\frac{\hbar^2}{2} \tag{A.26b}$$

$$M_i = \left(\frac{m_{\text{eff}\,i-1/2}^{-1}}{\Delta y_i} + \frac{m_{\text{eff}\,i+1/2}^{-1}}{\Delta y_{i+1}}\right)\frac{-2}{\Delta y_i + \Delta y_{i+1}}\frac{\hbar^2}{2} - \psi(y_i) + \chi_i(y_i) \tag{A.26c}$$

As can be seen in Eq. (A.26c), the main diagonal has added the values of the potential and the electron affinity. The terms M_0 and M_n are evaluated assuming Δy_0, Δy_{n+1} identical to Δy_1, Δy_n respectively.

The Schrödinger equation is solved using the Arnoldi algorithm [230], which evaluates the energy levels of the system up to a certain specified level.

Appendix B

Newton method to linearise the equations

The direct evaluation of the set of equations used in the simulator tends to converge slowly and diverges very easily unless a strong relaxation parameter between iterations is used. A common way to solve this issue consists of linearising the equations. In this way, the solver does not obtain a potential or a carrier density, but a residual part of it, which is added to the result of a previous iteration. There are many ways a system of equations can be linearised. One of the most popullars is called the Newton-Raphson method [231, 232], which is based on the Taylor series and uses the Jacobian $\mathrm{J}(\mathbf{f}(\mathbf{x}))$ matrix

$$\mathrm{J}(\mathbf{f}(\mathbf{x}))\,\delta\mathbf{x} = -\mathbf{f}(\mathbf{x}) \tag{B.1a}$$

$$\begin{bmatrix} \frac{\partial f_1}{\partial x_1} & \frac{\partial f_1}{\partial x_2} & \frac{\partial f_1}{\partial x_3} \\ \frac{\partial f_2}{\partial x_1} & \frac{\partial f_2}{\partial x_2} & \frac{\partial f_2}{\partial x_3} \\ \frac{\partial f_3}{\partial x_1} & \frac{\partial f_3}{\partial x_2} & \frac{\partial f_3}{\partial x_3} \end{bmatrix} \begin{bmatrix} \delta x_1 \\ \delta x_2 \\ \delta x_3 \end{bmatrix} = - \begin{bmatrix} f_1 \\ f_2 \\ f_3 \end{bmatrix} \tag{B.1b}$$

where $f_i(x_1, x_2, x_3...)$ are the equations, which depend on their corresponding variables x_i, and δx_i the corrections of the solution. The equations are rewritten, so they are equated to zero, that is $f_i(x_1, x_2, x_3...) = 0$ After each iteration, the solution at iteration k+1 is updated according to the scheme

$$x_i^{(k+1)} = x_i^k + \lambda \delta x_i^{(k+1)} \tag{B.2}$$

where the $\lambda \in [0, 1]$ term is a value used in the self-consistent loop, which follows a scheme similar to the one presented in [144, 145].

Another linearisation similar to this one which could has been used consists of obtaining the Hessian matrix, which is formed by the second partial derivative of each function. This method is usually faster than the Newton method used in this simulator, but its convergence can fail if the function crosses the abscissa axis, so we finally used the first derivative order to ensure the correct convergence. The Newton-Raphson method has been applied to the full set of equations of the simulator, including the generation and recombination processes. After this update, the simulator is able to converge in practically all the scenarios, using a very low number of iterations, even for very complex structures. For this model to work, an initial guess of the result is needed to improve the convergence, which is obtained from the results in equilibrium conditions. Once the algorithm has converged for the first bias value, the results are used as a starting point for the the next bias. Thus, if the bias steps are small, the simulator solves the equations in a very fast and efficient way.

B.1 Linearisation of the Poisson equation in Equilibrium

The Newton method has been applied to solve the Poisson equation in equilibrium conditions. In this situation, following the Equation (B.1), Poisson Equation (2.1) can be linearised in this way:

$$\nabla \cdot [\varepsilon (\mathbf{r}) \nabla (\psi (\mathbf{r}) + \delta\psi (\mathbf{r}))] + \rho (\mathbf{r}) + \delta\rho (\mathbf{r}) = 0 \tag{B.3}$$

where $\varepsilon (\mathbf{r})$ refers to the dielectric constant at each $\mathbf{r}$ position, $\psi (\mathbf{r})$ is the potential and $\rho (\mathbf{r}, \psi)$ the total charge density. The variables $\delta\psi (\mathbf{r})$ and $\delta\rho (\mathbf{r})$ are their corrections counterparts. Here we have omitted the potential dependence of the charge density just to simplify the notation. We can derive the charge density correction as a function of the potential to obtain a direct expression where we only evaluate this variable using the results from the last iteration (k):

$$\nabla \cdot \left[\varepsilon (\mathbf{r}) \nabla \left(\psi^{(k)} (\mathbf{r}) + \delta\psi^{(k+1)} (\mathbf{r})\right)\right] + \rho^{(k)} (\mathbf{r}) + \left.\frac{\partial\rho (\mathbf{r})}{\partial\psi}\right|^{(k)} \delta\psi^{(k+1)} (\mathbf{r}) = 0 \tag{B.4}$$

where the $^{(k)}$ and $^{(k+1)}$ superscripts stand for iterations k and $k+1$ of the algorithm, respectively.

Here we must derive the charge density Equation (2.3) seen in Section 2.2 as a function of the potential. The terms corresponding to the donor and acceptor concentrations, which depends on the impurity ionization, follow the equations [118]:

$$N_{\mathrm{D}}^{+\,(k)}(\mathbf{r}) = \frac{N_{\mathrm{D}}(\mathbf{r})}{1+\frac{n^{(k)}(\mathbf{r})}{N_{\mathrm{c}}(\mathbf{r})} g_{\mathrm{D}}(\mathbf{r}) \exp\left(\frac{E_{\mathrm{f}}(\mathbf{r})-E_{\mathrm{D}}(\mathbf{r})}{k_{\mathrm{B}}T}\right)} = \frac{N_{\mathrm{D}}(\mathbf{r})}{1+A_{\mathrm{D}}(\mathbf{r})\, n^{(k)}(\mathbf{r})} \tag{B.5a}$$

$$N_{\mathrm{A}}^{-\,(k)}(\mathbf{r}) = \frac{N_{\mathrm{A}}(\mathbf{r})}{1+\frac{p^{(k)}(\mathbf{r})}{N_{\mathrm{v}}(\mathbf{r})} g_{\mathrm{A}}(\mathbf{r}) \exp\left(\frac{E_{\mathrm{A}}(\mathbf{r})-E_{\mathrm{f}}(\mathbf{r})}{k_{\mathrm{B}}T}\right)} = \frac{N_{\mathrm{A}}(\mathbf{r})}{1+A_{\mathrm{A}}(\mathbf{r})\, p^{(k)}(\mathbf{r})} \tag{B.5b}$$

where the terms which do not depend on the electric potential nor the electron and hole densities have been grouped in A_{D} and A_{A} for the sake of simplicity. The $g_{\mathrm{D}}(\mathbf{r})$ ($g_{\mathrm{A}}(\mathbf{r})$) and the $E_{\mathrm{D}}(\mathbf{r})$ ($E_{\mathrm{A}}(\mathbf{r})$) terms are the ground-state degeneracy and impurity energy level of the donor (acceptor) impurities, respectively.

Fermi statistics are used to relate the potential with the electron and hole densities. The expressions for $n(\mathbf{r})$ and $p(\mathbf{r})$ can be seen in Equations (2.21), referred as $n_0(\mathbf{r},\psi)$ and $p_0(\mathbf{r},\psi)$, respectively. If we derive Equation (2.3), we obtain:

$$\left.\frac{\partial \rho(\mathbf{r})}{\partial \psi}\right|_{(k)} = \frac{q}{k_{\mathrm{B}}T}\left(-\frac{N_{\mathrm{D}}^{+\,(k)}(\mathbf{r})\, N_{\mathrm{c}}(\mathbf{r})\, \mathcal{F}_{-1/2}\left(\eta_{\mathrm{c}}^{(k)}(\mathbf{r})\right) A_{\mathrm{D}}(\mathbf{r})}{1+A_D(\mathbf{r})\, n^{(k)}(\mathbf{r})} - N_{\mathrm{c}}(\mathbf{r})\, \mathcal{F}_{-1/2}\left(\eta_{\mathrm{c}}^{(k)}(\mathbf{r})\right) - \right.$$
$$\left. - \frac{N_A^{-\,(k)}(\mathbf{r})\, N_{\mathrm{v}}(\mathbf{r})\, \mathcal{F}_{-1/2}\left(\eta_{\mathrm{v}}^{(k)}(\mathbf{r})\right) A_A(\mathbf{r})}{1+A_A(\mathbf{r})\, p^{(k)}(\mathbf{r})} - N_{\mathrm{v}}(\mathbf{r})\, \mathcal{F}_{-1/2}\left(\eta_{\mathrm{v}}^{(k)}(\mathbf{r})\right)\right) \tag{B.6}$$

where we have omitted the evaluation of the derivative of the traps, as their change between iterations tends to be low enough it has no effect on the convergence.

As we have seen, the electrostatic equations used in equilibrium conditions can be linearised using Equations (B.4) and (B.6). After that, they are implemented in the simulator using the finite differences discretization method. The procedure is similar to the one explained in Appendix A. The full discretized and linearised Poisson equation is the sum of Eq. (A.7), which would correspond to the terms of the last iteration k,

and the following correction terms:

$$\begin{aligned}\nabla\cdot\varepsilon\left(x_i,y_j\right)\nabla\delta\psi^{(k+1)}\left(x_i,y_j\right) = \frac{2}{\Delta x_{i+1}+\Delta x_i}\Bigg[&\frac{\delta\psi_{i+1,j}^{(k+1)}\varepsilon_{\mathrm{xx}\,i+1/2,j}}{\Delta x_{i+1}} - \\ &- \delta\psi_{i,j}^{(k+1)}\left(\frac{\varepsilon_{\mathrm{xx}\,i+1/2,j}}{\Delta x_{i+1}}+\frac{\varepsilon_{\mathrm{xx}\,i-1/2,j}}{\Delta x_i}\right)+\frac{\delta\psi_{i-1,j}^{(k+1)}\varepsilon_{\mathrm{xx}\,i-1/2,j}}{\Delta x_i}\Bigg]+ \\ &+\frac{2}{\Delta y_{j+1}+\Delta y_j}\Bigg[\frac{\delta\psi_{i,j+1}^{(k+1)}\varepsilon_{\mathrm{yy}\,i,j+1/2}}{\Delta y_{j+1}} - \\ &- \delta\psi_{i,j}^{(k+1)}\left(\frac{\varepsilon_{\mathrm{yy}\,i,j+1/2}}{\Delta y_{j+1}}+\frac{\varepsilon_{\mathrm{yy}\,i,j-1/2}}{\Delta y_j}\right)+\frac{\delta\psi_{i,j-1/2}^{(k+1)}\varepsilon_{\mathrm{yy}\,i,j-1/2}}{\Delta y_j}\Bigg]\end{aligned} \tag{B.7a}$$

$$\begin{aligned}\delta\rho\left(x_i,y_j\right) = \frac{q\delta\psi_{i,j}^{(k+1)}}{k_{\mathrm{B}}T}\Bigg(&-\frac{N_{\mathrm{D}\,i,j}^{+\,(k)}N_{\mathrm{c}\,i,j}\mathcal{F}_{-1/2}\left(\eta_{\mathrm{c\ i,j}}^{(k)}\right)A_{\mathrm{D}\,i,j}}{1+A_{\mathrm{D}\,i,j}n_{i,j}^{(k)}} - N_{\mathrm{c}\,i,j}\mathcal{F}_{-1/2}\left(\eta_{\mathrm{c}\,i,j}^{(k)}\right) - \\ &-\frac{N_{\mathrm{A}\,i,j}^{-\,(k)}N_{\mathrm{v}\,i,j}\mathcal{F}_{-1/2}\left(\eta_{\mathrm{v}\,i,j}^{(k)}\right)A_{\mathrm{A}\,i,j}}{1+A_{\mathrm{A}\,i,j}p_{i,j}^{(k)}} - N_{\mathrm{v}\,i,j}\mathcal{F}_{-1/2}\left(\eta_{\mathrm{v}\,i,j}^{(k)}\right)\Bigg)\end{aligned} \tag{B.7b}$$

So the full linearised and discretized equation for Poisson in equilibrium conditions is:

$$\mathcal{P}^{(k)}\left(x_i,y_j,\psi\right)+\nabla\cdot\varepsilon\left(x_i,y_j\right)\nabla\delta\psi^{(k+1)}\left(x_i,y_j\right)+\delta\rho\left(x_i,y_j\right)=0 \tag{B.8}$$

This is a simplified way of using the Newton method, where electron and hole densities are not linearised. Despite this, this method has been proved to be faster and more stable than using the Poisson equation directly.

B.2 Linearisation of the Poisson-Continuity equations

In this case, all the equations involved have been adapted to use the Newton method. The total system considers the Poisson and the continuity equations in one only matrix, where all the variables are updated at the same time. This way, the convergence is improved. The linearisation is specially useful when applied to the continuity equations, given their non-linear dependence with the potential.

As we defined in the previous Appendix, let us call $\mathcal{P}(\mathbf{r}, \psi, n, p)$ the Poisson equation, grouped all the terms in one side of the equation (that is, displacing the charge density in Eq. (2.1) to the left hand side of the equation), so that $P(\psi, n, p) = 0$. Similarly, let $\mathcal{W}_{\mathrm{n}}(\mathbf{r}, \psi, n)$ and $\mathcal{W}_{\mathrm{p}}(\mathbf{r}, \psi, p)$ be the continuity equations for electrons and holes, respectively, seen in Eq. (2.4), neglecting the temporal partial derivatives. By applying the Newton method seen in Eq. (B.1), we get the following system:

$$\begin{bmatrix} \frac{\partial \mathcal{P}}{\partial \psi} & \frac{\partial \mathcal{P}}{\partial n} & \frac{\partial \mathcal{P}}{\partial p} \\ \frac{\partial \mathcal{W}_{\mathrm{n}}}{\partial \psi} & \frac{\partial \mathcal{W}_{\mathrm{n}}}{\partial n} & \frac{\partial \mathcal{W}_{\mathrm{n}}}{\partial p} \\ \frac{\partial \mathcal{W}_{\mathrm{p}}}{\partial \psi} & \frac{\partial \mathcal{W}_{\mathrm{p}}}{\partial n} & \frac{\partial \mathcal{W}_{\mathrm{p}}}{\partial p} \end{bmatrix} \begin{bmatrix} \delta\psi^{(k+1)} \\ \delta n^{(k+1)} \\ \delta p^{(k+1)} \end{bmatrix} = - \begin{bmatrix} \mathcal{P}^{(k)} \\ \mathcal{W}_{\mathrm{n}}^{(k)} \\ \mathcal{W}_{\mathrm{p}}^{(k)} \end{bmatrix} \tag{B.9}$$

To implement this procedure, we must derive each of the equations by their corresponding variables (ψ, n and p). The resultant system is three times larger than the corresponding to the direct equations, although the matrices hold their sparsity. To solve this system, the Jacobian matrix must be inverted, what in large device structures requires a large time to evaluate. Despite this fact, the number of iterations required to converge is much lower, compensating the extra processing time for each iteration.

Let us start with the Poisson equation. To make the notation easier, we can rewrite it as:

$$\mathcal{P}(\mathbf{r}, \psi, n, p) = \mathcal{L}\psi(\mathbf{r}) + \rho(\mathbf{r}) = 0 \tag{B.10}$$

where $\mathcal{L}$ is the $\nabla\varepsilon\nabla$ operator. We can numerically linearise the equation following the Newton method seen in Eq. (B.1). So the first row of the matrices operation presented in Eq. (B.9) is

$$\mathcal{L}\left(\psi^{(k)}(\mathbf{r}) + \delta\psi^{(k+1)}(\mathbf{r})\right) + \rho^{(k)}(\mathbf{r}) + \delta\rho^{(k+1)}(\mathbf{r}) = 0 \tag{B.11}$$

where $\psi^{(k)}(\mathbf{r})$ and $\rho^{(k)}(\mathbf{r})$ are the potential and charge density of the previous iteration, and $\delta\psi^{(k+1)}(\mathbf{r})$ and $\delta\rho^{(k+1)}(\mathbf{r})$ are the calculated corrections added to the potential and the charge density, respectively. Once linearised and discretized, the $\mathcal{L}$ operator is applied to the correction term of the potential as in Eq. (B.7a), and the corresponding term for the charge density is:

$$\delta\rho^{(k+1)}\left(x_i, y_j\right) = q\left(-\delta n_{i,j}^{(k+1)} + \delta p_{i,j}^{(k+1)} + \delta {N_{\mathrm{D}}^{+}}_{i,j}^{(k+1)} - \delta {N_{\mathrm{A}}^{-}}_{i,j}^{(k+1)} + \delta N_{\mathrm{T}\,i,j}\right) \tag{B.12}$$

where the terms for the ionized impurities are given by the expressions

$$\delta {N_{\mathrm{D}}^{+}}_{i,j}^{(k+1)} = -\frac{{N_{\mathrm{D}}^{+}}_{i,j}^{(k)} n_{i,j}{}^{(k)} + \frac{1}{A_{\mathrm{D}\,i,j}}}{\delta} n_{i,j}^{(k+1)} \tag{B.13a}$$

$$\delta {N_{\mathrm{A}}^{+}}_{i,j}^{(k+1)} = -\frac{{N_{\mathrm{A}}^{-}}_{i,j}^{(k)} p_{i,j}{}^{(k)} + \frac{1}{A_{\mathrm{A}\,i,j}}}{\delta} p_{i,j}^{(k+1)} \tag{B.13b}$$

and the term associated with the trap density is evaluated as shown in Section B.3.9. The terms shown in Eq. (B.7a) and (B.12) are added to Eq. (A.7), resulting in the full discretized and linearised Poisson equation in non-equilibrium conditions, that is:

$$\mathcal{P}_{i,j}^{(k)}\left(\psi, n, p\right) + \mathcal{L}\delta\psi_{i,j}^{(k+1)} + \delta\rho_{i,j}^{(k+1)} = 0 \tag{B.14}$$

In a similar procedure, the continuity equations for electrons and holes can be linearised. The second and third rows of Eq. (B.9) are:

$$\nabla\left(\boldsymbol{J}_{\mathrm{n}}^{(k)}\left(\mathbf{r}\right) + \delta\boldsymbol{J}_{\mathrm{n}}^{(k+1)}\left(\mathbf{r}\right)\right) + G_{\mathrm{n}}^{(k)}\left(\mathbf{r}\right) - R_{\mathrm{n}}^{(k)}\left(\mathbf{r}\right) + \delta G_{\mathrm{n}}^{(k+1)}\left(\mathbf{r}\right) - \delta R_{\mathrm{n}}^{(k+1)}\left(\mathbf{r}\right) = 0 \tag{B.15a}$$

$$\nabla\left(\boldsymbol{J}_{\mathrm{p}}^{(k)}\left(\mathbf{r}\right) + \delta\boldsymbol{J}_{\mathrm{p}}^{(k+1)}\left(\mathbf{r}\right)\right) - G_{\mathrm{p}}^{(k)}\left(\mathbf{r}\right) + R_{\mathrm{p}}^{(k)}\left(\mathbf{r}\right) - \delta G_{\mathrm{p}}^{(k+1)}\left(\mathbf{r}\right) + \delta R_{\mathrm{p}}^{(k+1)}\left(\mathbf{r}\right) = 0 \tag{B.15b}$$

where the $\delta G^{(k+1)}\left(\mathbf{r}\right)$ and $\delta R^{(k+1)}\left(\mathbf{r}\right)$ terms include all the generation and recombination correction terms, which we study in the following Sections.

Let us start by focusing on the electron current density. The spatial derivative of $\boldsymbol{J}_{\mathrm{n}}^{(k)}\left(\mathbf{r}\right)$ can be evaluated hastily, following the procedure described in Appendix A.2. In the case of $\delta\boldsymbol{J}_{\mathrm{n}}^{(k+1)}\left(\mathbf{r}\right)$, the expression is split into four parts, which are each of the derivative terms, $\delta J_{\mathrm{n},i\pm1/2,j\pm1/2}$, obtained from applying Eq. (A.8) in the two directions x and y. If for one or more directions the currents are TE or TFE, their evaluations are substituted by the corresponding term. Focusing on the x direction, the equations

corresponding to the Drift-Diffusion core are:

$$\begin{aligned}\delta J^{(k+1)}_{\mathrm{n},i,j+1/2} =& \frac{q k_\mathrm{B} T \mu_{\mathrm{n},i,j+1/2}}{\Delta y_{j+1}} \left[\delta n^{(k+1)}_{i,j+1} B\left(\Gamma^{(k)}_{\mathrm{V}\,j+1}\right) - \delta n^{(k+1)}_{i,j} B\left(-\Gamma^{(k)}_{\mathrm{V}\,j+1}\right) + \right. \\ &\left. + \left(n^{(k)}_{i,j+1} B'\left(\Gamma^{(k)}_{\mathrm{V}\,j+1}\right) + n^{(k)}_{i,j} B'\left(-\Gamma^{(k)}_{\mathrm{V}\,j+1}\right)\right) \delta\Gamma^{(k+1)}_{\mathrm{V}\,j+1}\right]\end{aligned} \tag{B.16a}$$

$$\begin{aligned}\delta J_{\mathrm{n},i,j-1/2} =& \frac{q k_\mathrm{B} T \mu_{\mathrm{n},i,j-1/2}}{\Delta y_{j}} \left[\delta n^{(k+1)}_{i,j} B\left(\Gamma^{(k)}_{\mathrm{V}\,j}\right) - \delta n^{(k+1)}_{i,j-1} B\left(-\Gamma^{(k)}_{\mathrm{V}\,j}\right) + \right. \\ &\left. + \left(n^{(k)}_{i,j} B'\left(\Gamma^{(k)}_{\mathrm{V}\,j}\right) + n^{(k)}_{i,j-1} B'\left(-\Gamma^{(k)}_{\mathrm{V}\,j}\right)\right) \delta\Gamma^{(k+1)}_{\mathrm{V}\,j}\right]\end{aligned} \tag{B.16b}$$

where $B'(x)$ is the derivative of the Bernoulli function, given by:

$$B'(x) = \frac{e^x (1-x) - 1}{(e^x - 1)^2} \tag{B.17}$$

$\Gamma^{(k)}_{\mathrm{V}\,j}$ and $\Gamma^{(k)}_{\mathrm{H}\,i}$ are the normalized potential difference

$$\Gamma^{(k)}_{\mathrm{V}\,j} = \frac{\psi^{(k)}_{i,j} - \psi^{(k)}_{i,j-1}}{k_\mathrm{B} T} \quad \text{and} \quad \Gamma^{(k)}_{\mathrm{H}\,i} = \frac{\psi^{(k)}_{i,j} - \psi^{(k)}_{i-1,j}}{k_\mathrm{B} T} \tag{B.18}$$

and $\delta\Gamma^{(k+1)}_{\mathrm{V}\,j}$ and $\delta\Gamma^{(k+1)}_{\mathrm{H}\,i}$ are the correction terms for the potential difference:

$$\delta\Gamma^{(k+1)}_{\mathrm{V}\,j} = \frac{\delta\psi^{(k+1)}_{i,j} - \delta\psi^{(k+1)}_{i,j-1}}{k_\mathrm{B} T} \quad \text{and} \quad \delta\Gamma^{(k+1)}_{\mathrm{H}\,i} = \frac{\delta\psi^{(k+1)}_{i,j} - \delta\psi^{(k+1)}_{i-1,j}}{k_\mathrm{B} T} \tag{B.19}$$

Similar equations are obtained for the y direction. In the case of the continuity equation for holes, the obtained linearisation and discretization of the horizontal current density terms is:

$$\begin{aligned}\delta J^{(k+1)}_{\mathrm{p},i,j+1/2} =& \frac{q k_\mathrm{B} T \mu_{\mathrm{p},i,j+1/2}}{\Delta y_{j+1}} \left[\delta p^{(k+1)}_{i,j+1} B\left(-\Gamma^{(k)}_{\mathrm{V}\,j+1}\right) - \delta p^{(k+1)}_{i,j} B\left(\Gamma^{(k)}_{\mathrm{V}\,j+1}\right) - \right. \\ &\left. - \left(p^{(k)}_{i,j+1} B'\left(-\Gamma^{(k)}_{\mathrm{V}\,j+1}\right) + p^{(k)}_{i,j} B'\left(\Gamma^{(k)}_{\mathrm{V}\,j+1}\right)\right) \delta\Gamma^{(k+1)}_{\mathrm{V}\,j+1}\right]\end{aligned} \tag{B.20a}$$

$$\begin{aligned}\delta J^{(k+1)}_{\mathrm{p},i,j-1/2} =& \frac{q k_\mathrm{B} T \mu_{\mathrm{p},i,j-1/2}}{\Delta y_{j}} \left[\delta p^{(k+1)}_{i,j} B\left(-\Gamma^{(k)}_{\mathrm{V}\,j}\right) - \delta p^{(k+1)}_{i,j-1} B\left(\Gamma^{(k)}_{\mathrm{V}\,j}\right) - \right. \\ &\left. - \left(p^{(k)}_{i,j} B'\left(-\Gamma^{(k)}_{\mathrm{V}\,j}\right) + p^{(k)}_{i,j-1} B'\left(\Gamma^{(k)}_{\mathrm{V}\,j}\right)\right) \delta\Gamma^{(k+1)}_{\mathrm{V}\,j}\right]\end{aligned} \tag{B.20b}$$

Finally, for the full discretized and linearised electron continuity equation, we follow the Eq. (B.15), and add the correction terms to Eq. (A.13). Here we only include the full correction term corresponding to the current density. The correction terms assigned to the generation and recombination rates are explained in the following Sections. The correction terms for the electron continuity equations are:

$$-\delta R_{\mathrm{n},i,j}^{(k+1)}+\delta G_{\mathrm{n},i,j}^{(k+1)}=-\sum_{r}\delta R_{\mathrm{n},r,i,j}^{(k+1)}+\sum_{s}\delta G_{\mathrm{n},s,i,j}^{(k+1)}+\sum_{t}\delta U_{\mathrm{n},t,i,j}^{(k+1)} \tag{B.21a}$$

$$\begin{aligned}
\nabla\delta\boldsymbol{J}_{\mathrm{n},i,j}^{(k+1)} = \frac{2}{\Delta x_i+\Delta x_{i+1}}\Bigg[&\delta n_{i-1,j}^{(k+1)}B\left(-\Gamma_{\mathrm{H}\,i}^{(k)}\right)\frac{k_{\mathrm{B}}T\mu_{\mathrm{n},i-1/2,j}}{\Delta x_i}-\\
&-\delta n_{i,j}^{(k+1)}\left[B\left(-\Gamma_{\mathrm{H}\,i+1}^{(k)}\right)\frac{k_{\mathrm{B}}T\mu_{\mathrm{n},i+1/2,j}}{\Delta x_{i+1}}+B\left(\Gamma_{\mathrm{H}\,i}^{(k)}\right)\frac{k_{\mathrm{B}}T\mu_{\mathrm{n},i-1/2,j}}{\Delta x_i}\right]+\\
&+\delta n_{i+1,j}^{(k+1)}B\left(\Gamma_{\mathrm{H}\,i+1}^{(k)}\right)\frac{k_{\mathrm{B}}T\mu_{\mathrm{n},i+1/2,j}}{\Delta x_{i+1}}+\\
&+\left(n_{i+1,j}^{(k)}B'\left(\Gamma_{\mathrm{H}\,i+1}^{(k)}\right)+n_{i,j}^{(k)}B'\left(-\Gamma_{\mathrm{H}\,i+1}^{(k)}\right)\right)\delta\Gamma_{\mathrm{H}\,i+1}^{(k+1)}\frac{qk_{\mathrm{B}}T\mu_{\mathrm{n},i+1/2,j}}{\Delta x_{i+1}}-\\
&-\left(n_{i,j}^{(k)}B'\left(\Gamma_{\mathrm{H}\,i}^{(k)}\right)+n_{i-1,j}^{(k)}B'\left(-\Gamma_{\mathrm{H}\,i}^{(k)}\right)\right)\delta\Gamma_{\mathrm{H}\,i}^{(k+1)}\frac{qk_{\mathrm{B}}T\mu_{\mathrm{n},i-1/2,j}}{\Delta x_i}\Bigg]+\\
&+\frac{2}{\Delta y_j+\Delta y_{j+1}}\Bigg[\delta n_{i,j-1}^{(k+1)}B\left(-\Gamma_{\mathrm{V}\,j}^{(k)}\right)\frac{k_{\mathrm{B}}T\mu_{\mathrm{n},i,j-1/2}}{\Delta y_j}-\\
&-\delta n_{i,j}^{(k+1)}\left[B\left(-\Gamma_{\mathrm{V}\,j+1}^{(k)}\right)\frac{k_{\mathrm{B}}T\mu_{\mathrm{n},i,j+1/2}}{\Delta y_{j+1}}+B\left(\Gamma_{\mathrm{V}\,j}^{(k)}\right)\frac{k_{\mathrm{B}}T\mu_{\mathrm{n},i,j-1/2}}{\Delta y_j}\right]+\\
&+\delta n_{i,j+1}^{(k+1)}B\left(\Gamma_{\mathrm{V}\,j+1}^{(k)}\right)\frac{k_{\mathrm{B}}T\mu_{\mathrm{n},i,j+1/2}}{\Delta y_{j+1}}+\\
&+\left(n_{i,j+1}^{(k)}B'\left(\Gamma_{\mathrm{V}\,j+1}^{(k)}\right)+n_{i,j}^{(k)}B'\left(-\Gamma_{\mathrm{V}\,j+1}^{(k)}\right)\right)\delta\Gamma_{\mathrm{V}\,j+1}^{(k+1)}\frac{qk_{\mathrm{B}}T\mu_{\mathrm{n},i,j+1/2}}{\Delta y_{j+1}}-\\
&-\left(n_{i,j}^{(k)}B'\left(\Gamma_{\mathrm{V}\,j}^{(k)}\right)+n_{i,j-1}^{(k)}B'\left(-\Gamma_{\mathrm{V}\,j}^{(k)}\right)\right)\delta\Gamma_{\mathrm{V}\,j}^{(k+1)}\frac{qk_{\mathrm{B}}T\mu_{\mathrm{n},i,j-1/2}}{\Delta y_j}\Bigg]
\end{aligned} \tag{B.21b}$$

where the r, s, t subscripts refers to the different generation and recombination mechanisms, and $U_{\mathrm{n},t,i,j}$ corresponds to the generation-recombination mechanisms. Finally, the full linearised and discretized electron continuity equation is formed by Eq. (A.15) evaluated with the results obtained in the iteration k and the equations (B.21), giving:

$$\mathcal{W}^{(k)}_{\mathrm{n},i,j}(\psi,n)+\nabla\delta\boldsymbol{J}^{(k+1)}_{\mathrm{n},i,j}-\delta R^{(k+1)}_{\mathrm{n},i,j}+\delta G^{(k+1)}_{\mathrm{n},i,j}=0 \tag{B.22}$$

Similarly, for the full continuity equation for holes, following the Eq. (B.15), the next terms are included to Eq. (A.15):

$$\delta R^{(k+1)}_{\mathrm{p},i,j}-\delta G^{(k+1)}_{\mathrm{p},i,j}=\sum_r \delta R^{(k+1)}_{\mathrm{p},r,i,j}-\sum_s \delta G^{(k+1)}_{\mathrm{p},s,i,j}-\sum_t \delta U^{(k+1)}_{\mathrm{p},t\,i,j} \tag{B.23a}$$

$$\begin{aligned}
\nabla\delta\boldsymbol{J}^{(k+1)}_{\mathrm{p},i,j}=\frac{2}{\Delta x_i+\Delta x_{i+1}}\Bigg[&\delta p^{(k+1)}_{i-1,j}B\left(\Gamma^{(k)}_{\mathrm{H}\,i}\right)\frac{k_\mathrm{B}T\mu_{\mathrm{p},i-1/2,j}}{\Delta x_i}-\\
&-\delta p^{(k+1)}_{i,j}\left[B\left(\Gamma^{(k)}_{\mathrm{H}\,i+1}\right)\frac{k_\mathrm{B}T\mu_{\mathrm{p},i+1/2,j}}{\Delta x_{i+1}}+B\left(-\Gamma^{(k)}_{\mathrm{H}\,i}\right)\frac{k_\mathrm{B}T\mu_{\mathrm{p},i-1/2,j}}{\Delta x_i}\right]+\\
&+\delta p^{(k+1)}_{i+1,j}B\left(-\Gamma^{(k)}_{\mathrm{H}\,i+1}\right)\frac{k_\mathrm{B}T\mu_{\mathrm{p},i+1/2,j}}{\Delta x_{i+1}}-\\
&-\left(p^{(k)}_{i+1,j}B'\left(-\Gamma^{(k)}_{\mathrm{H}\,i+1}\right)+p^{(k)}_{i,j}B'\left(\Gamma^{(k)}_{\mathrm{H}\,i+1}\right)\right)\delta\Gamma^{(k+1)}_{\mathrm{H}\,i+1}\frac{qk_\mathrm{B}T\mu_{\mathrm{p},i+1/2,j}}{\Delta x_{i+1}}+\\
&+\left(p^{(k)}_{i,j}B'\left(-\Gamma^{(k)}_{\mathrm{H}\,i}\right)+p^{(k)}_{i-1,j}B'\left(\Gamma^{(k)}_{\mathrm{H}\,i}\right)\right)\delta\Gamma^{(k+1)}_{\mathrm{H}\,i}\frac{qk_\mathrm{B}T\mu_{\mathrm{p},i-1/2,j}}{\Delta x_i}\Bigg]+\\
+\frac{2}{\Delta y_j+\Delta y_{j+1}}\Bigg[&\delta p^{(k+1)}_{i,j-1}B\left(\Gamma^{(k)}_{\mathrm{V}\,j}\right)\frac{k_\mathrm{B}T\mu_{\mathrm{p},i,j-1/2}}{\Delta y_j}-\\
&-\delta p^{(k+1)}_{i,j}\left[B\left(\Gamma^{(k)}_{\mathrm{V}\,j+1}\right)\frac{k_\mathrm{B}T\mu_{\mathrm{p},i,j+1/2}}{\Delta y_{j+1}}+B\left(-\Gamma^{(k)}_{\mathrm{V}\,j}\right)\frac{k_\mathrm{B}T\mu_{\mathrm{p},i,j-1/2}}{\Delta y_j}\right]+\\
&+\delta p^{(k+1)}_{i,j+1}B\left(-\Gamma^{(k)}_{\mathrm{V}\,j+1}\right)\frac{k_\mathrm{B}T\mu_{\mathrm{p},i,j+1/2}}{\Delta y_{j+1}}-\\
&-\left(p^{(k)}_{i,j+1}B'\left(-\Gamma^{(k)}_{\mathrm{V}\,j+1}\right)+p^{(k)}_{i,j}B'\left(\Gamma^{(k)}_{\mathrm{V}\,j+1}\right)\right)\delta\Gamma^{(k+1)}_{\mathrm{V}\,j+1}\frac{qk_\mathrm{B}T\mu_{\mathrm{p},i,j+1/2}}{\Delta y_{j+1}}+\\
&+\left(p^{(k)}_{i,j}B'\left(-\Gamma^{(k)}_{\mathrm{V}\,j}\right)+p^{(k)}_{i,j-1}B'\left(\Gamma^{(k)}_{\mathrm{V}\,j}\right)\right)\delta\Gamma^{(k+1)}_{\mathrm{V}\,j}\frac{qk_\mathrm{B}T\mu_{\mathrm{p},i,j-1/2}}{\Delta y_j}\Bigg]
\end{aligned} \tag{B.23b}$$

where the superscripts r, s and t have the same meaning than for electrons. Thus, the final continuity equation for holes is formed by the term from Eq. (A.15) evaluated with the results from iteration k and the Equations (B.23b):

$$\mathcal{W}^{(k)}_{\mathrm{p},i,j}(\psi,p)+\nabla\delta\boldsymbol{J}^{(k+1)}_{\mathrm{p},i,j}+\delta R^{(k+1)}_{\mathrm{p},i,j}-\delta G^{(k+1)}_{\mathrm{p},i,j}=0 \tag{B.24}$$

B.3 Other correction terms

As we did with the Poisson and continuity equations, the rest of models explained in Chapter 2 have also been linearised. The following points describe the final equations applied in the simulator for the contact models, heterostructures and the considered generation and recombination rates.

In the case of the generation and recombination terms, they are added up and conform the total correction term for the rates seen in Eqs. (B.21a) and (B.23a).

B.3.1 Thermionic model for Schottky contacts

As explained in Section 2.3, the current density term at the ($\mathbf{r}_\mathrm{I}$) interface positions is substituted by the TE current definition. In the same way, its corresponding correction term is substituted in Eq. (B.15). Here we modify the spatial derivative as explained in Section A.3 to correctly evaluate the change of the widths due to the shift of the position of the current evaluation from the seminode to the node. Let us consider a discretized point, belonging to the interface positions, $i,j \in \mathbf{r}_\mathrm{I}$. The discretized and linearised term assigned to the TE model can be evaluated as

$$\delta J_{\mathrm{n},i,j}^{(k+1)}(n) = -q v_{\mathrm{th}\,i,j}^{\mathrm{n}} \delta n_{i,j}^{(k+1)} \tag{B.25a}$$

$$\delta J_{\mathrm{p},i,j}^{(k+1)}(p) = q v_{\mathrm{th}\,,i,j}^{\mathrm{p}} \delta p_{i,j}^{(k+1)} \tag{B.25b}$$

for electron and hole current densities, respectively. They substitute the current component in the corresponding direction in Eq. (B.22) and (B.24).

B.3.2 TFE in metal-semiconductor junctions

In metal-semiconductors junctions, the tunnel contributions are distributed. In this case, the Newton linearisation has been simplified, as the tunnel contribution is considered as a constant, as this value slightly change between iterations. In this case, for a position $i,j \in \mathbf{r}_\mathrm{B}$, where $\mathbf{r}_\mathrm{B}$ refers to the positions of the barrier in which tunnel is evaluated, the following term for electrons is added

$$\delta J_{\mathrm{n},i,j}^{(k+1)}(\psi,n) = -q v_{\mathrm{th}\,i,j}^{\mathrm{n}} \gamma_{\mathrm{n}\,i,j} N_{\mathrm{c}\,i,j} \left(\delta f_{\mathrm{s},i,j}^{\mathrm{n}}{}^{(k+1)} - \delta f_{\mathrm{m}\,i,j}^{\mathrm{n}}{}^{(k+1)} \right) \tag{B.26}$$

where the correction terms of the occupation functions are evaluated as

$$\delta {f_{\mathrm{s}}^{\mathrm{n}}}_{i,j}^{(k+1)} = \frac{\exp\left(-\mathcal{F}_{1/2}^{-1}\left(\frac{n_{i,j}^{(k)}}{N_{\mathrm{c}\,i,j}}\right)\frac{1}{N_{\mathrm{c}\,i,j}}\frac{\mathrm{d}\mathcal{F}_{1/2}^{-1}\left(\frac{n_{i,j}^{(k)}}{N_{\mathrm{c}\,i,j}}\right)}{\mathrm{d}(n/N_{\mathrm{c}})}\right)}{\left[1+\exp\left(-\mathcal{F}_{1/2}^{-1}\left(\frac{n_{i,j}^{(k)}}{N_{\mathrm{c}\,i,j}}\right)\right)\right]^2}\delta n_{i,j}^{(k+1)} \tag{B.27a}$$

$$\delta {f_{\mathrm{m}}^{\mathrm{n}}}_{i,j}^{(k+1)} = \frac{\exp\left(\frac{V_{\mathrm{bi}\,i,j}-\psi_{i,j}^{(k)}}{k_{\mathrm{B}}T}\right)\frac{1}{k_{\mathrm{B}}T}}{\left(1+\exp\left(\frac{V_{\mathrm{bi}\,i,j}-\psi_{i,j}^{(k)}}{k_{\mathrm{B}}T}\right)\right)^2}\delta\psi_{i,j}^{(k+1)} \tag{B.27b}$$

where V_{bi} is the built-in potential, and the derivative of the inverse operator of the Fermi function is approximated as:

$$\frac{\mathrm{d}\mathcal{F}^{-1}(u)}{\mathrm{d}u} = \frac{1-u^2\left(1+2\ln(u)\right)}{u\left(1-u^2\right)^2} + \frac{\left(\frac{3\sqrt{\pi}}{4}u\right)^{-1/3}\frac{\sqrt{\pi}}{2}}{\mathrm{A}^2}\left(\mathrm{A}+2.16\mathrm{B}\left(\mathrm{A}-1\right)^{3/2}\right) \tag{B.28}$$

with $\mathrm{A} = 1+\left[0.24+1.08\left(3\sqrt{\pi}u/4\right)^{2/3}\right]^{-2}$ and $\mathrm{B} = \left(3\sqrt{\pi}u/4\right)^{2/3}$, respectively.

The treatment for holes is very similar:

$$\delta {J_{\mathrm{p}}}_{,i,j}^{(k+1)}(\psi,p) = q v_{\mathrm{th}\,i,j}^{\mathrm{p}}\gamma_{\mathrm{p}\,i,j}N_{\mathrm{v}\,i,j}\left(\delta {f_{\mathrm{m}}^{\mathrm{p}}}_{i,j}^{(k+1)} - \delta {f_{\mathrm{s}}^{\mathrm{p}}}_{i,j}^{(k+1)}\right) \tag{B.29}$$

and the corresponding correction terms given by:

$$\delta {f_{\mathrm{s}}^{\mathrm{p}}}_{i,j}^{(k+1)} = \frac{\exp\left(\mathcal{F}_{1/2}^{-1}\left(\frac{p_{i,j}^{(k)}}{N_{\mathrm{v}\,i,j}}\right)\frac{1}{N_{\mathrm{v}\,i,j}}\frac{\mathrm{d}\mathcal{F}_{1/2}^{-1}\left(\frac{p_{i,j}^{(k)}}{N_{\mathrm{v}\,i,j}}\right)}{\mathrm{d}(p/N_{\mathrm{v}})}\right)}{\left[1+\exp\left(-\mathcal{F}_{1/2}^{-1}\left(\frac{p_{i,j}^{(k)}}{N_{\mathrm{v}\,i,j}}\right)\right)\right]^2}\delta p_{i,j}^{(k+1)} \tag{B.30a}$$

$$\delta {f_{\mathrm{m}}^{\mathrm{p}}}_{i,j}^{(k+1)} = \frac{\exp\left(\frac{V_{\mathrm{bi}\,i,j}-\psi_{i,j}^{(k)}-E_{\mathrm{g}\,i,j}}{k_{\mathrm{B}}T}\right)\frac{1}{k_{\mathrm{B}}T}}{\left(1+\exp\left(\frac{V_{\mathrm{bi}\,i,j}-\psi_{i,j}^{(k)}-E_{\mathrm{g}\,i,j}}{k_{\mathrm{B}}T}\right)\right)^2}\delta\psi_{i,j}^{(k+1)} \tag{B.30b}$$

B.3.3 Schottky Barrier lowering

As the barrier lowering depends on the electric field, the corresponding correction term can be obtained by deriving the Equation (2.15) with respect to the potential. In a system with the metal contact set to the left of the semiconductor, the corresponding expression is:

$$\delta\phi_{\delta\, i,j}^{(k+1)} = \frac{1}{2}\frac{\sqrt{q/4\pi\varepsilon_{\mathrm{s}}}}{\left|E_{i,j}^{(k)}\right|^{3/2}}\frac{\left|E_{i,j}^{(k)}\right|}{\Delta x_i}\left(\delta\psi_{i,j}^{(k+1)} - \delta\psi_{i+1,j}^{(k+1)}\right) = A_{\mathrm{BL}}^{(k)}\left(\delta\psi_{i,j}^{(k+1)} - \delta\psi_{i+1}^{(k+1)}\right) \quad \text{(B.31)}$$

This term is used to linearise Eq. (2.16), in which we move all the terms to the left-hand side and get the correction terms:

$$\psi_{i,j}^{(k)} + \delta\psi_{i,j}^{(k+1)} - \delta\phi_{\delta\, i,j}^{(k+1)} - \phi_{\delta\, i,j}^{(k)} - \psi_{0\, i,j}^{(k)} = 0. \quad \text{(B.32)}$$

Substituting Eq. (B.31) in (B.32), we obtain

$$\left(1 - A_{\mathrm{BL}}\right)\delta\psi_{i,j}^{(k+1)} + A_{\mathrm{BL}}^{(k)}\delta\psi_{i+1,j}^{(k+1)} = -\psi_{i,j}^{(k)} + \psi_{0\, i,j}^{(k)} + \phi_{\delta\, i,j}^{(k)} \quad \text{(B.33)}$$

This equation substitutes the corresponding one in the Poisson equation at $(i,j) \in \mathbf{r}_{\mathrm{I}}$, i.e., the metal interface positions.

B.3.4 Heterostructures

Let us consider an interface position $(i,j) \in \mathbf{r}_{\mathrm{I}}$, where two different semiconductors are in contact along the y direction. In that case, let (i^+,j) and (i^-,j) be the nodes in which (i,j) is divided, the former belonging to the right material and the latter to the left one. The correction term for the current in both positions, referred as $\delta J^{(k+1)}_{\mathrm{n},i^\pm,j}$, once discretized, can be evaluated as

$$\begin{aligned}\delta J^{(k+1)}_{\mathrm{n},i^\pm,j} =& q v^{\mathrm{n}}_{\mathrm{th}\,i^+,j} \exp\left(-\frac{\Delta E_{\mathrm{c}\,i^+,j}}{k_{\mathrm{B}}T}\right)(1+\gamma_{\mathrm{n}\,i,j}) \\ & \left[\delta n^{(k+1)}_{i^+,j} + \frac{n^{(k)}_{i^+,j}}{k_{\mathrm{B}}T}\left(\delta\psi^{(k+1)}_{i^+,j} - \delta\psi^{\mathrm{R}\,(k+1)}_{i,j}\right)\right] - \\ & - q v^{\mathrm{n}}_{\mathrm{th}\,i^-,j} \exp\left(-\frac{\Delta E_{\mathrm{c}\,i^-,j}}{k_{\mathrm{B}}T}\right)(1+\gamma_{\mathrm{n}\,i,j}) \\ & \left[\delta n^{(k+1)}_{i^-,j} + \frac{n^{(k)}_{i^-,j}}{k_{\mathrm{B}}T}\left(\delta\psi^{\mathrm{R}\,(k+1)}_{i,j} - \delta\psi^{(k+1)}_{i^-,j}\right)\right]\end{aligned} \tag{B.34a}$$

$$\begin{aligned}\delta J^{(k+1)}_{\mathrm{p},i^\pm,j} =& - q v^{\mathrm{p}}_{\mathrm{th}\,i^+,j} \exp\left(\frac{\Delta E_{\mathrm{v}\,i^+,j}}{k_{\mathrm{B}}T}\right)(1+\gamma_{\mathrm{p}\,i,j}) \\ & \left[\delta p^{(k+1)}_{i^+,j} + \frac{n^{(k)}_{i^+,j}}{k_{\mathrm{B}}T}\left(-\delta\psi^{(k+1)}_{i^+,j} + \delta\psi^{\mathrm{R}\,(k+1)}_{i,j}\right)\right] + \\ & + q v^{\mathrm{p}}_{\mathrm{th}\,i^-,j} \exp\left(\frac{\Delta E_{\mathrm{v}\,i^-,j}}{k_{\mathrm{B}}T}\right)(1+\gamma_{\mathrm{p}\,i,j}) \\ & \left[\delta p^{(k+1)}_{i^-,j} + \frac{p^{(k)}_{i^-,j}}{k_{\mathrm{B}}T}\left(-\delta\psi^{\mathrm{R}\,(k+1)}_{i,j} + \delta\psi^{(k+1)}_{i^-,j}\right)\right]\end{aligned} \tag{B.34b}$$

where ψ^{R} refers to the minimum value of potential at the barrier in the case of electrons, and the maximum for holes. This equation is general for both simple and SOS heterostructures, that is why the exact potential position has been specified, although in simple heterojunctions they share the same value.

In the case of semiconductor-oxide-semiconductor heterostructures, the procedure is exactly the same, just changing the nomenclature of Eq. (B.34) to fit with the SOS interfaces. The position (i^+,j) would correspond to the right interface, whereas (i^-,j) would refer to the left interface.

B.3.5 Local band to band tunnelling current

The generation-recombination term can be linearised using the Newton method. For the Hurkx model presented in Eq. (2.24), the new correction term that is added is

$$\begin{aligned}\delta U^{(k+1)}_{\text{Hurkx}\,i,j} = A\exp\left(-\frac{B}{\sqrt{C_{\text{K}\,i,j}}}\right)\times\\ \times\left[\left(\frac{\delta n^{(k+1)}_{i,j}B_{\text{H}\,i,j}\left(p^{(k)}_{i,j}A_{\text{H}\,i,j}-C_{\text{H}\,i,j}\right)}{A^2_{\text{H}\,i,j}B^2_{\text{H}\,i,j}}+\frac{\delta p^{(k+1)}_{i,j}A_{\text{H}\,i,j}\left(n^{(k)}_{i,j}B_{\text{H}\,i,j}-C_{\text{H}\,i,j}\right)}{A^2_{\text{H}\,i,j}B^2_{\text{H}\,i,j}}\right)C^{\alpha/2}_{\text{K}\,i,j}+\right.\\ \left.+\frac{n^{(k)}_{i,j}p^{(k)}_{i,j}-n^2_{\text{i}\,i,j}}{A_{\text{H}\,i,j}B_{\text{H}\,i,j}}\cdot D_{\text{K}\,i,j}\left(\frac{\delta\psi^{(k+1)}_{i,j}-\delta\psi^{(k+1)}_{i-1,j}}{\Delta x_i}E_{\text{x}\,i,j}+\frac{\delta\psi^{(k+1)}_{i,j}-\delta\psi^{(k+1)}_{i,j-1}}{\Delta y_j}E_{\text{y}\,i,j}\right)\right]\end{aligned} \tag{B.35}$$

where the elements $A_{\text{H}\,i,j}$, $B_{\text{H}\,i,j}$, $C_{\text{H}\,i,j}$, $C_{\text{K}\,i,j}$ and $D_{\text{K}\,i,j}$ correspond to

$$A_{\text{H}\,i,j} = n_{i,j} + n_{\text{i}\,i,j} \tag{B.36a}$$

$$B_{\text{H}\,i,j} = p_{i,j} + n_{\text{i}\,i,j} \tag{B.36b}$$

$$C_{\text{H}\,i,j} = n_{i,j}p_{i,j} + n^2_{\text{i}\,i,j} \tag{B.36c}$$

$$C_{\text{K}\,i,j} = E^2_{\text{x}\,i,j} + E^2_{\text{y}\,i,j} \tag{B.36d}$$

$$D_{\text{K}\,i,j} = BC^{\frac{\alpha-3}{2}}_{\text{K}\,i,j} + \alpha C^{-\frac{\alpha}{2}}_{\text{K}\,i,j} \tag{B.36e}$$

and the rest of constants follow the nomenclature seen in Section 2.6.

Considering only the Kane model, the equation simplifies to:

$$\begin{aligned}\delta U^{(k+1)}_{\text{Kane}\,i,j} =& A\exp\left(-\frac{B}{\sqrt{C_{\text{K}\,i,j}}}\right)D_{\text{K}\,i,j}\times\\ &\times\left(\frac{\delta\psi^{(k+1)}_{i,j}-\delta\psi^{(k+1)}_{i-1,j}}{\Delta x_i}E_{\text{x}\,i,j}+\frac{\delta\psi^{(k+1)}_{i,j}-\delta\psi^{(k+1)}_{i,j-1}}{\Delta y_j}E_{\text{y}\,i,j}\right)\end{aligned} \tag{B.37}$$

This model could be applied in the non-local approach although, due to the relation between remote nodes, the Jacobian matrix would lost its sparsity and the time required to solve the system would be highly increased.

B.3.6 SRH recombination

Here we evaluate the correction term associated with the SRH recombination, seen in Eq. (2.27). If we call

$$A_{i,j}^{(k)} = \tau_{\mathrm{n}\,i,j}\left[p_{i,j}^{(k)} + n_{\mathrm{i}\,i,j}\exp\left(\frac{-E_{\mathrm{T}\,i,j}}{k_{\mathrm{B}}T}\right)\right] + \tau_{\mathrm{p}\,i,j}\left[n_{i,j}^{(k)} + n_{\mathrm{i}\,i,j}\exp\left(\frac{E_{\mathrm{T}\,i,j}}{k_{\mathrm{B}}T}\right)\right] \tag{B.38}$$

and

$$B_{i,j}^{(k)} = p_{i,j}^{(k)} n_{i,j}^{(k)} - n_{\mathrm{i}\,i,j}^{2}\left(\mathbf{r}\right) \tag{B.39}$$

the correction term is

$$\delta R_{\mathrm{SRH}\,i,j}^{(k+1)} = \delta p_{i,j}^{(k+1)} \frac{n_{i,j}^{(k)} A_{i,j}^{(k)} - B_{i,j}^{(k)} \tau_{\mathrm{n}\,i,j}}{\left(A_{i,j}^{(k)}\right)^2} + \delta n_{i,j}^{(k+1)} \frac{p_{i,j}^{(k)} A_{i,j}^{(k)} - B_{i,j}^{(k)} \tau_{\mathrm{p}\,i,j}}{\left(A_{i,j}^{(k)}\right)^2} \tag{B.40}$$

which is added to the $\delta R_{i,j}$ total correction recombination term.

B.3.7 Auger generation/recombination

In the same way as it was added the correction term in the SRH recombination, it is possible to add the corresponding term for this process as the partial derivative with respect to the electron and hole densities from Eq. (2.28). We obtain

$$\begin{aligned}\delta U_{\mathrm{Aug}\,i,j}^{(k+1)} = {} & \delta n_{i,j}^{(k+1)}\left[C_{\mathrm{n}\,i,j}\left(2n_{i,j}^{(k)}p_{i,j}^{(k)} - n_{\mathrm{i}\,i,j}^{2}\right) + C_{\mathrm{p}\,i,j}\left(p_{i,j}^{(k)}\right)^2\right] + \\ & + \delta p_{i,j}^{(k+1)}\left[C_{\mathrm{p}\,i,j}\left(2n_{i,j}^{(k)}p_{i,j}^{(k)} - n_{\mathrm{i}\,i,j}^{2}\right) + C_{\mathrm{n}\,i,j}\left(n_{i,j}^{(k)}\right)^2\right]\end{aligned} \tag{B.41}$$

B.3.8 Radiative recombination

We follow the same derivation process with Eq. (2.29), which gives

$$\delta R_{\mathrm{Rad}\,i,j} = B_{\mathrm{Rad}\,i,j}\left(\delta n_{i,j}^{(k+1)} p_{i,j}^{(k)} + \delta p_{i,j}^{(k+1)} n_{i,j}^{(k)}\right) \tag{B.42}$$

In the case of light generation, there is no correction term, as it is independent of the potential and charge densities.

B.3.9 Traps at interfaces

The interface charge can be also linearised using the Newton method. The associated correction term is obtained deriving the interface charge density shown in Eq. (2.33) by the selected of carrier, electron or hole. In the case of electrons, it is given by:

$$\delta Q_{\mathrm{it}\,i,j}^{\mathrm{a}\,(k+1)} = \\ -q\int_{-\infty}^{\infty} \frac{D_{\mathrm{it}\,i,j}^{\mathrm{a}\,(k)}\left(E-E_{\mathrm{i}\,i,j}\right)\exp\left(\frac{E-E_{\mathrm{f}\,i,j}}{k_{\mathrm{B}}T}\right)}{k_{\mathrm{B}}T\left(1+\exp\left(\frac{E-E_{\mathrm{f}\,i,j}}{k_{\mathrm{B}}T}\right)\right)^2} \left.\frac{\partial\left(E_{\mathrm{f}\,i,j}-E_{\mathrm{i}\,i,j}\right)}{\partial p}\right|_{(k)} \delta p_{i,j}^{(k+1)}\mathrm{d}\left(E-E_{\mathrm{i}\,i,j}\right) \tag{B.43}$$

while in the case of holes can be expressed as:

$$\delta Q_{\mathrm{it}\,i,j}^{\mathrm{d}\,(k+1)} = \\ q\int_{-\infty}^{\infty} \frac{D_{\mathrm{it}\,i,j}^{\mathrm{d}\,(k)}\left(E-E_{\mathrm{i}\,i,j}\right)\exp\left(\frac{E-E_{\mathrm{f}\,i,j}}{k_{\mathrm{B}}T}\right)}{k_{\mathrm{B}}T\left(1+\exp\left(\frac{E-E_{\mathrm{f}\,i,j}}{k_{\mathrm{B}}T}\right)\right)^2} \left.\frac{\partial\left(E_{\mathrm{f}\,i,j}-E_{\mathrm{i}\,i,j}\right)}{\partial n}\right|_{(k)} \delta n_{i,j}^{(k+1)}\mathrm{d}\left(E-E_{\mathrm{i}\,i,j}\right) \tag{B.44}$$

where

$$\left.\frac{\partial\left(E_{\mathrm{f}\,i,j}-E_{\mathrm{i}\,i,j}\right)}{\partial p}\right|_{(k)} = -\frac{k_{\mathrm{B}}T}{N_{\mathrm{v}\,i,j}}\frac{\mathrm{d}\mathcal{F}_{1/2}^{-1}\left(\frac{p_{i,j}^{(k)}}{N_{\mathrm{v}\,i,j}}\right)}{\mathrm{d}p/N_{\mathrm{v}}} \tag{B.45a}$$

$$\left.\frac{\partial\left(E_{\mathrm{f}\,i,j}-E_{\mathrm{i}\,i,j}\right)}{\partial n}\right|_{(k)} = \frac{k_{\mathrm{B}}T}{N_{\mathrm{c}\,i,j}}\frac{\mathrm{d}\mathcal{F}_{1/2}^{-1}\left(\frac{n_{i,j}^{(k)}}{N_{\mathrm{c}\,i,j}}\right)}{\mathrm{d}n/N_{\mathrm{c}}} \tag{B.45b}$$

The derivative of the inverse operator of the Fermi function can be found in Eq. (B.28). These equations can be used for all the described DoS profiles in Section 2.8. The correction terms are added to the correction terms of the charge density in Eq. (B.12) in this way

$$\delta N_{\mathrm{T}\,i,j}^{(k+1)} = \Delta Q_{\mathrm{it}\,i,j}^{\mathrm{d}}{}^{(k+1)} + \Delta Q_{\mathrm{it}\,i,j}^{\mathrm{a}}{}^{(k+1)} \tag{B.46}$$

Appendix C

Boundary conditions

During the simulations, the evaluated device is enclosed in a 2D system, surrounded by boundary conditions [233]. SAMANTA has two kind of border conditions: Dirichlet and Neumann. The former is used in contacts, whereas the latter is placed in the rest of borders.

Contacts can be placed inside the system too, as one material block. However, only the borders of these blocks are considered in the evaluation. Figure C.1 is an example of a phototransistor, where the different borders are highlighted.

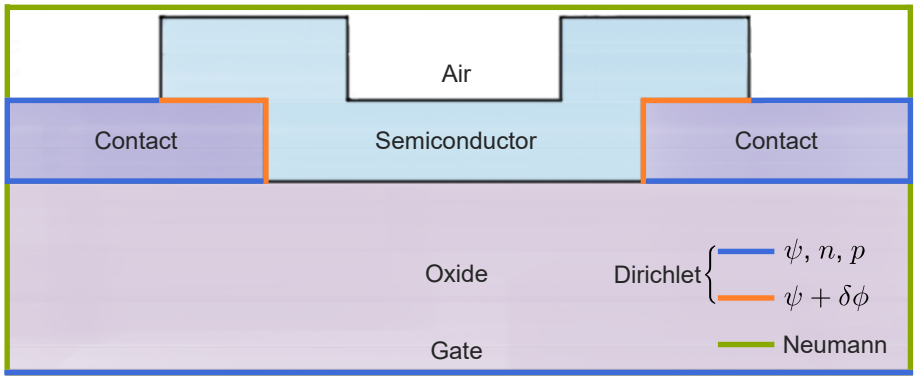

Figure C.1: Schematic of a phototransistor with the different boundary conditions highlighted. Blue borders fix the potential and charge densities. Orange borders set the potential, which can be shifted by the barrier lowering $\delta\phi$. Green borders enable Neumann conditions.

Neumann conditions match the potential and charge densities at the borders to the values of the closest point normal to the interface. Consider the interface points $\boldsymbol{I}$ and

be the $\boldsymbol{i}$ points the closest positions to each point of the interface that does not belong to the interface itself, that is $\boldsymbol{i} \not\subseteq \boldsymbol{I}$, then:

$$\psi(\boldsymbol{I}) = \psi(\boldsymbol{i}) \tag{C.1a}$$

$$n(\boldsymbol{I}) = n(\boldsymbol{i}) \tag{C.1b}$$

$$p(\boldsymbol{I}) = p(\boldsymbol{i}) \tag{C.1c}$$

In the case of Dirichlet conditions, the potential is fixed, unless barrier lowering is enabled. Now, let $\boldsymbol{I}$ be the metal interface points. The potential value is determined as $\psi(\boldsymbol{I}) = \phi_{\mathrm{m}}(\boldsymbol{I}) - \chi_{\mathrm{sc}}(\boldsymbol{I})$. In equilibrium and ohmic conditions, charge carriers are fixed too, following Eq. (2.21) and setting $n(\boldsymbol{I}) = n_0(\boldsymbol{I})$ and $p(\boldsymbol{I}) = p_0(\boldsymbol{I})$. In the case of contacts with TE or TFE current models, charge carriers are evaluated as part of the continuity equations using Equations (2.6), (2.17) and (2.19). Finally, in metal-oxide interfaces, charge carriers at the metal interface are set to zero.

Appendix D

Materials parameters

This Appendix collects the material parameters applied in the simulations carried out in this work. Some of them has "this work" as reference. It means their values are the ones used to fit with the experimental results. Table D.1 has the default magnitudes for Silicon, without any degradation, while Tables D.2 and D.3 contain the evaluated parameters for the two studied 2D materials, Molybdenum Ditelluride and Molybdenum Disellenide, respectively.

D.1 Silicon

Parameter	Value
ε_{r} (ε_0)	11.9
$m_{\mathrm{eff}}^{\mathrm{n}}$ (m_0)	0.91
$m_{\mathrm{eff}}^{\mathrm{p}}$ (m_0)	0.49
χ (eV)	4.05
E_{g} (eV)	1.12
N_{c} (cm^{-3})	2.82×10^{19}
N_{v} (cm^{-3})	1.83×10^{19}
n_{i} (cm^{-3})	8.89×10^{9}
μ_{n} $\left(\mathrm{cm}^2\,\mathrm{V}^{-1}\,\mathrm{s}^{-1}\right)$	1500
μ_{p} $\left(\mathrm{cm}^2\,\mathrm{V}^{-1}\,\mathrm{s}^{-1}\right)$	400

Table D.1: Material parameters used for Si. Obtained from [234].

D.2 Molybdenum Ditelluride

Parameter	Value	Ref
$\varepsilon_\perp$ (ε_0)	10.4	[235]
$\varepsilon_\parallel$ (ε_0)	22.2	[235]
$m_{\mathrm{eff}}^{\mathrm{n}}$ (m_0)	0.55	[236]
$m_{\mathrm{eff}}^{\mathrm{p}}$ (m_0)	0.64	[236]
χ (eV)	4	This work
E_{g} (eV)	1.07	This work
N_{c} (cm^{-3})	1.31×10^{19}	[206]
N_{v} (cm^{-3})	1.28×10^{19}	[206]
n_{i} (cm^{-3})	5.09×10^{9}	[237]
μ_{n} ($\mathrm{cm}^2\,\mathrm{V}^{-1}\,\mathrm{s}^{-1}$)	0.06	This work
μ_{p} ($\mathrm{cm}^2\,\mathrm{V}^{-1}\,\mathrm{s}^{-1}$)	1.24	This work

Table D.2: Material parameters used for $MoTe_2$.

D.3 Molybdenum Disulphide

Parameter	Value	Ref
$\varepsilon_\perp$ (ε_0)	7.6	[235]
$\varepsilon_\parallel$ (ε_0)	16.1	[235]
$m_{\mathrm{eff}}^{\mathrm{n}}$ (m_0)	0.49	[236]
$m_{\mathrm{eff}}^{\mathrm{p}}$ (m_0)	0.43	[236]
χ (eV)	4	[238]
E_{g} (eV)	1.29	[239]
N_{c} (cm^{-3})	7.35×10^{19}	[236]
N_{v} (cm^{-3})	8.00×10^{19}	[236]
n_{i} (cm^{-3})	1.12×10^{9}	[237]
μ_{n} ($\mathrm{cm}^2\,\mathrm{V}^{-1}\,\mathrm{s}^{-1}$)	7.5	This work
μ_{p} ($\mathrm{cm}^2\,\mathrm{V}^{-1}\,\mathrm{s}^{-1}$)	0.01	This work

Table D.3: Material parameters used for MoS_2.

Part VI

References

List of publications

Referenced papers

- **J.M. Gonzalez-Medina**, F.G. Ruiz, E.G. Marin, A. Godoy and F. Gámiz. Simulation study of the electron mobility in few-layer MoS_2 metal-insulator-semiconductor field-effect transistors. Solid State Electronics, 114:30-34, Jul 2015.
- E.G. Marin, I.M. Tienda-Luna, F.G. Ruiz, **J.M. Gonzalez-Medina**, A. Godoy and F. Gámiz. Analytic Potential and Charge Model of Semiconductor Quantum Wells. IEEE Transactions on Electron Devices, 62(12):4186-4191, Oct 2015.
- C. Martinez-Blanque, E.G. Marin, A. Toral, **J.M. Gonzalez-Medina**, F. G. Ruiz, A. Godoy and F. Gámiz. Electrostatic performance of InSb, GaSb, Si and Ge p-channel nanowires, Journal of Physics D: Applied Physics, 50:495106, Oct 2017.
- S. Riazimehr, S. Kataria, **J.M. Gonzalez-Medina**, S. Wagner, M. Shaygan, S. Suckow, F.G. Ruiz, O. Engström, A. Godoy, and M.C. Lemme. High Responsivity and Quantum Efficiency of Graphene/Silicon Photodiodes Achieved by Interdigitating Schottky and Gated Regions, ACS Photonics, 6(1):107-115, Oct 2018.
- A. Toral-Lopez, E.G. Marin, **J.M. Gonzalez-Medina**, F.J. Romero, F.G. Ruiz, D.P. Morales, N. Rodriguez and A. Godoy. Assessment of three electrolyte-molecule electrostatic interaction models for 2D material based BioFETs, Nanoscale Advances, 1:1077-1085, Nov 2018.
- A. Toral-Lopez, E.G. Marin, F. Pasadas, **J.M. Gonzalez-Medina**, F.G. Ruiz, D. Jimenez and A. Godoy. GFET Asymmetric Transfer Response Analysis through Access Region Resistances, Nanomaterials, 9:1027, Jul 2019.

Conference contributions

- **J.M. Gonzalez-Medina**, F.G. Ruiz, A. Godoy, E.G. Marin and F. Gámiz. Simulation of the phonon-limited electron mobility in multi-layer MoS_2 field-effect transistors. *10^{th} Spanish Conference on Electron Devices 2015.*

- F.G. Ruiz, B. Biel, **J.M. Gonzalez-Medina**, A. Toral, E.G. Marin, I.M. Tienda-Luna and A. Godoy. Calculation of the Ballistic Current of Few-Layer MoS_2 Field-Effect Transistors. *19^{th} International Conference on Electron Dynamics in Semiconductors, Optoelectronics and Nanostructures 2015.*

- E.G. Marin, F.G. Ruiz, A. Godoy, **J.M. Gonzalez-Medina**, I.M. Tienda-Luna and F. Gámiz. On the influence of the back-gate bias on InGaAs Trigate MOSFETs. *EUROSOI-ULIS 2016.*

- C. Martinez-Blanque, A. Toral, **J.M. Gonzalez-Medina**, E.G. Marin, F.G. Ruiz, A. Godoy and F. Gámiz. Numerical study of p-type InSb and GaSb nanowires. *11^{th} Spanish Conference on Electron Devices 2017.*

- C. Martinez-Blanque, F.G. Ruiz, L. Donetti, A. Toral, **J.M. Gonzalez-Medina**, E.G. Marin and A. Godoy. Gate capacitance performance of p-type InSb and GaSb nanowires. *EUROSOI-ULIS 2017.*

- A. Toral-Lopez, **J.M. Gonzalez-Medina**, E.G. Marin, A. Marin-Sanchez, A. Medina F.G. Ruiz and A. Godoy. Simulation of 2D semiconductor based MOSFETs *12^{th} Spanish Conference on Electron Devices 2018.*

- Z. Stanojevic, Oskar Baumgartner, F. Schanovsky, G. Strof, C. Kernstock, M. Karner, **J.M. Gonzalez-Medina**, F.G. Ruiz, A. Godoy and F. Gámiz. Scaling FDSOI technology down to 7 nm - A physical modeling study based on 3D phase-space subband Boltzmann transport. *EUROSOI-ULIS 2018.*

- F.G. Ruiz, E.G. Marin, C. Martinez-Blanque, I.M. Tienda-Luna, **J.M. Gonzalez-Medina**, A. Toral, L. Donetti and A. Godoy. Hole mobility of cylindrical GaSb nanowires. *EUROSOI-ULIS 2018.*

- **J.M. Gonzalez-Medina**, E.G. Marin, A. Toral-Lopez, F.G. Ruiz and A. Godoy. Numerical Investigation of the Photogating Effect in $MoTe_2$ Photodetectors. *Simulation of Semiconductor Processes and Devices (SISPAD) 2019.*

Bibliography

[1] Erin Mahoney. Sending American Astronauts to Moon in 2024: NASA Accepts Challenge, April 2019.

[2] C. E. Shannon. A mathematical theory of communication. *Bell System Technical Journal*, 27(3):379–423, jul 1948.

[3] J. Bardeen and W. H. Brattain. The Transistor, A Semi-Conductor Triode. *Physical Review*, 74:230–231, July 1948.

[4] Richard C. Koch. Transistor Radio Apparatus, 1955.

[5] R. G. Arns. The other transistor: early history of the metal-oxide semiconductor field-effect transistor. *Engineering Science & Education Journal*, 7(5):233–240, oct 1998.

[6] Science: Problem child. Retrieved in 2009. Available online: `http://content.time.com/time/magazine/article/0,9171,818829,00.html`, 1953.

[7] Gordon E. Moore. Cramming more components onto integrated circuits, reprinted from electronics, volume 38, number 8, april 19, 1965, pp.114 ff. *IEEE Solid-State Circuits Society Newsletter*, 11(3):33–35, sep 2006.

[8] M. Ieong. Silicon Device Scaling to the Sub-10-nm Regime. *Science*, 306(5704):2057–2060, dec 2004.

[9] Henry H. Radamson, Xiaobin He, Qingzhu Zhang, Jinbiao Liu, Hushan Cui, Jinjuan Xiang, Zhenzhen Kong, Wenjuan Xiong, Junjie Li, Jianfeng Gao, Hong Yang, Shihai Gu, Xuewei Zhao, Yong Du, Jiahan Yu, and Guilei Wang. Miniaturization of CMOS. *Micromachines*, 10(5):293, apr 2019.

[10] S. E. Thompson, M. Armstrong, C. Auth, M. Alavi, M. Buehler, R. Chau, S. Cea, T. Ghani, G. Glass, T. Hoffman, C.-H. Jan, C. Kenyon, J. Klaus, K. Kuhn, Z. Ma, B. Mcintyre, K. Mistry, A. Murthy, B. Obradovic, R. Nagisetty, P. Nguyen, S. Sivakumar, R. Shaheed, L. Shifren, B. Tufts, S. Tyagi, M. Bohr, and Y. El-Mansy. A 90-nm Logic Technology Featuring Strained-Silicon. *IEEE Transactions on Electron Devices*, 51(11):1790–1797, nov 2004.

[11] Els Parton and Peter Verheyen. Strained silicon — the key to sub-45 nm CMOS. *III-Vs Review*, 19(3):28–31, apr 2006.

[12] John Robertson and Robert M. Wallace. High-K materials and metal gates for CMOS applications. *Materials Science and Engineering: R: Reports*, 88:1–41, feb 2015.

[13] Gang He, Zhaoqi Sun, Guang Li, and Lide Zhang. Review and Perspective of Hf-based High-k Gate Dielectrics on Silicon. *Critical Reviews in Solid State and Materials Sciences*, 37(3):131–157, jul 2012.

[14] Chun Zhao, Ce Zhao, Stephen Taylor, and Paul Chalker. Review on non-volatile memory with high-k dielectrics: Flash for generation beyond 32 nm. *Materials*, 7(7):5117–5145, jul 2014.

[15] Ahmad Ehteshamul Islam. Current Status of Reliability in Extended and Beyond CMOS Devices. *IEEE Transactions on Device and Materials Reliability*, 16(4):647–666, dec 2016.

[16] A. Chaudhry and M.J. Kumar. Controlling short-channel effects in deep-submicron SOI MOSFETs for improved reliability: A review. *IEEE Transactions on Device and Materials Reliability*, 4(1):99–109, mar 2004.

[17] M. Jurczak, N. Collaert, A. Veloso, T. Hoffmann, and S. Biesemans. Review of FINFET technology. In *2009 IEEE International SOI Conference*. IEEE, oct 2009.

[18] Renewable Energy Market Report 2018 - Market Trends and Projections to 2023. Technical report, International Energy Agency, 2018.

[19] D. M. Chapin, C. S. Fuller, and G. L. Pearson. A New Silicon p-n Junction Photocell for Converting Solar Radiation into Electrical Power. *Journal of Applied Physics*, 25(5):676–677, may 1954.

[20] Hector Cotal, Chris Fetzer, Joseph Boisvert, Geoffrey Kinsey, Richard King, Peter Hebert, Hojun Yoon, and Nasser Karam. III–V multijunction solar cells for concentrating photovoltaics. *Energy Environment Science*, 2(2):174–192, 2009.

[21] Corsin Battaglia, Andres Cuevas, and Stefaan De Wolf. High-efficiency crystalline silicon solar cells: status and perspectives. *Energy & Environmental Science*, 9(5):1552–1576, 2016.

[22] Daniel Aiken, Edwin Dons, Sang-Soo Je, Nathaniel Miller, Fredrick Newman, Pravin Patel, and John Spann. Lattice-matched solar cells with 40% average efficiency in pilot production and a roadmap to 50%. *IEEE Journal of Photovoltaics*, 3(1):542–547, jan 2013.

[23] Lazard. Lazard's Levelized Cost of Energy Analysis. 2018. Available online: `https://www.lazard.com/media/450784/lazards-levelized-cost-of-energy-version-120-vfinal.pdf`.

[24] R.W. Keyes. Fundamental limits of silicon technology. *Proceedings of the IEEE*, 89(3):227–239, mar 2001.

[25] H. P. Boehm, A. Clauss, G. O. Fischer, and U. Hofmann. Das adsorptionsverhalten sehr dünner kohlenstoff-folien. *Zeitschrift für anorganische und allgemeine Chemie*, 316(3-4):119–127, jul 1962.

[26] A. H. Castro Neto, F. Guinea, N. M. R. Peres, K. S. Novoselov, and A. K. Geim. The electronic properties of graphene. *Reviews of Modern Physics*, 81(1):109–162, jan 2009.

[27] Bernardo Marinho, Marcos Ghislandi, Evgeniy Tkalya, Cor E. Koning, and Gijsbertus de With. Electrical conductivity of compacts of graphene, multi-wall carbon nanotubes, carbon black, and graphite powder. *Powder Technology*, 221:351–358, may 2012.

[28] Toshiaki Enoki, Masatsugu Suzuki, and Morinobu Endo. *Graphite Intercalation Compounds and Applications*. Oxford University Press, 2003.

[29] K. S. Novoselov, A. K. Geim, S. V. Morozov, D. Jiang, Y. Zhang, S. V. Dubonos, I. V. Grigorieva, and A. A. Firsov. Electric Field Effect in Atomically Thin Carbon Films. *Science*, 306(5696):666–669, oct 2004.

[30] Ed Gerstner. Nobel prize 2010: Andre geim & konstantin novoselov. *Nature Physics*, 6(11):836–836, oct 2010.

[31] Victor Yu. Aristov, Grzegorz Urbanik, Kurt Kummer, Denis V. Vyalikh, Olga V. Molodtsova, Alexei B. Preobrajenski, Alexei A. Zakharov, Christian Hess, Torben Hänke, Bernd Büchner, Ivana Vobornik, Jun Fujii, Giancarlo Panaccione, Yuri A. Ossipyan, and Martin Knupfer. Graphene Synthesis on Cubic SiC/Si Wafers. Perspectives for Mass Production of Graphene-Based Electronic Devices. *NANO Letters*, 10:992–995, 2010.

[32] Xinming Li, Li Tao, Zefeng Chen, Hui Fang, Xuesong Li, Xinran Wang, Jian-Bin Xu, and Hongwei Zhu. Graphene and related two-dimensional materials: Structure-property relationships for electronics and optoelectronics. *Applied Physics Reviews*, 4(2):021306, jun 2017.

[33] Chul-Ho Lee, Gwan-Hyoung Lee, Arend M. van der Zande, Wenchao Chen, Yilei Li, Minyong Han, Xu Cui, Ghidewon Arefe, Colin Nuckolls, Tony F. Heinz, Jing Guo, James Hone, and Philip Kim. Atomically thin p-n junctions with van der Waals heterointerfaces. *Nature Nanotechnology*, 9:676–681, 2014.

[34] Peng Zhang, Lulu Ma, Feifei Fan, Zhi Zeng, Cheng Peng, Phillip E. Loya, Zheng Liu, Yongji Gong, Jiangnan Zhang, Xingxiang Zhang, Pulickel M. Ajayan, Ting Zhu, and Jun Lou. Fracture toughness of graphene. *Nature Communications*, 5(1), apr 2014.

[35] Herbert Kroemer. Nobel Lecture: Quasielectric fields and band offsets: teaching electrons new tricks. *Reviews of Modern Physics*, 73:783–793, Oct 2001.

[36] Zhuang Liu, Joshua T. Robinson, Xiaoming Sun, and Hongjie Dai. PEGylated Nanographene Oxide for Delivery of Water-Insoluble Cancer Drugs. *Journal of the American Chemical Society*, 130(33):10876–10877, aug 2008.

[37] Yong Liu, Dingshan Yu, Chao Zeng, Zongcheng Miao, and Liming Dai. Biocompatible Graphene Oxide-Based Glucose Biosensors. *Langmuir*, 26(9):6158–6160, may 2010.

[38] Jae Hwan Jung, Doo Sung Cheon, Fei Liu, Kang Bum Lee, and Tae Seok Seo. A graphene oxide based immuno-biosensor for pathogen detection. *Angewandte Chemie International Edition*, 49(33):5708–5711, jul 2010.

[39] Cheng Xiang Lim, Hui Ying Hoh, Priscilla Kailian Ang, and Kian Ping Loh. Direct voltammetric detection of DNA and pH sensing on epitaxial graphene: An insight into the role of oxygenated defects. *Analytical Chemistry*, 82(17):7387–7393, sep 2010.

[40] Salma Siddique, Muhammad Zahir Iqbal, and Hamid Mukhtar. Cholesterol immobilization on chemical vapor deposition grown graphene nanosheets for biosensors and bioFETs with enhanced electrical performance. *Sensors and Actuators B: Chemical*, 253:559–565, dec 2017.

[41] Chun-Yu Chan, Feng Yan, and Mo Yang. Chemical vapor deposition grown graphene DNA field-effect transistor biosensor with gold nanoparticles signal amplification. In *2016 IEEE 29th International Conference on Micro Electro Mechanical Systems (MEMS)*. IEEE, jan 2016.

[42] A. Toral-Lopez, E. G. Marin, J. M. Gonzalez-Medina, F. J. Romero, F. G. Ruiz, D. P. Morales, N. Rodriguez, and A. Godoy. Assessment of three electrolyte–molecule electrostatic interaction models for 2d material based BioFETs. *Nanoscale Advances*, 1(3):1077–1085, 2019.

[43] K. S. Novoselov, V. I. Fal'ko, L. Colombo, P. R. Gellert, M. G. Schwab, and K. Kim. A roadmap for graphene. *Nature*, 490(7419):192–200, oct 2012.

[44] Aaron Bostwick, Taisuke Ohta, Thomas Seyller, Karsten Horn, and Eli Rotenberg. Quasiparticle dynamics in graphene. *Nature Physics*, 3(1):36–40, dec 2006.

[45] K. I. Bolotin, K. J. Sikes, Z. Jiang, M. Klima, G. Fudenberg, J. Hone, P. Kim, and H. L. Stormer. Ultrahigh electron mobility in suspended graphene. *Solid State Communications*, 146(9-10):351–355, jun 2008.

[46] N.D. Arora, J.R. Hauser, and D.J. Roulston. Electron and hole mobilities in silicon as a function of concentration and temperature. *IEEE Transactions on Electron Devices*, 29(2):292–295, feb 1982.

[47] Michael S. Shur. *Handbook Series On Semiconductor Parameters - Volume 1: Si, Ge, C (Diamond), Gaas, Gap, Gasb, Inas, Inp, Insb*. World Scientific Publishing Co Pte Ltd, 1996.

[48] Dae-Hyun Kim and Jesús A. del Alamo. Scalability of sub-100 nm InAs HEMTs on InP substrate for future logic applications. *IEEE Transactions on Electron Devices*, 57(7):1504–1511, jul 2010.

[49] H. J. Hrostowski, F. J. Morin, T. H. Geballe, and G. H. Wheatley. Hall effect and conductivity of InSb. *Physical Review*, 100(6):1672–1676, dec 1955.

[50] B. R. Nag and G. M. Dutta. Electron mobility in InP. *Journal of Physics C: Solid State Physics*, 11(1):119–123, jan 1977.

[51] Su Han Kim, Jae Hyung Lee, Jin-Sung Park, Min-Soo Hwang, Hong-Gyu Park, Kyoung Jin Choi, and Won Il Park. Performance optimization in gate-tunable schottky junction solar cells with a light transparent and electric-field permeable graphene mesh on n-si. *Journal of Materials Chemistry C*, 5(12):3183–3187, 2017.

[52] Samuel W. LaGasse, Prathamesh Dhakras, Kenji Watanabe, Takashi Taniguchi, and Ji Ung Lee. Gate-tunable graphene–WSe 2 heterojunctions at the schottky–mott limit. *Advanced Materials*, 31(24):1901392, apr 2019.

[53] Chun-Chung Chen, Chia-Chi Chang, Zhen Li, A. F. J. Levi, and Stephen B. Cronin. Gate tunable graphene-silicon Ohmic/Schottky contacts. *Applied Physics Letters*, 101(22):223113, nov 2012.

[54] Frank Schwierz. Graphene transistors. *Nature Nanotechnology*, 5:487–495, 2010.

[55] L. Britnell, R. V. Gorbachev, R. Jalil, B. D. Belle, F. Schedin, A. Mishchenko, T. Georgiou, M. I. Katsnelson, L. Eaves, S. V. Morozov, N. M. R. Peres, J. Leist, A. K. Geim, K. S. Novoselov, and L. A. Ponomarenko. Field-Effect Tunneling Transistor Based on Vertical Graphene Heterostructures. *Science*, 335(6071):947–950, feb 2012.

[56] Thanasis Georgiou, Rashid Jalil, Branson D. Belle, Liam Britnell, Roman V. Gorbachev, Sergey V. Morozov, Yong-Jin Kim, Ali Gholinia, Sarah J. Haigh, Oleg Makarovsky, Laurence Eaves, Leonid A. Ponomarenko, Andre K. Geim, Kostya S. Novoselov, and Artem Mishchenko. Vertical field-effect transistor based on graphene–WS2 heterostructures for flexible and transparent electronics. *Nature Nanotechnology*, 8(2):100–103, dec 2012.

[57] D. Jena. Tunneling Transistors Based on Graphene and 2-D Crystals. *Proceedings of the IEEE*, 101(7):1585–1602, July 2013.

[58] Oliver Gröning, Shiyong Wang, Xuelin Yao, Carlo A. Pignedoli, Gabriela Borin Barin, Colin Daniels, Andrew Cupo, Vincent Meunier, Xinliang Feng, Akimitsu Narita, Klaus Müllen, Pascal Ruffieux, and Roman Fasel. Engineering of robust topological quantum phases in graphene nanoribbons. *Nature*, 560(7717):209–213, aug 2018.

[59] Alberto Ciarrocchi, Dmitrii Unuchek, Ahmet Avsar, Kenji Watanabe, Takashi Taniguchi, and Andras Kis. Polarization switching and electrical control of interlayer excitons in two-dimensional van der waals heterostructures. *Nature Photonics*, 13(2):131–136, dec 2018.

[60] Jahan M. Dawlaty, Shriram Shivaraman, Jared Strait, Paul George, Mvs Chandrashekhar, Farhan Rana, Michael G. Spencer, Dmitry Veksler, and Yunqing Chen. Measurement of the optical absorption spectra of epitaxial graphene from terahertz to visible. *Applied Physics Letters*, 93(13):131905, sep 2008.

[61] A. K. Geim and K. S. Novoselov. The rise of graphene. *Nature Materials*, 6(3):183–191, mar 2007.

[62] R. R. Nair, P. Blake, A. N. Grigorenko, K. S. Novoselov, T. J. Booth, T. Stauber, N. M. R. Peres, and A. K. Geim. Fine Structure Constant Defines Visual Transparency of Graphene. *Science*, 320(5881):1308–1308, jun 2008.

[63] Jiao Xu, Young Jae Song, Jin-Hong Park, and Sungjoo Lee. Graphene/black phosphorus heterostructured photodetector. *Solid-State Electronics*, 144:86–89, jun 2018.

[64] L. Britnell, R. M. Ribeiro, A. Eckmann, R. Jalil, B. D. Belle, A. Mishchenko, Y. J. Kim, R. V. Gorbachev, T. Georgiou, S. V. Morozov, A. N. Grigorenko, A. K. Geim, C. Casiraghi, A. H. C. Neto, and K. S. Novoselov. Strong Light-Matter Interactions in Heterostructures of Atomically Thin Films. *Science*, 340(6138):1311–1314, may 2013.

[65] Yuanbo Zhang, Tsung-Ta Tang, Caglar Girit, Zhao Hao, Michael C. Martin, Alex Zettl, Michael F. Crommie, Y. Ron Shen, and Feng Wang. Direct observation of a widely tunable bandgap in bilayer graphene. *Nature*, 459(7248):820–823, jun 2009.

[66] Wei Cao, Jiahao Kang, Wei Liu, Yasin Khatami, Deblina Sarkar, and Kaustav Banerjee. 2d electronics: Graphene and beyond. In *2013 Proceedings of the European Solid-State Device Research Conference (ESSDERC)*. IEEE, sep 2013.

[67] K. S. Novoselov, A. Mishchenko, A. Carvalho, and A. H. Castro Neto. 2D materials and van der Waals heterostructures. *Science*, 353(6298):aac9439, jul 2016.

[68] A. K. Geim and I. V. Grigorieva. Van der waals heterostructures. *Nature*, 499:419–425, 2013.

[69] `https://www.materialscloud.org/`.

[70] Qiu Jin, Ning Liu, Biaohua Chen, and Donghai Mei. Mechanisms of semiconducting 2h to metallic 1t phase transition in two-dimensional MoS_2 nanosheets. *The Journal of Physical Chemistry C*, 122(49):28215–28224, nov 2018.

[71] Yun Zhao, Yong Chen, Ye-Hua Zhang, and Shu-Feng Liu. Recent advance in black phosphorus: Properties and applications. *Materials Chemistry and Physics*, 189:215–229, mar 2017.

[72] Michele Buscema, Dirk J. Groenendijk, Sofya I. Blanter, Gary A. Steele, Herre S. J. van der Zant, and Andres Castellanos-Gomez. Fast and Broadband Photoresponse of Few-Layer Black Phosphorus Field-Effect Transistors. *Nano Letters*, 14(6):3347–3352, may 2014.

[73] Andres Castellanos-Gomez, Leonardo Vicarelli, Elsa Prada, Joshua O Island, K L Narasimha-Acharya, Sofya I Blanter, Dirk J Groenendijk, Michele Buscema, Gary A Steele, J V Alvarez, Henny W Zandbergen, J J Palacios, and Herre S J van der Zant. Isolation and characterization of few-layer black phosphorus. *2D Materials*, 1(2):025001, jun 2014.

[74] Diao Li, Henri Jussila, Lasse Karvonen, Guojun Ye, Harri Lipsanen, Xianhui Chen, and Zhipei Sun. Polarization and Thickness Dependent Absorption Properties of Black Phosphorus: New Saturable Absorber for Ultrafast Pulse Generation. *Scientific Reports*, 5(1), oct 2015.

[75] Th. Böker, R. Severin, A. Müller, C. Janowitz, R. Manzke, D. Voß, P. Krüger, A. Mazur, and J. Pollmann. Band structure of mos_2, $mose_2$, and $\alpha - mote_2$: angle-resolved photoelectron spectroscopy and *ab initio* calculations. *Physical Review B*, 64:235305, Nov 2001.

[76] A. Kumar and P. K. Ahluwalia. Electronic structure of transition metal dichalcogenides monolayers 1H-MX2 (M = Mo, W; X = S, Se, Te) from ab-initio theory: new direct band gap semiconductors. *The European Physical Journal B*, 85(6), jun 2012.

[77] Won Seok Yun, S. W. Han, Soon Cheol Hong, In Gee Kim, and J. D. Lee. Thickness and strain effects on electronic structures of transition metal dichalcogenides: 2h-MX2 semiconductors (M=Mo, W; X=S, Se, Te). *Physical Review B*, 85(3), jan 2012.

[78] Jason K. Ellis, Melissa J. Lucero, and Gustavo E. Scuseria. The indirect to direct band gap transition in multilayered mos2 as predicted by screened hybrid density functional theory. *Applied Physics Letters*, 99:261908, 2011.

[79] B. Radisavljevic, A. Radenovic, J. Brivio, V. Giacometti, and A. Kis. Single-layer MoS_2 transistors. *Nature Nanotechnology*, 6:147–150, 2011.

[80] Likai Li, Yijun Yu, Guo Jun Ye, Qingqin Ge, Xuedong Ou, Hua Wu, Donglai Feng, Xian Hui Chen, and Yuanbo Zhang. Black phosphorus field-effect transistors. *Nature Nanotechnology*, 9(5):372–377, mar 2014.

[81] Stefano Larentis, Babak Fallahazad, and Emanuel Tutuc. Field-effect transistors and intrinsic mobility in ultra-thin $MoSe_2$ layers. *Applied Physics Letters*, 101(22):223104, nov 2012.

[82] Han Wang, Lili Yu, Yi-Hsien Lee, Yumeng Shi, Allen Hsu, Matthew L. Chin, Lain-Jong Li, Madan Dubey, Jing Kong, and Tomás Palacios. Integrated circuits based on bilayer MoS_2 transistors. *Nano Letters*, 12:4674–4680, 2012.

[83] Ahmet Avsar, Ivan J. Vera-Marun, Jun You Tan, Kenji Watanabe, Takashi Taniguchi, Antonio H. Castro Neto, and Barbaros Özyilmaz. Air-Stable Transport in Graphene-Contacted, Fully Encapsulated Ultrathin Black Phosphorus-Based Field-Effect Transistors. *ACS Nano*, 9(4):4138–4145, mar 2015.

[84] L. Liu, S. B. Kumar, Y. Ouyang, and J. Guo. Performance limits of monolayer transition metal dichalcogenide transistors. *IEEE Transactions on Electron Devices*, 58(9):3042–3047, September 2011.

[85] Marco Bernardi, Maurizia Palummo, and Jeffrey C. Grossman. Extraordinary sunlight absorption and one nanometer thick photovoltaics using two-dimensional monolayer materials. *Nano Letters*, 13(8):3664–3670, jul 2013.

[86] F. H. L. Koppens, T. Mueller, Ph. Avouris, A. C. Ferrari, M. S. Vitiello, and M. Polini. Photodetectors based on graphene, other two-dimensional materials and hybrid systems. *Nature Nanotechnology*, 9(10):780–793, oct 2014.

[87] Tobias J. Octon, V. Karthik Nagareddy, Saverio Russo, Monica F. Craciun, and C. David Wright. Fast high-responsivity few-layer MoTe2 photodetectors. *Advanced Optical Materials*, 4(11):1750–1754, aug 2016.

[88] Andreas Bablich, Satender Kataria, and Max Lemme. Graphene and Two-Dimensional Materials for Optoelectronic Applications. *Electronics*, 5(4):13, mar 2016.

[89] Michele Buscema, Dirk J. Groenendijk, Gary A. Steele, Herre S. J. van der Zant, and Andres Castellanos-Gomez. Photovoltaic effect in few-layer black phosphorus PN junctions defined by local electrostatic gating. *Nature Communications*, 5(1), aug 2014.

[90] José Luceño-Sánchez, Ana Díez-Pascual, and Rafael Peña Capilla. Materials for Photovoltaics: State of Art and Recent Developments. *International Journal of Molecular Sciences*, 20(4):976, feb 2019.

[91] Yuka Tsuboi, Feijiu Wang, Daichi Kozawa, Kazuma Funahashi, Shinichiro Mouri, Yuhei Miyauchi, Taishi Takenobu, and Kazunari Matsuda. Enhanced photovoltaic performances of graphene/Si solar cells by insertion of a MoS2 thin film. *Nanoscale*, 7(34):14476–14482, 2015.

[92] Munkhbayar Batmunkh, Munkhjargal Bat-Erdene, and Joseph G. Shapter. Black Phosphorus: Synthesis and Application for Solar Cells. *Advanced Energy Materials*, 8(5):1701832, oct 2017.

[93] Simon A. Svatek, Elisa Antolin, Der-Yuh Lin, Riccardo Frisenda, Christoph Reuter, Aday J. Molina-Mendoza, Manuel Munoz, Nicolas Agrait, Tsung-Shine Ko, David Perez de Lara, and Andres Castellanos-Gomez. Gate tunable photovoltaic effect in MoS_2 vertical p-n homostructures. *J. Mater. Chem. C*, 5:854–861, 2017.

[94] Prashant Kumar, Jing Liu, Pranay Ranjan, Yaowu Hu, Sharma SRKC Yamijala, Swapan K. Pati, Joseph Irudayaraj, and Gary J. Cheng. Alpha lead oxide (α-PbO): A new 2D material with visible light sensitivity. *Small*, 14(12):1703346, feb 2018.

[95] F. Withers, O. Del Pozo-Zamudio, A. Mishchenko, A. P. Rooney, A. Gholinia, K. Watanabe, T. Taniguchi, S. J. Haigh, A. K. Geim, A. I. Tartakovskii, and K. S. Novoselov. Light-emitting diodes by band-structure engineering in van der waals heterostructures. *Nature Materials*, 14(3):301–306, feb 2015.

[96] Y. J. Zhang, T. Oka, R. Suzuki, J. T. Ye, and Y. Iwasa. Electrically Switchable Chiral Light-Emitting Transistor. *Science*, 344(6185):725–728, apr 2014.

[97] Deep Jariwala, Tobin J. Marks, and Mark C. Hersam. Mixed-dimensional van der Waals heterostructures. *Nature Materials*, 16(2):170–181, aug 2016.

[98] M. Amani, D. H. Lien, D. Kiriya, J. Xiao, A. Azcatl, J. Noh, S. R. Madhvapathy, R. Addou, S. KC, M. Dubey, K. Cho, R. M. Wallace, S. C. Lee, J.-H. He, J. W. Ager, X. Zhang, E. Yablonovitch, and A. Javey. Near-unity photoluminescence quantum yield in MoS2. *Science*, 350(6264):1065–1068, nov 2015.

[99] Dehui Li, Rui Cheng, Hailong Zhou, Chen Wang, Anxiang Yin, Yu Chen, Nathan O. Weiss, Yu Huang, and Xiangfeng Duan. Electric-field-induced strong enhancement of electroluminescence in multilayer molybdenum disulfide. *Nature Communications*, 6(1), jul 2015.

[100] Humberto R. Gutiérrez, Nestor Perea-López, Ana Laura Elías, Ayse Berkdemir, Bei Wang, Ruitao Lv, Florentino López-Urías, Vincent H. Crespi, Humberto Terrones, and Mauricio Terrones. Extraordinary room-temperature photoluminescence in triangular ws2 monolayers. *Nano Letters*, 13(8):3447–3454, 2013. PMID: 23194096.

[101] S. Saqib Shams, Ruoyu Zhang, and Jin Zhu. Graphene synthesis: a Review. *Materials Science-Poland*, 33(3):566–578, sep 2015.

[102] Jiawen You, Md Delowar Hossain, and Zhengtang Luo. Synthesis of 2D transition metal dichalcogenides by chemical vapor deposition with controlled layer number and morphology. *Nano Convergence*, 5(1), sep 2018.

[103] Seolhee Yoo, Sangsig Kim, and Yong-Won Song. Lithography-free fabrication of field effect transistor channels with randomly contact-printed black phosphorus flakes. *Materials Science in Semiconductor Processing*, 86:58–62, nov 2018.

[104] Rafik Addou, Luigi Colombo, and Robert M. Wallace. Surface Defects on Natural MoS_2. *ACS Applied Materials & Interfaces*, 7(22):11921–11929, 2015. PMID: 25980312.

[105] Li Lin, Jincan Zhang, Haisheng Su, Jiayu Li, Luzhao Sun, Zihao Wang, Fan Xu, Chang Liu, Sergei Lopatin, Yihan Zhu, Kaicheng Jia, Shulin Chen, Dingran Rui, Jingyu Sun, Ruiwen Xue, Peng Gao, Ning Kang, Yu Han, H. Q. Xu, Yang Cao, K. S. Novoselov, Zhongqun Tian, Bin Ren, Hailin Peng, and Zhongfan Liu. Towards super-clean graphene. *Nature Communications*, 10(1), apr 2019.

[106] Liu Wang, Jiansheng Jie, Zhibin Shao, Qing Zhang, Xiaohong Zhang, Yuming Wang, Zheng Sun, and Shuit-Tong Lee. MoS2/si heterojunction with vertically standing layered structure for ultrafast, high-detectivity, self-driven visible-near infrared photodetectors. *Advanced Functional Materials*, 25(19):2910–2919, mar 2015.

[107] Rup K. Chowdhury, Rishi Maiti, Arup Ghorai, Anupam Midya, and Samit K. Ray. Novel silicon compatible p-WS_2 2D/3D heterojunction devices exhibiting broadband photoresponse and superior detectivity. *Nanoscale*, 8(27):13429–13436, 2016.

[108] Changli Li, Qi Cao, Faze Wang, Yequan Xiao, Yanbo Li, Jean-Jacques Delaunay, and Hongwei Zhu. Engineering graphene and TMDs based van der waals heterostructures for photovoltaic and photoelectrochemical solar energy conversion. *Chemical Society Reviews*, 47(13):4981–5037, 2018.

[109] Changsik Kim, Inyong Moon, Daeyeong Lee, Min Sup Choi, Faisal Ahmed, Seunggeol Nam, Yeonchoo Cho, Hyeon-Jin Shin, Seongjun Park, and Won Jong Yoo. Fermi level pinning at electrical metal contacts of monolayer molybdenum dichalcogenides. *ACS Nano*, 11(2):1588–1596, jan 2017.

[110] Kyung-Ah Min, Jinwoo Park, Robert M Wallace, Kyeongjae Cho, and Suklyun Hong. Reduction of Fermi level pinning at Au–MoS2 interfaces by atomic passivation on Au surface. *2D Materials*, 4(1):015019, nov 2016.

[111] R. N. Sajjad, W. Chern, J. L. Hoyt, and D. A. Antoniadis. Trap Assisted Tunneling and Its Effect on Subthreshold Swing of Tunnel FETs. *IEEE Transactions on Electron Devices*, 63(11):4380–4387, November 2016.

[112] Lang Zeng, Zheng Xin, Shao-Wen Chen, Gang Du, Jin-Feng Kang, and Xiao-Yan Liu. Remote phonon and impurity screening effect of substrate and gate dielectric on electron dynamics in single layer MoS_2. *AIP*, 103, 2013.

[113] Haining Wang, Changjian Zhang, and Farhan Rana. Surface recombination limited lifetimes of photoexcited carriers in few-layer transition metal dichalcogenide MoS_2. *Nano Letters*, 15(12):8204–8210, nov 2015.

[114] Vikram Passi, Amit Gahoi, Enrique G. Marin, Teresa Cusati, Alessandro Fortunelli, Giuseppe Iannaccone, Gianluca Fiori, and Max C. Lemme. Ultralow specific contact resistivity in metal–graphene junctions via contact engineering. *Advanced Materials Interfaces*, 6(1):1801285, nov 2018.

[115] Wei Cao, Jiahao Kang, Wei Liu, and Kaustav Banerjee. A Compact Current–Voltage Model for 2D Semiconductor Based Field-Effect Transistors Considering Interface Traps, Mobility Degradation, and Inefficient Doping Effect. *IEEE Transactions on Electron Devices*, 61(12):4282–4290, dec 2014.

[116] Dragica Vasileska, Stephen M. Goodnick, and Gerhard Klimeck. *Computational Electronics, Semiclassical and Quantum Device Modeling and Simulation*. Taylor & Francis Group, 2010.

[117] Yee Sin Ang, Hui Ying Yang, and L. K. Ang. Universal Scaling Laws in Schottky Heterostructures Based on Two-Dimensional Materials. *Physical Review Letters*, 121(5), aug 2018.

[118] Kwok K. Ng Simon M. Sze. *Physics of Semiconductor Devices*. Wiley-Interscience, 3 edition, 2006.

[119] Yuanyue Liu, Paul Stradins, and Su-Huai Wei. Van der Waals metal-semiconductor junction: Weak Fermi level pinning enables effective tuning of Schottky barrier. *Science Advances*, 2(4):e1600069, apr 2016.

[120] Kyounghoon Yang, Jack R. East, and George I. Haddad. Numerical modeling of abrupt heterojunctions using a thermionic-field emission boundary condition. *Solid-State Electronics*, 36(3):321 – 330, 1993.

[121] C. Y. Chang and S. M. Sze. Carrier transport across metal-semiconductor barriers. *Solid-State Electronics*, 13:727–740, 1970.

[122] Yuji Ando and Tomohiro Itoh. Calculation of transmission tunneling current across arbitrary potential barriers. *Journal of Applied Physics*, 61(4):1497–1502, 1987.

[123] Gregor Cernivec, Andri Jagomägi, Franc Smole, and Marko Topic. Numerical and experimental indication of thermally activated tunneling transport in {CIS} monograin layer solar cells. *Solid-State Electronics*, 52(1):78–85, 2008.

[124] Nacer Debbar. Investigation of the dark electrical characteristics of the lateral metal-semiconductor-metal photodetectors using two-dimensional numerical simulation. *International Journal of Numerical Modelling: Electronic Networks, Devices and Fields*, 24(4):335–344, jul 2010.

[125] Eric Bersch, Sylvie Rangan, Robert Allen Bartynski, Eric Garfunkel, and Elio Vescovo. Band offsets of ultrathin high-κ oxide films with Si. *Physical Review B*, 78:085114, Aug 2008.

[126] Abhinandan Borah, Punnu Jose Sebastian, Ankur Nipane, and James T. Teherani. An Intuitive Equivalent Circuit Model for Multilayer Van Der Waals Heterostructures. *IEEE Transactions on Electron Devices*, pages 1–7, 2018.

[127] M.S. Lundstrom and R.J. Schuelke. Modeling semiconductor heterojunctions in equilibrium. *Solid-State Electronics*, 25(8):683 – 691, 1982.

[128] J. Verschraegen and M. Burgelman. Numerical modeling of intra-band tunneling for heterojunction solar cells in SCAPS. *Thin Solid Films*, 515(15):6276–6279, 2007. Proceedings of Sympodium O on Thin Film Chalcogenide Photovoltaic Materials, EMRS 2006 Conference.

[129] M. G. Bardon, H. P. Neves, R. Puers, and C. Van Hoof. Pseudo-Two-Dimensional Model for Double-Gate Tunnel FETs Considering the Junctions Depletion Regions. *IEEE Transactions on Electron Devices*, 57(4):827–834, April 2010.

[130] Arnab Biswas, Surya Shankar Dan, Cyrille Le Royer, Wladyslaw Grabinski, and Adrian M. Ionescu. TCAD simulation of SOI TFETs and calibration of non-local band-to-band tunneling model. *Microelectronic Engineering*, 98:334 – 337, 2012. Special issue MNE 2011 - Part II.

[131] G. A. M. Hurkx, D. B. M. Klaassen, and M. P. G. Knuvers. A new recombination model for device simulation including tunneling. *IEEE Transactions on Electron Devices*, 39(2):331–338, 1992.

[132] W. Shockley and W. T. Read. Statistics of the Recombinations of Holes and Electrons. *Physical Review*, 87(5):835–842, sep 1952.

[133] R. N. Hall. Recombination processes in semiconductors. *The Institution of Electrical Engineers*, 1960.

[134] Siegfried Selberherr. *Analysis and Simulation of Semiconductor Devices*. Springer-Verlag Wien, 1 edition, 1984.

[135] Haining Wang, Changjian Zhang, and Farhan Rana. Ultrafast dynamics of defect-assisted electron–hole recombination in monolayer MoS_2. *Nano Letters*, 15(1):339–345, dec 2014.

[136] Jenny Nelson. *The Physics of Solar Cells*. Imperial College Press, 2003.

[137] Nacer Debbar. Theoretical study of the DC and transient characteristics of a lateral Schottky barrier photodiode for application as high-speed photodetector. *International Journal of Numerical Modelling: Electronic Networks, Devices and Fields*, 29(2):333–342, jun 2015.

[138] Enrique González Marín. *Modeling and Simulation of Semiconductor Nanowires for Future Technology Nodes*. PhD thesis, Universidad de Granada, 2014.

[139] N. G. Nilsson. Empirical approximations for the Fermi energy in a semiconductor with parabolic bands. *Applied Physics Letters*, 33(7):653–654, oct 1978.

[140] Enrique González Marín. *Modelling and Simulaton of Semiconductor Nanowires for Future Technology Nodes*. PhD thesis, University of Granada, 2014.

[141] David Esseni, Pierpaolo Palestri, and Luca Selmi. *Nanoscale MOS Transistors, Semi-Classical Transport an Applications*. Cambridge University Press, 2011.

[142] Paul Harrison. *Quantum Wells, Wires and Dots*. Wiley-Interscience, 2005.

[143] Marc Baldo. *Introduction to Nanoelectronics*. MIT OpenCourseWare, 2010.

[144] Oskar Baumgartner, Zlatan Stanojevic, Klaus Schnass, Markus Karner, and Hans Kosina. VSP-a Quantum-electronic Simulation Framework. *Journal of Computer Electronics*, 12(4):701–721, December 2013.

[145] R. W. Hockney and J. W. Eastwood. *Computer Simulation Using Particles*. IOP Publishing Ltd, 1988.

[146] Melinda Y. Han, Barbaros Özyilmaz, Yuanbo Zhang, and Philip Kim. Energy band-gap engineering of graphene nanoribbons. *Physical Review Letters*, 98:206805, 2007.

[147] Kin Fai Mak, Changgu Lee, James Hone, Jie Shan, and Tony F. Heinz. Atomically thin MoS_2: A new direct-gap semiconductor. *Physical Review Letters*, 105:136805, 2010.

[148] H. Peelaers and C.G. Van de Walle. Effects of strain on band structure and effective masses in MoS_2. *Physical Review B*, 86:241401, 2012.

[149] Albert Polman and Harry A. Atwater. Photonic design principles for ultrahigh-efficiency photovoltaics. *Nature Materials*, 11:174–177, 2012.

[150] Theresia Knobloch, Gerhard Rzepa, Yury Yu. Illarionov, Michael Waltl, Franz Schanovsky, Bernhard Stampfer, Marco M. Furchi, Thomas Mueller, and Tibor Grasser. A physical model for the hysteresis in MoS2 transistors. *IEEE Journal of the Electron Devices Society*, 6:972–978, 2018.

[151] Michael K. L. Man, Skylar Deckoff-Jones, Andrew Winchester, Guangsha Shi, Gautam Gupta, Aditya D. Mohite, Swastik Kar, Emmanouil Kioupakis, Saikat Talapatra, and Keshav M. Dani. Protecting the properties of monolayer MoS2 on silicon based substrates with an atomically thin buffer. *Scientific Reports*, 6(1), feb 2016.

[152] Kristen Kaasbjerg, Kristian S. Thygesen, and Karsten W. Jacobsen. Phonon-limited mobility in n-type single-layer MoS_2 from first principles. *Physical Review B*, 85:115317, 2012.

[153] Zhun-Yong Ong and Massimo V. Fischetti. Mobility enhancement and temperature dependence in top-gated single-layer MoS_2. *Physical Review B*, 88:165316, 2013.

[154] Branimir Radisavljevic and Andras Kis. Mobility engineering and a metal-insulator transition in monolayer MoS_2. *Nature Materials*, 12:815–820, 2013.

[155] Lang Zeng, Zheng Xin, Shao-Wen Chen, Gang Du, Jin-Feng Kang, and Xiao-Yan Liu. Phonon-limited electron mobility in single-layer MoS_2. *Chinese Physical Letter*, 31, 2014.

[156] Britton W. H. Baugher, Hugh O. H. Churchill, Yafang Yang, and Pablo Jarillo-Herrero. Intrinsic electronic transport properties of high-quality monolayer and bilayer MoS_2. *Nano Letters*, 13(9):4212–4216, 2013.

[157] Sunkook Kim, Aniruddha Konar, Wan-Sik Hwang, Jong Hak Lee, Jiyoul Lee, Jaehyun Yang, Changhoon Jung, Hyoungsub Kim, Ji-Beom Yoo, Jae-Young Choi, Yong Wan Jin, Sang Yoon Lee, Debdeep Jena, Woong Choi, and Kinam Kim. High-mobility and low-power thin-film transistors based on multilayer MoS_2 crystals. *Nature Communications*, 3(1011), 2012.

[158] F. G. Ruiz, B. Biel, J. M. Gonzalez-Medina, A. Toral, E. G. Marin, I. M. Tienda-Luna, and A. Godoy. Calculation of the ballistic current of few-layer MoS_2 field-effect transistors. In *19^{th} International Conference on Electron Dynamics in Semiconductors, Optoelectronics and Nanostructures*, 2015.

[159] Tawinan Cheiwchanchamnangij and Walter R. L. Lambrecht. Quasiparticle band structure calculation of monolayer, bilayer, and bulk MoS_2. *Physical Review B*, 85:205302, 2012.

[160] Eugene S. Kadantsev and Pawel Hawrylak. Electronic structure of a single MoS_2 monolayer. *Solid State Communications*, 152:909–913, 2012.

[161] Yongqing Cai, Jinghua Lan, Gang Zhang, and Yong-Wei Zhang. Lattice vibrational modes and phonon thermal conductivity of monolayer MoS_2. *Physical Review B*, 89:035438, 2014.

[162] Yi Ding, Yanli Wang, Jun Ni, Lin Shi, Siqi Shi, and Weihua Tang. First principles study of structural, vibrational and electronic properties of graphene-like MX_2 (M=Mo, Nb, W, Ta; X=S, Se, Te) monolayers. *Physica B*, 406:2254–2260, 2011.

[163] D A Greenwood. The boltzmann equation in the theory of electrical conduction in metals. *Proceedings of the Physical Society*, 71(4):585–596, apr 1958.

[164] L. L. Moseley and T. Lukes. A simplified derivation of the kubo-greenwood formula. *American Journal of Physics*, 46(6):676–677, jun 1978.

[165] J.M. Gonzalez-Medina, F.G. Ruiz, E.G. Marin, A. Godoy, and F. Gámiz. Simulation study of the electron mobility in few-layer mos2 metal-insulator-semiconductor field-effect transistors. *Solid-State Electronics*, 114:30 – 34, 2015.

[166] M. Lundstrom. *Fundamental of Carrier Transport*. Cambridge University Press, New York. USA, 2009.

[167] F. Driussi and D. Esseni. Simulation study of coulomb mobility in strained silicon. *IEEE Transactions on Electron Devices*, 56(9):2052–2059, Sept 2009.

[168] F. Gamiz, F. Jiménez-Molinos, J. B. Roldán, and P. Cartujo-Cassinello. Coulomb scattering model for ultrathin silicon-on-insulator inversion layers. *Applied Physics Letters*, 80(20):3835–3837, 2002.

[169] F. Gámiz, J. A. López-Villanueva, J. A. Jiménez-Tejada, I. Melchor, and A. Palma. A comprehensive model for coulomb scattering in inversion layers. *Journal of Applied Physics*, 75(2):924–934, 1994.

[170] D. Esseni and A. Abramo. Modeling of electron mobility degradation by remote coulomb scattering in ultrathin oxide mosfets. *IEEE Transactions on Electron Devices*, 50(7):1665–1674, July 2003.

[171] H. R. Huff and D. C. Gilmer. *High Dielectric Constant Materials*. Springer-Verlag, 2005.

[172] E. G. Marin, F. G. Ruiz, A. Godoy, I. M. Tienda-Luna, C. Martínez-Blanque, and F. Gámiz. Theoretical interpretation of the electron mobility behavior in InAs nanowires. *Journal of Applied Physics*, 116(17):174505, 2014.

[173] Kristen Kaasbjerg, Kristian S. Thygesen, and Antti-Pekka Jauho. Acoustic phonon limited mobility in two-dimensional semiconductors: Deformation potential and piezoelectric scattering in monolayer mos_2 from first principles. *Phys. Rev. B*, 87:235312, Jun 2013.

[174] M. Casalino, L. Sirleto, M. Iodice, N. Saffioti, M. Gioffrè, I. Rendina, and G. Coppola. Cu/p-Si Schottky barrier-based near infrared photodetector integrated with a silicon-on-insulator waveguide. *Applied Physics Letters*, 96(24):241112, jun 2010.

[175] A. B. Kuzmenko, E. van Heumen, F. Carbone, and D. van der Marel. Universal optical conductance of graphite. *Physical Review Letters*, 100(11), mar 2008.

[176] Fengnian Xia, Thomas Mueller, Yu ming Lin, Alberto Valdes-Garcia, and Phaedon Avouris. Ultrafast graphene photodetector. *Nature Nanotechnology*, 4(12):839–843, oct 2009.

[177] Muhammed Emre Ayhan, Golap Kalita, Masaharu Kondo, and Masaki Tanemura. Photoresponsivity of silver nanoparticles decorated graphene–silicon schottky junction. *RSC Adv.*, 4(51):26866–26871, 2014.

[178] Thomas Mueller, Fengnian Xia, and Phaedon Avouris. Graphene photodetectors for high-speed optical communications. *Nature Photonics*, 4(5):297–301, mar 2010.

[179] Wee Shing Koh, Choon How Gan, Wee Kee Phua, Yuriy A. Akimov, and Ping Bai. The potential of graphene as an ITO replacement in organic solar cells: An optical perspective. *IEEE Journal of Selected Topics in Quantum Electronics*, 20(1):36–42, jan 2014.

[180] Yingjie Ma and Linjie Zhi. Graphene-based transparent conductive films: Material systems, preparation and applications. *Small Methods*, 3(1):1800199, oct 2018.

[181] Xiaohong An, Fangze Liu, Yung Joon Jung, and Swastik Kar. Tunable Graphene–Silicon Heterojunctions for Ultrasensitive Photodetection. *Nano Letters*, 13(3):909–916, feb 2013.

[182] Sarah Riazimehr, Andreas Bablich, Daniel Schneider, Satender Kataria, Vikram Passi, Chanyoung Yim, Georg S. Duesberg, and Max C. Lemme. Spectral sensitivity of graphene/silicon heterojunction photodetectors. *Solid-State Electronics*, 115:207–212, 2016.

[183] Yuxuan Lin, Xinming Li, Dan Xie, Tingting Feng, Yu Chen, Rui Song, He Tian, Tianling Ren, Minlin Zhong, Kunlin Wang, and Hongwei Zhu. Graphene/semiconductor heterojunction solar cells with modulated antireflection and graphene work function. *Energy Environment Science*, 6(1):108–115, 2013.

[184] M. G. Ancona. Electron transport in graphene from a diffusion-drift perspective. *IEEE Transactions on Electron Devices*, 57(3):681–689, March 2010.

[185] Xin Gan, Ruitao Lv, Haoyue Zhu, Lai-Peng Ma, Xuyang Wang, Zexia Zhang, Zheng-Hong Huang, Hongwei Zhu, Wencai Ren, Mauricio Terrones, and Feiyu Kang. Polymer-coated graphene films as anti-reflective transparent electrodes for Schottky junction solar cells. *Journal of Materials Chemistry A*, 4(36):13795–13802, 2016.

[186] M. Massicotte, P. Schmidt, F. Vialla, K. G. Schädler, A. Reserbat-Plantey, K. Watanabe, T. Taniguchi, K. J. Tielrooij, and F. H. L. Koppens. Picosecond photoresponse in van der Waals heterostructures. *Nature Nanotechnology*, 11(1):42–46, oct 2015.

[187] Hyung-Youl Park, Woo-Shik Jung, Dong-Ho Kang, Jaeho Jeon, Gwangwe Yoo, Yongkook Park, Jinhee Lee, Yun Hee Jang, Jaeho Lee, Seongjun Park, Hyun-Yong Yu, Byungha Shin, Sungjoo Lee, and Jin-Hong Park. Extremely Low Contact Resistance on Graphene through n-Type Doping and Edge Contact Design. *Advanced Materials*, 28(5):864–870, nov 2015.

[188] Xinming Li, Hongwei Zhu, Kunlin Wang, Anyuan Cao, Jinquan Wei, Chunyan Li, Yi Jia, Zhen Li, Xiao Li, and Dehai Wu. Graphene-On-Silicon Schottky Junction Solar Cells. *Advanced Materials*, 22(25):2743–2748, apr 2010.

[189] Yi Song, Xinming Li, Charles Mackin, Xu Zhang, Wenjing Fang, Tomás Palacios, Hongwei Zhu, and Jing Kong. Role of Interfacial Oxide in High-Efficiency Graphene–Silicon Schottky Barrier Solar Cells. *Nano Letters*, 15(3):2104–2110, feb 2015.

[190] Xinming Li, Miao Zhu, Mingde Du, Zheng Lv, Li Zhang, Yuanchang Li, Yao Yang, Tingting Yang, Xiao Li, Kunlin Wang, Hongwei Zhu, and Ying Fang. High Detectivity Graphene-Silicon Heterojunction Photodetector. *Small*, 12(5):595–601, dec 2015.

[191] Han Liu, Adam T. Neal, Zhen Zhu, Zhe Luo, Xianfan Xu, David Tománek, and Peide D. Ye. Phosphorene: An unexplored 2d semiconductor with a high hole mobility. *ACS Nano*, 8(4):4033–4041, 2014. PMID: 24655084.

[192] Antonio Di Bartolomeo, Filippo Giubileo, Giuseppe Luongo, Laura Iemmo, Nadia Martucciello, Gang Niu, Mirko Fraschke, Oliver Skibitzki, Thomas Schroeder, and Grzegorz Lupina. Tunable Schottky barrier and high responsivity in graphene/Si-nanotip optoelectronic device. *2D Materials*, 4(1):015024, nov 2016.

[193] Antonio Di Bartolomeo, Giuseppe Luongo, Filippo Giubileo, Nicola Funicello, Gang Niu, Thomas Schroeder, Marco Lisker, and Grzegorz Lupina. Hybrid graphene/silicon schottky photodiode with intrinsic gating effect. *2D Materials*, 4(2):025075, apr 2017.

[194] Sarah Riazimehr, Satender Kataria, Rainer Bornemann, Peter Haring Bolívar, Francisco Javier Garcia Ruiz, Olof Engström, Andres Godoy, and Max C. Lemme. High Photocurrent in Gated Graphene-Silicon Hybrid Photodiodes. *ACS Photonics*, 4(6):1506–1514, 2017.

[195] Sarah Riazimehr, Satender Kataria, Jose M. Gonzalez-Medina, Stefan Wagner, Mehrdad Shaygan, Stephan Suckow, Francisco G. Ruiz, Olof Engström, Andres Godoy, and Max C. Lemme. High Responsivity and Quantum Efficiency of Graphene/Silicon Photodiodes Achieved by Interdigitating Schottky and Gated Regions. *ACS Photonics*, 6(1):107–115, oct 2018.

[196] Yanbin An, Ashkan Behnam, Eric Pop, and Ant Ural. Metal-semiconductor-metal photodetectors based on graphene/p-type silicon schottky junctions. *Applied Physics Letters*, 102(1):013110, jan 2013.

[197] Martin A. Green. Self-consistent optical parameters of intrinsic silicon at 300k including temperature coefficients. *Solar Energy Materials and Solar Cells*, 92(11):1305–1310, nov 2008.

[198] N. Z. Butt, B. K. Sarker, Y. P. Chen, and M. A. Alam. Substrate-Induced Photofield Effect in Graphene Phototransistors. *IEEE Transactions on Electron Devices*, 62(11):3734–3741, Nov 2015.

[199] Xintong Zhang, Lining Zhang, Zubair Ahmed, and Mansun Chan. Origin of nonideal graphene-silicon schottky junction. *IEEE Transactions on Electron Devices*, 65(5):1995–2002, may 2018.

[200] Oldwig von Roos. A simple theory of back surface field (BSF) solar cells. *Journal of Applied Physics*, 49(6):3503–3511, jun 1978.

[201] Subash Adhikari, Chandan Biswas, Manh-Ha Doan, Sung-Tae Kim, Chandramouli Kulshreshtha, and Young Hee Lee. Minimizing Trap Charge Density towards an Ideal Diode in Graphene-Silicon Schottky Solar Cell. *ACS Applied Materials & Interfaces*, 11(1):880–888, dec 2018.

[202] Lili Yu, Yi-Hsien Lee, Xi Ling, Elton J. G. Santos, Yong Cheol Shin, Yuxuan Lin, Madan Dubey, Efthimios Kaxiras, Jing Kong, Han Wang, and Tomás Palacios. Graphene/MoS_2 hybrid technology for large-scale two-dimensional electronics. *Nano Letters*, 14(6):3055–3063, 2014.

[203] Michele Buscema, Joshua O. Island, Dirk J. Groenendijk, Sofya I. Blanter, Gary A. Steele, Herre S. J. van der Zant, and Andres Castellanos-Gomez. Photocurrent generation with two-dimensional van der Waals semiconductors. *Chemical Society Reviews*, 44(11):3691–3718, 2015.

[204] Hehai Fang and Weida Hu. Photogating in Low Dimensional Photodetectors. *Advanced Science*, 4(12):1700323, oct 2017.

[205] Bastian Miller, Eric Parzinger, Anna Vernickel, Alexander W. Holleitner, and Ursula Wurstbauer. Photogating of mono- and few-layer MoS2. *Applied Physics Letters*, 106(12):122103, mar 2015.

[206] Marco M. Furchi, Dmitry K. Polyushkin, Andreas Pospischil, and Thomas Mueller. Mechanisms of Photoconductivity in Atomically Thin MoS_2. *Nano Letters*, 14(11):6165–6170, 2014. PMID: 25299515.

[207] Hai Huang, Jianlu Wang, Weida Hu, Lei Liao, Peng Wang, Xudong Wang, Fan Gong, Yan Chen, Guangjian Wu, Wenjin Luo, Hong Shen, Tie Lin, Jinglan Sun, Xiangjian Meng, Xiaoshuang Chen, and Junhao Chu. Highly sensitive visible to infrared MoTe2 photodetectors enhanced by the photogating effect. *Nanotechnology*, 27(44):445201, sep 2016.

[208] `https://cmr.fysik.dtu.dk/c2db/c2db.html`.

[209] Claudia Ruppert, Ozgur Burak Aslan, and Tony F. Heinz. Optical properties and band gap of single- and few-layer MoTe2 crystals. *Nano Letters*, 14(11):6231–6236, oct 2014.

[210] Cesar E. P. Villegas and A. R. Rocha. Elucidating the optical properties of novel heterolayered materials based on MoTe2–InN for photovoltaic applications. *The Journal of Physical Chemistry C*, 119(21):11886–11895, may 2015.

[211] Ignacio Gutiérrez Lezama, Ashish Arora, Alberto Ubaldini, Céline Barreteau, Enrico Giannini, Marek Potemski, and Alberto F. Morpurgo. Indirect-to-Direct

Band Gap Crossover in Few-Layer $MoTe_2$. *Nano Letters*, 15(4):2336–2342, mar 2015.

[212] Jiahao Kang, Wei Liu, Deblina Sarkar, Debdeep Jena, and Kaustav Banerjee. Computational study of metal contacts to monolayer transition-metal dichalcogenide semiconductors. *Phys. Rev. X*, 4:031005, Jul 2014.

[213] Kai Sotthewes, Rik van Bremen, Edwin Dollekamp, Tim Boulogne, Krystian Nowakowski, Daan Kas, Harold J. W. Zandvliet, and Pantelis Bampoulis. Universal Fermi-Level Pinning in Transition-Metal Dichalcogenides. *The Journal of Physical Chemistry C*, 123(9):5411–5420, feb 2019.

[214] Debdeep Jena, Kaustav Banerjee, and Grace Huili Xing. Intimate contacts. *Nature Materials*, 13(12):1076–1078, dec 2014.

[215] Yohta Sata, Rai Moriya, Satoru Masubuchi, Kenji Watanabe, Takashi Taniguchi, and Tomoki Machida. N- and p-type carrier injections into WSe_2 with van der Waals contacts of two-dimensional materials. *Japanese Journal of Applied Physics*, 56(4S):04CK09, mar 2017.

[216] Yuan Liu, Hao Wu, Hung-Chieh Cheng, Sen Yang, Enbo Zhu, Qiyuan He, Mengning Ding, Dehui Li, Jian Guo, Nathan O. Weiss, Yu Huang, and Xiangfeng Duan. Toward Barrier Free Contact to Molybdenum Disulfide Using Graphene Electrodes. *Nano Letters*, 15(5):3030–3034, apr 2015.

[217] Xu Cui, Gwan-Hyoung Lee, Young Duck Kim, Ghidewon Arefe, Pinshane Y. Huang, Chul-Ho Lee, Daniel A. Chenet, Xian Zhang, Lei Wang, Fan Ye, Filippo Pizzocchero, Bjarke S. Jessen, Kenji Watanabe, Takashi Taniguchi, David A. Muller, Tony Low, Philip Kim, and James Hone. Multi-terminal transport measurements of MoS_2 using a van der waals heterostructure device platform. *Nature Nanotechnology*, 10(6):534–540, apr 2015.

[218] Chong Lin, Zhengfei Gao, and Jian Jin. Boosting Alkaline Hydrogen Evolution Activity with Ni-Doped MoS_2/Reduced Graphene Oxide Hybrid Aerogel. *ChemSusChem*, dec 2018.

[219] Yanguang Li, Hailiang Wang, Liming Xie, Yongye Liang, Guosong Hong, and Hongjie Dai. MoS_2 Nanoparticles Grown on Graphene: An Advanced Catalyst for the Hydrogen Evolution Reaction. *Journal of the American Chemical Society*, 133(19):7296–7299, may 2011.

[220] Andres Castellanos-Gomez, Jorge Quereda, Herko P. van der Meulen, Nicolás Agraït, and Gabino Rubio-Bollinger. Spatially resolved optical absorption spectroscopy of single- and few-layer MoS_2 by hyperspectral imaging. *Nanotechnology*, 27(11):115705, feb 2016.

[221] Andreas Pospischil, Markus Humer, Marco M. Furchi, Dominic Bachmann, Romain Guider, Thomas Fromherz, and Thomas Mueller. CMOS-compatible graphene photodetector covering all optical communication bands. *Nature Photonics*, 7(11):892–896, sep 2013.

[222] Dung-Sheng Tsai, Keng-Ku Liu, Der-Hsien Lien, Meng-Lin Tsai, Chen-Fang Kang, Chin-An Lin, Lain-Jong Li, and Jr-Hau He. Few-layer MoS2 with high broadband photogain and fast optical switching for use in harsh environments. *ACS Nano*, 7(5):3905–3911, apr 2013.

[223] Guangjian Wu, Xudong Wang, Yan Chen, Zhen Wang, Hong Shen, Tie Lin, Weida Hu, Jianlu Wang, Shantao Zhang, Xiangjian Meng, and Junhao Chu. Ultrahigh photoresponsivity MoS2 photodetector with tunable photocurrent generation mechanism. *Nanotechnology*, 29(48):485204, oct 2018.

[224] Domenico De Fazio, Ilya Goykhman, Duhee Yoon, Matteo Bruna, Anna Eiden, Silvia Milana, Ugo Sassi, Matteo Barbone, Dumitru Dumcenco, Kolyo Marinov, Andras Kis, and Andrea C. Ferrari. High responsivity, large-area graphene/MoS2 flexible photodetectors. *ACS Nano*, 10(9):8252–8262, sep 2016.

[225] Nengjie Huo and Gerasimos Konstantatos. Ultrasensitive all-2d MoS2 phototransistors enabled by an out-of-plane MoS2 PN homojunction. *Nature Communications*, 8(1), sep 2017.

[226] O. Salehzadeh, N. H. Tran, X. Liu, I. Shih, and Z. Mi. Exciton kinetics, quantum efficiency, and efficiency droop of monolayer MoS2 light-emitting devices. *Nano Letters*, 14(7):4125–4130, jun 2014.

[227] Jinsu Pak, Ilmin Lee, Kyungjune Cho, Jae-Keun Kim, Hyunhak Jeong, Wang-Taek Hwang, Geun Ho Ahn, Keehoon Kang, Woo Jong Yu, Ali Javey, Seungjun Chung, and Takhee Lee. Intrinsic optoelectronic characteristics of MoS2 phototransistors via a fully transparent van der waals heterostructure. *ACS Nano*, 13(8):9638–9646, jul 2019.

[228] G. Smith. *Numerical Solution of Partial Differential Equations: Finite Diference Methods*. Oxford University Press, New York. USA, third edition, 1985.

[229] D.L. Scharfetter and H.K. Gummel. Large-signal analysis of a silicon read diode oscillator. *IEEE Transactions on Electron Devices*, 16(1):64–77, jan 1969.

[230] H. Hernández, J. E. Román, A. Tomás, and V. Vidal. Arnoldi methods in slepc. *Universitat Politècnica de València*, 2006.

[231] Endre Süli. *An introduction to numerical analysis*. Cambridge University Press, Cambridge, 2003.

[232] Amparo Gil. *Numerical methods for special functions*. Society for Industrial and Applied Mathematics, Philadelphia, 2007.

[233] Alexander H.D. Cheng and Daisy T. Cheng. Heritage and early history of the boundary element method. *Elsevier*, 29, 2005.

[234] Landolt-Börnstein. *Numerical data and Functional Relationships in Science and Technology Quantum Structures*. Springer, Berlin, first edition edition, 2001.

[235] Akash Laturia, Maarten L. Van de Put, and William G. Vandenberghe. Dielectric properties of hexagonal boron nitride and transition metal dichalcogenides: from monolayer to bulk. *npj 2D Materials and Applications*, 2(1), mar 2018.

[236] Filip A. Rasmussen and Kristian S. Thygesen. Computational 2d materials database: Electronic structure of transition-metal dichalcogenides and oxides. *The Journal of Physical Chemistry C*, 119(23):13169–13183, jun 2015.

[237] Ming-Kwei Lee Simon M. Sze. *Semiconductor Devices: Physics and Technology*. Wiley, 3 edition, 2012.

[238] R. Schlaf, O. Lang, C. Pettenkofer, and W. Jaegermann. Band lineup of layered semiconductor heterointerfaces prepared by van der Waals epitaxy: Charge transfer correction term for the electron affinity rule. *Journal of Applied Physics*, 85(5):2732–2753, mar 1999.

[239] L. Gmelin. *Gmelin handbook of inorganic and organometallic chemistry*. Springer-Verlag, 1995.